Plasma diagnosis of reactive high power impulse magnetron sputtering (HiPIMS) discharges

by

Michael Bowes

The University of Liverpool
Department of Electrical Engineering and Electronics

Thesis submitted in accordance with the requirements of the University of Liverpool for the degree of Doctor of Philosophy

Liverpool, June 2014

Declaration

I hereby declare that this thesis is my own work and no further sources of information have been used other than the references cited. Neither this thesis nor any part of it have been submitted to any other university or institution for the application of another degree or qualification.

Signed: _____(Michael Bowes)

Date: _____

For Alessandra

Abstract

Reactive HiPIMS discharges have been investigated by employing a selection of plasma diagnostic techniques. Plasma dynamics in a reactive HiPIMS discharge were studied by means of a single Langmuir probe which revealed electron and positive ion densities of the order of $10^{17} - 10^{18}$ m^{-3} in typical substrate positions, the temporal evolutions of which exhibited a dual-peak structure attributed to the propagation of an ion acoustic wave or the compression and subsequent rarefaction of the process gas caused by the intense 'sputter wind'. The compression phase is also thought to be the cause of the quenching of the effective electron temperature observed during the on-time with the rarefaction phase being responsible for the increase in the effective electron temperature toward the end of the voltage pulse.

Negative ion dynamics in the afterglow of a reactive HiPIMS discharge were also studied by means of a Langmuir probe for a range of oxygen partial pressures. The extended afterglow was found to be highly electronegative with the negative ion-to-electron ratio (α) at 3 milliseconds after the pulse termination reaching values of almost 400 for the highest oxygen partial pressures. By comparing results to a simple plasma-chemical model, it is speculated that increased negative ion formation occurs for higher oxygen partial pressures due to the increased availability of oxygen metastables that are formed in the active phase. Despite exhibiting a strong correlation, a comparison to the α values determined by photodetachment revealed an overestimation by a factor of $8 - 15$ when employing the Langmuir probe method. Furthermore, from photodetachment measurements the O^- ion density was observed to peak in the early afterglow at values of the order of 10^{17} m^{-3}. It was also concluded that a negative ion flux of approximately $10^{17} - 10^{18}$ m^{-2} s^{-1} could be expected at the chamber walls and substrate surface once the plasma afterglow transitions into an ion-ion state, which could have implications for many plasma processing methods.

Time-averaged energy distributions of oxygen negative ions obtained using energy-resolved mass spectrometry during reactive HiPIMS of Ti in an Ar/O_2 gas mixture revealed three distinct populations of O^- ions at varying energies. The peak of the high-energy population was found to correspond to the value of average applied target potential during the pulse on-time. Comparison to a Thompson energy distribution of sputtered particles suggested that O^- ions are sputtered from the target surface before undergoing acceleration in the cathode sheath. A study of the attenuation of the high-energy O^- ion population as a function of the pressure-distance product yielded an effective total cross section of 2×10^{-19} m^2 for O^- interacting with the background Ar/O_2 gas mixture for both Ti and Nb targets.

During reactive HiPIMS of different target materials, a correlation between O^- emission and the ion-induced secondary electron emission coefficient was found. In addition, large differences in the high-energy O^- yield were also observed when employing differ-

ent inert gases mixed with O_2, which was also attributed to changes in the ion-induced secondary electron emission coefficient.

The deposition rates in reactive HiPIMS of TiO_2 using different inert gases were measured by means of a quartz crystal microbalance. In contrast to the trends predicted by SRIM as well as those measured in DCMS, the power normalized deposition rate, D_n, was found to increase with the mass of inert gas in both metallic and reactive modes, with the exception of the Xe/O_2 gas mixture. The observed increase of D_n with the mass of inert gas was partially attributed to a decreased return effect in the heavier gases. For the case of Kr/O_2, the normalized deposition rate measured in HiPIMS was found to be 87% of that measured in equivalent DCMS operation despite no attempt at optimization.

Publications

Research performed during the period of this study has, so far, resulted in the following publications

1. **M. Bowes** and J. W. Bradley, "Behaviour of oxygen negative ions during the afterglow of a reactive HiPIMS discharge", *J. Phys. D: Appl. Phys.* **47**, 265202 (2014)

2. **M. Bowes** and J. W. Bradley, "Inert gas effects on the deposition rate of TiO_2 during reactive HiPIMS", *Surf. Coat. Technol.* **250**, 2 (2014)

3. **M. Bowes**, P. Poolcharuansin and J. W. Bradley, "Negative ion energy distributions in reactive HiPIMS of Ti and Nb in an Ar/O_2 atmosphere", *56th Annual SVC Technical Conference Proceedings* (2013)

4. **M. Bowes**, P. Poolcharuansin and J. W. Bradley, "Negative ion energy distributions in reactive HiPIMS", *J. Phys. D: Appl. Phys.* **46**, 045204 (2013)

5. S. Scribbins, **M. Bowes** and J. W. Bradley, "The spatial distribution of negative oxygen ion densities in a dc reactive magnetron discharge", *J. Phys. D: Appl. Phys.* **46**, 045203 (2013)

6. P. Poolcharuansin, **M. Bowes**, T. J. Petty, J. W. Bradley, "Ionized metal flux fraction measurements in HiPIMS discharges", *J. Phys. D: Appl. Phys.* **45**, 322001 (2012)

Contents

List of Figures

List of Tables

Physical constants, abbreviations and notation

Physical constants

e	-	elementary charge	=	1.6022×10^{-19} C
k_{B}	-	Boltzmann constant	=	1.3807×10^{-23} J K^{-1}
m_{e}	-	electron mass	=	9.1094×10^{-31} kg
m_{u}	-	atomic mass unit	=	1.6605×10^{-27} kg
h	-	Planck constant	=	6.6261×10^{-34} J s
c	-	Speed of light in a vacuum	=	2.9979×10^{8} m s^{-1}
ϵ_0	-	permittivity of free space	=	8.8542×10^{-12} F m^{-1}
μ_0	-	permeability of free space	=	$4\pi \times 10^{-7}$ H m^{-1}

Abbreviations

AC	-	alternating current
ALP	-	advanced Langmuir probe
AZO	-	aluminium-doped zinc oxide
CIV	-	critical ion velocity
CVD	-	chemical vapour deposition
DC	-	direct current
DCMS	-	direct current magnetron sputtering
DLC	-	Diamond-like carbon
EEDF	-	electron energy distribution function
EII	-	electron impact ionization
EQP	-	Electrostatic quadrupole
HiPIMS	-	high power impulse magnetron sputtering
HPPMS	-	high power pulsed magnetron sputtering
IC	-	integrated circuit
IED(F)	-	ion energy distribution (function)
IGBT	-	insulated-gate bipolar transistor
IPVD	-	ionized physical vapour deposition
ISEE	-	ion-induced secondary electron emission
MCC	-	Monte Carlo collisions
MFC	-	mass flow controller
MFPMS	-	mid-frequency pulsed magnetron sputtering
MPPMS	-	modulated pulsed power magnetron sputtering
MSIU	-	mass spectrometer interface unit
OML	-	orbital-motion-limited
PEEK	-	polyether ether ketone
PIC	-	particle-in-cell

PVD	-	physical vapour deposition
RF	-	radio frequency
RFEA	-	retarding field energy analyser
RGA	-	residual gas analysis
SEEC	-	secondary electron emission coefficient
TCO	-	transparent conductive oxide
SEM	-	secondary electron multiplier
TTL	-	transistor-transistor logic
QCM	-	quartz crystal microbalance
QMS	-	quadrupole mass spectrometer

Notation

A_p	-	probe surface area
A_t	-	target surface area
α	-	electronegativity
$\mathbf{B}$	-	magnetic field vector
$\Gamma_\mathrm{i,e,-}$	-	ion, electron, negative ion flux
γ	-	electron-to-negative ion temperature ratio
γ_se	-	secondary electron emission coefficient
$\gamma_\mathrm{se,p}$	-	ion-induced secondary electron emission coefficient
D_L	-	laser beam diameter
δ	-	duty cycle
d	-	target-to-substrate distance
$\mathbf{E}$	-	electric field vector
E_p	-	energy per HiPIMS pulse
$\mathcal{E}_\mathrm{aff}$	-	electron affinity
$\mathcal{E}_\mathrm{iz}$	-	ionization energy
f	-	pulse frequency
$g(\mathrm{e})$	-	Druyvesteyn electron distribution
$I_\mathrm{i,sat}$	-	ion saturation current
$I_\mathrm{e,sat}$	-	electron saturation current
I_p	-	probe current
I_e	-	electron probe current
I_i	-	ion probe current
I_d	-	discharge current
$I_\mathrm{d-peak}$	-	peak discharge current
$\overline{I_\mathrm{d}}$	-	time-averaged discharge current
j_{peak}	-	peak discharge current density

Λ_0 - characteristic diffusion length
λ_D - Debye length
λ_x - mean free path for species x
l_p - length of Langmuir probe tip
M_i - ion mass
$\dot{m}_x$ - mass flow rate of x
$n_\mathrm{i,e}$ - ion, electron number density
n_- - negative ion number density
P_d - discharge power
$\overline{P_\mathrm{d}}$ - time-averaged discharge power
$\mathcal{P}_\mathrm{peak}$ - peak discharge power density
Φ - plasma potential
ϕ - work function
p - pressure
$r_\mathrm{gi,ge}$ - ion, electron gyroradius
r_p - radius of Langmuir probe tip
r_c - Langmuir probe collection radius
σ_x - collisional cross section for species x
s - sheath width
$T_\mathrm{i,e}$ - ion, electron temperature
T_eff - effective electron temperature
T_gas - neutral gas temperature
τ - pulse width
t_on - HiPIMS pulse on-time
t_off - HiPIMS pulse off-time
t_trans - ion transit time (EQP)
U_s - surface binding energy
V_0 - initial discharge potential
V_b - probe bias potential
V_d - applied discharge potential
$\overline{V_\mathrm{d}}$ - time-averaged discharge potential
V_f - floating potential
$\bar{v_\mathrm{e}}$ - thermal electron velocity
χ - gas-phase transmission probability
ω_p - plasma frequency

Chapter 1

Introduction

From the Greek word $\pi\lambda\alpha\sigma\mu\alpha$, meaning a 'formed' or 'moulded' fluid, a *plasma* in physics can be thought of, in principle, as an ionized gas. The term was first applied to a 'region containing balanced charges of ions and electrons' in an ionized gas by Irving Langmuir in 1928 [1], which he likened to blood plasma which 'carries around red and white corpuscles and germs' [2]. When the temperature of a neutral gas is at or near the atomic ionization energy, the decomposition of atoms into positively charged ions and electrons occurs. The presence of a relatively large population of these charged particles makes a plasma distinct from a neutral gas as the long-range Coulomb interactions between them dominate over short-range binary collisions, resulting in a vast array of complex collective dynamical phenomena.

Plasmas are ubiquitous in the universe, making up stars, nebulae and the interstellar medium, accounting for approximately 99% of the observable universe. Terrestrial plasmas are less prevalent, but exist in lightning, fluorescent lamps, laboratory experiments and industrial processes. The impact of man-made, technological plasmas pervades almost every aspect of modern life with plasma-assisted processes being responsible for the micro-electronic fabrication of integrated circuits (ICs) used in much of modern technology as well as the deposition of thin films used in flat-panel displays, solar cells and magnetic films for data storage devices. Deposition processes, broadly speaking, can be separated into two categories; chemical and physical vapour deposition, often abbreviated to CVD and PVD, respectively.

PVD involves the vaporization of a target material by a physical process, such as direct vacuum heating or physical bombardment by energetic particles. The vaporized material subsequently condenses onto a substrate, thereby forming a thin film coating with dimensions of the order of nanometres to tens of microns. The physical bombardment and ejection of atoms from a target is referred to as 'physical sputtering' and typically employs the use of a plasma discharge as a source of energetic ions. Early plasma-assisted sputter deposition processes suffered from much lower deposition rates than their vacuum evaporation counterparts and so their use was marginalized. However, with the inven-

tion of the magnetically-enhanced glow discharge (i.e. magnetron discharge) operation at lower pressures was possible by confining a dense plasma adjacent to the target surface, resulting in much higher deposition rates [3]. Furthermore, due to its non-thermal nature, magnetron sputtering allows the synthesis of materials outside of thermodynamic equilibrium [4]. These two aspects combined to establish magnetron sputtering as an industrial mainstay in the deposition of thin films and the fabrication of ICs.

The challenges posed by the advancing technology in IC fabrication demanded uniform deposition into increasingly high aspect ratio trenches and vias. In conventional direct current magnetron sputtering (DCMS), the majority of sputtered particles are neutral and therefore difficult to control with much of the deposition occurring on trench side-walls rather than at its base. However, if the sputtered vapour is ionized prior to deposition, it can readily be collimated and accelerated by static electric fields. This offers the major advantages of being able to deposit into high aspect ratio trenches as well as tailoring film properties by controlling the ion bombardment energy at the substrate. When $> 50\%$ of the depositing species is ionized, the deposition technique is referred to as ionized physical vapour deposition (IPVD).

First introduced by Kouznetsov *et al.* [5] in 1999, one IPVD method is an extreme case of pulsed DC magnetron sputter deposition now known as high power impulse magnetron sputtering (HiPIMS). In HiPIMS, a high power unipolar voltage pulse is applied to the cathode for a short time, generating a very high density plasma in front of the sputter target surface which ionises a large fraction of the sputtered vapour [5, 6]. Increased ionisation of the sputtered vapour has also been shown to increase thin film adhesion, hardness, density and improve surface roughness (see review [7] and references therein). Furthermore, in reactive sputter deposition whereby a reactive gas such as oxygen or nitrogen is introduced to the discharge to deposit metal compound coatings, the increased plasma density in HiPIMS serves to enhance plasma chemistry and improve deposition of oxides and nitrides [8]. Reactive HiPIMS also has the potential of offering attractive properties such as hysteresis-free operation [9, 10], high fractions of ionized sputtered vapour [11], higher deposition rates than reactive DCMS [12] as well as superior quality coatings [13–16]. However, during reactive magnetron sputter deposition of oxides, negative oxygen ion species are formed [17–20], some of which reach very high energies and can have detrimental effects on the deposited thin films [21–24].

It is the goal of this thesis to aid in the understanding of the reactive HiPIMS discharge as well as the dynamics and formation of negative oxygen ion species, particularly high-energy O^- ions, by means of employing a selection of plasma diagnostic techniques that include Langmuir probes, energy-resolved mass spectrometry and laser-aided photodetachment. A variety of different discharge conditions are investigated, and the effects of the choice of target material and inert gas are studied with regards to O^- ion formation with the latter also being explored for its effects on the deposition rate of TiO_2.

Chapter 2

Review of background

This chapter aims to provide a brief and qualitative introduction to the basics of plasma physics and how the plasma state is utilized in low-temperature plasma processing methods, particularly with regards to magnetron sputter deposition. The key processes directly related to magnetron sputter deposition such as physical sputtering, thin film deposition and secondary electron emission are introduced. Additionally, magnetron sputtering in the presence of reactive gases is also considered as is the formation of negative ion species which occurs when the chosen reactive gas is electronegative (e.g. oxygen). Finally, the main characteristics of high power impulse magnetron sputtering (HiPIMS) are outlined along with relevant discharge physics. It is not the purpose of this chapter to act as a detailed description of the subject of plasma physics or magnetron sputter deposition, for more thorough discussions the reader is directed to references [25–28]

2.1 Introduction to plasma physics

By supplying sufficient energy to a neutral gas, it is possible to ionise the gas atoms/molecules resulting in a mixture of 'free' ions and electrons along with any residual neutral gas. This mixture of charged particles is referred to as a *plasma*, a term first coined by Irving Langmuir in 1928 [1]. As identified by Frank-Kamenezki [29], plasma can be thought of as the fourth fundamental state of matter, however, this picture can be confusing and it has been argued that the transition from gas to plasma is unlike those between solids, liquids and gases in a thermodynamic sense [30] and is, strictly speaking, not a *phase of matter*. In any case, Chen [27] defines a plasma as *a quasineutral gas of charged and neutral particles which exhibits collective behaviour*. "Collective behaviour" refers to the long-range Coulomb forces between the charged particles dominating over local binary collisions and the property of "quasineutrality" requires the plasma to be electrically neutral on macroscopic length scales, but small microscopic deviations occur and are important in understanding plasma dynamics.

Possibly the most important property of a plasma is its high conductivity, which

very effectively shields out any externally applied electric fields. If a positively charged electrode is placed inside a plasma, then the negatively charged plasma species (typically electrons) will be drawn towards the surface of the electrode. Assuming no electron losses at the electrode surface, a *sheath* of electrons will form around the electrode and cancel its charge containing any electric field within the cloud. This fundamental behaviour ensures that quasineutrality in the plasma bulk is maintained, however, due to thermal motion of the electrons, small potentials can leak into the bulk plasma. For this reason, electric fields can penetrate a small distance into the plasma and the electron sheath has a finite thickness given by the characteristic shielding distance, often referred to as the Debye length, λ_{D}. The same applies to a negatively charged surface, around which a cloud of ions would form. In fact, a sheath will form around any surface immersed in a plasma which is held at a potential other than the plasma potential which includes the chamber walls, substrate surfaces and invasive diagnostic instruments. In the majority of cases, chamber surfaces are grounded and the higher mobility of electrons compared with ions results in the increased loss of electrons near the chamber walls and so a positive space-charge is set up between the wall and bulk plasma. This space-charge layer, or sheath, is important in determining plasma particle interactions with solid surfaces and also acts to confine electrons to the plasma bulk. It is necessary to understand the properties of the sheath in order to predict the effects that the plasma may have on a substrate surface and also to interpret data collected using invasive diagnostic techniques. Furthermore, the plasma responds to any perturbation caused by external electric fields on a time scale determined by the characteristic plasma oscillation frequency, ω_{p}. Other plasma parameters are often functions of λ_{D} and/or ω_{p}.

Although naturally occurring plasmas are somewhat of a rarity on Earth, being limited to a few phenomena such as lightning and the polar aurorae, plasmas are ubiquitous in most of the rest of the universe. It is thought that approximately 99% of all observable matter is in the plasma 'state', including stars, nebulae, and the interstellar medium. As such, plasmas exist over a large range of parameter values varying by many orders of magnitude in size, density and temperature. Laboratory microplasma jets used in research can exist on the micron scale (10^{-6} m), whereas intergalactic nebulae can stretch to lengths of 10^{25} m covering approximately 31 orders of magnitude. Plasma densities cover a similar range, from the very diffuse interstellar medium (10^{-1} m^{-3}) to extremely dense plasmas produced by high power lasers in inertial confinement fusion research (10^{32} m^{-3}). Due to the vast parameter space in which plasmas fit, it is often convenient to categorize them based on their properties. The investigations undertaken in this thesis concern low-pressure and low-temperature plasmas, which are discussed below in §2.2.

2.2 Low-temperature technological plasmas

In general, one method of classifying plasmas is based on the relationship between the ion and electron temperatures, T_i and T_e, respectively. If the electron temperature is much greater than the ion temperature ($T_\mathrm{e} \gg T_\mathrm{i}$), then the plasma is termed a *non-thermal* (or low-temperature) plasma. Conversely, if the electron temperature is approximately equal to the ion temperature ($T_\mathrm{e} \approx T_\mathrm{i}$), the plasma is referred to as a thermal (or high-temperature plasma). An important application of thermal plasmas is their use in nuclear fusion, whereby a mixture of light elements (typically deuterium and tritium) is heated to a temperature of 100 million degrees Kelvin resulting in a completely ionized high-temperature plasma in which nuclear fusion reactions can occur. However, the work in this thesis concerns electrically driven low-pressure, low-temperature plasma discharges which are routinely used in processes such as plasma-enhanced etching, sputtering and deposition in the fabrication of microelectronics. For this reason, the discharges are often referred to as technological plasmas. Technological plasmas are usually weakly ionized, meaning only a small fraction of the gas particles undergo ionization (typically on the order of 0.01-1%) and so interactions between charged particles and neutrals are often non-negligible.

There are many different technological plasma discharge configurations which make use of different geometries and heating mechanisms to ignite and sustain the plasma. In the simplest case, consider a pair of parallel-plate electrodes immersed in a gas as shown in figure 2.1. By applying a high potential difference to the electrodes, any residual free electrons existing in the gas or those emitted from the electrode surface due to cosmic radiation are accelerated by the electric field and collide with neutral gas atoms. A fraction of the collision events will result in excitation and ionization, whereby the former results in de-excitation and emission of (typically) visible radiation, which ultimately gives plasma discharges their characteristic glow. The latter, termed *electron impact ionization*, results in additional electrons and newly formed ions. In cascade fashion, the additional electrons can participate in further ionization events provided that they gain sufficient energy in the electric field thereby releasing more electrons and so on. This initial phase of the discharge is referred to as a *Townsend avalanche*, after British physicist John Sealy Townsend. The newly created ions are then accelerated towards the cathode and release more electrons via ion-induced secondary electron emission (see §2.2.1.2). In addition to electron emission, the ion bombardment of the cathode can result in the physical ejection of atoms from the cathode surface in a phenomena known as sputtering (see §2.2.1.1). The continued emission of secondary electrons and ionization of neutrals sustains the plasma in a steady state with a constant current. This type of discharge is called a direct current (DC) glow discharge.

DC glow discharges require the driving electrodes to be made from a conductive ma-

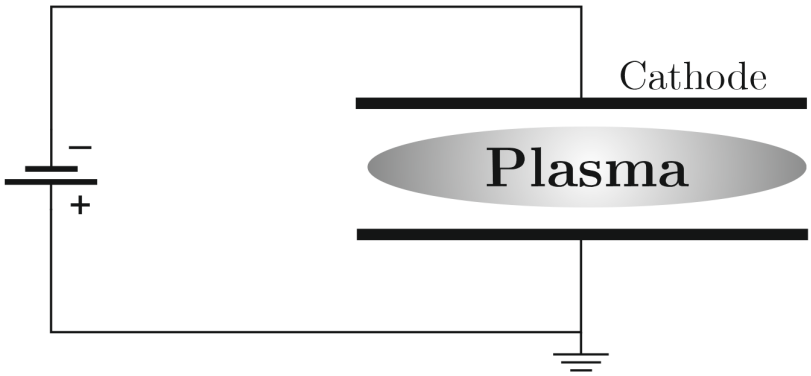

Figure 2.1. Schematic illustration of a simple parallel plate direct current glow discharge.

terial, however, by using a time-varying potential difference it is possible to cover the electrodes in an insulating layer, to facilitate sputter deposition of dielectric materials. One common discharge configuration involves driving the electrode by applying a high voltage radio-frequency (RF) signal to it while it is immersed in the gas/plasma (capacitively coupled) or to an antenna outside of the chamber and not in direct contact with the plasma (inductively coupled). Alternatively, it is possible to use a pulsed potential waveform instead. Pulsed DC discharges operate typically with a frequency on the order of kHz, employing short pulse lengths on the order of microseconds which allow for much higher peak currents and voltages for the same average power as a DC discharge. Pulsed discharges hold several advantages over DC discharges, such as reducing arc damage at the cathode by preventing positive charge build-up on any insulating part of the cathode. Moreover, the higher current densities during the 'on-phase' leads to the generation of a denser plasma and higher ion fluxes to the cathode, which for sputtering applications can result in a higher sputter yield when compared with the equivalent DC discharge. A review of gas discharges and their applications is given by Bogaerts *et al.* [31].

A very important discharge type for sputtering applications is the *magnetron discharge* and the work presented in this thesis concerns the use of an extreme case of the pulsed DC magnetron discharge used in a plasma-assisted process known as high power impulse magnetron sputtering, or HiPIMS, in which the current density during the on-phase is typically two orders of magnitude greater than the time-averaged value. See §2.3 for general information on the magnetron discharge, HiPIMS is covered in §2.4.

2.2.1 Important processes in technological plasmas

Low-temperature technological plasma discharges are extremely complex environments due to their interdisciplinary nature, combining many areas of research including electromagnetism, fluid dynamics, gas-phase reaction chemistry, surface science,

atomic/molecular physics and, of course, plasma physics. The important processes relevant to the work presented in this thesis are outlined in the sections below. The most important process in a magnetron discharge, at least from an applications perspective, is physical sputtering of a cathodic target by bombarding it with high energy ions (see §2.2.1.1) and the subsequent deposition onto a substrate (see §2.2.1.3). In addition to sputtering, ion bombardment of the target surface also leads to secondary electron emission, which is outlined in §2.2.1.2. In reactive discharges, in which a reactive gas such as oxygen or nitrogen is introduced alongside an inert gas (typically argon), gas-phase and surface reaction chemistry both play a vital role. Particularly important to the work presented here is the formation mechanisms of negative ion species in the presence of an electronegative gas which occur in both volumetric and surface reaction processes. A brief overview of reactive sputtering is given in §2.2.1.4 and negative ion formation mechanisms are covered in chapter 3.

2.2.1.1 Sputtering

Sputtering is a physical (non-thermal) process by which a solid or liquid target is bombarded by heavy energetic particles resulting in the subsequent ejection of atoms from the target surface. These energetic particles are usually positive ions from a plasma, as is the case in conventional cathodic sputtering. The ejected material then diffuses through the chamber and is deposited onto a substrate where thin film formation occurs. A basic illustration of the physical sputtering process is shown in figure 2.2. Sputter deposition is a widely used technique to deposit high quality thin films onto a substrate, for which there are many applications ranging from anti-reflective optical coatings and electronic displays to magnetic media and hard coatings for tools.

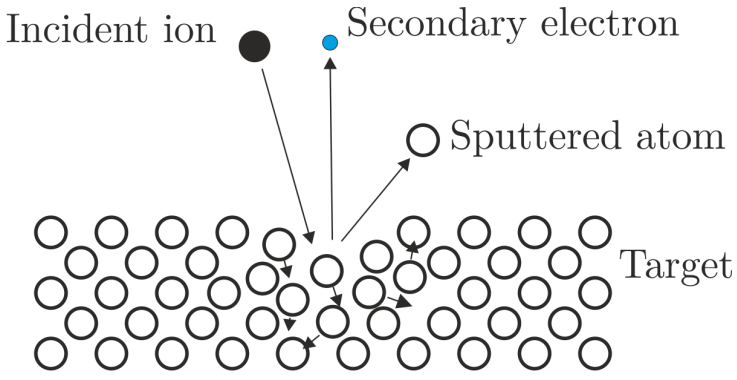

Figure 2.2. Schematic of the basic physical sputtering process.

The energetic ions used to bombard the target surface are typically formed in an argon gas discharge and accelerated through the cathode sheath towards the target surface. In low pressure conditions (the collisionless sheath approximation), the impacting ions have energies on the order of the cathode potential ($E_\mathrm{i} = 300 - 1000$ eV) which results in a

higher removal rate of atoms from the target surface. A measure of this removal rate is the so-called *sputter yield*, Y, which is defined as the ratio between the number of ejected atoms to the number of incident ions.

$$Y = \frac{\text{ejected atoms}}{\text{incident ions}} \tag{2.1}$$

The sputtering mechanism is energy dependent and, in general, Y increases with increasing ion energy until a maximum yield is reached. Generally speaking, there are four types of physical sputtering, which can be categorised by the energy of the incident particle, however, for the vast majority of applications, the target potential is typically on the order of 0.5-1 kV and the so-called *knock-on* regime is the most common form of sputtering in industrial applications. In this regime, the collisions can be considered using simple conservation of momentum arguments and hence the maximum energy imparted onto a target atom with mass M_t by an incident ion normal to the target surface with mass M_i is shown to be

$$E_\mathrm{max} = E_\mathrm{i}\frac{4M_\mathrm{t}M_\mathrm{i}}{(M_\mathrm{t}+M_\mathrm{i})^2} \tag{2.2}$$

For a target atom to be ejected, E_max must exceed the atomic binding energy of the target material. As can be seen from equation 2.2, the maximum energy transferred occurs when $M_\mathrm{i} = M_\mathrm{t}$ and so matching the two masses can be important to the sputtering yield. However, it is often the case that argon is chosen as the main process gas for inert gas sputtering as it is relatively inexpensive when compared with other rare gases such as krypton and xenon. Mixtures of inert and reactive gases (e.g. oxygen or nitrogen) are used in the reactive deposition of oxide and nitride compounds (see §2.2.1.4). It is also possible that the sputtered particles from the target induce further sputtering if a significant fraction of the sputtered vapour undergoes ionisation. This increased ionisation of the sputtered vapour is important in processes such as arc vaporisation and HiPIMS, but is typically negligible in conventional DCMS.

Energy distribution of sputtered particles

There exists a threshold energy, E_th, for the incident ions, below which physical sputtering becomes impossible. As implied by equation (2.2), the amount of energy transferred from the incident ion to the target atom is a function of the ratio between the masses of the two particles. However, it is often the case (especially in plasma processing) that $E_\mathrm{i} \gg E_\mathrm{th}$ and under such conditions the sputtered particles are ejected from the target surface with a cascade-type energy distribution as described by Sigmund-Thompson theory [32–34]:

$$f(E) \propto \frac{E}{(E+U_s)^3} \tag{2.3}$$

where E is the energy of the sputtered particle and U_s is the surface binding energy (typically approximated to the enthalpy of vaporisation of the target material). This expression gives a maximum in the energy distribution where $E = U_s/2$. Typical values for U_s are found between 3 and 10 eV, such that the characteristic energy of sputtered atoms is generally between 1 and 5 eV and hence much higher than room temperature. Indeed, the energy of the sputtered atoms is often over an order of magnitude higher than the corresponding thermal evaporation energy for an equivalent particle flux. In the literature, equation 2.3 is often referred to as the Thompson energy distribution of sputtered particles and an example of its shape is illustrated in figure 2.3.

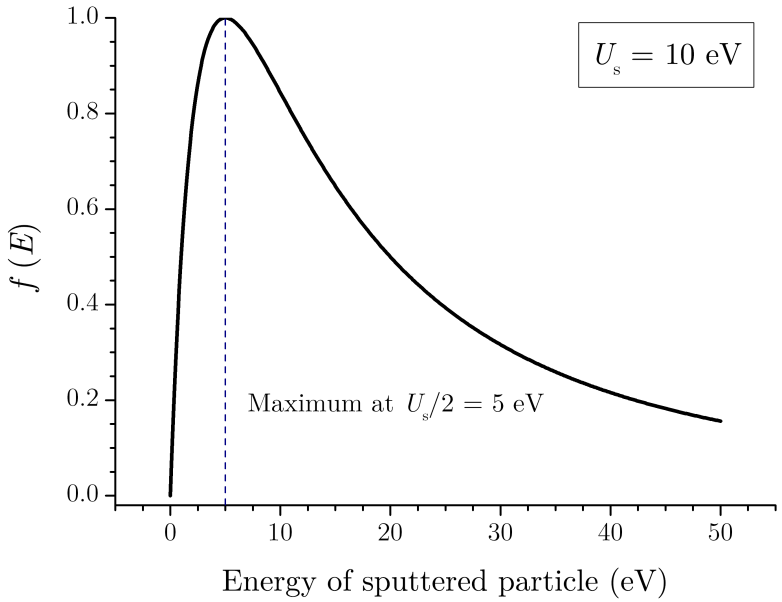

Figure 2.3. Normalized Thompson energy distribution of sputtered particles for the case of $U_s = 10$ eV. The maximum is shown to occur at $U_s/2$.

2.2.1.2 Secondary electron emission

As well as sputtering atoms from the target surface, the production of electrons via heavy particle bombardment at the cathode can be a very important process in sustaining the plasma. There are two main mechanisms by which secondary electrons are produced by heavy particles at the target surface; *potential* emission and *kinetic* emission.

Potential electron emission

When an incoming ion with an incident energy of the order of 100 eV approaches a solid surface, a deep potential well is set up in front of the target surface. Electrons from within the conduction band of the target surface are able to quantum tunnel through the well to the ion and neutralise it. After this process, there are two possible outcomes. If the electron from the target surface enters the ground state of the atom, the excess energy produced by the neutralisation ($\mathcal{E}_{\text{iz}}$) can be absorbed by a second electron within the conduction band of the target metal. If and only if the excess energy is greater than twice the work function (ϕ) of the target metal will electron ejection occur (a process known as *Auger emission* [35]). Considering that both the electron captured by the incoming ion and the ejected electron are located at the top of the conduction band, potential electron emission occurs if

$$\mathcal{E}_{\text{iz}} > 2\phi \tag{2.4}$$

As there is no kinetic energy threshold for this process, potential electron emission is fairly constant for incident ion energies below 1 keV [35]. Experimental data of the measured yields ($\gamma_{\text{se,p}}$) for different incident ions satisfies a least-squares fit [36]:

$$\gamma_{\text{se,p}} \approx 0.032\,(0.78\mathcal{E}_{\text{iz}} - 2\phi) \tag{2.5}$$

Due to the relatively low energy threshold for potential emission, it is generally the primary means of electron emission by heavy particles in most sputter deposition applications.

Kinetic electron emission

The second mechanism by which electrons are liberated from a target surface is known as kinetic emission. This process is associated with the ionisation of target atoms following the penetration of an incident particle (ion or atom) into the target and requires more energy than potential emission (typical threshold of $1 - 2$ keV). The electrons are liberated by direct ionisation of target atoms or by secondary ionisation from recoils within the target crystal structure. Due to the comparatively higher energy thresholds for kinetic emission as compared to potential emission, kinetic emission does not make a significant contribution to the secondary electron emission yield for most sputter deposition processes. However, the threshold energies for kinetic emission for insulating materials are typically lower and therefore it may become a more important mechanism for reactive sputtering where the target surface is covered, to some extent, by an insulating layer of oxide, nitride or carbide [37].

2.2.1.3 Deposition

Non-thermal low-pressure processing discharges are able to deposit films of improved quality and properties when compared to high-temperature thermal equilibrium deposition. Furthermore, high-temperature thin films can be deposited at low temperatures, typically saving processing costs and allowing films to be deposited onto temperature-sensitive substrates.

Sputtered (or evaporated) material undergoes a phase-transition during thin-film formation and as such involves the processes of nucleation and growth. During the early stages of thin film formation, a number of sputtered atoms condense onto a (semi-)permanent position on the substrate to form a so-called *nucleation site* - points on the substrate where further growth occurs. After a short time, the film consists of a typically uniform distribution of mobile island formations which then begin to coalesce in a somewhat liquid-like state until the film forms a continuous structure. These events typically account for the first few hundred Å of thin film growth.

Physical sputter deposition

Physical sputter deposition is capable of depositing films with excellent uniformity, good surface smoothness and adhesion onto both small and large area substrates. Neglecting any losses and assuming that all the sputtered material is deposited onto the substrate, the deposition rate for physical sputter deposition is

$$D_{\text{sput}} = \frac{Y\Gamma_{\text{i}}}{n_{\text{f}}}\frac{A_{\text{t}}}{A_{\text{s}}} \tag{2.6}$$

where Γ_{i} is the incident ion flux, n_{f} is the density of the deposited film, A_{t} is the target area sputtered, A_{s} is the substrate area and Y is the sputtering yield. For a typical argon discharge with 1 keV argon ions impinging upon the target surface, the sputtering yield is approximately 1 and the operating pressure is typically on the order of 10^{-3} Torr where the mean free path of sputtered particle is larger than the target-to-substrate distance. A typical deposition rate for such a process is on the order of 1 nm/min.

As shown in §2.2.1.1, the energy of sputtered atoms arriving at the substrate is typically 1.5 to 5 eV. At these energies, the impinging ions improve the bonding and adhesion by facilitating mixing and diffusion between sputtered atoms and the substrate material.

Ion bombardment of the substrate

As mentioned above, ion bombardment of the substrate has proven to influence the properties of the growing film significantly [38]. The energy of the ions bombarding the substrate can be somewhat tailored by applying a negative bias to the substrate and is indeed employed in many commercial applications. For insulating substrates, an RF driven bias is applied rather than DC. Different ion energies can effect the growing film in different ways. For example, low energy ($10 - 30$ eV) ions can improve film density and adhesion by increasing surface mobility of deposited atoms whereas high energy ions (> 50 eV) can produce high compressive stress within the film due to recoil implantation. Very high energy ions (> 200 eV) can even resputter the deposited film, reducing the economy of the sputter deposition process. This is a particular concern for reactive sputter deposition in the presence of electronegative gases due to the formation of high energy negative ions in the discharge.

2.2.1.4 Reactive sputtering process

Without using compound target materials, it is possible to deposit compound materials such as high refractive index materials (e.g. TiO_2), wear-resistant coatings (e.g. TiN) and transparent conductive oxides (e.g. Al-doped zinc oxide, AZO) by introducing a reactive gas (such as oxygen or nitrogen) into the plasma during the sputtering of a metal target. By referring to equation 2.2, it is clear that neither nitrogen (N = 14 amu) nor oxygen (O = 16 amu) are preferred for sputtering due to their low atomic masses. It is for this reason that a rare gas such as argon (Ar = 40 amu) is introduced in order to aid with the sputtering.

In the plasma state, the reactive gas is *activated* and becomes more chemically reactive than when in the gas phase. The rare gas also aids in this process by facilitating Penning ionisation and excitation processes and allows the reactive gas to react readily with the target surface via two main mechanisms;

- **Chemisorption** in which the reactive gas forms a monolayer of target-gas compound on the target surface (this is often referred to as target *poisoning*).
- **Ion implantation** by which positive reactive gas ions are accelerated through the cathode sheath and implanted into the target material to depths typically on the order of several nm.

If the reactive gas flow is sufficient to cover the entire target surface with a thin layer of compound (i.e. the target is fully "poisoned"), the sputtering rate is greatly reduced. Several different methods have been employed in order to avoid this. One method is to use a pulsed power supply to periodically discharge the target surface which

helps to avoid unwanted arcing. Another is the active feedback control of the reactive gas flow by monitoring the change in the partial pressure of the reactive gas by either mass spectroscopy, optical emission spectroscopy or by monitoring the change in the impedance of the plasma discharge. This allows the partial pressure of the reactive gas to be maintained at a given ratio to the inert gas which prevents the target from being fully poisoned. In some configurations, the inert gas inlet is located directly above the target surface while the reactive gas is injected away from the target and into the substrate region. This allows an inert gas "blanket" to form over the target surface and helps to reduce target poisoning while providing sufficient reactive gas flow to the substrate in order to allow the formation of stoichiometric compounds.

In reactive deposition, the reaction rates of the reactive gases with the depositing material are of extreme importance. If a given reaction is too slow for instance, the deposited film may not have sufficient time to combine with the reactive gas in order to form a stoichiometric compound before being buried by further deposition. The reaction rate is sensitive to many parameters such as the reactivity and availability of reactive species, bombardment during deposition, energy released upon condensation and the surface temperature of the substrate. It is often desirable to enhance the bombardment of a growing film by biasing the substrate with a negative potential in order to accelerate ions towards the growing film. This concurrent bombardment has been shown to enhance chemical reactions and densify the depositing film [38].

Negative ion formation

Reactive sputter deposition in the presence of electronegative gases results in the formation of negative ion species in the discharge. Negative ions can form via either gas-phase or surface reactions. In general, the negative ions generated in the bulk of a non-thermal discharge possess energies on the order of the heavy particle temperature which is typically only slightly higher than room temperature (several hundred Kelvin). For this reason, these low-energy negative ions are confined within the discharge bulk by the positive plasma sheath. In contrast, negative ions generated near surfaces are accelerated into the bulk plasma by the potential contained within the sheath adjacent to that surface. Hence it is possible for high-energy negative ions to originate from surfaces with large negative potentials with respect to the plasma potential, such as the cathode surface, and enter the discharge.

The work presented here concerns the formation of negative ions in a magnetron discharge, with particular emphasis on the aforementioned high-energy negative ions. A brief overview of the magnetron discharge is given in §2.3 and for more information regarding negative ions in magnetron sputtering the reader is referred to chapter 3 and sections therein.

2.3 Magnetron discharge

In diode sputtering, the pressure required to maintain a sufficiently dense plasma is comparably high when compared to a magnetron sputtering source. By the application of magnetic fields, a magnetron source deflects secondary electrons emitted by the cathode to a region adjacent to the target surface. A combination of orthogonal magnetic and electric fields results in the electrons experiencing an $\mathbf{E} \times \mathbf{B}$ drift. The confined electrons produce an increased ionisation probability in the volume above the target surface. This consequently results in a high density plasma forming in this region, from which ions can be drawn towards the target surface such that the sputtering process can operate at a lower pressure. Additionally, due to the main ion generation region being located close to the target surface the bombarding ions lose minimal energy and avoid charge-exchange collisions during transport to the target surface. Further development lead to the invention of the *unbalanced* magnetron source, by which the magnetic field is intentionally unbalanced to allow a portion of the magnetic field lines to extend beyond the region adjacent to the target and further into the discharge. Directing some of the secondary electrons away from the target surface facilitates plasma generation downstream of the target in the substrate region, allowing a biased substrate to attract ions in order to steadily bombard a growing film. As discussed previously in §2.2.1.3, this bombardment of a growing film has been proven to strongly influence the film structure and properties. The invention of the magnetron sputtering source allowed sputter deposition technology to be employed for the first time on an industrial scale.

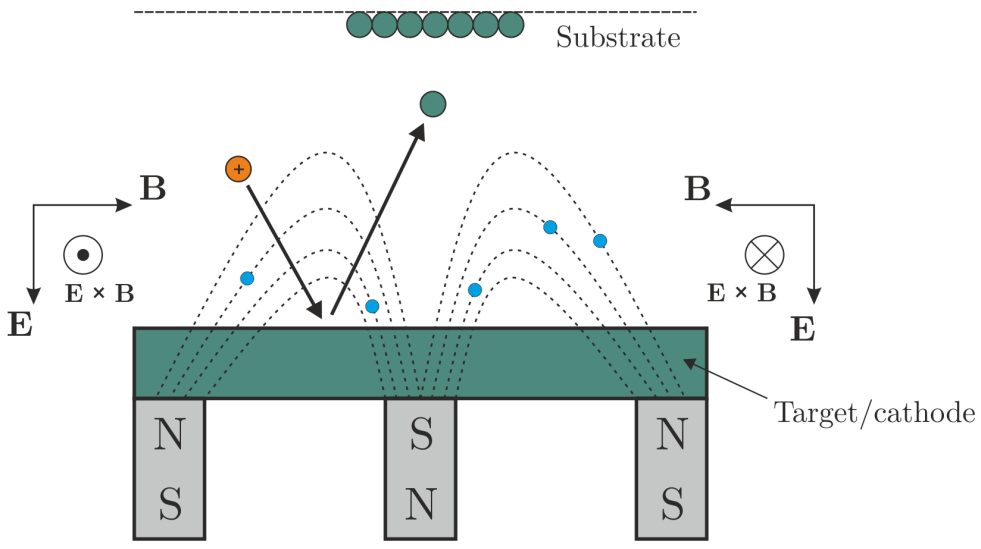

Figure 2.4. A simple illustration of the cross section of a circular planar magnetron, showing ions, sputtered atoms and electrons. The directions of the magnetic and electric fields are also shown.

The most widespread magnetron source configuration is the planar configuration in which the magnets are arranged behind the target surface in either a concentric circular

(figure 2.4) or rectangular formation (see figure 2.5). A drawback of this configuration is the non-uniformity of the deposition pattern. Since the magnetic field is non-uniform across the target surface there is preferential sputtering at the regions where the radial component of the magnetic field is highest, resulting in the characteristic *racetrack* erosion pattern shown in figure 2.5. This is obviously uneconomical and alternative configurations have been developed to combat this issue. One particularly successful variation is the rotating cylindrical configuration in which a cylindrical target is rotated about a set of stationary magnets in a manner that ensures an almost uniform sputter patter and vastly improves target utilization [39].

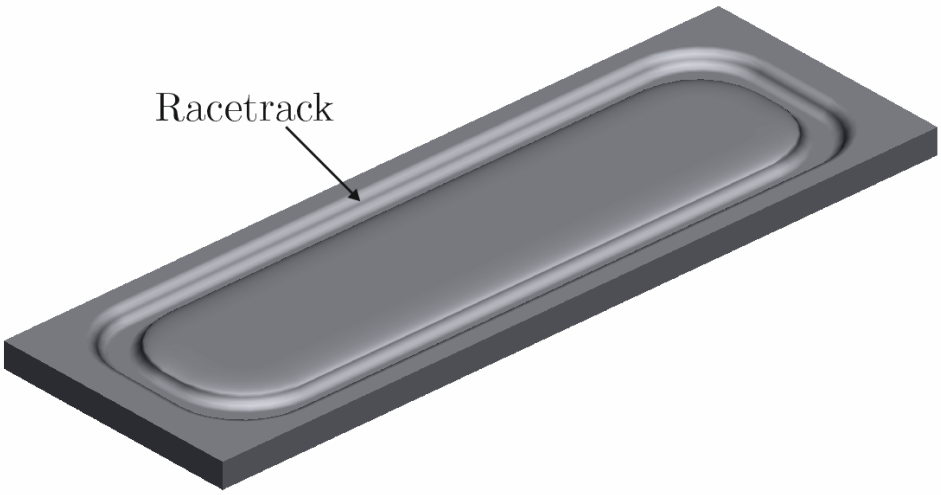

Figure 2.5. A representation of a rectangular planar magnetron target with the erosion racetrack labelled.

Magnetron discharges can be driven by a number of different power supplies, the most frequently used being DC, RF and pulsed DC. As with diode sputtering, the conventional DC configuration is restricted to metallic and metallic compound sputter deposition and the RF configuration is used to provide arc-free sputter deposition of dielectric materials. Pulsed DC, often used in the kHz range, can also be used to sputter dielectric materials, but can operate without the requirement of a matching network which is essential for efficient RF operation. Moreover, high power pulsed DC can be employed to provide increased ionization of the sputtered vapor [5]. This approach to magnetron sputtering, known as high power pulsed magnetron sputtering (HPPMS) or high power impulse magnetron sputtering (HiPIMS), has gained much interest over the past 15 years due to its potential for producing improved overall thin film quality when compared with conventional pulsed DC and DCMS deposition. For the remainder of this thesis, this technique will be referred to as high power impulse magnetron sputtering or HiPIMS.

2.4 High power impulse magnetron sputtering

First introduced by Kouznetsov *et al.* [39], HiPIMS involves powering a magnetron discharge with high amplitude unipolar pulses (typically $500 - 2000$ V) that provide peak power densities that are $2 - 3$ orders of magnitude higher than conventional DC operation [40]. For example, the peak power density during a HiPIMS pulse is typically on the order of $1 - 10$ kW cm^{-2} whereas conventional DC power densities are often on the order of $3 - 10$ W cm^{-2}. To prevent damage being caused to the target, the duty cycle of HiPIMS operation is very low (0.1 to 5%) such that the average power density is kept equivalent to that of conventional DCMS. In some instances, a low-power DC discharge is maintained in the HiPIMS off-phase to allow for operation at lower pressure by preventing the discharge from being extinguished in between pulses. This technique is often referred to as pre-ionization and also has the benefit of reducing the delay of the pulsed discharge current on-set [41].

Due to the high power densities supplied to the plasma during the on-time of a HiPIMS pulse, a high ionisation fraction of sputtered vapour is observed (up to 90% in the case of titanium [6]). Higher ionisation of the sputtered vapour allows for greater control of the film growth process via the use of a substrate bias to control the energy of the ions arriving at the substrate. Increased ionisation of the sputtered vapour has also been shown to increase thin film adhesion [42], hardness [15], density and improve surface roughness [43] of the deposited film and it also allows for high quality thin films to be deposited at lower temperatures when compared to those grown using DC magnetron sputter deposition [14]. However, the downside to an increased ionisation fraction is that some of the ionised sputtered vapour will be attracted back towards the target surface, lowering the deposition rate [44]. Indeed, HiPIMS has been almost universally reported to show lower deposition rates when compared to DCMS when operated at equivalent powers [45].

2.4.1 The HiPIMS discharge

Although the HiPIMS set-up is very similar to the conventional DC magnetron and pulsed DC magnetron discharge configuration, the manner in which energy is delivered to the discharge (i.e. in impulses) produces significantly different discharge physics. The main facets of the relevant characteristics of HiPIMS and the associated discharge physics are briefly outlined below. A more thorough review of the fundamental aspects of HiPIMS and applications have been the subject of several review articles [7, 40, 46, 47], which include discussions on more exotic discharge physics that are beyond the scope of this thesis, such as anomalous transport of electrons [48–51] and spoke formation [52–56].

Voltage-current waveforms

As mentioned previously, HiPIMS power supplies deliver a high amplitude voltage impulse on the order of $300 - 2000$ V to a target surface with a pulse width generally in the range $25 - 500$ μs, drawing peak discharge current densities on the order of kWcm^{-2}. The absolute value of the peak current is largely determined by the size of the target. An example of a HiPIMS voltage-current-time waveform is presented in figure 2.6. The shape of the temporal variations in the applied potential and discharge current are dependent on many factors. Firstly, the inductance of the power supply circuit and the energy stored in the driving capacitor play major roles in both applying and sustaining the potential at the cathode, respectively. Other discharge parameters such as target material, gas pressure, gas species, magnetic field configuration and chamber geometry also significantly affect the shape of HiPIMS waveforms.

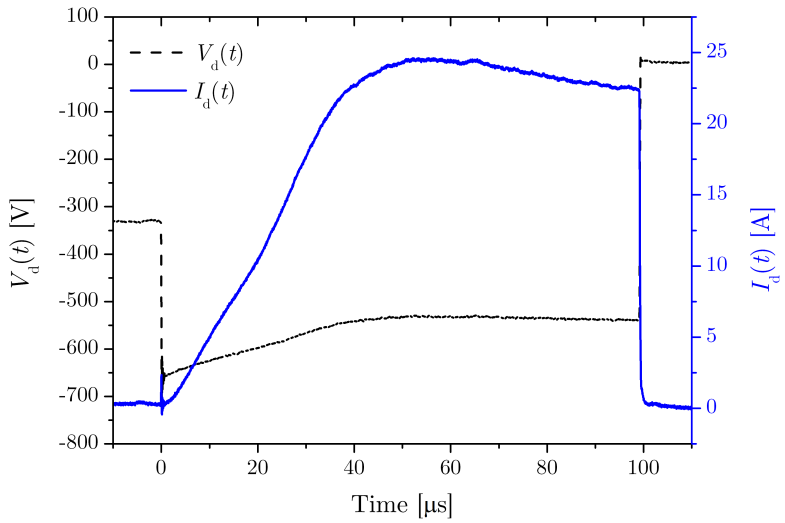

Figure 2.6. Applied target potential $V_d(t)$ (black dash) and measured discharge current $I_d(t)$ (blue line) during HiPIMS of a 75 mm diameter titanium target in argon at a pressure of 0.4 Pa.

The voltage-current-time waveform presented in figure 2.6 was obtained from the experimental set-up described in chapter 4 in which a pre-ionizing unit was employed (note the non-zero potential prior to the pulse on-set at $t = 0$). When operating without the use of a pre-ionizer, the discharge current experiences a delayed on-set as the plasma re-ignites after being extinguished during the relatively long off-phase following the previous pulse. The delayed on-set is dependent on the gas pressure/composition, target material and applied target potential [57]. Anders *et al.* [58] analysed HiPIMS current-voltage-time waveforms to identify the on-set of self-sputtering within the discharge and Horwat and Anders [59] found evidence of gas rarefaction and compression in the HiPIMS current waveform. Due to vast range of experimental and physical processes that influence the

shape of the waveforms it is often difficult to directly compare investigations by using waveforms alone. It has been proposed by Arcos *et al.* [60] that HiPIMS current-voltage characteristics measured during the pulse on-phase could be used to compliment the current-voltage-time waveforms in order to more readily identify different plasma regimes.

Ionization of sputtered vapor

Possibly the most attractive feature of HiPIMS and indeed the major motivation for its development, is the increased ionization of sputtered vapour when compared with conventional DC and pulsed DC magnetron sputter deposition techniques [6]. By concentrating the discharge power into short pulses, it is possible to achieve high target current densities of several amperes per square centimetre which sustains a very dense plasma for the duration of the pulse and provides high ion fluxes at the substrate with a significant fraction of the metal flux being ionized [5,6]. As a result, this high ion flux acts to increase surface mobility of the deposited film atoms through momentum transfer collisions. Some improved properties of deposited films such as increased film density and reduced roughness have been attributed to this increased surface mobility of the adatoms caused by ionic bombardment [15]. Another method of increasing the surface mobility of adatoms includes heating the substrate to a optimum temperature for a particular phase formation, however, this method, unlike ionic bombardment, isn't suitable for heat-sensitive substrate materials.

By applying a negative bias to the substrate, it is possible to control the energy of the impinging ions and, to some extent, tailor the phase composition of the growing thin film. For example, Konstantinidis *et al.* [14] demonstrated that titanium oxide could be deposited in the rutile phase more readily by using a substrate bias of -150 V. Other works by Lin *et al.* [61] showed that the crystalline phase of deposited tantalum thin films can change from the beta phase to the alpha phase by employing a substrate bias of -100 V.

Gas rarefaction

The sputtered flux from the target during magnetron sputter deposition undergoes momentum transfer collisions with the background gas atoms in front of the target surface. The thermalization of the sputtered vapour results in local gas heating and gas density reduction adjacent to the target. This gas rarefaction phenomenon in magnetron sputtering was first reported by Hoffman then by Rossnagel and Kaufman [62,63] where the pressure of the background gas in the pre-target region was measured during DCMS by means of a pressure probe. Due to the higher sputtered flux and stronger "sputter wind" during the pulse on-phase in HiPIMS, it is expected that the gas heating and rarefaction effects

may be exaggerated in comparison to rarefaction in DCMS. Monte Carlo simulations by Kadlec [64] predicted that the momentum transfer from sputtered titanium to argon gas atoms can result in heating the neutral gas up to approximately 1 eV ($\approx 11,000$ K) in the vicinity of the target erosion track. A simulation of the spatio-temporal evolution of Ar gas density during a HiPIMS pulse is shown in figure 2.7. It is clear that the region immediately in front of the target surface becomes rarefied by approximately an order of magnitude. Furthermore, this local density reduction in front of the target is accompanied by a local density increase in the substrate region as the Ar gas that was close to the target compresses at the wall.

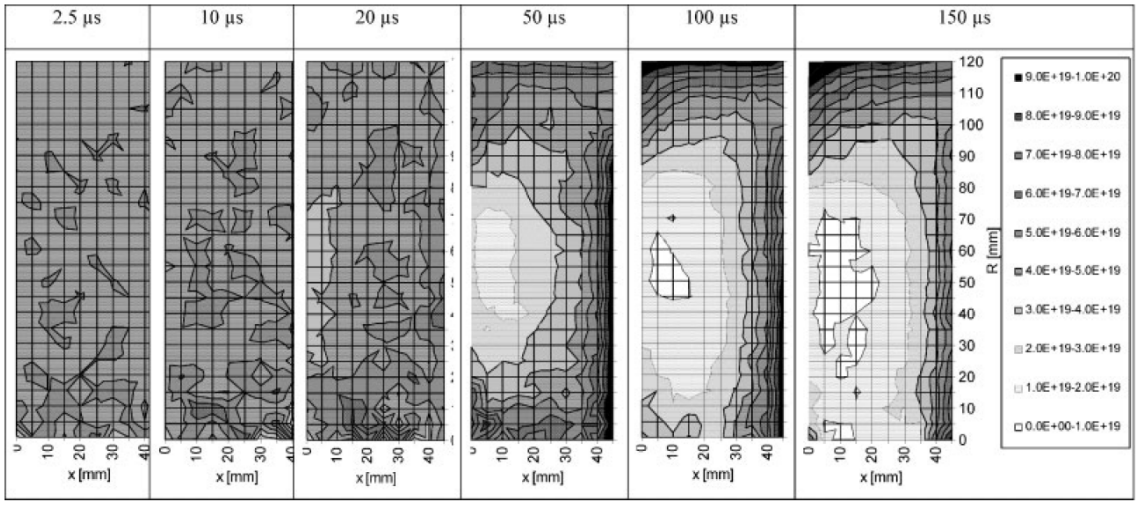

Figure 2.7. Simulation of the spatio-temporal evolution of the number density of Ar gas in front of a titanium during a HiPIMS pulse. Number density units are in m^{-3}. Reproduced from [64].

This supposition has been supported by spatio-temporally resolved optical imaging of plasma emissions as performed by Liebig *et al.* [65] and Hecimovic *et al.* [66], where both sets of authors observed a decrease in the Ar^0 neutral emissivity above the target surface during the HiPIMS on-phase. Horwat and Anders [59] used current-time waveforms as evidence for strong compression and rarefaction effects in the pre-target region for HiPIMS of copper in argon where a strong pressure-dependent compression phase was shown to precede the rarefaction phase. It was also suggested by the same authors [59] that another, more straightforward effect may contribute to gas heating. An elevated target surface temperature due to previous HiPIMS pulses may also be responsible for background gas heating and density reduction. Indeed, the effect has been reported by Anders for a hot niobium target [40]. Gas rarefaction effects can be important when considering the transport of backscattered and sputtered particles from the target through the discharge to the substrate.

Self-sputtering

It has already been stated that during HiPIMS, a significant fraction of the sputtered vapour becomes ionized and that this leads to an increased metal ionic flux at the substrate. However, this necessitates that a fraction of the ionized vapour will be back-attracted to the target and contribute to the sputtering process (self-sputtering) [58]. When using very high power densities (> 1 kW cm^{-2}) during sufficiently long pulses (> 100 μs), the probability of sputtered vapour being ionized increases as does the gas density reduction due to higher sputtered flux, resulting in a situation where the metallic vapour becomes the dominant process gas rather than the inert gas (typically argon). Typically this is an unwanted situation as the self-sputtering yield is usually not sufficiently larger than the inert gas sputter yield and the primary ion cannot contribute to deposition at the substrate thereby reducing the deposition rate. Indeed, this loss of sputtered vapour by back-attraction is often cited at one of the reasons for the observed reduced deposition rate in HiPIMS when compared to DCMS [44]. Furthermore, the potential energy of singly-charged metal ions is typically less than that of the process gas and often not sufficient to cause secondary electron emission. However, if a large fraction of the sputtered vapour becomes multiply-charged, then secondary electron emission may be sufficient to allow sustained self-sputtering. Indeed, if the self-sputtering yield of the target material, the number of multiply charged metal ions and the ionization probability of the sputtered vapour are sufficiently high, then it is possible for the discharge to be sustained without the use of a background gas (i.e. in high vacuum) and could be used to facilitate the deposition of ultra pure thin films [67].

Deposition rate

It has been widely reported that HiPIMS generally suffers a decrease in power normalized deposition rate when compared with equivalent DCMS [45]. This issue has been a cause for concern, particularly for those in the industrial sector where power efficiency is of great importance, and so the reasons for this apparent decrease in coating efficiency have come under intense scrutiny. As discussed by Anders [44], the term *deposition rate* can have several different definitions. For the most part and unless explicitly stated, the deposition rate discussed here refers to the *normalized static deposition rate*, which is a measure of the change in thickness of the deposited film per unit time, per unit of power and so is typically given in units of nm s^{-1} W^{-1} or Å s^{-1} W^{-1}.

Deposition rates in HiPIMS are often compared to the equivalent DCMS set-up, however, there are distinct physical differences between the two processes that can be used to explain the observed disparity in the deposition rate measurements. Firstly, as pointed out by Emmerlich *et al.* [68], it is non-physical to directly compare static power normal-

ized deposition rates measured in HiPIMS with those found in DCMS due to the so-called *yield effect*. In general HiPIMS employs higher absolute target potentials than DCMS of the same average power, thus HiPIMS suffers a necessary decrease in the average discharge current as the discharge power is defined as the product of the discharge current and the discharge potential. The loss in the discharge current could be compensated only if the sputtering yield increased proportionally with absolute target potential, however, the increase is found to be sub-proportional with increasing ion velocity (i.e. increasing target potential). Another important effect influencing deposition rate in HiPIMS is the *return effect*, which is related to the ionization of a significant proportion of the sputtered vapour and the subsequent back-attraction of newly-formed metal ions to the target surface. These effects and other phenomena relevant to deposition rates in HiPIMS are discussed further in [44] and also in chapter 8.

Interestingly, normalized deposition rates in reactive HiPIMS have been shown to be both lower [11] and higher [12, 69] than those measured in DCMS. Although the reasons for the apparent higher deposition rate are unclear, they have been attributed to reduced poisoning as a consequence of increased gas rarefaction [69] and the ability to deposit stoichiometric compounds with a reduced reactive gas partial pressure (i.e. less poisoning) could be due to increased reactive gas bombardment at the substrate during the HiPIMS off-phase [44]. Another factor that must be taken into account during reactive HiPIMS, and one that is considered in chapter 8, is the formation of high-energy negative ions in the presence of electronegative gases. Bombardment of the substrate by these energetic species can cause densification and/or re-sputtering of the deposited thin film, effectively reducing the static deposition rate [21].

Plasma properties of the HiPIMS discharge

The HiPIMS process is a form of plasma-assisted physical vapour deposition (PVD) and so, as one would expect, the plasma parameters play a crucial role in the overall process and can often be directly linked to the deposited thin film properties. Understanding the interactions between plasma species, background neutrals and the target/substrate/chamber surfaces is of utmost importance in order to tailor and optimise the HiPIMS process, and indeed any plasma process, for a desired application. An array of different plasma diagnostic techniques ranging from invasive electrostatic probe measurements (e.g. Langmuir probe) to non-invasive optical measurements (e.g. optical emission spectroscopy, OES) are available with which to determine basic plasma parameters in HiPIMS discharges. The plasma diagnostic techniques relevant to this thesis are described in chapter 4.

The Langmuir probe is a simple yet versatile technique which has been widely employed to measure spatio-temporal plasma parameters such as the ion/electron density,

the electron energy distribution and the effective electron temperature in HiPIMS discharges [70–76]. The electron density measured during the HiPIMS discharge on-phase is typically $2-3$ orders of magnitude larger than that found in DCMS. Work performed by Bohlmark *et al.* [72] demonstrated that the peak electron density reaches values on the order of 10^{19} m^{-3} compared with that measured in DCMS (10^{16} m^{-3}). Time-resolved measurements [71] show that large ion densities (10^{17} m^{-3}) can persist for several milliseconds after the end of the pulse on-phase resulting in the presence of both argon and metal ions [77] long after the termination of the pulse. Anders and Yushkov [78] attribute these extended decay times to long-lived argon metastables. The peak electron density is also observed to increase with gas pressure [71], applied power [79] and discharge current [80]. In reactive HiPIMS, the peak electron densities are observed to be slightly lower than those found in metallic mode; for example 10^{18} m^{-3} for an Ar/O_2 mixture [81]. Electron temperatures are observed to be typically lower in HiPIMS than in DCMS due to the electron temperature quenching effect [74] of metal ions which are more readily ionised and excited and can be the dominate ion species during the on-phase in a HiPIMS discharge, whereas gas ions tend to dominate in DCMS discharges. Poolcharuansin and Bradley [76] presented electron energy distribution function (EEDF) data obtained using time-resolved Langmuir probe analyses (see figure 2.8). These data suggested the existence of three distinct electron energy populations in the initial phase of the HiPIMS pulse; super-thermal, hot and cold electrons representing effective electron temperature ranges of $70-100$, $5-7$ and $0.8-1$ eV, respectively. The low-energy, cold electrons are thought to be remnants of previous pulses whereas the high energy super-thermal electrons are claimed to arise from the rapid expansion of the sheath as the potential pulse is applied to the target. The hot electrons are generated as a result of secondary emission from the target and subsequent acceleration in the target sheath and also from electron impact ionization caused by the super-thermal population. Ross *et al.* [82] report a stable electron temperature of 1.2 eV from 20 μs into the on-phase until the end of the pulse during HiPIMS of titanium in argon.

Spatio-temporal measurements of the plasma potential can also be obtained by means of a Langmuir probe, but it is often more convenient, particularly for time-resolved measurements, to use an electron-emitting (emissive) probe. Using an emissive probe, Liebig and Bradley [83] observed highly negative plasma potential values exceeding -300 V during the ignition phase of the HiPIMS pulse and close to the target surface, before settling to about -20 V during the 'stable' phase of the pulse. Mishra *et al.* [84] also report highly negative plasma potentials during the ignition phase (approximately -150 V) and also calculate very high electric fields on the order of several kV/m within the discharge, in both the radial and axial components.

OES and energy-resolved mass spectrometry are very useful diagnostic tools which are widely employed to measure ion composition in plasma discharges. The latter can

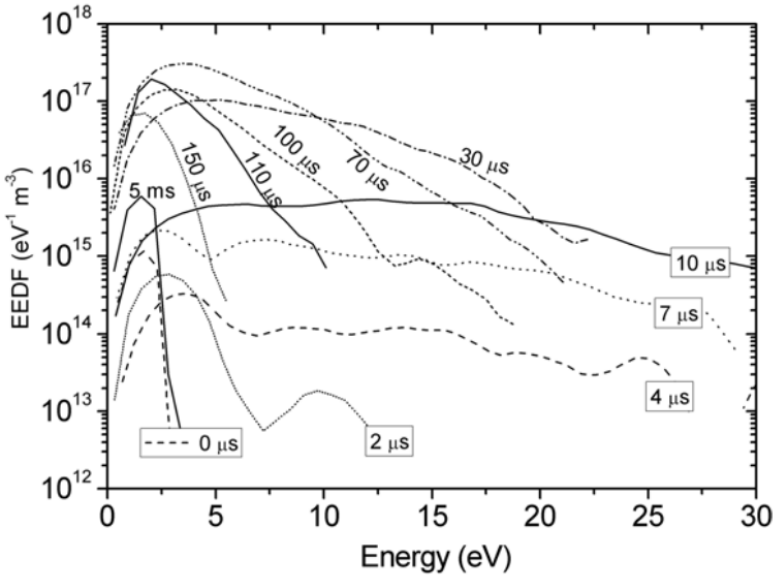

Figure 2.8. EEDFs measured at different times during a HiPIMS pulse using a Langmuir probe. At earlier times, the EEDFs show an extended tail, revealing the presence of energetic electrons at the start of the pulse. Reproduced from [76].

also provide measurements of ion energy distributions for different species. Energy distributions of sputtered particles generally follow a Sigmund-Thompson energy distribution (equation 2.3). Measurements performed by Bohlmark *et al.* [85] showed that Ti^+ ion energy distributions measured during HiPIMS of a titanium target posses a high energy tail stretching up to 100 eV, while only extending to 40 eV for the case of DCMS. Furthermore, energy-resolved mass spectrometry measurements revealed the presence of multiply charged ions at a typical substrate position (10 cm above the target surface) in low pressure conditions [75, 86]. Ion bombardment at the substrate has been shown to greatly affect the properties of the growing thin film by increasing the surface mobility of adatoms and can be used to grow high-temperature thin films far from thermal equilibrium [87]. For this reason, knowledge of the ion energy distributions at the substrate are of great importance when considering applications for the deposited thin film. For reactive sputtering in the presence of electronegative gases, the bombardment of the growing film by high-energy negative ions is also an important consideration and has been shown to significantly affect film properties [21–24].

2.4.2 Reactive HiPIMS

Although the general discharge characteristics of non-reactive HiPIMS are somewhat (if not completely) understood, this is not the case for reactive HiPIMS. All of the effects discussed in §2.4.1 are still applicable to reactive HiPIMS, however, it is complicated by the changing condition of the target (target *poisoning*) and the more involved plasma chem-

istry. The reactive gas interacts with the metal target by forming a layer of metal-gas compound on its surface, hence changing important target properties such as the secondary electron emission coefficient (SEEC) and the sputtering yield. Plasma chemistry is complicated simply due to the presence of more species, but also due to the increased activation of the reactive species by the high electron density present in HiPIMS discharges which is thought to aid in the deposition of oxides and nitrides [8].

The characteristics of the reactive sputtering process depend heavily on the flow rate of the reactive gas. The flow rate of the reactive gas and the target/chamber geometries determine the extent to which the target surface is covered by a compound ('poisoned') and results in a hysteresis effect as illustrated in figure 2.9. As the target surface becomes covered in compound, a change in the applied target potential is required in order to maintain a constant discharge power, which is often attributed to the difference in the SEEC of the metallic target surface when compared with that of its compound. Consider the sputtering of titanium in the presence of oxygen; titanium oxide has a lower SEEC than that of metallic titanium [88] and so it is expected that, to maintain constant discharge power, an increased absolute target potential would be required. Indeed, this is what is predicted and observed by Depla *et al.* [88] in reactive DCMS of titanium in an argon/oxygen atmosphere. However, as shown in figure 2.9, the reverse is true for reactive HiPIMS of titanium in the same gas mixture. This was also reported by Aiempanakit *et al.* [89], who proposed the reasoning being the favoured sputtering of oxygen from the titanium oxide surface and the consequential increase in back-attracted O^+ ions, which increase the target surface SEEC when compared with an Ar^+ dominated discharge.

A major concern, particularly for industry, is the significantly lower deposition rate recorded in some instances of reactive HiPIMS when compared with equivalent pulsed DCMS [90–92]. During reactive sputter deposition, it is often desirable to operate in the unstable *transition* regime of the hysteresis curve. In doing so, it is possible to achieve higher deposition rates whilst simultaneously permitting the deposition of a stoichiometric compound thin film. In DCMS, operating within the hysteresis transition zone is extremely difficult without the use of an active feedback control system. However, it has been reported that the hysteresis effect in reactive HiPIMS may be suppressed or even eliminated without the need for active feedback control [9]. Work performed by Kubart *et al.* [10] identified a relationship between the width of the hysteresis transition zone during deposition of TiO_2 and the frequency of the HiPIMS discharge. It was argued that when employing a high repetition rate, gas rarefaction in front of the target is reduced as a result of the lower discharge current when compared with a discharge operating with a lower frequency and the same average power. It was proposed that the reduction of the gas rarefaction effect leads to a larger reactive gas density in the pre-target region and thus a greater degree of target poisoning. For low frequency HiPIMS discharges (and higher peak discharge current), the gas rarefaction effect is increased, however, the oxygen has

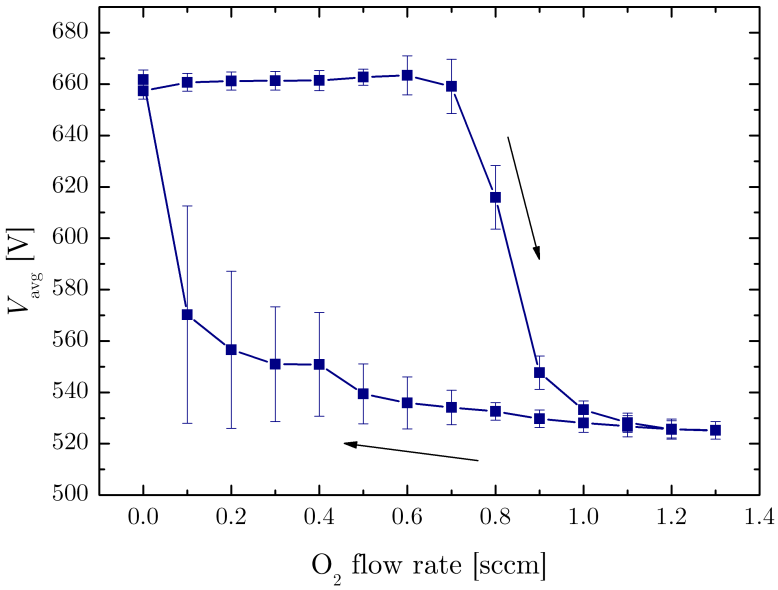

Figure 2.9. Absolute values of the average applied target potential, V_{avg}, during the on-phase of HiPIMS of titanium against the oxygen flow rate. A clear hysteresis effect is observed.

enough time to refill the pre-target volume in the long off-time thereby still permitting a high degree of target poisoning. It was found that the hysteresis was minimized by employing a discharge frequency between 2 and 4 kHz. Aiempanakit *et al.* [14] also found that at a frequency 4 kHz, the measured deposition rate during HiPIMS of TiO_2 was 97% of the rate recording in the equivalent DCMS process.

Reactive HiPIMS has been used to successfully deposit a number of functional thin films, many with superior properties compared to those grown using DC and pulsed DCMS. For example, CrN coatings exhibited improved performance in abrasive wear tests over those deposited by arc bond sputtering [13], TiO_2 coatings grown using reactive HiPIMS were found to have increased density and refractive index compared to those grown using reactive DCMS [14,93] and ZnO films were observed to be smoother and more dense compared to those deposited by pulsed DCMS [43]. Many of the differences observed in films deposited by reactive HiPIMS can be attributed to the increased ion irradiation of the developing film and increased activation of the reactive species [15]. Enhanced surface mobility resulting from the increased ion flux [11] allows for densification of the deposited coating, changes in microstructure and improved hardness of TiN films [15]. However, if the bombarding ion energies are too high, damage to the coating is a possibility. For example, high-energy negative ions are formed in the presence of electronegative gases and have been associated with increased resistivity in transparent conductive oxides [24]. Negative ions in magnetron sputter deposition are considered in the following chapter.

With the offering of superior quality coatings and improved deposition rates when

compared with more conventional deposition methods, the reactive HiPIMS process has much potential and certainly warrants further research, something that this thesis aims to contribute towards.

Chapter 3

Negative ions in reactive magnetron sputtering

3.1 Introduction

In order to deposit compound thin films using magnetron sputter deposition, a metal target may be sputtered in the presence of a *reactive* working gas such as nitrogen, oxygen, fluorine or a combination of different gases often with a noble gas constituent. This so-called reactive sputtering of a pure metal target is typically preferential (in economic terms) to non-reactive sputtering of an expensive ready-made compound target in the presence of an inert working gas. However, reactive sputter deposition has process stability issues which must first be overcome, such as the hysteresis effect outlined in the previous chapter (see §2.4.2). Furthermore, when introducing electronegative gases into the plasma discharge (e.g. fluorine, hydrogen and oxygen) negative ion species are formed, which consequently complicates plasma energy and particle balance [94] as well as the interpretation of plasma diagnostic data such as Langmuir probe I-V characteristics due to modifications of the sheath properties [95]. The role of negative ions can be significant for many modern plasma processing methods and therefore it is important to study and understand how they form and how they can influence the process.

Negative ion formation and loss mechanisms are discussed in §3.2 and the roles that they play in reactive magnetron sputtering are outlined in §3.3 with particular emphasis placed on oxygen-containing discharges.

3.2 Negative ion formation and destruction mechanisms

There are two principle formation mechanisms by which negative species are generated in plasma discharges; *volumetric* processes which occur in the gas-phase and *surface*

reactions which occur at chamber walls, substrates and target surfaces. Likewise, negative ions may be lost via these two principle processes.

3.2.1 Volumetric processes

One of the key aspects of low-temperature reactive plasma processing is the enhanced chemistry offered by plasma-chemical reactions driven by energetic electrons. In low-temperature plasmas the neutral gas temperature is typically around, or just above, room temperature and so reactions with an energy threshold are driven by electrons. Negative ions in plasmas are generally formed via electron attachment to neutral species:

$$\mathrm{e}^- + \mathrm{A} \rightarrow \left(\mathrm{A}^-\right)^* \rightarrow \mathrm{A}^- + \Delta E \tag{3.1}$$

where an unstable intermediate state, $(\mathrm{A}^-)^*$, is formed. ΔE represents the internal energy of A, the electron energy and electron affinity, $\mathcal{E}_{\mathrm{aff}}$, of A. This energy can be released via photon emission (radiative attachment) or through a collision with a third body. However, these reactions are both relatively unlikely in low-pressure plasmas due to small cross sections and low density conditions. The most probable formation mechanism for negative ions in low-pressure, low-temperature plasmas is the *dissociative attachment* of small molecules [96]:

$$\mathrm{e}^- + \mathrm{AB} \rightarrow \left(\mathrm{AB}^-\right)^* \rightarrow \mathrm{A}^- + \mathrm{B} \tag{3.2}$$

The formation of stable negative ions in this way can occur if A has a positive electron affinity, $\mathcal{E}_{\mathrm{aff}} > 0$. If $\mathcal{E}_{\mathrm{aff}} < 0$ then A^- will be unstable and consequently undergo autodetachment: $\mathrm{A}^- \rightarrow \mathrm{A} + \mathrm{e}^-$, hence stable negative ions exist only for strongly electronegative gases.

In the first step of equation 3.2, any excess energy cannot be carried away as a collisional loss because the electron is captured. For this reason, dissociative electron attachment is a *resonant* process and so the energy range is relatively narrow. The measured cross section for the production of oxygen negative ions as a function of electron temperature is shown in figure 3.1, which can be seen to peak at around $T_{\mathrm{e}} \approx 6.5\,\mathrm{eV}$. The shape of this peak is typical of a resonant process. The second maximum beyond 15 eV is due to polar dissociation (p. 250 in [28]) and isn't significant for most low-pressure discharges due to the high electron energy threshold.

It is also possible for negative ions to form via charge transfer reactions, such as

$$\mathrm{A}^- + \mathrm{B} \rightarrow \mathrm{A} + \mathrm{B}^- \tag{3.3}$$

which is favoured if B has a higher electron affinity than A. This process can also produce negative molecular ions. For example, in oxygen discharges, O_2^- and O_3^- can be

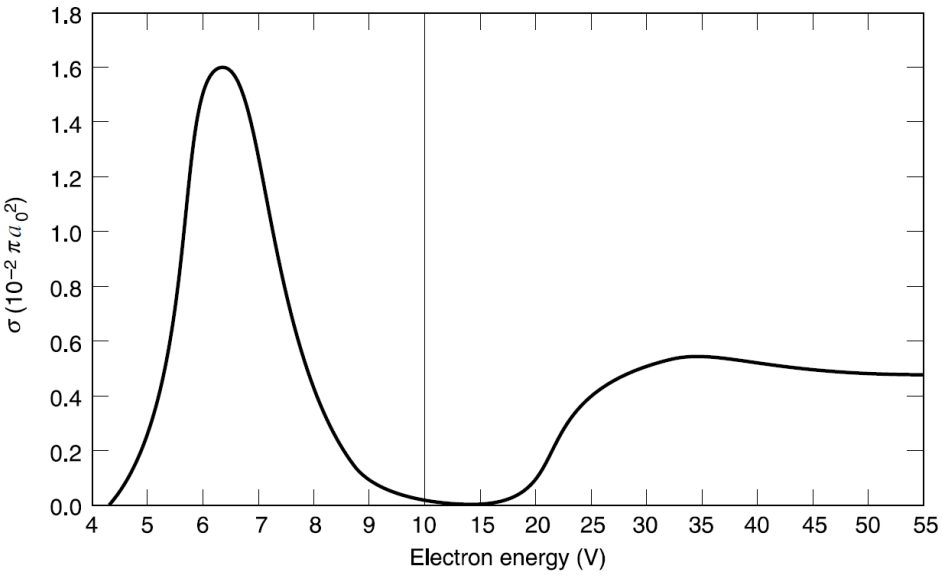

Figure 3.1. Total measured cross section of oxygen negative ion production in O_2 by electron impact. Reproduced from p. 251 in [28].

formed via charge transfer reactions of excited metastable oxygen [97] and ozone with O^-, respectively.

However, it is generally accepted that dissociative electron attachment is the primary volumetric formation mechanism of negative ions in low-pressure plasma discharges [96]. Dissociative electron attachment can also occur when the molecule, AB, is in an excited metastable state. For the case of oxygen, attachment to metastable O_2 ($A\,^3\Sigma_u^+$, $C\,^3\Delta_u$, $c\,^1\Sigma_u^-$) is thought to be particularly important during the afterglow of pulsed discharges as the drop in electron temperature favours this reaction over dissociative attachment to the oxygen ground state which has a higher threshold energy [98]. It has also been suggested by Ding *et al.* [99] that attachment to high Rydberg states of O_2 is also important.

Attachment cross sections can also be strongly influenced by the rotational and vibrational modes of the molecule. This is particularly true for hydrogen and deuterium, where the cross section for dissociative electron attachment for the vibrational mode $\nu = 1$ is a factor of 10^4 smaller than for $\nu = 4$ [96]. Furthermore, the increased internal energy of the excited molecule means that the threshold electron energy is reduced when compared with dissociative attachment reactions involving the molecular ground state. The combination of these two effects results in dissociative electron attachment to hydrogen molecules being the fully dominant process for negative ion formation in hydrogen discharges [100]. This has implications for hydrogen/deuterium negative ion sources which are routinely used to generate neutral beams for use in thermonuclear fusion research [101]. These effects have also been reported for oxygen, but the effects are not as remarkable as those observed for hydrogen [96].

Negative ions can be lost via several different reaction pathways involving collisions with electrons or heavy particles. For example, electron impact detachment,

$$e^- + A^- \rightarrow A + 2e^-, \tag{3.4}$$

can be an important loss channel of negative ions, however, only for high electron temperatures. The peak of the cross section for this reaction is typically centred around an electron temperature that is a factor of $10 - 20$ higher than electron affinity, $\mathcal{E}_{\text{aff}}$ [28], due to the Coulomb repulsion between the negative ion and electron. A more probable loss mechanism of negative ions in a low-pressure discharge is positive-negative ion recombination:

$$A^- + B^+ \rightarrow A + B^*. \tag{3.5}$$

At large separation distances, the potential energy of the $A^- + B^+$ state lies above the $A + B^*$ state. However, due to the attractive Coulomb force between the negative and positive ions, the potential energy of the $A^- + B^+$ state decreases with the nuclear separation distance, eventually dropping below that of the $A + B^*$ state at a distance, R_x. Following Lieberman (p. 257 in [28]), the energy separation between these two states can be estimated by

$$\Delta\mathcal{E} \sim \frac{\mathcal{E}_{\text{izB}}}{n^2} - \mathcal{E}_{\text{affA}} \tag{3.6}$$

where $\mathcal{E}_{\text{izB}}$ is the ionization energy of B, n is the principal quantum number of B^* and $\mathcal{E}_{\text{affA}}$ is the electron affinity of A. For A taken to be atomic oxygen (O) and B to be argon (Ar), $\mathcal{E}_{\text{affA}} \approx 1.5$ eV and $\mathcal{E}_{\text{izB}} \approx 16$ eV, and assuming a principal quantum number, $n \approx 3$, $\Delta\mathcal{E}$ is found to be relatively small with a value of approximately 0.3 eV. Due to the typically small values of $\Delta\mathcal{E}$, the nuclear separation distance at which the potential energies of the two states in equation 3.5 intercept (R_x) can be large, resulting in ion-ion recombination possessing a significant cross section.

Another important negative ion destruction mechanism in oxygen discharges is the associative detachment of negative atomic oxygen with neutral oxygen:

$$O^- + O \rightarrow (O_2^-)^* \rightarrow O_2 + e^- \tag{3.7}$$

where the intermediate $(O_2^-)^*$ state autodetaches. The ground state of O_2^- is stable against autodetachment as it lies below the O_2 ground state, however, many of the excited states of O_2^- sit above the neutral ground state and readily undergo autodetachment (p. 260 in [28]). This results in equation 3.7 having a large reaction rate constant even at thermal energies where $k_{\text{adet}} \sim 3 \times 10^{-16}\,\text{m}^3\,\text{s}^{-1}$.

3.2.1.1 Global models

To model the complex chemical processes in plasma discharges, so-called *global models* are often employed. Although the spatial distributions of plasma parameters are assumed rather than calculated, or ignored completely for the case of zero-dimensional models, global models can provide a valuable insight to the evolution and scaling of plasma parameters in complex multi-species discharges. An alternative to global models are particle-in-cell (PIC) simulations, which present several advantages over the former. For example, the rate coefficients used in global models are calculated assuming a Maxwellian distribution of electrons, while PIC simulations are able to model the distributions. However, PIC models are very computationally expensive and, despite the assumptions made, global models can be used to ascertain correlations between various plasma parameters. A global model uses volume-averaged quantities and constitutes a system of conservation equations for all species to be considered. For instance, the evolution of the density of species A can be written in the form of a first order differential equation,

$$\frac{\mathrm{d}n_\mathrm{A}}{\mathrm{d}t} = \text{formation terms} - \text{destruction terms} - \text{wall loss term}. \tag{3.8}$$

An example of a formation term for negative ions would be $k_\mathrm{att} n_\mathrm{e} n_\mathrm{A}$ where k_att is the reaction rate coefficient for attachment of electrons to neutral species A, n_A is the number density of A and n_e is the electron number density. Additionally, quasi-neutrality of the charged species must also be satisfied;

$$\sum_i Z n_i^+ = \sum_j Z n_j^- + n_\mathrm{e} \tag{3.9}$$

where n_i^+ is the ith positive ion species, n_j^- is the jth negative ion species. As the power absorbed by the discharge is coupled almost exclusively to electrons in low-pressure, low-temperature plasmas, the evolution of the electron temperature T_e can be obtained by examining power balance. Following the text by Lieberman and Lichtenberg [28], the power balance in the discharge must also be considered by equating the power absorbed by the discharge, P_abs, to the power lost via collisions and at surfaces. By summing over all heavy neutral and ion species (j and j^+, respectively) the power balance equation can be written as

$$\frac{P_\mathrm{abs}}{V} = \sum_j \left[e\mathcal{E}_\mathrm{c}^{(j)} k_\mathrm{iz}^{(j)} n_j n_\mathrm{e} + k_\mathrm{w}^{(j^+)} e \left(\mathcal{E}_\mathrm{e} + \mathcal{E}_\mathrm{i}\right) n_{(j^+)} \right] \tag{3.10}$$

where $\mathcal{E}_\mathrm{c}$ is the collisional energy loss for each electron-ion pair created for the neutral j, $\mathcal{E}_\mathrm{e,i}$ is the kinetic energy lost at a surface for electrons (e) and ions (i), k_iz^j is the ionization rate coefficient of the neutral j and $k_\mathrm{w}^{j^+}$ is the rate coefficient for wall losses of the positive ion j^+. Negative ion energy losses to the walls are often neglected when the

discharge is active as the low-temperature negative ions generated in the plasma volume are generally confined to the discharge bulk by wall sheaths. However, the positive ion flux to the walls is partially dependent upon the negative ion content in the discharge [102]. In the afterglow, the situation is different and, given enough time, the sheaths at the chamber walls eventually collapse, allowing negative ions to be transported to plasma-facing surfaces. This feature of pulsed discharges is discussed further in section §3.2.2. The reader is referred to Ch. 10 of [28] for a much more thorough description of electronegative plasma equilibria.

3.2.2 Surface processes

As well as volumetric formation and destruction, negative ions can also be generated and lost via surface or near-surface processes. Surface conversion of ionic or neutral species via *resonant electron transfer* is one such process that has been investigated substantially [103] due to its relevance to many surface processing techniques.

In most low-pressure plasma discharges, ions are accelerated toward surfaces by electric fields contained within boundary layers (sheaths). As a bombarding positive ion approaches a metallic surface, the atomic levels of the incoming ion overlap with those at the metallic surface, allowing electrons to transfer from the valance band of the metal to unoccupied atomic energy levels of the ion. A schematic diagram of the potential energy levels for an ion approaching a metallic surface and undergoing resonant electron capture is shown in figure 3.2.

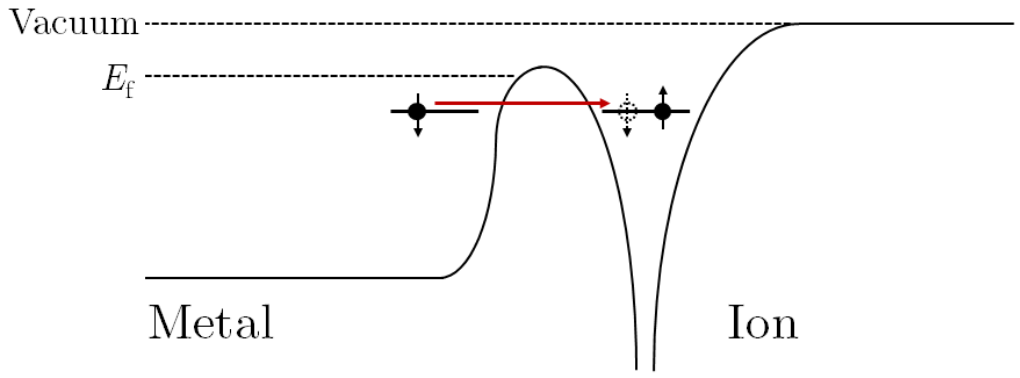

Figure 3.2. Schematic of the resonant electron capture process by an ion close to a metallic surface. The Fermi level of the metal is denoted by E_f and the energy level of the vacuum is also shown.

Once the positive ion has been neutralized, the neutral atom can then capture an additional electron if the distance of closest approach is sufficiently small. The affinity level of the incoming neutral shifts down and broadens due to the overlapping metallic and atomic wave functions, permitting the formation of negative ions [104]. This resonant capture of electrons and the subsequent survival probability of the negative ion is sensitive

to the distance of closest approach of the projectile, the work function of the metal surface [105] and the grazing angle of the incident projectile [106]. Such electron transitions can also result in the production of highly excited metastable states.

All of the above discussion concerns negative ion formation at clean metallic surfaces, however, the situation becomes more complex when considering insulating surfaces or metal surfaces with a monolayer of insulating compound (i.e. conditions similar to those found in reactive magnetron sputter deposition operating in 'poisoned' mode). A dielectric surface is characterized by a band gap separating the last filled and first free energy states. If the band gap is larger than the work function of the clean metal, this implies that a shorter distance of closest approach is required to achieve resonant electron capture. However, the very existence of a band gap could also reduce electron losses to the surface thereby more efficiently preserving surface generated negative ions.

Several studies [107–109] have investigated the formation of negative ions scattered from metallic surfaces exposed to oxygen. Negative ion yields for a clean Mg surface were found to be small, however, it was found that with increasing oxygen exposure, the negative ion yield from Mg and Al surfaces increased markedly before reaching a plateau at exposures above 5 Langmuir (L) units (1 L = 10^{-6} Torr s). This agrees well with measurements performed by Mahieu *et al.* [110], which demonstrated a dramatic increase in oxygen negative ion (O^-) formation during reactive magnetron sputtering of a Y target operated in poisoned mode (i.e. high oxygen flow rates) when compared with operation in metallic mode (i.e. low oxygen flow rates). Therefore, it appears that negative ion formation occurs much more readily on surfaces over which a thin oxide layer has formed.

In addition to formation at surfaces and somewhat akin to volumetric processes, negative ions can also be formed via near-surface plasma-chemical reactions. In low-pressure discharges, plasma-facing surfaces are covered by sheaths, in which a finite electric field exists. Acceleration of positive ions toward the surfaces and subsequent collisions inside the sheath can result in the near-surface formation of negative ions. Due to the increased ion temperature in the sheath as compared to that found in the plasma, the sheath chemistry can vary significantly from that of the plasma bulk. However, lower electron densities in the sheath may mean these mechanisms are not as significant as surface charge-exchange processes.

3.3 Negative ions in reactive magnetron sputter deposition

The presence of negative ions within a magnetron discharge affects several major aspects of the processing conditions, most notably the composition of the ion fluxes incident upon the substrate and chamber walls. For example, the positive ion flux exiting a discharge

is partially related to the negative ion-to-electron ratio (i.e. the electronegativity) within the discharge [102]. Additionally, negative ions formed at the target surface can be accelerated within the cathode sheath and bombard the developing thin film at the substrate. The functional properties of deposited thin films have been shown to be influenced significantly by substrate fluxes [38] and some effects have been attributed directly to the bombardment by high-energy negative ions [111–115]. As such, it is important to understand the discharge conditions during reactive magnetron sputter deposition of oxides and how they relate to substrate fluxes and ultimately, film properties. Knowledge of negative ion densities, mass/energy distributions and their fluxes forms a key aspect of this understanding.

3.3.1 Negative ion energy distributions

As discussed in the sections above, negative ions can be formed via several different mechanisms in reactive magnetron discharges containing electronegative gases. Due to this, the energy distributions of negative ion species generally exhibit separate energy populations as illustrated in figure 3.3. Low-energy negative ions are typically generated via plasma-chemical reactions such as dissociative electron attachment and are confined to the plasma bulk by wall sheaths. Negative ions that originate from surface reactions occurring at the cathode are subsequently accelerated through the cathode fall region and can arrive at the substrate with energies corresponding to the absolute cathode potential (typically $200 - 1000$ eV) if collisions are minimal. If high-energy negative ions undergo many collisions before sampling, they will contribute to the low-energy population. Medium-energy populations can also be observed at the substrate and are a consequence of high-energy negative ions undergoing dissociation en route to the substrate with the energy being divided according to the mass ratio of the products.

Several authors [17, 19, 110, 112, 116–118] have reported on the energy distribution of negative oxygen ions in reactive magnetron sputtering under different conditions. Zeuner *et al.* [17] reported on the negative ion energy distributions during the reactive DCMS of silicon in an argon/oxygen atmosphere and suggested that high-energy O^- ions correspond to the target potential and are a consequence of acceleration in the cathode sheath following low-energy electron attachment at the target surface. However, Mišina *et al.* [118] reported an energy shift of the high-energy O^- ion peak to higher energies than the target potential, suggesting that the discrepancy is a result of additional kinetic energy transfer during the sputtering process. Mráz and Schneider [116] further supported the validity of this mechanism by demonstrating that O^- ion energy distributions obtained during DCMS operation compared favourably with a model based on Sigmunds linear collision cascade sputtering theory. In contrast, the same authors also observed that this model is insufficient when describing the high-energy population of the O^- energy distributions

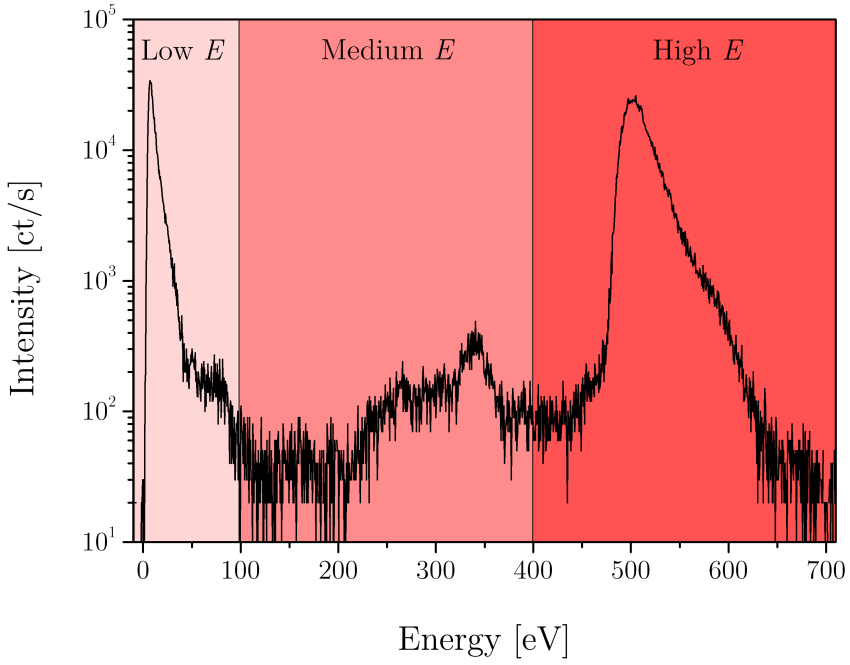

Figure 3.3. O^- ion energy spectrum recorded during high power impulse magnetron sputtering of titanium in an Ar/O_2 discharge. Three distinct energy populations (low, medium and high) are highlighted.

during pulsed DCMS [18]. It was suggested that during pulsed DC operation the O^- ion energy distributions can be well described exclusively by the target potential distribution function and not by the notion of O^- ions sputtered from the target surface [116].

More recently, Mahieu *et al.* [110] adapted a binary collision Monte Carlo simulation (SiMTRA) to model mass, energy and angular distributions of high-energy negative ions during reactive sputtering of metal targets in an argon/oxygen atmosphere and found good agreement with experiments. In the same study, it was also demonstrated that the intensity of the measured high-energy O^- ions decreased with increasing O_2 partial pressure beyond the hysteresis transition. It was then suggested that the amount of high energy O^- ions produced is related to the material-dependent sputter yield and the condition of the target surface and not to the oxygen partial pressure, hence supporting the notion of sputtered O^- ions. By measuring the O^- ion energy distributions during reactive magnetron sputtering of thirteen different target materials, Mahieu and Depla [19] reported that high-energy O^- ion formation is strongly correlated to the ion-induced secondary electron coefficient of the target material during the magnetron sputtering of oxides.

Although much emphasis is placed on the production of O^- ions during reactive magnetron sputter deposition of oxides, negative oxygen compound species are also present. Figure 3.4 shows the time-averaged energy distributions of oxygen and titanium oxide negative ions observed during HiPIMS of titanium in an Ar/O_2 discharge. Consistent

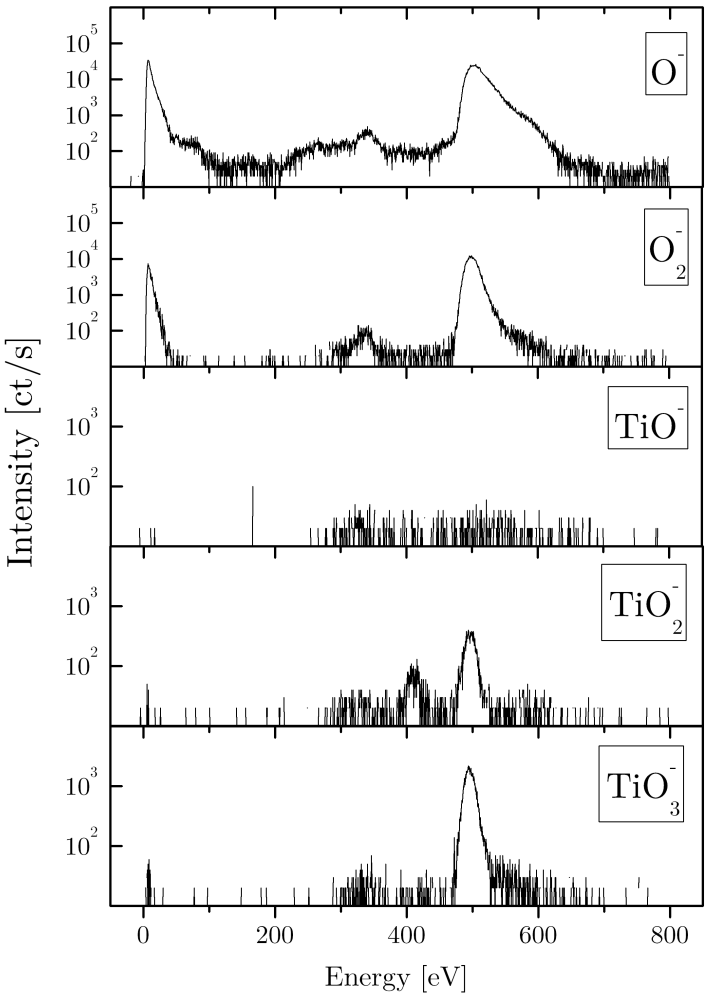

Figure 3.4. Time-averaged energy distributions of oxygen and titanium oxide negative ions measured during reactive HiPIMS of titanium in an Ar/O_2 discharge.

with other reports [19, 117, 118], O^- is indeed the most abundant species, however, there are also significant intensities of TiO_2^- and TiO_3^- detected predominantly in the high-energy population. This is reasonable, as it suggests that titanium oxide negative ions are formed exclusively at the target surface before undergoing acceleration in the cathode sheath.

3.3.2 Negative ion mass spectra

Mass spectrometry is a widely employed diagnostic technique used to measure positive and negative ions as well as neutral species present in plasma discharges. When properly implemented, it can be used to monitor plasma composition and to help in determining plasma chemistry. As such, it can also be employed as a method of process control in many applications of plasma-assisted technology. However, one must use caution when

using this technique as mass spectra are generally obtained at a chosen pass energy and may provide a false representation of the plasma composition. For instance, as shown in figure 3.4, titanium oxide negative ions exist only at high energies and therefore would go undetected in mass spectra measured at a low pass energy.

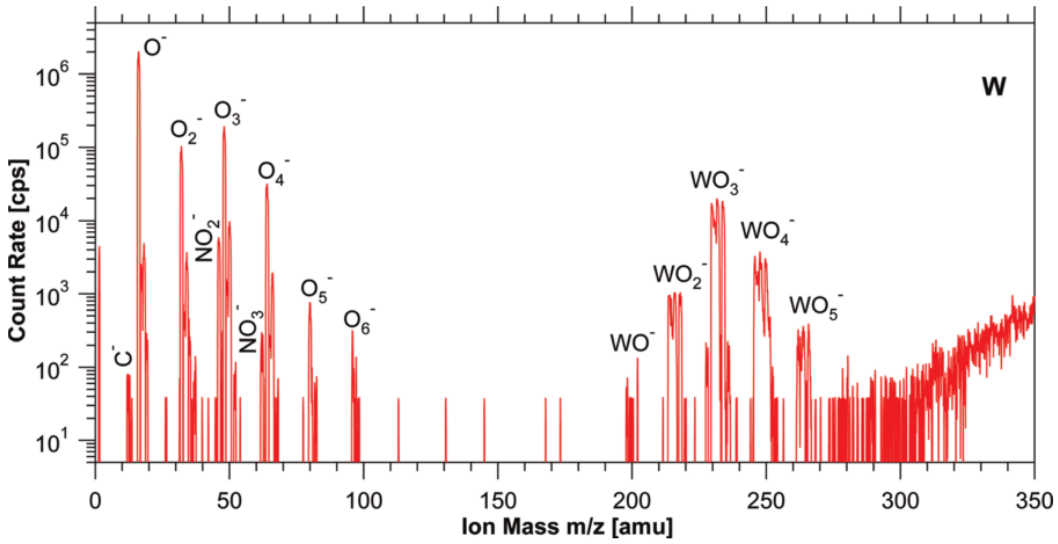

Figure 3.5. Negative ion mass spectrum obtained during reactive magnetron sputtering of a W target in an Ar/O_2 discharge. Reproduced from [112].

An example of a mass spectrum of negative species is shown in figure 3.5, which was recorded during magnetron sputtering of a tungsten target in an Ar/O_2 discharge. In addition to atomic oxygen negative ions, molecular oxygen negative ions (O_x^- with $x = 1$ to 6) and metal oxide negative ions are also found. A set of peaks occurring at large mass-to-charge ratios ($m/z > 200$) indicate the presence of tungsten oxide negative ions with satellite peaks indicative of the natural isotopes of tungsten. Impurities due to residual gas results in peaks corresponding to NO_2^- and NO_3^-. Even with small amounts of nitrogen gas, these peaks are clearly detectable due to their high electron affinities: 2.3 and 3.9 eV, respectively [112]. From figure 3.5 it is apparent that O^- is the most abundant negative species by approximately an order of magnitude, which is typically the case for most magnetron discharges [19, 117, 118] and justifies the attention paid to it by many of the studies centred on negative ion generation during the magnetron sputter deposition of oxides.

Although much work has been performed investigating the mass and energy spectra of negative ion species in reactive DCMS and reactive pulsed DCMS, before the work presented in this thesis there has been little reported on the mass and energy distributions of negative ions in reactive HiPIMS.

3.3.3 Spatial distributions of negative ions in a magnetron discharge

Although the energy-resolved mass spectrometer technique allows for mass spectra and mass-resolved energy distributions of negative ions arriving at a substrate to be determined readily, there is a significant drawback. The sampling orifice of a mass spectrometer is typically grounded, resulting in the formation of an ion sheath in front of the orifice containing a potential barrier that is on the order of the local electron temperature ($1-4$ eV). Negative ions generated in the plasma bulk via plasma-chemical reactions such as dissociative electron attachment possess energy on the order of the background gas temperature ($300-1000$ K) and as such are unable to overcome this potential barrier. Hence, these low-energy negative ions go undetected using this technique and other means must be employed to determine the absolute local negative ion density in a plasma. One tried and tested method is laser-aided photodetachment [119], which was used by Scribbins *et al.* [120] to determine the spatial distribution of oxygen negative ions during reactive DCMS of titanium in an Ar/O_2 discharge (see figure 3.6).

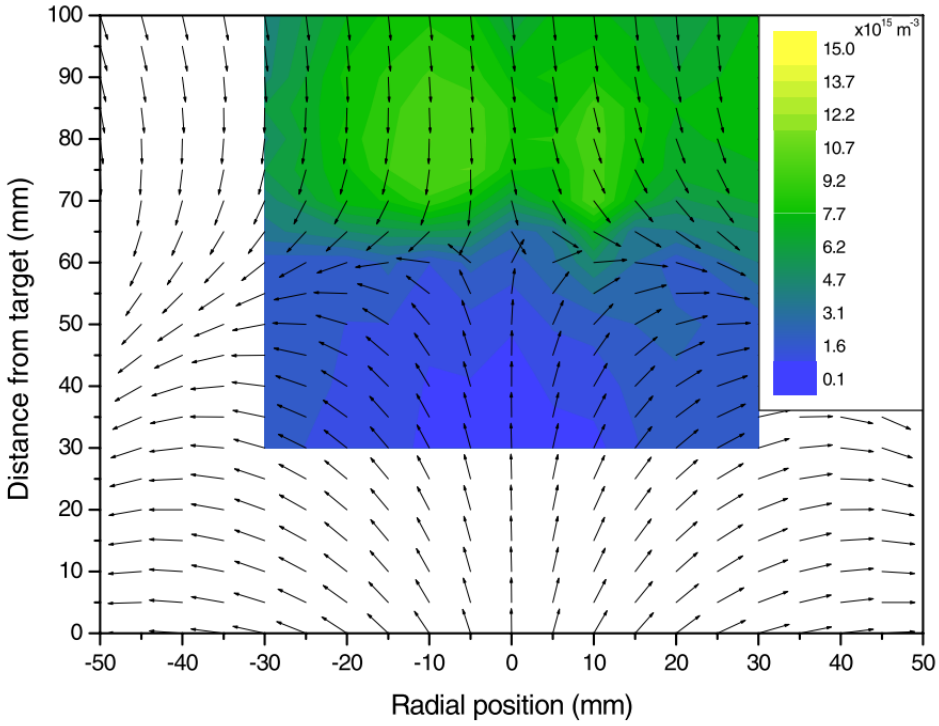

Figure 3.6. Two-dimensional plot of the O^- ion density as measured in an Ar/O_2 DC magnetron discharge at a total pressure of 1.59 Pa and an oxygen partial pressure of 0.31 Pa. The magnetic field vectors are also shown. Reproduced from [120].

From figure 3.6, the highest concentrations of O^- ions are observed to be located outside of the last closed field lines of the magnetic trap, appearing in an annulus around the central axis of the discharge. This general distribution was similar to those predicted

by a particle-in-cell/Monte Carlo collisions (PIC/MCC) model developed by Bultinck and Bogaerts [121]. As the formation of negative ions in the discharge occurs primarily via electron attachment reactions and most electrons are confined to the magnetic trap, it is expected that O^- ions are generated predominantly in this region. However, the negative ions do not remain in this region for several reasons. Due to the large Larmor radii of the heavy negative ions in comparison to electrons, the negative ions are not trapped by the magnetic field. Also, the negative plasma potential adjacent to the cathode [122] forces the negative ions to accumulate in regions of positive plasma potential, namely above the magnetic trap. As argued by Bultinck and Bogaerts [121], the low O^- density in the magnetic trap region may also be due to higher local positive ion densities resulting in increased losses of negative ions via recombination reactions with positive ions (in this case Ar^+, O^+ and O_2^+).

It is observed in both experimental measurements [120] and in simulations [121] that at increased oxygen partial pressure, the region of high O^- density expands somewhat and flattens out to a more uniform distribution about the central axis of the discharge. However, the general shape of the spatial distribution does not alter significantly and the highest negative ion concentrations in a magnetron discharge are generally located outside of the magnetic trap in typical substrate positions. The presence of negative ions in the discharge has the affect of altering the Bohm criterion [95] and hence changing the positive ion flux to the substrate surface [102] affecting film development.

3.3.4 Effects of negative ions on deposited films

As discussed above, low-energy negative ions confined to the plasma bulk influence the positive ion flux to the substrate. The positive ion flux incident upon the substrate is decreased for increasing negative ion density when compared with a nominally identical electropositive discharge with the same positive ion density [102]. Ion-assisted magnetron sputter deposition typically results in the densification of the developing thin film via increased surface mobility of the adatoms, hence large negative ion populations may adversely effect the density of the deposited coating. In contrast however, it has been shown that bombardment of carbon thin films by energetic negative carbon ions can increase the quality of DLC coatings [123].

Bombardment of the substrate by high-energy negative ions formed at the target surface (in particular O^- ions [113]) has been shown to significantly influence thin film growth in reactive DCMS [112–114] and can also cause the re-sputtering of the deposited film [124]. Furthermore, it has been reported that bombardment by energetic negative ions is detrimental to both the structural [111] and electrical [11, 23, 125] properties of transparent conductive oxides (TCOs).

Nguyen *et al.* [23] deposited aluminium-doped zinc oxide (AZO) thin films using an

off-axis DCMS system in order to reduce high-energy negative ion bombardment. When compared with AZO films deposited on substrates placed directly opposite the target surface, those deposited off-axis exhibited improvements in both electrical and optical properties. Furthermore, only slight differences in grain sizes were reported and it was suggested that the increased resistivity for films bombarded by high-energy negative ions was due to a lower carrier concentration rather than reduced carrier mobility. These results certainly suggest that energetic bombardment by oxygen negative ions generated at the AZO target surface can be detrimental to the quality of the deposited film.

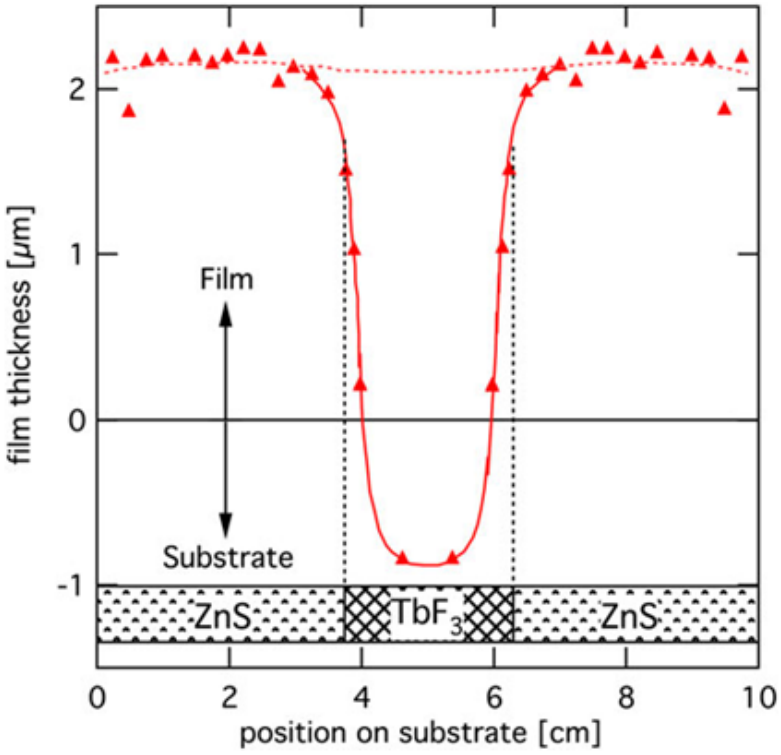

Figure 3.7. Thickness of ZnS-TbF_3 film deposited via diode cosputtering of a compound target (indicated) as a function of substrate position. Reproduced from [126].

Hanak and Pellicane [126] investigated the effects of focused secondary electron and negative ion bombardment of a growing film during the (diode) co-sputtering of two different target materials. Although film deposition occurred at the substrate directly above the ZnS target, growth over the TbF_3 was suppressed. In fact, etching of the substrate directly above the TbF_3 target was observed instead. The measured film thickness is shown in figure 3.7 for different substrate positions. It was postulated that the etching was caused by a focused beam of F^- ions ejected from the target and subsequently enhanced by chemical erosion due to formation of volatile fluorides. Cuomo *et al.* [21] reported in a later publication that this etching of the substrate also occurs in the absence of chemical sputtering. The invention of magnetron sputtering helped to reduce this effect as it allowed for operation at lower voltages when compared with diode sputtering, thereby re-

ducing the energy of the negative ions accelerated through the cathode sheath. However, bombardment of the developing film by negative ions may be more significant for HiPIMS operation [24] as a consequence of the higher discharge voltages used in comparison to DCMS and pulsed DC systems.

3.4 Thesis overview

In this thesis, a selection of plasma diagnostic techniques, the details of which are provided in chapter 4, have been employed in order to investigate various aspects of reactive HiPIMS discharges. In chapter 5, a Langmuir probe was employed to measure the spatial and temporal variations in plasma parameters including ion and electron density, plasma potential, floating potential and effective electron temperature for a variety of different discharge conditions. The temporal evolution of the negative oxygen ion density was estimated by studying the ion-to-electron saturation currents as measured by a Langmuir probe and also compared to laser-aided photodetachment measurements in chapter 6. Negative ion energy distributions were measured by means of energy-resolved mass spectrometry and presented in chapter 7. The formation of high-energy O^- ions originating from the target surface is discussed while changes in pressure, target-to-substrate distance, pulse width, target material and inert gas choice are investigated with regards to their effects on high-energy O^- ions arriving at the substrate. In chapter 8, power normalized deposition rates in reactive HiPIMS of Ti in discharges containing different inert gases mixed with oxygen are measured using a quartz crystal microbalance and compared to those obtained during inert gas-only HiPIMS as well as to measurements made during reactive DCMS in nominally equivalent discharges. Finally, a summary of the findings and conclusions drawn from the investigations presented in this thesis is presented in chapter 9 along with suggestions for any future work.

Chapter 4

Experimental apparatus

This chapter will outline the equipment used to perform the experiments presented in this thesis. In §4.1, the basic experimental set-up will be introduced, including the key aspects of the vacuum chamber and pumping arrangement, the magnetron sputtering source and the power supplies. The plasma diagnostic techniques that were employed throughout the investigations are outlined in §4.2.

4.1 Experimental set-up

4.1.1 Vacuum system

Aside from the set-up used to acquire laser-aided photodetachment measurements (described in chapter 6), all experiments were performed in a stainless-steel cylindrical vacuum chamber with a diameter of 260 mm and a height of 300 mm. See figure 4.1 for a schematic diagram of the experimental set-up. The chamber was pumped down to an ultimate pressure in the range of 10^{-4} Pa via a combination of a rotary vane pump (Edwards E2M28) and a turbomolecular pump (Edwards EXT75DX). The pressure was monitored using three pressure gauges (P1, P2 and P3 in figure 4.1). P1 indicates an active Pirani gauge (BOC Edwards APG100) for monitoring pressures from atmosphere down to 10^{-2} Pa, P2 - an active inverted magnetron gauge for monitoring pressures in the range $10^{-2} - 10^{-4}$ Pa and P3 was a capacitance manometer (MKS Baratron® 628A) used for monitoring the working pressure, typically in the range of $0.1 - 2$ Pa, during experiments. The desired working pressure was obtained by introducing process gases at the required flow rates through two identical mass flow controllers (MKS, 1179A). Process gases used include argon, neon, krypton, xenon and oxygen - the oxygen inlet was used exclusively for oxygen and the second gas inlet was used only for inert gases. The baffle valve between the chamber and pumping system was occasionally used to decrease the pumping speed in order to obtain higher working pressures. Plasma diagnostics, which are described in more detail in §4.2, were mounted to feedthroughs positioned on the side

and top of the vacuum chamber. The axial position of the magnetron and quadrupole mass spectrometer (Hiden Analytical EQP300) could be varied, while the home-made Langmuir probe was able to move radially as indicated in figure 4.1. A modified flange was constructed to allow the EQP to sample from two radial positions, namely along the central axis and directly above the target racetrack (approximately 20 mm from the center, as shown in figure 4.1).

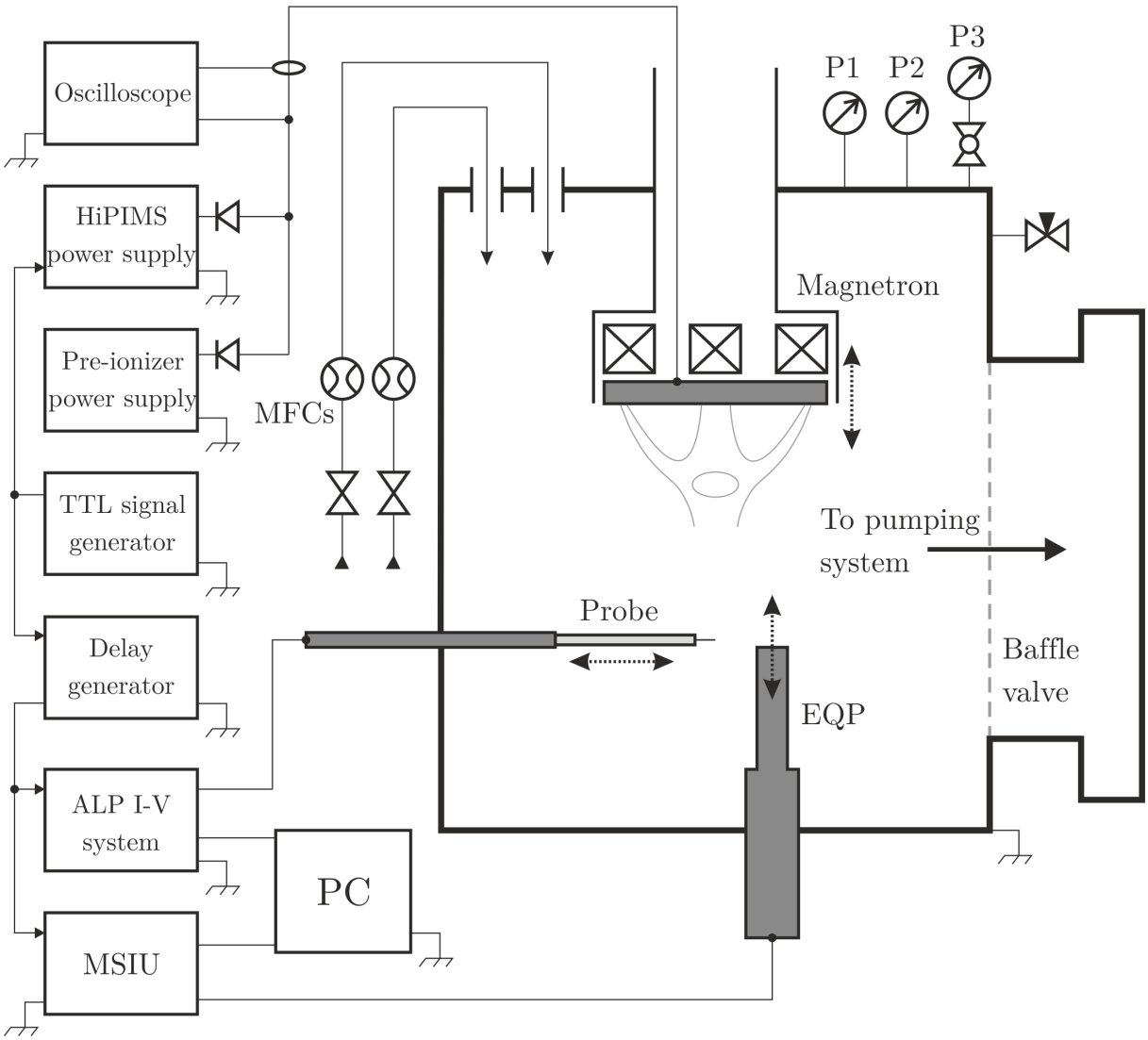

Figure 4.1. A schematic diagram showing the vacuum vessel equipped with three pressure gauges (P1, P2, P3), two gas inlets controlled by means of two mass flow controllers (MFCs), a magnetron sputtering source and a pumping system throttled by a butterfly baffle valve. A Langmuir probe and quadrupole mass spectrometer (EQP) are also illustrated, accompanied by an appropriate electronic block diagram of the power, timing and acquisition systems.

4.1.2 Magnetron sputtering source

The magnetron sputtering source (GENCOA Ltd.) used was an unbalanced, circular planar magnetron with a target diameter of 75 mm. Using an annular clamp, the target was mounted onto a copper cooling element that was directly water-cooled at a rate of 1 l min^{-1} kW^{-1}. When attached, the clamp protrudes above the target surface by approximately 4 mm. An aluminium ring was mounted on the outside of the magnetron source such that the top of the ring was flush with the top of the clamp, serving as an anode.

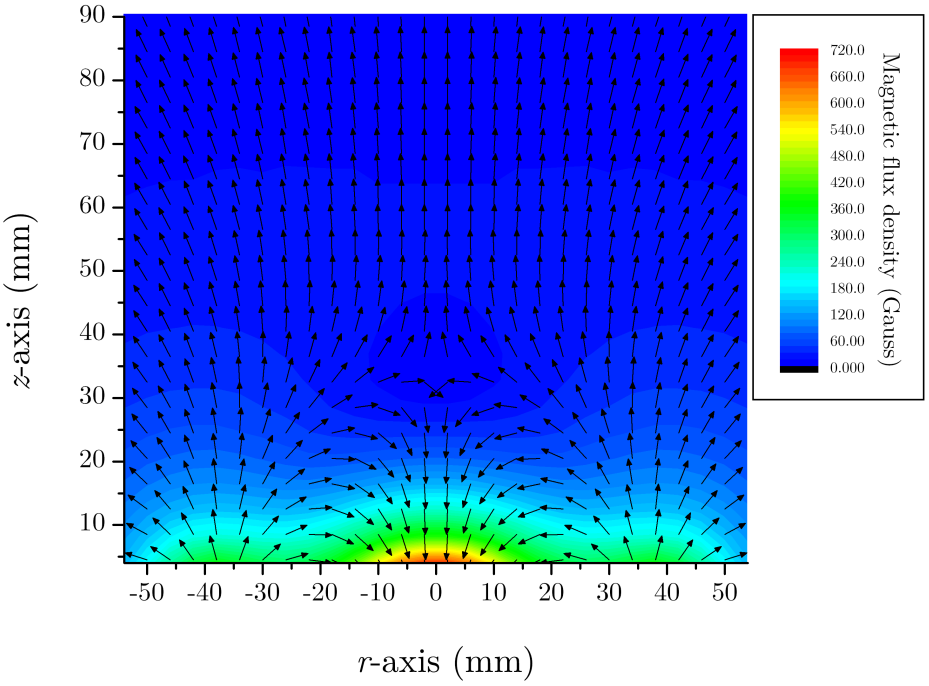

Figure 4.2. The measured magnetic field configuration produced by the magnetron sputtering source. The magnetic null is located at $z \sim 30$mm and the target surface is at $z = 0$ mm (not shown due to measurement restrictions that are explained in the text).

The unbalanced magnetic field is produced by an arrangement of permanent magnetics mounted behind the target and is shown in figure 4.2. The target surface is located at $z = 0$. Magnetic flux density measurements were made using a digital Gauss meter and axial probe (Hirst GM04), with a spatial resolution of 4 mm. Note that measurements of the magnetic field below $z = 4$ mm were not possible due to obstruction of the axial probe by the target clamp. The unbalanced shape of the magnetic field is clear as outside of the magnetic trap, some lines continue upward towards the substrate plane. Characteristic of this configuration is a region of zero magnetic flux density ($\mathbf{B} = 0$), often referred to as a *magnetic null*, which is located along the center axis ($r = 0$) at $z \sim 30$ mm. At $r \sim 20$ mm, the radial component of the magnetic field is at its maximum ($B_\text{r} \sim 650$ G). It is

in this region where the $\mathbf{E} \times \mathbf{B}$ confinement of electrons is at its strongest, giving rise to a greater ionization probability and higher plasma density. The higher plasma density results in increased local ion bombardment of the target (increased sputtering) and a greater degree of erosion. This effect gives magnetron targets their distinctive 'racetrack' erosion patterns.

4.1.3 Power supplies

4.1.3.1 HiPIMS power supply

The magnetron source was powered by an in-house built HiPIMS power supply [127]. The principle of operation of the impulse power supply is as follows. During the pulse off-time, a large capacitor is charged by a DC charging circuit and during the on-time the stored energy is delivered to the magnetron cathode via an electronic switch, in this case an insulated-gate bipolar transistor (IGBT) that could be triggered either by an internal TTL signal generator or externally. The IGBT was protected by a current-limiting resistor (10 Ω, 500 W). A block diagram of the power supply is given in figure 4.3 The AC voltage input is controlled using a Variac, which then determines the DC charging voltage applied to the capacitor and ultimately the output voltage of the impulse. The maximum output voltage is −950 V.

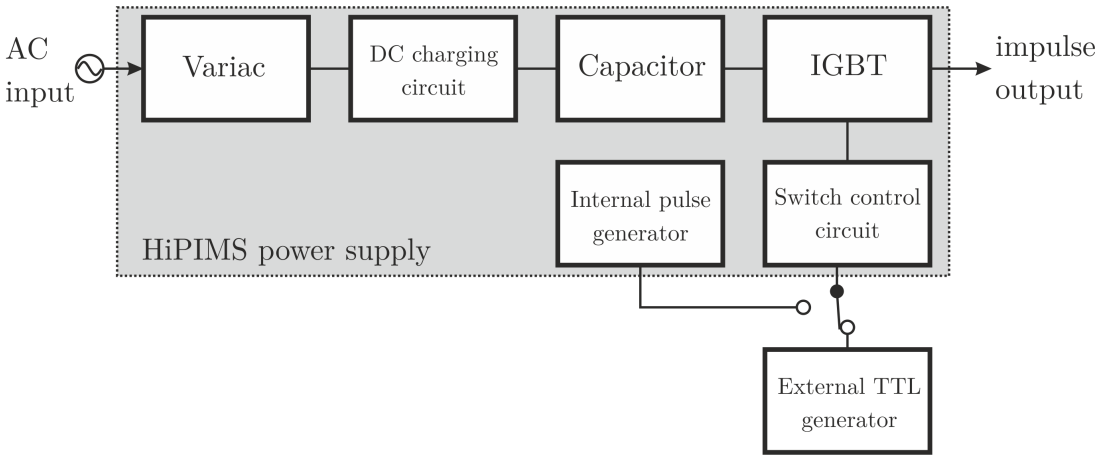

Figure 4.3. A simplified block diagram of the HiPIMS power supply, including external AC and trigger inputs.

The discharge can be characterised by measuring the time-dependent discharge current, $I_\mathrm{d}(t)$, and voltage, $V_\mathrm{d}(t)$, which were obtained using using a DC coupled current probe (Tektronix TCP202) and a passive high voltage probe (Tektronix P5100), respectively. The output from both probes was monitored using a digital oscilloscope (Tektronix TDS3014, 100 MHz bandwidth). The discharge power can also be monitored in real-time using the oscilloscope, as given by

$$P_{\mathrm{d}}(t) = I_{\mathrm{d}}(t)V_{\mathrm{d}}(t). \tag{4.1}$$

However, it is often desirable to quote time-averaged power, particularly when attempting to compare the HiPIMS process with different magnetron sputtering system configurations (e.g. DCMS). The time-averaged power can be calculated by averaging the power during a single pulse and multiplying by the duty cycle, $\delta = t_{\mathrm{on}}/(t_{\mathrm{on}} + t_{\mathrm{off}}) = \tau f$:

$$\overline{P_{\mathrm{d}}} = \frac{\delta}{\tau}\int_0^{\tau} I_{\mathrm{d}}(t)V_{\mathrm{d}}(t)\,\mathrm{d}t = f\int_0^{\tau} I_{\mathrm{d}}(t)V_{\mathrm{d}}(t)\,\mathrm{d}t \tag{4.2}$$

where τ is the pulse length and f is the pulse frequency. The average energy delivered per pulse can also be calculated: $E_{\mathrm{p}} = \overline{P_{\mathrm{d}}}/f$. An example of the discharge current, voltage and power waveform is presented in figure 4.4 with relevant parameters given in table 4.1. Current and power density measurements are calculated assuming a uniform distribution over the entire target surface area ($A_{\mathrm{t}} \sim 44$ cm^2). However, in reality the current and power in a magnetron discharge are largely localized over the target racetrack and furthermore into high-density ionization zones in HiPIMS discharges. Therefore the true local current and power densities in HiPIMS are likely to be much higher than the values given here.

Parameter	Value
Pressure, p	0.8 Pa
Pulse width, τ	100 μs
Pulse frequency, f	100 Hz
Initial voltage, V_0	-700 V
Peak current, I_{peak}	28.5 A
Peak power, P_{peak}	12.6 kW
Peak current density, j_{peak}	0.65 A cm^{-2}
Peak power density, $\mathcal{P}_{\mathrm{peak}}$	0.29 kW cm^{-2}
Pulse energy, E_{p}	0.79 J
Averaged power, $\overline{P_{\mathrm{d}}}$	79 W

Table 4.1. HiPIMS discharge process parameters as obtained from the voltage-current-power-time waveforms shown in figure 4.4.

4.1.3.2 Pre-ionizing power supply

As illustrated in figure 4.1, there is a pre-ionizing power supply unit installed alongside the HiPIMS impulse unit. Examining the waveforms in figure 4.4, one may notice that discharge current lags somewhat behind the application of the target potential by approximately 15 μs. The origins of this delayed current on-set have been investigated by Yushkov and Anders [57] and it was shown in all cases that the length of the time delay is inversely proportional to the applied potential, however, the magnitude of the delay is

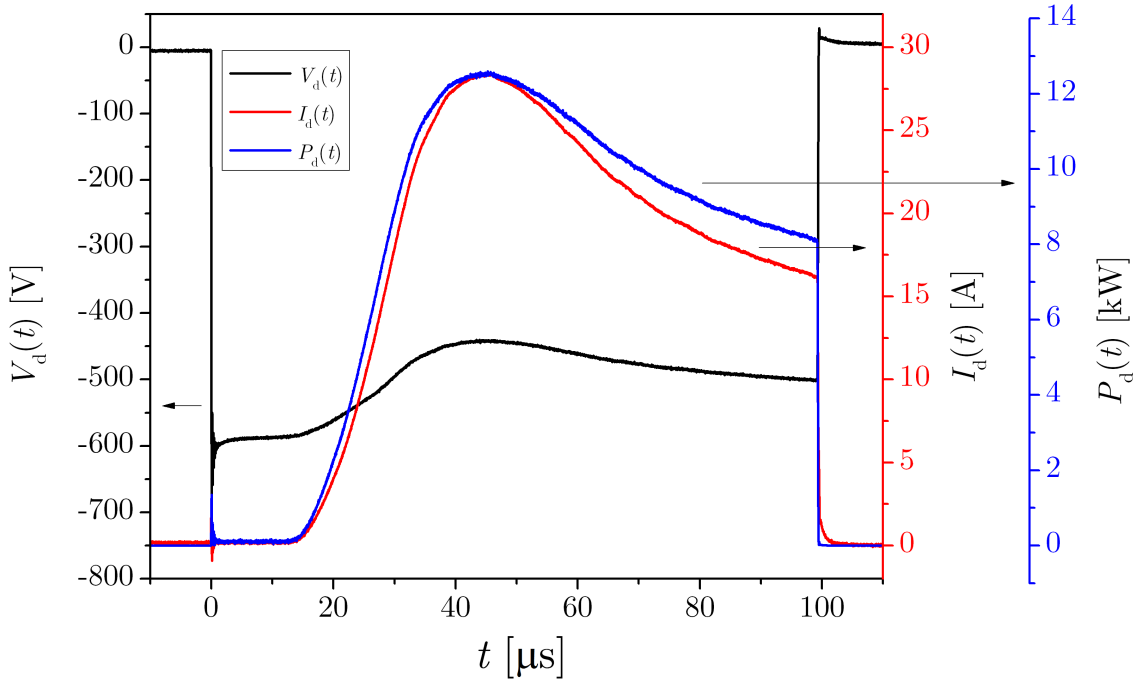

Figure 4.4. Discharge current, voltage and power waveforms of a HiPIMS discharge operated in argon at a pressure of 0.8 Pa with a pulse width of 100 μs and a repetition rate of 100 Hz. Other key parameters are given in table 4.1. The waveforms presented are the result of averaging over 64 pulses.

also a function of both material and gas properties such as the secondary electron emission coefficient and operating gas pressure.

Vašina *et al.* [128] suggested using a low-current DC power supply to generate a low-density plasma in front of the cathode during the HiPIMS off-time. In doing so, the current lag time was reduced markedly, facilitating HiPIMS operation at lower pressures and voltages. The use of a pre-ionizer also permits the use of pulse widths on the order of a few μs, which would be impossible with delay times of the order of 10 μs.

In the experiments presented here, the pre-ionizing unit was a DC power supply capable of applying a potential of -1 kV when no load is present and was connected to the magnetron target in parallel with the HiPIMS power supply as shown in figure 4.1. A current-limiting resistor (40 kΩ, 40 W) was connected between the output of the pre-ionizer and the cathode. Additionally, a diode was used at the output of both the pre-ionizer and the HiPIMS unit to prevent the backflow of current from one power supply to the other. In this configuration, power can only be delivered to the cathode via one supply at a time; in this case, whichever applies the higher absolute voltage. The pre-ionizing unit and its operational characteristics are discussed in more detail in [75] and [127].

4.1.4 Operating in poisoned mode

In reactive sputter deposition of oxides, the oxygen flow rate, $\dot{m}_{O_2}$, is a critical parameter that influences the plasma properties as well as the target and substrate condition. As oxygen is introduced into the chamber, it reacts to form an oxide compound at the substrate and target surfaces. At small $\dot{m}_{O_2}$, there is no discernible difference in the process conditions as the oxygen is being consumed in the formation of an oxide at a rate higher than it is being introduced to the chamber. At this point, the discharge is said to be operating in *metallic mode*. However, beyond a critical point, the oxygen flow rate becomes sufficient to react with the entire substrate and target surface areas; the discharge now operates in *poisoned mode* with a layer of oxide covering the target.

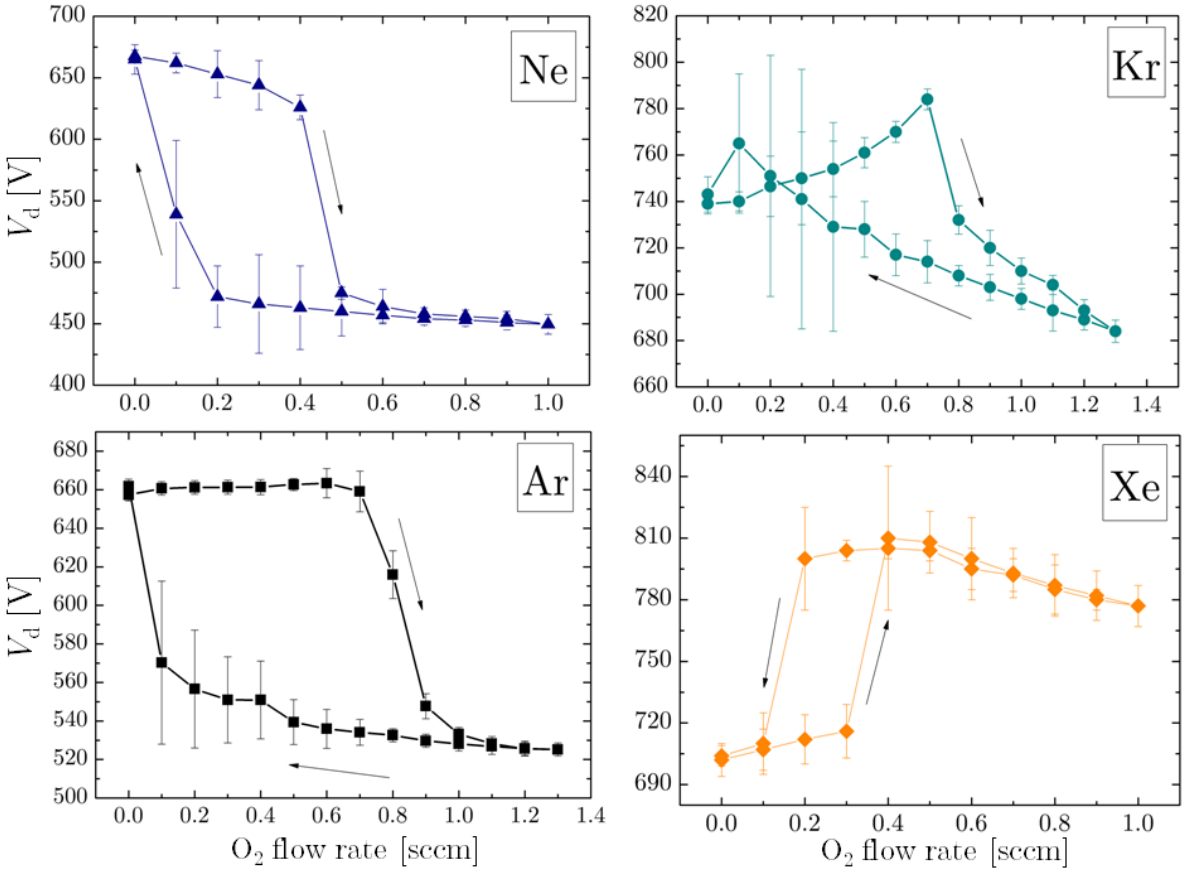

Figure 4.5. The average discharge voltage ($\overline{V_d}$) behaviour during reactive HiPIMS of Ti in a gas mixture of Ne, Ar, Kr or Xe with O_2 as a function of the O_2 flow rate. The inert gas flow rate was kept constant at 3.5 sccm.

This transition is identified by an abrupt change in the oxygen partial pressure, deposition rate and applied target potential. As $\dot{m}_{O_2}$ is greater than the rate of consumption by the substrate and target, the chamber pressure is able to increase with added oxygen. Sputter yields of metal oxide targets are typically much lower than those of the pure metal target (see chapter 8), thus the transition from metallic to poisoned mode can be observed by measuring deposition rate as a function of oxygen flow rate. Furthermore,

oxides often posses markedly different secondary electron emission coefficients than their metallic counterparts and an associated change in the applied target potential required to maintain a constant average discharge power can be observed during the transition.

Figure 4.5 shows the recorded average discharge potential, $\overline{V_{\mathrm{d}}}$, applied during the on-time of reactive HiPIMS of Ti in O_2 mixed with Ne, Ar, Kr and Xe. Notice that the curves follow different paths depending upon whether the O_2 flow is being increased or decreased. $\overline{V_{\mathrm{d}}}$ is observed to decrease in poisoned mode when Ne, Ar or Kr are mixed with O_2, but is seen to increase for the Xe/O_2 mixture. The relationship between the applied target potential and the target condition is related to the changing ion-induced secondary electron emission coefficient and reduction behaviour of the oxide being bombarded by ions [88].

Another method of monitoring the hysteresis transition in oxygen-containing discharges is by measuring the emission of high energy O^- ions from the target surface. Figure 4.6 shows the integrated intensity of the high energy O^- ion signal, I_{O^-}, normalized to the maximum signal intensity, measured during HiPIMS of Ti in an Ar/O_2 discharge as a function of the O_2 flow rate. From figure 4.6, a dramatic increase in I_{O^-} is observed in poisoned mode, as the oxygen flow rate increases beyond 0.7 sccm. As can be seen from figure 4.5, this increase in I_{O^-} is coincident with the decrease of $V_{\mathrm{d}}(t)$ in the Ar/O_2 discharge.

Striking a balance between a high enough oxygen flow rate to deposit a stoichiometric compound with a low enough oxygen flow rate to reduce target poisoning and achieve a high deposition rate is often desired. However, this typically requires operation at some point in the transition region and without some form of real-time process feedback system, finding this balance is difficult. Due to the lack of a feedback control system and the desire to investigate the effects of high energy negative ions in this thesis, almost all reactive HiPIMS discharges are operated in poisoned mode. In order to obtain different oxygen partial pressures, the O_2 flow rate is increased beyond the hysteresis transition point before being incrementally adjusted until the desired O_2 partial pressure is achieved.

4.2 Diagnostic techniques

In order to deduce information regarding plasma properties and to elicit an understand of plasma behaviour, it is necessary to make some form of practical measurement using plasma diagnostic techniques. Broadly speaking, plasma diagnostics can be categorized into invasive and non-invasive techniques. Invasive techniques typically involve inserting a material object, such as an electrostatic probe, into the discharge in order to obtain readings. Obviously, the object will in some way disturb the discharge and it is the aim of invasive diagnostic techniques to keep this perturbation to a minimum, or at least to understand the perturbation such that it may be accounted for. Non-invasive methods

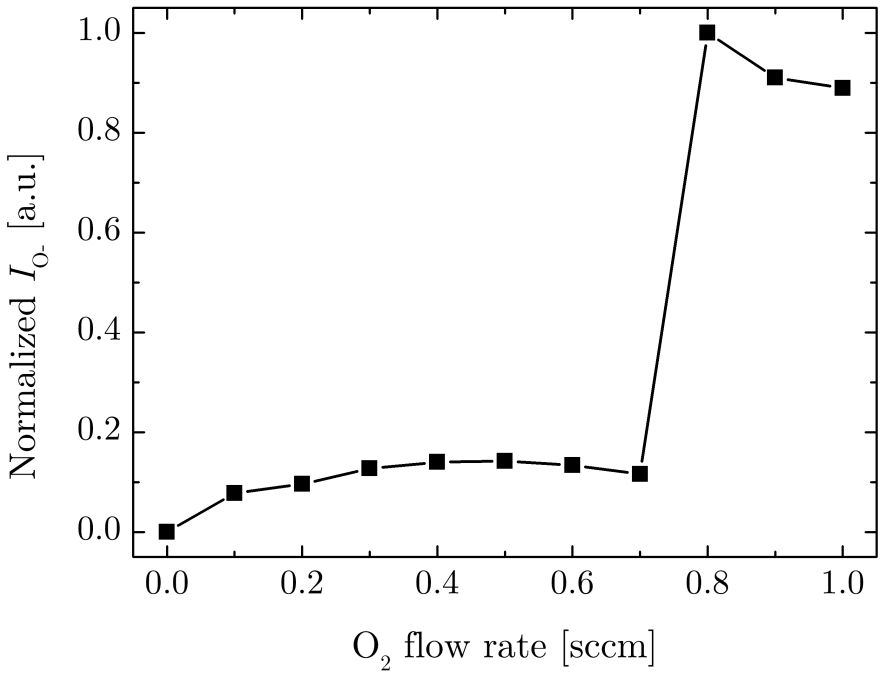

Figure 4.6. The integrated intensity of high energy O^- ions, I_{O^-}, for different oxygen flow rates during reactive HiPIMS of Ti in an Ar/O_2 discharge.

generally rely upon the use of electromagnetic radiation, either measuring radiation emitted directly by the discharge (e.g. optical emission spectroscopy) or via some form of interaction with a known source of incident electromagnetic radiation such as scattering (e.g. Thomson scattering) or absorption (e.g. optical absorption spectroscopy).

A major proportion of the works in this thesis involve determining the properties of negative ions, particularly O^- ions. There are two main experimental methods by which measurements of negative ion properties are typically obtained: energy-resolved mass spectrometry (see §4.2.2) and laser-aided photodetachment (see §4.2.3). The former method requires having a physical sampling orifice positioned within in the discharge or embedded within a plasma-facing surface. For this reason, it is a very useful tool for investigating the properties of negative ions exiting the discharge and impinging upon any process surfaces (e.g. the substrate). A drawback of this technique is its inability to sample low-energy negative ions which are confined to the plasma bulk. The latter method, laser-aided photodetachment, involves illuminating a column of plasma with a laser beam with sufficient energy density to detach electrons from negative ions. Any detached electrons are detected using an electrostatic probe and used to infer negative ion properties. As shown in chapter 6, it is also possible to determine negative ion densities using a Langmuir probe.

In brief, the diagnostic techniques used in this thesis include a cylindrical Langmuir probe, a quadrupole energy-resolved mass spectrometer (Hiden Analytical EQP300) and

a laser-aided photodetachment system. A quartz crystal microbalance deposition monitor (Inficon Maxtek TM-400), or QCM, was also used to measure thin film deposition rates. All methods given above can be classified as invasive techniques, as they require the presence of a physical probe placed within the plasma discharge. See below for a brief description of each diagnostic technique.

4.2.1 Langmuir probe

The Langmuir probe is, beginning with the works of Mott-Smith and Langmuir on "collectors in gaseous discharges" in 1926 [129], one of the oldest and most simple plasma diagnostic techniques which, in essence, involves immersing an electrode into the discharge and measuring the current drawn from it at a range of different applied potentials. The measured probe current, I_p, is plotted as a function of the applied bias potential, V_b, to produce an I-V characteristic. Using knowledge of physical processes that occur at the interface between the plasma and the probe surface, it is possible to extract plasma parameters such as charged particle density, electron temperature and plasma potential from a measured I-V characteristic.

4.2.1.1 Principles of operation

An illustration of an example I-V curve is given in figure 4.7 with the key features shown. Ion current is typically designated as negative, while electron current is positive. When the probe is biased highly negative with respect to the plasma potential, $V_\mathrm{b} \ll \Phi$, electron collection is suppressed and the probe current is equal to the ion saturation current, $I_\mathrm{i,sat}$. Conversely, when $V_\mathrm{b} \gg \Phi$, the probe current is equal to the electron saturation current, $I_\mathrm{e,sat}$. The floating potential, V_f, occurs when ion and electron current contributions are equal, therefore the probe measures a net zero current. In the transition region, between the ion and electron saturation currents and where $V_\mathrm{b} < \Phi$, electron collection is partially retarded by the negative bias potential with respect to Φ. It is from this region that the electron temperature, T_e, may be determined. Below is a breakdown of the different plasma parameters than may be extracted from a Langmuir probe I-V characteristic.

Electron temperature, T_e

Assuming the electrons are Maxwellian, the electron density can be described by the Boltzmann relation,

$$n\left(\mathbf{r}\right) = n_0 \exp\left[\frac{e\left(V\left(\mathbf{r}\right) - \Phi\right)}{k_\mathrm{B} T_\mathrm{e}}\right]. \tag{4.3}$$

Correspondingly, the electron current for Maxwellian electrons is

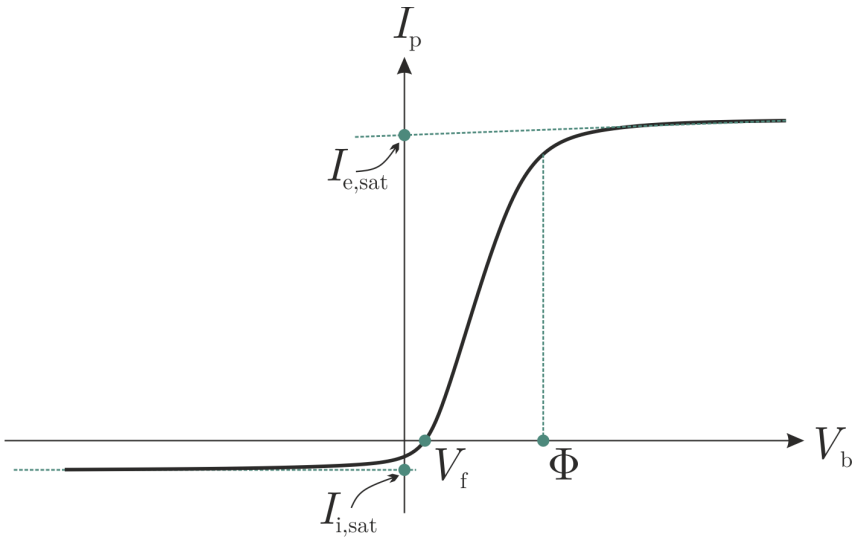

Figure 4.7. An idealized example of a Langmuir probe I-V characteristic, with the probe current, I_p plotted a function of the probe bias, V_b. The ion and electron saturation currents, $I_\mathrm{i,e,sat}$, floating potential, V_f, and plasma potential, Φ, are indicated.

$$I_\mathrm{e} = I_\mathrm{e,sat} \exp\left[\frac{e\left(V\left(\mathbf{r}\right) - \Phi\right)}{k_\mathrm{B}\mathrm{T_e}}\right] \tag{4.4}$$

where the electron saturation current is given by

$$I_\mathrm{e,sat} = \frac{1}{4} e A_\mathrm{p} n_\mathrm{e} \bar{v_\mathrm{e}}. \tag{4.5}$$

Here A_p is the surface area of the probe tip and $\bar{v_\mathrm{e}} = (8k_\mathrm{B}T_\mathrm{e}/m_\mathrm{e}\pi)^{1/2}$ is the thermal electron velocity. From equation 4.4, it is clear that plotting $\ln(I_\mathrm{e})$ against V_b will yield a straight line in the transition region with a gradient that is inversely proportional to the electron temperature (in units of eV). However, before this method can be applied the ion contribution to the probe current must be subtracted; $I_\mathrm{e} = I_\mathrm{p} - I_\mathrm{i,sat}$. Given that the electrons are Maxwellian, this method for obtaining T_e holds for any probe geometry and is independent of collisions [130]. Strictly speaking, the same relationship holds for ions when $V_\mathrm{b} > \Phi$ where the ion contribution to the probe current will be retarded. Although, as $I_\mathrm{i} \ll I_\mathrm{e}$ and $T_\mathrm{i} \ll T_\mathrm{e}$, it isn't possible to extract information about the ion temperature from a Langmuir probe I-V characteristic.

Electron density, n_e

If T_e and $I_\mathrm{e,sat}$ are known, then equation 4.5 can be used to find the electron density. However, accurately measuring $I_\mathrm{e,sat}$ can be troublesome. In an ideal case, since the average electron velocity is larger than the ion velocity by a factor of $(M_\mathrm{i}/m_\mathrm{e})^{1/2}$, the ratio of electron-to-ion saturation current would be $I_\mathrm{e,sat}/I_\mathrm{i,sat} > 200$ for argon ions. In the pres-

ence of a magnetic field, electron transport across magnetic field lines is greatly inhibited, whereas ion diffusion is not so affected due to the larger mass and lower gyration frequency when compared to electrons. This results in a decrease in the value of $I_{\mathrm{e,sat}}/I_{\mathrm{i,sat}}$ and an underestimation of the electron density. Furthermore, in regions of high electron density, the probe bias required to reach electron saturation may draw such a large current that it depletes the local electron population, thereby perturbing the local plasma conditions.

An alternative method for obtaining electron density, and indeed electron temperature, is to extract the electron energy distribution function (EEDF) directly from the transition region of the I-V characteristic using the Druyvesteyn formulation [131] where the EEDF can be obtained by

$$g_{\mathrm{e}}(V) = \frac{2m_{\mathrm{e}}}{e^2 A_{\mathrm{p}}} \left(\frac{2eV}{m_{\mathrm{e}}}\right)^{1/2} \frac{\mathrm{d}^2 I_{\mathrm{e}}}{\mathrm{d}V^2} \tag{4.6}$$

where $V = \Phi - V_{\mathrm{b}}$. It is then possible to obtain electron density and effective electron temperature from

$$n_{\mathrm{e}} = \int_0^\infty g_{\mathrm{e}}(\mathcal{E})\,\mathrm{d}\mathcal{E} \tag{4.7}$$

and

$$T_{\mathrm{eff}} = \frac{2}{3}\langle\mathcal{E}\rangle = \frac{2}{3n_{\mathrm{e}}} \int_0^\infty \mathcal{E} g_{\mathrm{e}}(\mathcal{E})\,\mathrm{d}\mathcal{E}, \tag{4.8}$$

respectively. However, obtaining $\mathrm{d}^2 I_{\mathrm{e}}/\mathrm{d}V^2$ from measured I-V characteristics requires a high signal-to-noise ratio and can be very difficult to accomplish in transient plasmas without statistical smoothing of the data.

Floating potential, V_{f}

The floating potential is readily obtained from an I-V characteristic as illustrated in figure 4.7. V_{f} is defined at the point where ion and electron currents are equal and is therefore the potential at which $I_{\mathrm{p}} = 0$. One may naively think that by submerging an electrically floating conductor into a plasma, the conductor would obtain the same potential as the surrounding plasma, however, V_{f} is negative with respect to Φ as a consequence of the higher electron mobility when compared with that of ions.

Plasma potential, Φ

There are two regularly employed methods of obtaining the plasma potential, Φ from an I-V characteristic. Firstly, the plasma potential can be found at the meeting point of linear fits to the transition region and the electron saturation region; the so-called 'knee'

of the I-V characteristic (see figure 4.8a). Φ can also be found at the point where the second derivative of electron probe current with respect to the probe bias is equal to zero, $\mathrm{d}^2 I_\mathrm{e}/\mathrm{d}V_\mathrm{b}^2 = 0$ (see figure 4.8b). The second method, akin to the obtaining of the EEDF from the transition region, requires a smooth I-V characteristic and a high signal-to-noise ratio.

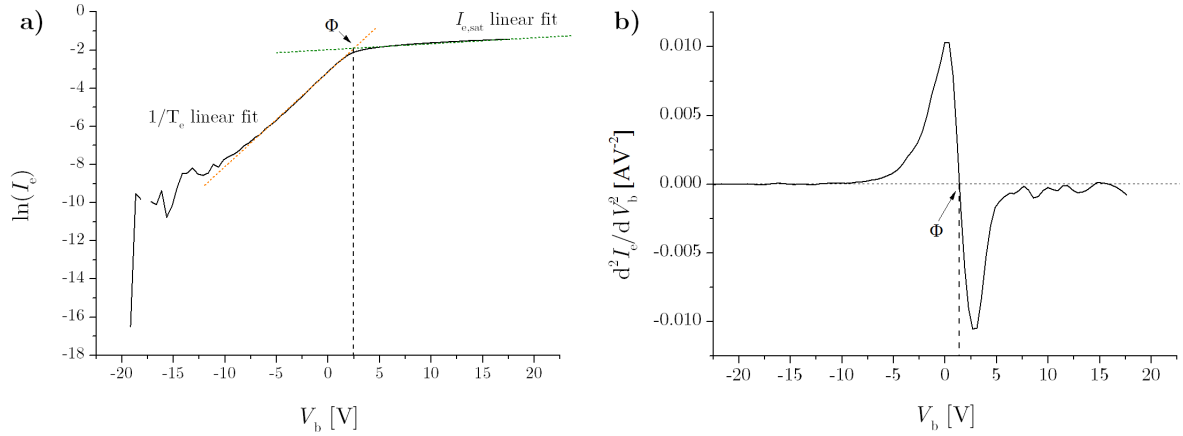

Figure 4.8. Two methods of finding the plasma potential, Φ: (a) finding the meeting point of linear fits to the transition and electron saturation regions, and (b) at the point where $\mathrm{d}^2 I_\mathrm{e}/\mathrm{d}V_\mathrm{b}^2 = 0$. Here, $\Phi \approx 2.5$ V.

Ion density, n_i

As mentioned above, determining the electron density from a measured value of $I_\mathrm{e,sat}$ can often be troublesome and inaccurate. In comparison, ion collection does not draw as high currents from the plasma and, in most industrial applications, it can be assumed that the magnetic field does not significantly affect the ion trajectories. Therefore, it is often desirable to obtain plasma densities by interpreting the collection of ions rather than electrons. However, as it turns out, this is not a straightforward task.

In order to understand the collection of ions by a probe and relate I_i to properties of the plasma, it is necessary to consider the region between the plasma and the probe (i.e. the *sheath*). The thickness of the sheath, s, is typically assumed to be of the order of the Debye length, $s \sim \lambda_D$, which is often used as a characteristic length over which to describe different collection regimes. For example, the condition $\lambda_D < \lambda_\mathrm{c}$ must hold for the collisonless approximation, where λ_c is the ion mean free path. For $\lambda_D > \lambda_\mathrm{c}$, collision events in the sheath must be considered, which are discussed in [130]. Moreover, for ion collection to be unaffected by magnetic fields, it must be that $r_\mathrm{gi} > \lambda_D$ where r_gi is the ion gyroradius. For the conditions encountered in this thesis, $\lambda_\mathrm{c} \sim 10^{-2}$ m, $\lambda_D \sim 10^{-5} - 10^{-3}$ m and even in regions close to the target where $B \sim 500G$, $r_\mathrm{gi} \sim 10^{-2}$ m. Therefore, ion trajectories are considered to be unaffected by the presence of magnetic fields and their transport through the sheath is assumed to be collisionless.

Even given the above approximations, analysis of probe I-V characteristics is still a non-trivial exercise and a number of theories exist concerning particle collection [130, 132–134], of which the validity and applicability are still an active area of discussion. Moreover, some theories are only formulated for specific probe-shapes such as spherical or cylindrical and some require the use of computer simulations [135].

Due to practical convenience, almost all Langmuir probes are constructed from simple wires, giving them a cylindrical geometry as in the work presented here. However, in contrast to planar probe analysis the sheath thickness is not always negligible when compared to the probe dimensions and ion trajectories in the sheath must be considered. This was first recognized by Mott-Smith and Langmuir [129] in their orbital-motion-limited (OML) theory of ion collection. OML theory asserts that the collected current is limited only by the angular momentum of the orbiting ions and assumes an infinitely large sheath, a condition which is typically given as $r_\mathrm{p} \ll s$, where r_p is the radius of the probe tip. In the ion saturation region, the bias applied to the probe is largely negative with respect to Φ and, according to Child's law, this results in an expansion of the sheath with its thickness being determined by

$$s = \frac{\sqrt{2}}{3}\lambda_\mathrm{D}\left(\frac{2eV_0}{k_\mathrm{B}\mathrm{T_e}}\right)^{3/4} \tag{4.9}$$

where $V_0 = \Phi - V_\mathrm{b}$ for negative V_b, and is the potential difference contained between the sheath edge and the surface of the probe. For typical values of the electron temperature and plasma potential found in processing plasmas (e.g. $T_\mathrm{e} = 2$ eV and $\Phi = 5$ V), a probe bias of -60 V gives $s \sim 20\lambda_\mathrm{D}$, easily satisfying the condition $r_\mathrm{p} \ll s$. Assuming the validity of OML theory and following Chen [134], in the limit of $T_\mathrm{i} \to 0$, the collected ion current is given by

$$I_\mathrm{i} \approx A_\mathrm{p} n_\mathrm{i} e \frac{\sqrt{2}}{\pi}\left[\frac{e\left(\Phi - V_\mathrm{b}\right)}{M_\mathrm{i}}\right]^{1/2} \tag{4.10}$$

It is noted that the ion current to the probe given by equation 4.10 scales with $|\Phi - V_\mathrm{b}|^{1/2}$, as opposed to the collisionless Child law which scales with $|\Phi - V_\mathrm{b}|^{3/4}$. The weaker scaling of I_i in OML theory is a result of not all ions entering the sheath being collected by the probe. From equation 4.10, it is clear that a plot of $I_\mathrm{i}^2 - V_\mathrm{b}$ should yield a linear relationship, the gradient of which can be used to determine n_i^2. It is in this way that values of n_i presented in this thesis are determined.

Electronegativity, α

As discussed in chapter 3, negative ions are generated in reactive discharges containing electronegative gases. As pointed out by Braithwaite and Allen [95], the presence of

negative ions in the discharge alters the Bohm criterion which necessitates sonic ion flow at the sheath edge. As the Boltzmann relation holds for electrons (equation 4.3), it is assumed that negative ions in the plasma bulk also obey the Boltmann relation:

$$n_- = n_{-0} \exp\left(\frac{e\phi}{k_B T_-}\right) \tag{4.11}$$

where n_{-0} is the negative ion density far away from the sheath edge and ϕ is the potential inside the sheath.

As shown by Braithwaite and Allen [95] and later by Sheridan *et al.* [102], the positive ion flux to a surface is partially determined by the concentration of negative ions in the discharge. Following [102], it is possible to determine an expected value of the positive ion current exiting the plasma through the sheath and to the probe:

$$I_i = n_{e0} c_s A_p e \gamma^{-1/2} \left[\left(\frac{1}{2}\right)^{1/\gamma} + \frac{\alpha}{2}\right] \tag{4.12}$$

where n_{e0} is the electron density far away from the sheath edge, $c_s = (k_B T_e/M_i)^{1/2}$ is the electropositive ion acoustic speed, $\gamma = T_e/T_-$ and $\alpha = n_-/n_e$ is the electronegativity of the discharge. As discussed in further detail in §6.3.1.3, using measured values of the ion and electron saturation currents along with equations 4.5 and 4.12 it is possible to obtain estimates of both α and n_- using a Langmuir probe [136, 137]. This method is not as robust as, for instance, laser-aided photodetachment (see §4.2.3) in determining values of n_-, however, it does have the benefit of being much easier to implement.

4.2.1.2 Probe and acquisition system

A schematic diagram of the Langmuir probe used in this thesis is shown in figure 4.9 with dimensions labelled. As the Langmuir probe is an invasive technique, the electrode needs to designed in such a way to minimise the perturbation to the plasma. As such, the Langmuir probe tip was constructed using thin tungsten wire (99.95% purity) with $r_p = 50\,\mu$m and a length $l_p = 4 - 6$ mm determined using a digital calliper. The tungsten wire was mounted inside a coaxial system of three alumina ceramic tubes. The outer ceramic tube (T1) was extended by the use of a more narrow second ceramic tube (T2) placed within it, which serves to reduce perturbation to the plasma. A third ceramic tube (T3) was nested within T2 to prevent the probe tip from coming into contact with the exposed outer surface of T2. In sputtering discharges, it is possible for the exposed ceramic probe to become coated in a conducting layer. If the probe stem comes into contact with this deposited layer, the effective probe area is increased thereby producing false current readings and potentially disturbing the plasma. T3 was mounted into a PEEK socket embedded with a brass connector to which the tungsten wire was soldered. The brass connector was plugged directly into the stainless steel stem through which an insulated

copper wire was fed to a glass-metal seal terminated by a coaxial cable fitted with a BNC connector. The integrity of the connection between the stainless steel stem and the PEEK socket was reinforced using DuPont™ Kapton® polyimide tape. The stainless steel stem was mounted onto the vacuum chamber through a KF40 flange equipped with a compression port.

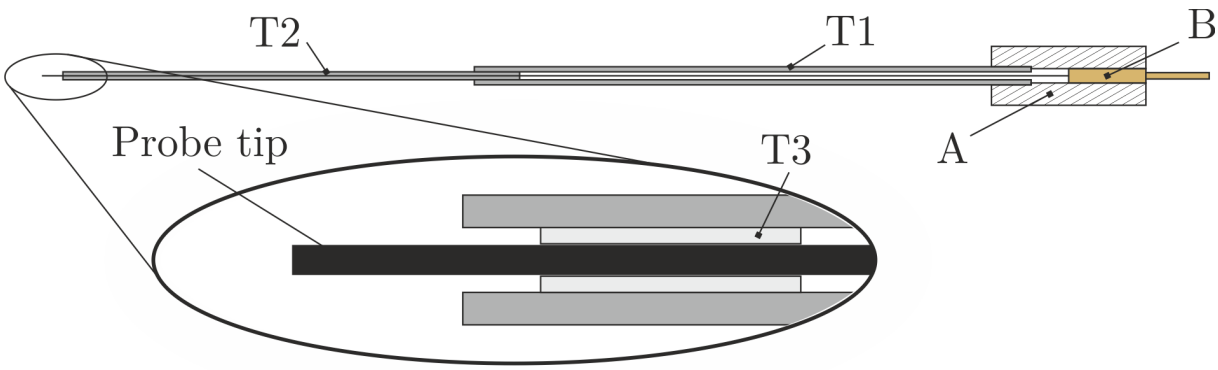

Figure 4.9. Schematic of the Langmuir probe showing the tungsten wire (⌀ 100 μm, $l_p = 4$ to 6 mm) encased within three coaxial ceramic tubes: T1 ($\varnothing_{outside}$ 2.0 mm, $\varnothing_{inside}$ 1.0 mm, $l = 10$ cm), T2 ($\varnothing_{outside}$ 1.0 mm, $\varnothing_{inside}$ 0.5 mm, $l = 10$ cm) and T3 ($\varnothing_{outside}$ 0.5 mm, $\varnothing_{inside}$ 150 μm, $l = 3$ cm). T3 was inserted into a PEEK holder (A, $\varnothing_{outside}$ 6 mm) which also contained a brass connector pin (B) to which the tungsten wire was soldered.

The probe tip was connected to an acquisition system (Impedans ALP) via BNC connector. The acquisition system was capable of rapidly acquiring probe current measurements for a wide range of voltages (−150 V to 150 V), up to a maximum current reading of 150 mA. The maximum resolution of current and voltage measurements was 4.5 mV and 4.5 nA, respectively. Each individual data point for an I-V trace was averaged over 10 readings and each trace was acquired 10 times before an overall mean was found, giving an effective average over 100 I-V curves. Before any analysis was performed, a background signal was recorded in the absence of a plasma, and subtracted from measured I-V characteristics.

Time-resolved measurements in HiPIMS operation were performed via synchronization of the internal delay generator of the acquisition system with the pulsed discharge potential. The acquisition system delay generator was capable of a time-resolution (Δt) of 12.5 ns. However, it was found that I-V characteristics obtained using $\Delta t < 500$ ns were too noisy to allow sufficient analysis. Specific details regarding the parameters used to obtain time-resolved measurements differ for each experiment and are given in the relevant chapters.

4.2.2 Quadrupole mass spectrometer

As a diagnostic technique, quadrupole mass spectrometry is a powerful and versatile tool and is capable of performing *in situ* time-resolved measurements of the densities and energy distributions of positive and negative ions as well as neutral species with microsecond resolution. Being mass-selective, this technique is particularly useful in understanding the plasma chemistry in complex environments containing many different species, such as those found in reactive magnetron sputtering. For a detailed treatment of quadrupole mass spectrometry as applied to reactive plasmas, the reader is referred to [138] and references therein.

4.2.2.1 Principles of operation

The quadrupole mass spectrometer (QMS) used in the work presented in this thesis was the EQP300 manufactured by Hiden Analytical Limited (Warrington, UK). A schematic representation of the EQP300 probe and its main components is shown in figure 4.10. The instrument consists of several main parts which include the sampling office, ion focusing optics, an energy analyser, a quadrupole and an ion-counting secondary electron multiplier (SEM). For neutral gas analysis, an electron emitting filament located behind the orifice is used to ionize sampled residual gas. Regardless of the ion source, the sampled ions are then focused through the instrument via a system electromagnetic lenses. The ions are passed through the 45° electrostatic energy analyser, which selects ions with respect to their energy and passes them through to the quadrupole mass analyser. The quadrupole separates ions based on their mass-to-charge ratio (m/z) such that only ions of a particular m/z value reach the detector. As the measurement relies heavily on the ion trajectory being unobstructed, the QMS and detector must be housed inside a vacuum chamber and held at low pressure. The operating pressure of the SEM detector is $\leq 5 \times 10^{-4}$ Pa and therefore the QMS requires differential pumping separate from the main vacuum chamber. Here a combination of a rotary pump (Edwards E2M2) and turbomolecular pump (Pfeiffer Balzers TMU-064) was used to obtain the required operating pressure, achieving an ultimate vacuum pressure of $\sim 10^{-5}$ Pa.

4.2.2.2 EQP components

A schematic diagram showing the major components of the EQP300 is given in figure 4.10 and brief overview of the function of each is provided below.

Sampling orifice: A small sampling orifice located at the front of the probe is necessary to maintain a sufficiently low operating pressure inside the EQP whilst allowing for a pressure in the range of 10^{-1} Pa to be maintained in the processing chamber. In the

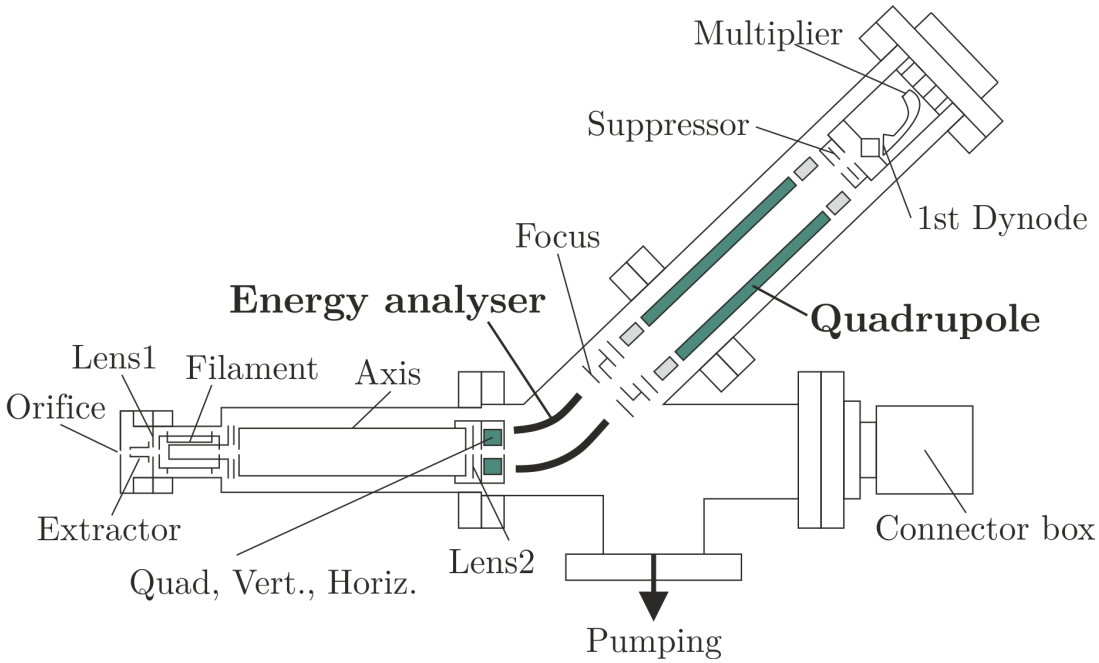

Figure 4.10. Diagram of the EQP300 with the major components and ion optics labelled.

experiments presented here, a orifice diameter of 100 μm was used, which allowed for high signal readings without compromising the integrity of the EQP vacuum chamber. The use of a sampling orifice also implies that any ion sampling occurs as a line-of-sight measurement of ion *flux*, rather than density.

Extractor: Located directly behind the sampling orifice is the extractor electrode, to which a negative potential is applied to attract positive ion species. The polarity of V_{ext} (and other ion optics) is reversed for negative ion sampling.

Lens1: With the extractor electrode, lens1 forms an electrostatic lens to focus the sampled ions through the ionisation cage containing an electron-emitting filament and into the axis drift tube. Hamers *et al.* [139] demonstrated that the focal length of the electrostatic lens is dependent upon ion energy and if inappropriate potentials, V_{ext} and V_{lens1}, are applied to the ion optics chromatic aberration of the ion beam occurs.

Filament: The electron-emitting filament is not used for ion sampling modes, however, it is energised for residual gas analysis (RGA) mode. Electrons are generated via thermionic emission from the filament, typically made from tungsten or thoriated iridium for oxygen gas mixtures. Ions are subsequently formed via electron impact ionisation and channelled through the EQP by the electrostatic lenses.

Axis, Quad, Vert., Horiz. and Lens2: The ion drift tube (axis) is held at a potential

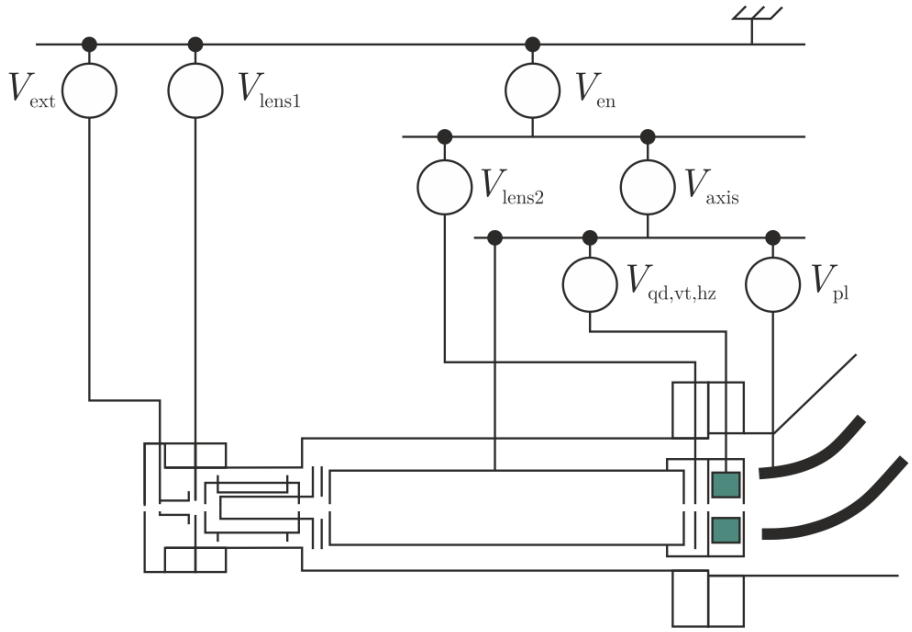

Figure 4.11. The front-end of the EQP300, including ion sampling components, drift tube and energy analyser. The power supply references are given, where open circles represent a voltage source. Electrodes supplying the filament and cage used in RGA mode are not shown.

that determines the energy of the ions entering the energy analyser. The axis potential is set by potentials separately applied to two electrodes: $V_{\text{axis}} + V_{\text{en}}$ (as shown in figure 4.11) where $V_{\text{axis}} = -40$ V and is kept constant and V_{en} can be varied (note that the polarity is reversed for negative ion sampling). The quad, vertical and horizontal electrodes form a quadrupole lens which usually does not require alteration, but can be tuned to control beam alignment and correct for any beam astigmatism. Lens2 works to transform the divergent beam in the drift tube to a parallel beam at the entrance of the energy analyser.

Energy analyser: Ions enter the energy analyser with an energy determined by the initial kinetic energy of the ion, $\mathcal{E}_{\text{i}}$, and the energy gained in the drift tube, giving a total ion kinetic energy:

$$\mathcal{E}_{\text{k}} = \mathcal{E}_{\text{i}} - q\left(V_{\text{axis}} + V_{\text{en}}\right) \tag{4.13}$$

for ions with a charge of q. The transmission energy of the energy analyser, $\mathcal{E}_{\text{EA}}$, is determined by its geometry and the potential applied to its plates, V_{pl}. For the Hiden EQP energy analyser, $\mathcal{E}_{\text{EA}} = 5.5qV_{\text{pl}}$ and is independent of the ion mass. For successful transmission, the kinetic energy of the ion at the entrance of the energy analyser must equal $\mathcal{E}_{\text{EA}}$, hence

$$\begin{aligned} \mathcal{E}_{\text{i}} - q\left(V_{\text{axis}} + V_{\text{en}}\right) &= 5.5qV_{\text{pl}} \\ \mathcal{E}_{\text{i}} &= q\left(5.5V_{\text{pl}} + V_{\text{axis}} + V_{\text{en}}\right). \end{aligned} \tag{4.14}$$

For $5.5V_{\mathrm{pl}} = -V_{\mathrm{axis}}$, it is straightforward to determine the energy of the incident ion since successful transmission occurs for $\mathcal{E}_{\mathrm{i}} = qV_{\mathrm{en}}$. As $V_{\mathrm{axis}} = -40$ V is kept constant, V_{pl} is kept constant at a potential of 7.27 V. For singly-charged ions, $\mathcal{E}_{\mathrm{i}} = V_{\mathrm{en}}$ and the recorded energy distribution does not require correction (assuming chromatic aberrations are suppressed). For energy distributions of multiply-charged ions, the measured value of V_{en} must be multiplied by the corresponding ion charge.

Focus: The focus lens decelerates the ions exiting the energy analyser and focuses the beam into the quadrupole mass filter.

Quadrupole: As the energy analyser is responsible for separation of ions with respect to their kinetic energies, the quadrupole mass filter is responsible for ion separated with respect to their charge-to-mass ratios (m/z). A schematic of a quadrupole mass filter is shown in figure 4.12. A quadrupole consists of four parallel rods driven by RF and DC, with opposite rods held at the same potential. The time-dependent electric field between the rods results in ions only of a selected m/z to have stable trajectories, with other ions being lost to the rods or chamber walls.

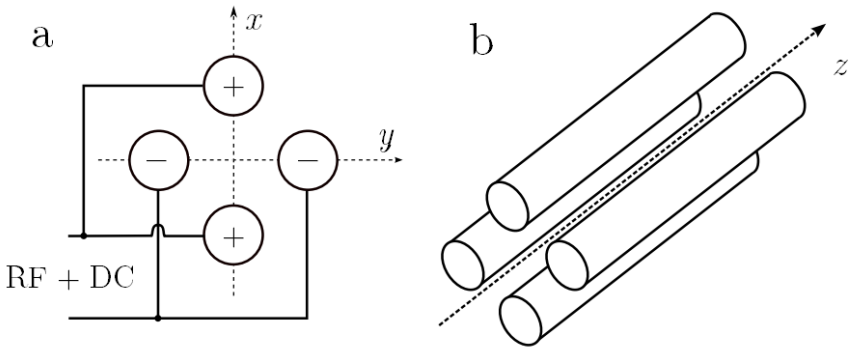

Figure 4.12. Cross-section (a) and schematic diagram (b) of a cylindrical quadrupole mass filter, after [138]. Ions travel in the z direction and are deflected in the x and y directions by the electric field generated via the application of the same RF and DC bias to opposite rods.

The mass filter system has a number of electrodes associated with it. $V_{\Delta \mathrm{m}}$ determines the mass resolution at low mass, V_{res} is used for high mass and V_{trans} is a *virtual* potential which determines the transit energy of ions through the quadrupole. V_{trans} is set to 3 V and it is recommended by the manufacturer that this remains constant.

Detector: The EQP is fitted with an off-axis continuous dynode electron multiplier, or secondary electron multiplier (SEM), operating in pulsed mode. To accelerate the ions exiting the mass filter, a potential is applied to the 1st dynode. Impinging ions cause the emission of secondary electrons, which are subsequently accelerated through the

continuous dynode by a high positive potential set by the multiplier. Multiple impacts cause a cascade-like process which has the effect of amplifying the ion-count signal. It is worth noting here that SEM detectors are subject to degradation and amplification decreases over time. This is remeidied by increasing the multiplier potential. This process and other aspects of tuning the EQP and acquiring data are outlined in appendix A.

4.2.3 Laser-aided photodetachment

Laser-aided photodetachment is a well-established [119] technique for determining negative ion densities and temperatures, although emphasis is placed on the former here. Photodetachment methods were initially developed in response to the desire to understand hydrogen negative ion sources, particularly for their use in energetic neural beam generation for thermonuclear fusion applications [140], but have been applied to other devices containing negative ion species, such as magnetron sputtering sources [120,137,141]. The fundamental principles of operation are discussed below.

4.2.3.1 Principles of operation

As the name suggests, laser-aided photodetachment involves firing a pulsed laser beam through a plasma discharge such that electrons are detached from negative ion species. In the system presented here, these photoelectrons are subsequently collected by a positively biased probe (with respect to the plasma potential) located in the vicinity of the laser beam and aligned parallel to the beam axis. Figure 4.13 shows a simplified version of this geometry. Here, the *eclipse* photodetachment method is employed, which involves 'shadowing' the probe using a blocking wire as shown in figure 4.13. This prevents ablation of the probe surface by the laser beam, which can result in spurious current measurements [142].

As stated above, the collection probe is biased positively with respect to the plasma potential such that in the absence of a laser pulse the recorded probe current I_p is the electron saturation current and directly proportional to the electron density, n_e. The incident laser pulse and the subsequent detachment of electrons from negative ions causes a temporary and local increase in n_e. This increase in electron density, Δn_e, results in a corresponding increase in the measured probe current, ΔI_p. Under the assumptions that all negative ions in the collection volume are destroyed, all photodetached electrons are collected by the probe, and that contributions to ΔI_p come exclusively from photodetached electrons, then $\Delta n_\mathrm{e} = n_-$. The local value of electronegativity, α, can then be determined directly:

$$\frac{\Delta I_\mathrm{p}}{I_\mathrm{p}} = \frac{\Delta n_\mathrm{e}}{n_\mathrm{e}} = \frac{n_-}{n_\mathrm{e}} = \alpha. \tag{4.15}$$

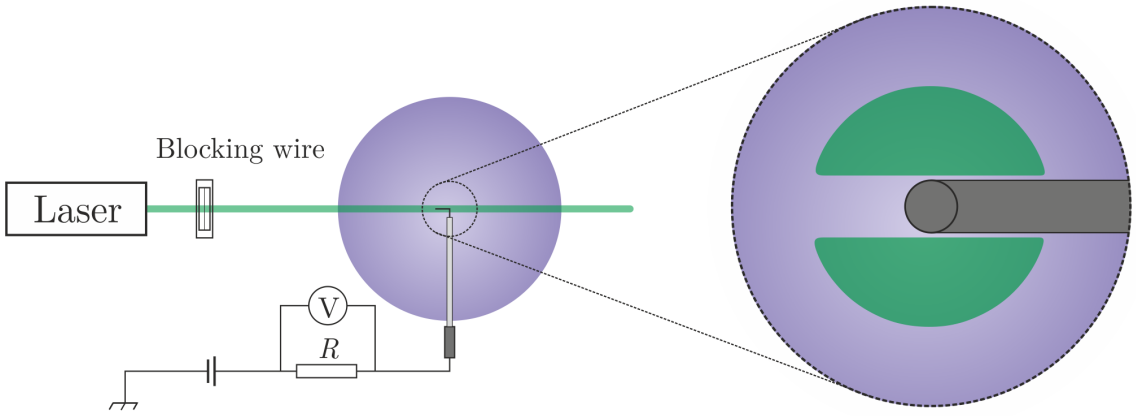

Figure 4.13. A schematic diagram showing the shadowing of the collection probe in a photodetachment set-up. The current collected by the positively biased probe can be obtained by measuring the potential drop across a known resistor R.

Furthermore, n_e can be determined from the I-V characteristic of the probe allowing a value for the local negative ion density, n_-, to be obtained. Of course, the accuracy of this measurement relies upon the validity of the assumptions mentioned above. It is crucial, therefore, that the correct choice of laser parameters are chosen.

The photon energy ($h\nu$) of the laser beam must be chosen such that photodetachment of electrons from relevant negative ions occurs but single photoionization of neutrals is avoided. Hence, $\mathcal{E}_{\text{aff}} < h\nu < \mathcal{E}_{\text{iz}}$ where $\mathcal{E}_{\text{aff}}$ is the electron affinity of the species of interest and $\mathcal{E}_{\text{iz}}$ is the ionization energy of any neutrals in the discharge. For atomic oxygen, $\mathcal{E}_{\text{aff}} = 1.46$ eV and $\mathcal{E}_{\text{iz}} = 13.6$ eV, as such the second harmonic of a Nd:YAG laser ($\lambda = 532$ nm, $\nu = 5.6 \times 10^{14}$ Hz) can be used for the purpose of photodetachment of electrons from O^- ions as $(h\nu)_{\text{Nd:YAG}} = 2.33$ eV. It is worth noting that $\mathcal{E}_{\text{iz-Ar}} = 15.75$ eV, hence this choice of laser is also valid for an Ar/O_2 gas mixture as used in this thesis. Detachment of O_2^- ions would also occur, however, it has been reported that O_2^- ions account for less than 2% of the total negative ion concentration [141].

It is also assumed that all negative ions in the beam path are destroyed, however, this is dependent upon not just the photon energy, but the energy density of the laser pulse, E/S, and the photodetachment cross section, σ_{pd}. The fraction of negative ions that experience photodetachment following the laser pulse, as a ratio of the local negative ion density prior to the laser pulse is given as [119]

$$\frac{\Delta n_-}{n_-} = 1 - \exp\left(-\frac{\sigma_{\text{pd}}}{h\nu}\frac{E}{S}\right) \tag{4.16}$$

where, E is the laser pulse energy, S is the cross-sectional area of the beam and for the case of O^- ions $\sigma_{\text{pd}} = 6.5 \times 10^{-18}$ cm^2 [143, 144]. For sufficient laser energy density, $\Delta n_-/n_- \to 1$ and equation 4.15 holds. Using equation 4.16, for a frequency-doubled

Nd:YAG laser detecting O^- ions, the required laser energy density is approximately 300 mJ cm^{-2}.

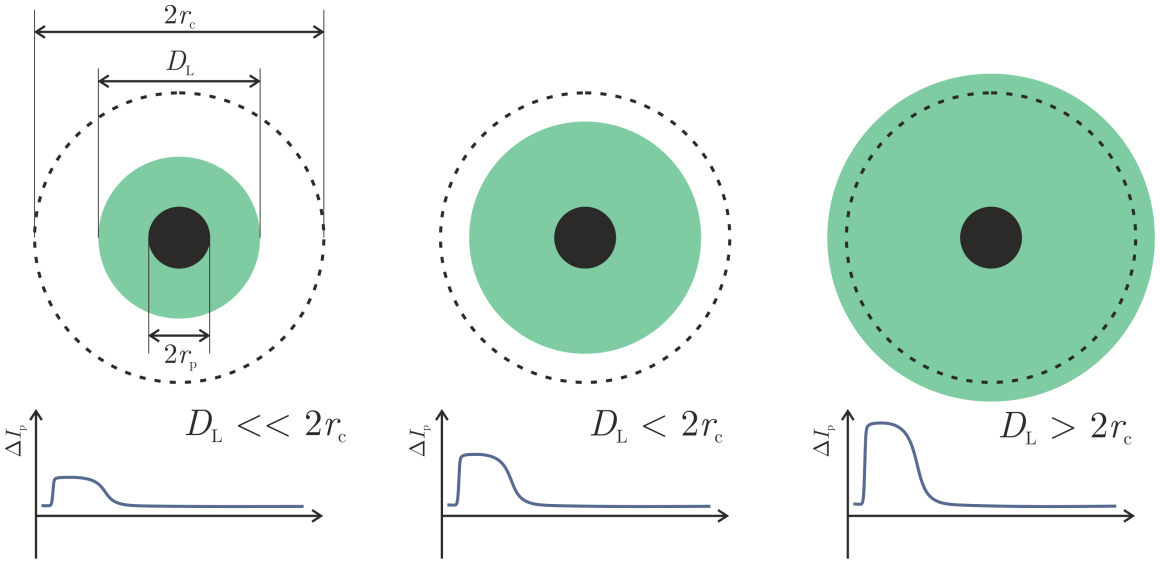

Figure 4.14. From left-to-right, the laser diameter, D_L, is increased to cover a greater proportion of the collection diameter, $2r_c$, and the measured ΔI_p increases until $D_L > 2r_c$.

Another important laser parameter to consider is the beam diameter, D_L. The electrostatic probe has a finite collection radius, r_c, given by [145]

$$r_c \approx r_p + As \tag{4.17}$$

where r_p is the probe radius, s is the sheath width and A is a multiplication factor between 2 and 3. If $D_L < 2r_c$, increasing D_L results in an increase in the measurement of ΔI_p as more negative ions in the collection area undergo photodetachment (see figure 4.14). When $D_L = 2r_c$, the cross-sectional area of the discharge undergoing photodetachment is equal to the probe collection area and so the measured value of ΔI_p saturates and no longer increases for larger D_L. Values of r_c can be experimentally determined; Devynck *et al.* [100] found that $r_c = 1 - 2$ mm in a laser photodetachment set-up for measuring negative ions in a volume H^- source. It was found that any increase in D_L beyond 2 mm had no effect on the amplitude of ΔI_p. The laser-aided photodetachment diagnostic used in this thesis was applied to a HiPIMS discharge operating in an Ar/O_2 gas mixture, the details of which are described in chapter 6.

4.2.4 Quartz crystal microbalance

A quartz crystal microbalance is an instrument frequently used to provide *in situ* measurements of deposition rate and film thickness.

4.2.4.1 Principles of operation

Quartz crystal exhibits the piezoelectric effect and by applying an alternating current to the surface of two electrodes separated by a quartz crystal, an oscillation within the crystal is induced. The resonant frequency of this oscillation is partially dependent upon the mass of the crystal. When the electrode atop the crystal is deposited upon, the effective mass of the crystal increases and the resonant frequency shifts according to the Sauerbrey equation [146]:

$$\Delta f = -\frac{2f_0^2}{A\sqrt{\rho_q \mu_q}}\Delta m \tag{4.18}$$

where f_0 is the initial resonant frequency, A is the area between electrodes, ρ_q is the density of quartz, μ_q is the shear modulus of quartz and Δm is the change in mass. As can be seen from equation 4.18, when the electrode is deposited on (i.e. $\Delta m > 0$) the frequency shift is negative thereby reducing the resonant frequency. Assuming the deposition is uniform and that all other factors are constant, this change in resonance can be directly related to the mass of the thin film. Moreover, if the film density is known or estimated then a film thickness and deposition rate can be calculated.

The instrument consisted of a quartz crystal coated with gold electrodes, which was mounted into a water-cooled stainless steel holder. The electrodes on the crystal were connected to a microbalance monitor (Inficon Maxtek TM-400) which applied the alternating current to the electrodes and also displayed real-time deposition rate and film thickness measurements in units of Å/sec and kÅ, respectively. Water-cooling was applied to ensure the crystal remained in the operating temperature range (0 to 50°C). The input parameter of film density was changed depending upon the material of the film being deposited. For metallic deposition of titanium, the film density was assumed to be the bulk density of titanium, 4.51 g/cm^2, and for reactive deposition of titanium oxide the film was assumed to be stoichiometric TiO_2 compound, 4.26 g/cm^2. The DAC output of the monitor provided a voltage reading in the range $0 - 5$ V in steps of 0.05 V, with each step corresponding to a change in film thickness of 1 Å (i.e. 0.05 V/Å). Rather than reading directly from the display of the monitor, this output potential was monitored as a function of time using a voltage probe and oscilloscope in order to reliability acquire deposition rates over a set time period. More details regarding the QCM experimental set-up are presented in chapter 8.

Chapter 5

Plasma dynamics in a reactive HiPIMS discharge

5.1 Introduction

Knowledge of the dynamics and spatial distributions of plasma parameters are integral to understanding the HiPIMS discharge. Furthermore, as the properties of deposited thin films are heavily influenced by plasma parameters, it is particularly important to understand them for process optimization.

Langmuir probes offer a relatively straightforward method to investigate spatiotemporal plasma parameters. Indeed, several authors [70–76] have reported on both the spatial and temporal variation of plasma parameters in HiPIMS as measured using electrostatic probe diagnostics. Measurements of electron energy distribution functions (EEDFs) and electron saturation currents have routinely revealed a peak electron densities of the order of 10^{18} m^{-3}, for example in [70–72]. Gudmundsson *et al.* [147] have also shown that a high electron density ($n_e \sim 10^{17}$ m^{-3}) persists for at least 800 μs into the afterglow. The electron density has been observed to increase with gas pressure [71], discharge current [80] and applied discharge power [79]. Moreover, electron density also varies with choice of target material; n_e was found to increase by a factor of two during HiPIMS of chromium when compared with titanium [73].

Langmuir probes have also been used extensively to study EEDFs, typically obtained from the Druyvesteyn formula (equations 4.6 and 4.7). The EEDF has been found to contain multiple populations at different energies. For example, Vetushka and Ehiasarian [73] reported the presence of an electron population with an effective temperature of $6 - 7$ eV in the early stages of the discharge pulse ($t < 40$ μs) alongside a lower energy population with an effective temperature of ~ 1 eV. Poolcharuansin and Bradley [76] extended this work using an increased time resolution and reported the presence of three distinct electron populations in the very early stages of the discharge pulse ($t < 4$ μs);

super-thermal, hot and cold electrons representing effective electron temperature ranges of $70-100$, $5-7$ and $0.8-1$ eV, respectively. Čada *et al.* [81] reported on plasma parameters of a reactive Ar/O_2 HiPIMS discharge as measured using a Langmuir probe. Peak plasma densities were found to be just under 10^{18} m^{-3} and almost independent of discharge pressure. Effective electron temperatures in the range $0.5-2.0$ eV were recorded during the active phase of the pulse, with T_{eff} rapidly dropping to values of < 0.3 eV in the discharge afterglow. Unfortunately, investigations regarding the plasma parameters in reactive HiPIMS discharges have been somewhat exiguous, and require further exploration. Therefore, it is the aim of this chapter to characterise the plasma dynamics of a reactive HiPIMS discharge to provide somewhat of a guide for the subsequent studies contained within this thesis.

5.2 Experimental set-up

The vacuum chamber set-up is described in §4.1 and shown in figure 4.1. The magnetron was equipped with a 3 in. (75 mm) Ti target and energised using a combination of the HiPIMS impulse unit and the pre-ionizing power supply, both described in §4.1.3. The pulse width and frequency of the discharge voltage pulse were fixed at 100 μs and 100 Hz, respectively, and a constant average discharge power $\overline{P_{\text{d}}} = 100$ W was used throughout all experiments presented in this chapter. A simplified schematic of the experimental set-up is shown in figure 5.1. The gas inlets were located behind the magnetron with the Ar and O_2 flow rates being set by separate, but identical mass flow controllers. The total working gas pressure, p_{total}, was varied from 0.4 to 1.6 Pa, with a proportionally constant oxygen partial pressure, $p_{O_2} = 0.2p_{\text{total}}$.

A single cylindrical Langmuir probe was placed in the vacuum chamber and moved radially, parallel to the target surface. The housing of the magnetron was moved orthogonally to the Langmuir probe to allow for measurements at different axial positions. The radial position $r = 0$ was defined as the discharge centreline and the axial position of the target surface was defined as $z = 0$. The magnetic null is located at position $r = 0, z = 30$ mm, as indicated in figure 5.1. The probe position was varied between $r = 0-40$ mm, and $z = 50-100$ mm. To obtain time-resolved Langmuir probe measurements, the internal delay generator of the acquisition system was synchronized to the discharge pulse and used to step through the entire on-time and a portion of the discharge afterglow. A time range $t = 0-300$ μs was used with a time-step, Δt, of 1 μs with $t = 0$ defined as the on-set of the discharge voltage pulse. Each data point was recorded 5 times and each full I-V trace was recorded 5 times again before an average was found to produce a single I-V characteristic. The bias voltage of the probe was varied from -70 V to $+20$ V with a resolution of 0.05 V. In between data acquisition runs, a potential of -150 V was applied to the probe tip in order to sputter clean depositions from its surface.

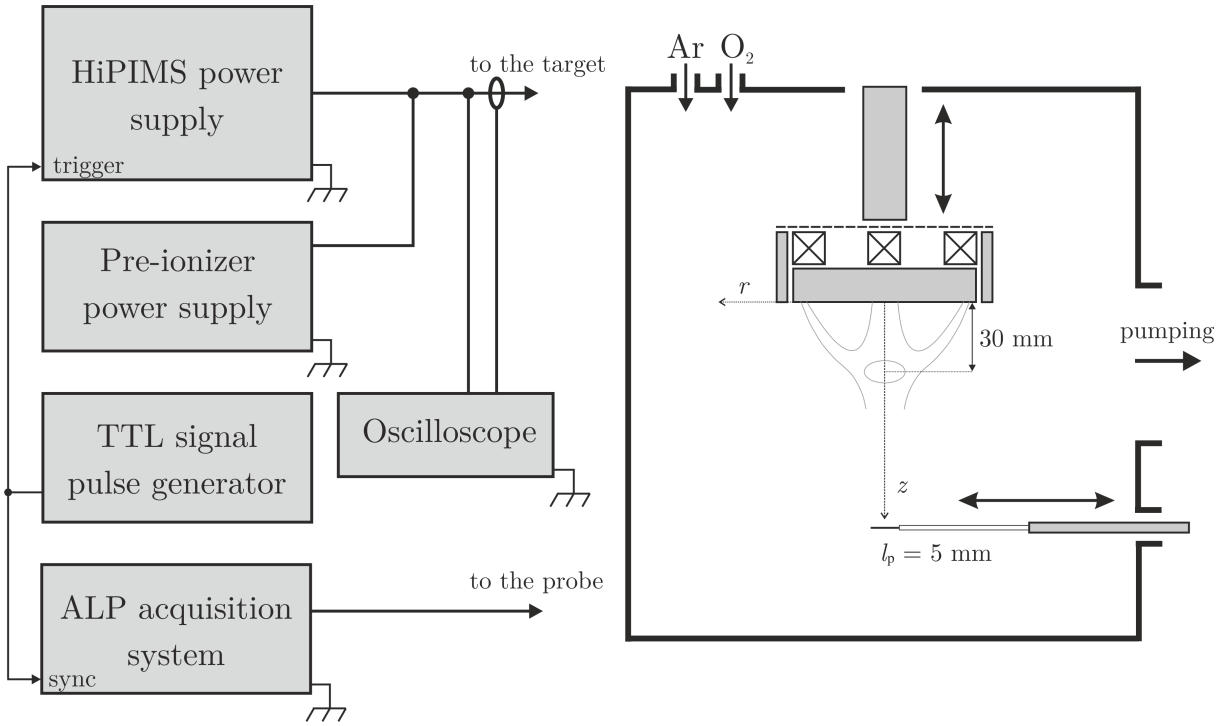

Figure 5.1. A schematic representation of the experimental set-up. The location of the magnetic null is displayed on the discharge centreline at an axial distance of 30 mm from the target surface.

The orbital-limited-motion (OML) theory [129,148] was used to infer positive ion densities (equation 4.10). In order to determine n_i using the OML approach, the ionic mass, M_i, must be known, or at least estimated. In pure Ar discharges, this is straightforward as Ar^+ is typically the dominant positive species. However, in a reactive discharge containing multiple gases, the ion current is likely to consist of contributions from multiple positive species. Moreover, multiply-charged ions are also present in HiPIMS discharge.

The proportions of the constituent positive ions were estimated by means of energy-resolved mass spectrometry. An example of a mass spectrum obtained in an Ar/O_2 discharge with $p_\mathrm{total} = 0.4$ Pa at a position along the discharge centre and 100 mm away from the target surface is presented in figure 5.2. The measured signal intensities are normalized to Ar^+. As seen in figure 5.2, the most abundant positive ions are identified as Ar^+, Ar^{2+}, O^+, O^{2+} and Ti^+. Since the mass spectrum only shows the intensities sampled from a set pass energy (5 eV in this case) and not the entire energy range, it is more accurate to calculate ion proportions using the integral values of the energy distributions. The energy distributions of the main positive ions are displayed in figure 5.3 alongside their corresponding fractions.

The average positive ion mass is obtained by $\overline{M_\mathrm{i}} = \sum_i kM_i$ where k is the ion fraction as shown in figure 5.3 and M_i is the ion mass of the i^{th} species. The calculated time-averaged fractions were 0.13, 0.27, 0.51, 0.06 and 0.03 for O^+, O^{2+}, Ar^+, Ar^{2+} and Ti^+, respectively, yielding an average ion mass, $\overline{M_\mathrm{i}} \approx 35$ amu. This was the value used as the

effective positive ion mass when calculating ion densities using the OML approach. The influence of negative ions on the positive ion flux is neglected due to the low α values measured in the times investigated (see chapter 6).

Although a time-averaged value of the effective positive ion mass is used here, it is worth noting that the positive ion composition is likely to vary both spatially and temporally. For instance, it is expected that during times of high discharge current density and at positions adjacent to the target surface, the metal ion fraction will be increased. Furthermore, dissociation of O_2 molecules into O atoms is more likely at positions closer to the target due to an increased probability of O_2 molecules experiencing electron impact collisions, resulting in a larger O^+/O_2^+ ratio. However, for the relatively low discharge power densities employed here the ratio between metallic ions to background gas ions is expected to be low. Moreover, at typical substrate positions (e.g. axial distances of $z = 50 - 100$ mm, as investigated here) the O^+/O_2^+ ratio is also expected to be small. Hence, the positive ion fractions displayed in figure 5.3 are sufficient to describe the average positive ion mass for the times and spatial positions explored in this chapter.

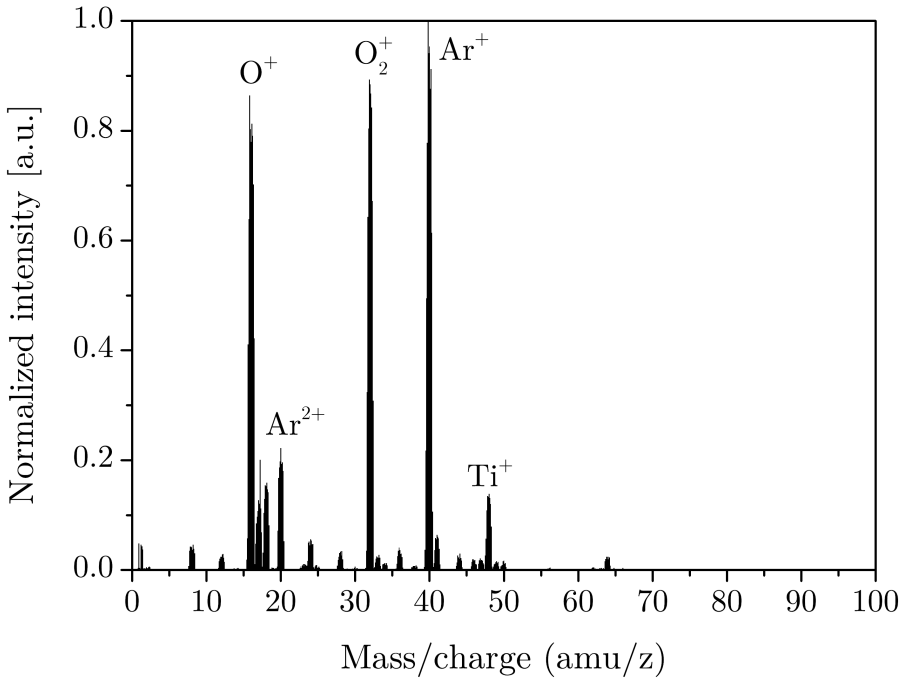

Figure 5.2. Positive ion mass spectrum obtained from an Ar/O_2 discharge held at a pressure of 0.4 Pa with the EQP orifice placed at a position $r = 0$ mm, $z = 100$ mm in the chamber. The intensity is normalized to Ar^+.

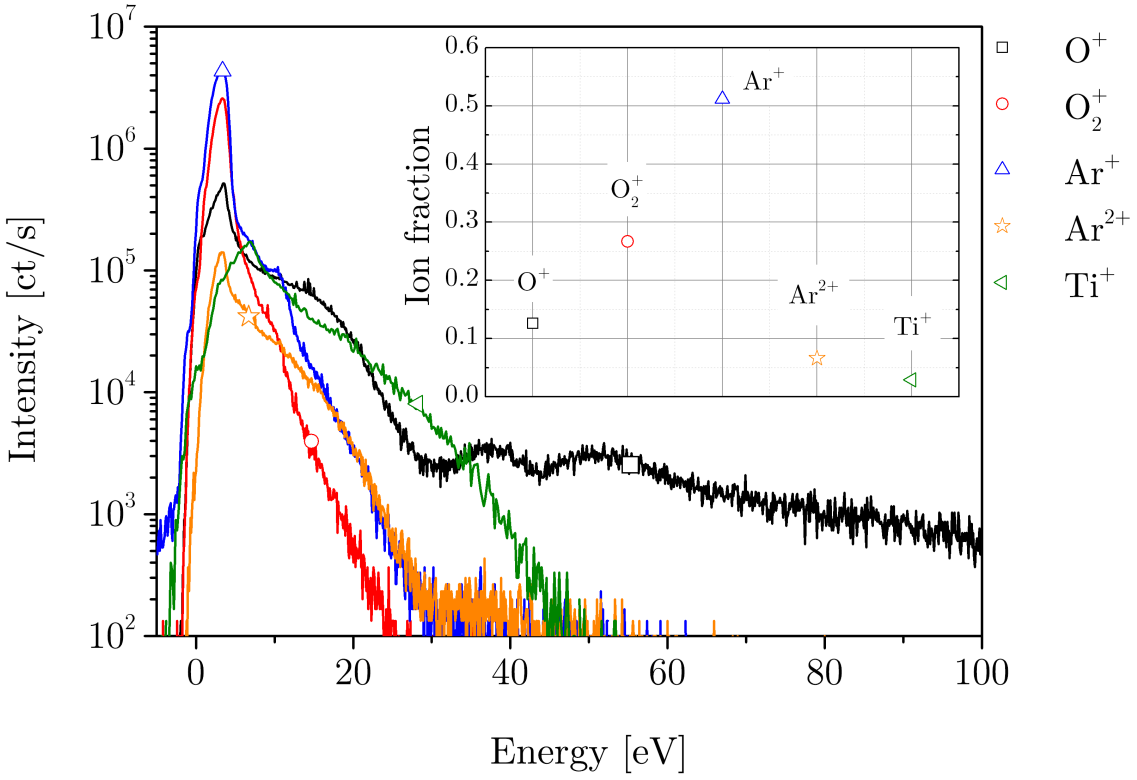

Figure 5.3. The energy distributions of O^+, O^{2+}, Ar^+, Ar^{2+} and Ti^+ obtained from an Ar/O_2 discharge held at a pressure of 0.4 Pa with the EQP orifice placed at a position $r = 0$ mm, $z = 100$ mm in the chamber. The corresponding ion fractions are inset.

5.3 Results and discussion

5.3.1 Plasma dynamics at varying pressures

5.3.1.1 Discharge voltage and current waveforms

The time-evolution of the applied target potential, $V_d(t)$, and discharge current, $I_d(t)$, during a pre-ionized HiPIMS pulse in an Ar/O_2 discharge for different working pressures are shown in figure 5.4. The pre-ionizer level is evident before the application of the HiPIMS pulse (i.e. $t < 0$). Although the shape of the waveform varies only somewhat across the pressure range, it is clear that for increased pressure a lower target voltage is required to obtain the same average discharge power of 100 W. This is, of course, accompanied by a corresponding increase in the discharge current with operating pressure. There is some evidence of a steeper increase in the discharge current following the on-set of the pulse ($0 < t < 25\ \mu$s) for a pressure of 0.4 Pa compared with the other cases. Yushkov and Anders [57] reported that the delayed on-set of the discharge current in HiPIMS is inversely proportional to the operating gas pressure, and so it is conjectured that observations here may be a result of changing target conditions. The lower oxygen

flow rate used at a pressure of 0.4 Pa could have resulted in a reduced proportion of the target being covered in an oxide layer thereby effecting secondary electron emission. The higher pressures all follow identical trends, suggesting a constant target condition. The increased oxygen flow rate used to maintain a constant oxygen content of 20% may have resulted in the complete poisoning of the target for operating pressures $0.8 - 1.6$ Pa.

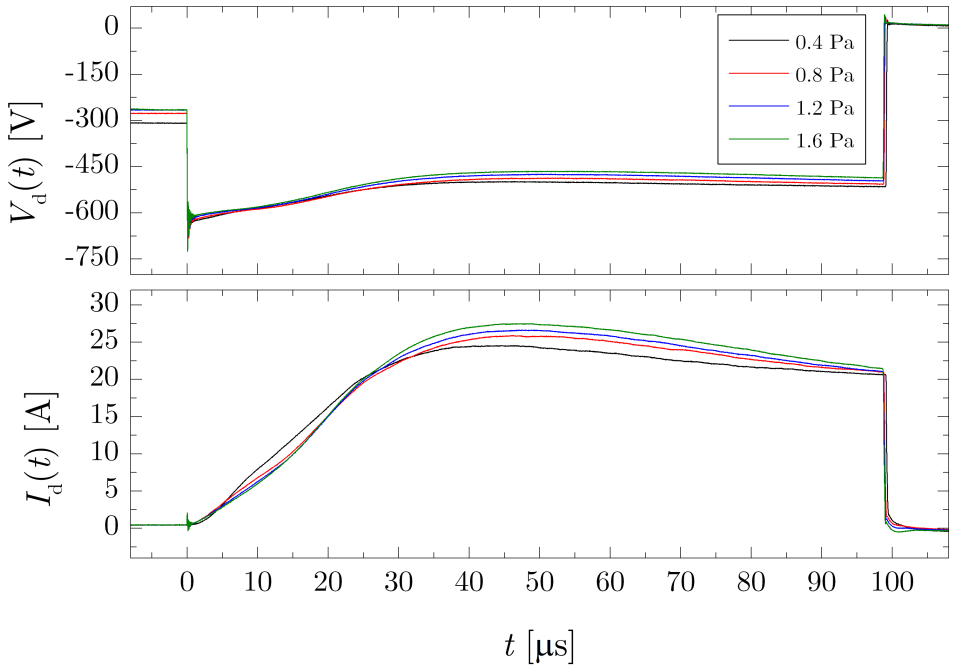

Figure 5.4. The time-evolution of the target potential, $V_d(t)$, and discharge current, $I_d(t)$ for an Ar/O_2 discharge operating at 0.4, 0.8, 1.2 and 1.6 Pa.

The peak power density changed very little between pressures with values from $0.28 - 0.29$ kW cm^{-2} across the investigated pressure range, corresponding to peak current densities of $0.55 - 0.62$ A cm^{-2}. Power and current densities were calculated over the entire target surface area, $A_t = 44$ cm^2.

5.3.1.2 Plasma density

A set of Langmuir probe characteristics from different times in the discharge pulse are shown in figure 5.5 for $p_{O_2} = 0.2p_{total}$ where $p_{total} = 0.4$ Pa. It is clear that both the electron an ion saturation currents are significantly higher during the on-time ($t = 60$ and 80 μs) than in the off-time ($t = 150$ and 300 μs). Also evident is the shift of the floating potential from ~ -10 V in the on-time to approximately 0 V in the off-time. The transition region is also more narrow for I-V characteristics in the off-time, reflecting a lower effective electron temperature.

Figure 5.6 shows the calculated positive ion densities for four different operating pres-

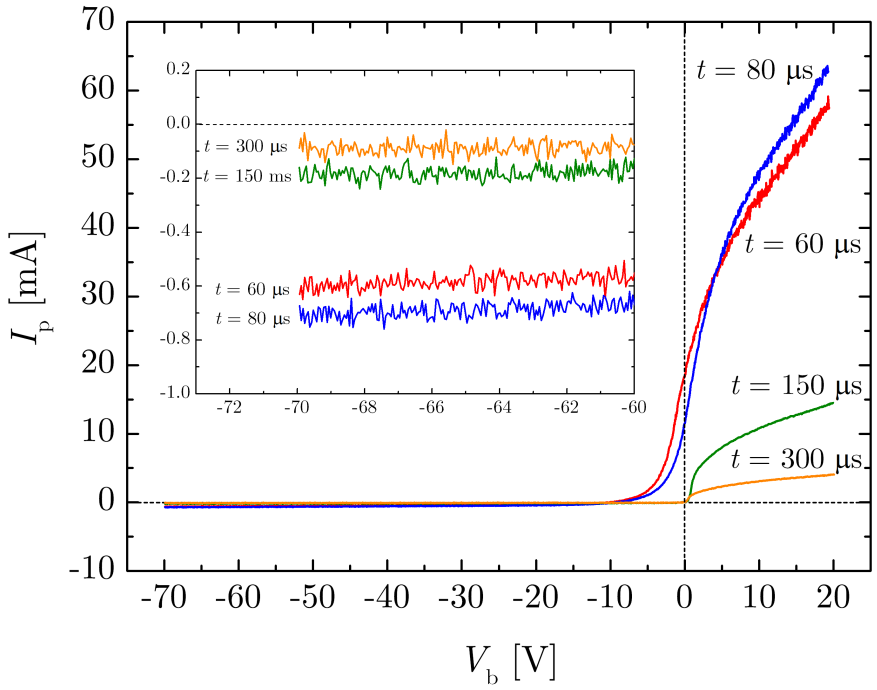

Figure 5.5. Example I-V characteristics obtained at different times in both the pulse on-time ($t = 60$ and 80 μs) and off-time ($t = 150$ and 300 μs) in an Ar/O_2 discharge where $p_{O_2} = 0.2p_{total}$ and $p_{total} = 0.4$ Pa. Inset is an expanded view of the ion saturation region.

sures: $p_{total} = 0.4$, 0.8, 1.2 and 1.6 Pa. The tip of the Langmuir probe was located at a position 100 mm above the target surface and long the centreline (i.e. $z = 100$ mm and $r = 0$ mm). The temporal evolution of n_i has a dual-peak structure with the initial peak increasing in amplitude and occurring at a later time for increasing pressure. The first peaks in density occur at times $t = 22$, 28, 33, and 38 μs with respective values of 1.2, 1.8, 2.2 and 2.4×10^{17} m^{-3} for increasing pressure. Gylfason *et al.* [149] reported the existence of a ion acoustic wave travelling away from the target surface with a velocity that decreased for increasing gas pressure, which is consistent with the observations presented here. The second peak in ion density is somewhat larger than the initial peak and appears to be almost independent of operating pressure, with values ranging from $3.1 - 3.4 \times 10^{17}$ m^{-3} across the pressure range. This invariance of plasma density during the on-time for different gas pressures in an Ar/O_2 HiPIMS discharge was also reported by Čada *et al.* [81] as well as by Poolcharuansin and Bradley [76, 127] in Ar-only discharges. The latter suggested that the dominance of metal ions over gas ions in the later stages of the pulse on-time may result in an ion density independent of working gas pressure.

The decay in ion density is somewhat delayed compared to the corresponding discharge current in figure 5.4. The voltage pulse is terminated at $t = 100$ μs, but the decay in n_i does not begin until $t = 103 - 104$ μs. This could be due to transport of ionized

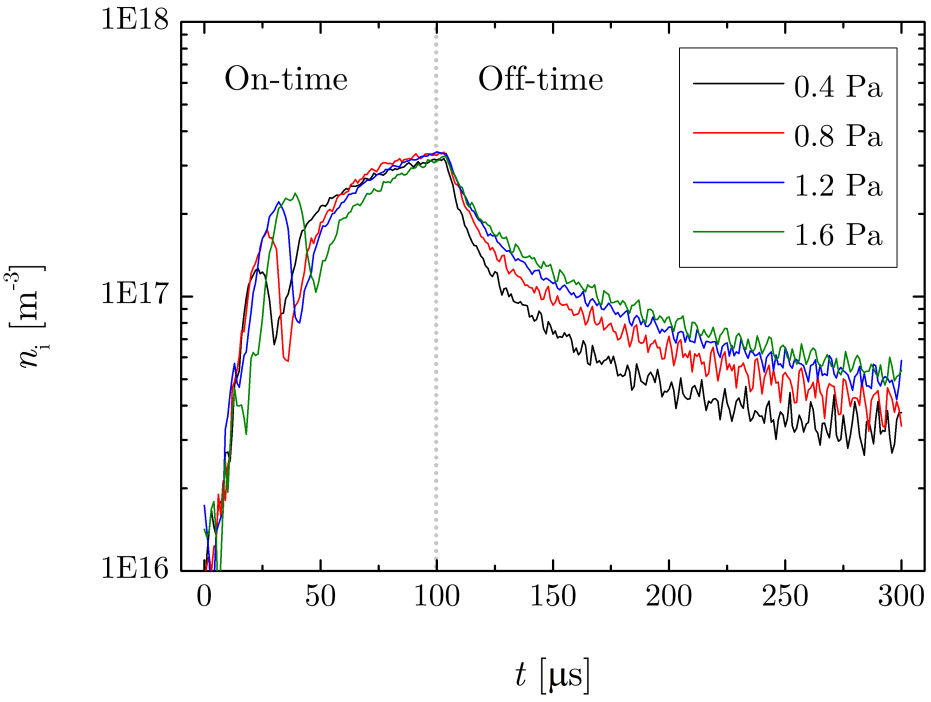

Figure 5.6. Time-evolution of the ion density, n_i, at position $z = 100$ mm, $r = 0$ mm in an Ar/O_2 discharge operating at pressures 0.4, 0.8, 1.2 and 1.6 Pa. The pulse terminates at $t = 100\ \mu$s.

target vapour from regions adjacent to the target reaching the probe after the pulse termination. A similar, but extended delay in the plasma density decay following the voltage pulse termination was also reported by Pajdarová *et al.* [150]. The ion densities decay rapidly for $t > 104\,\mu$s, however, a dense plasma persists into the afterglow. The ion density is observed to decay more rapidly at lower pressures and the measured density is approximately 5×10^{16} m^{-3} at $t = 300\ \mu$s (i.e. 200 μs into the off-time). Anders and Yushkov [78] speculate that argon metastable states are responsible for the relatively high plasma densities observed in the off-time.

A two-stage exponential decay is observed, with the first rapid decay occurring in the first 50 μs of the off-time and a second decay, commencing at $t \sim 200\mu$s. The characteristic decay times for the first (τ_1) and second decays (τ_2) are given in table 5.1. τ_1 increases with pressure, however, the same trend is not observed in τ_2. There is a significant increase in τ_2 between gas pressures of 0.4 and 0.8 Pa, however, it appears to plateau at $\sim 70\mu$s for $p \geq 0.8$ Pa. The initial decay is due to the loss of energetic, ionizing electrons to the chamber walls [131, 151] and is longer for higher pressures due to a decreased mean free path and increased collision frequency, ν_c [152].

Alami *et al.* [79] observed a secondary peak in the plasma density in the off-time, as inferred from the time-evolution of the electron saturation current. It was suggested by the authors that the peak observed in the off-time was due to a plasma wave formed

during the on-time reflecting off the chamber walls. This secondary peak is not observed here, due to the restricted time range (the secondary peak typically occurred at $t > 400\mu$s in [79]). The time range was restricted to $0-300\mu$s as the pre-ionizer potential is reapplied at $t \sim 300\mu$s [127].

Pressure (Pa)	τ_1 (μs)	τ_2 (μs)
0.4	11.5	34.3
0.8	13.7	73.4
1.2	14.3	69.3
1.6	15.5	72.4

Table 5.1. Characteristic decay times for the first (τ_1) and second (τ_2) exponential decays of ion density for four different operating pressures.

For comparison, electron densities were obtained using equation 4.7 for the cases $p =$ 0.4 and 1.6 Pa with a time-resolution of 10 μs and are shown in figure 5.7. The calculated values of n_e agree well with the values of n_i in figure 5.6; n_e appears to be pressure independent with peak values of approximately 2.6×10^{17} m^{-3}, which is about 80% of the peak value of n_i. Furthermore, the dual-peak structure is also evident in n_e and is exhibiting the same pressure dependence (i.e. the first peak occurring later at a higher pressure) despite the reduced temporal resolution.

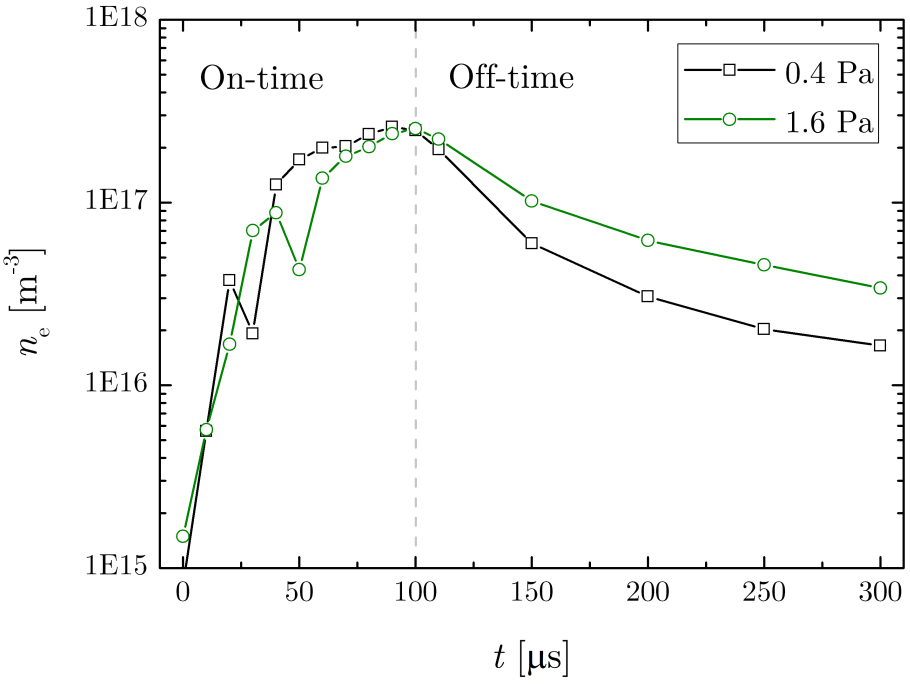

Figure 5.7. Time-evolution of the electron density, n_e, at position $z = 100$ mm, $r = 0$ mm in an Ar/O_2 discharge operating at pressures 0.4 and 1.6 Pa. The pulse terminates at $t = 100\,\mu$s.

5.3.1.3 Effective electron temperature

As reported by Poolcharuansin *et al.* [76], multiple populations of electrons can exist in a HiPIMS discharge, particularly in the early stages of the pulse on-time. The highest energy population are thought to comprise of beam-like electrons, and hence cannot be described by a definite temperature (i.e. non-Maxwellian velocity distribution). When the electron velocity distribution is not known, or consists of multiple distinct populations, it is often desirable to describe the average electron energy using an *effective* electron temperature, T_{eff}. In HiPIMS discharges, the density of the highest energy electron population is approximately 2 orders of magnitude lower than that of the colder groups and the energy difference between the lower energy populations is only significant in the very early pulse on-time ($t < 5$ μs) [76], so the assignment of a single-valued effective electron temperature is instructive in this case.

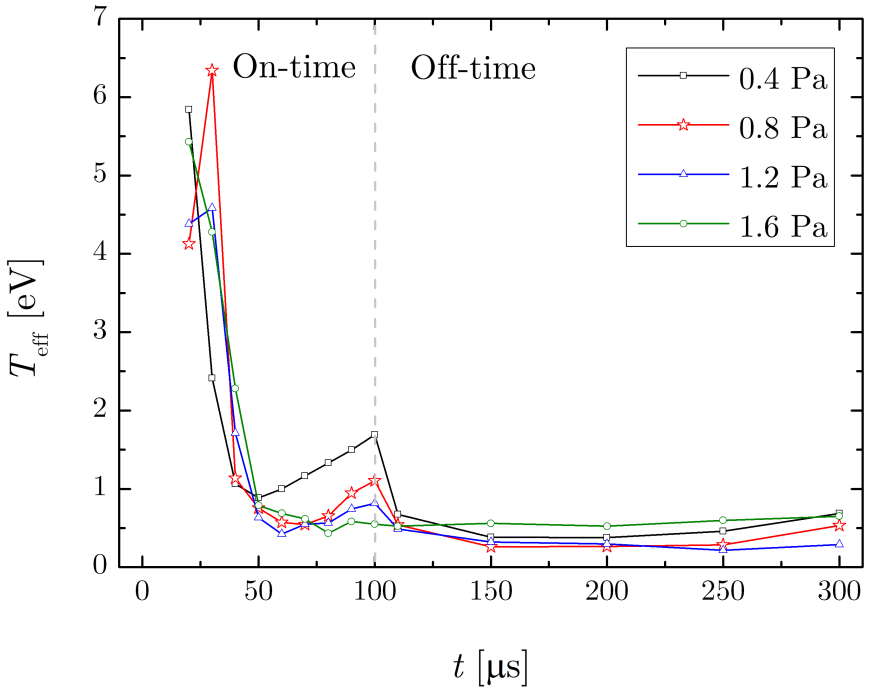

Figure 5.8. Time-evolution of the effective electron temperature, T_{eff}, at position $z =$ 100 mm, $r = 0$ mm in an Ar/O_2 discharge operating at pressures 0.4, 0.8, 1.2 and 1.6 Pa. The pulse terminates at $t = 100$ μs.

The temporal evolution of T_{eff}, as calculated using equation 4.8, is shown in figure 5.8 for the four different operating pressures. In the initial stages of the pulse, T_{eff} is high (> 6 eV at $t = 20\mu$s) before decreasing rapidly, as in [76]. As the plasma density increases, T_{eff} is quenched and reaches a minimum of ~ 0.5 eV during the on-time at $t \sim 55$ μs. Beyond this minimum, T_{eff} increases in all cases with the exception of $p = 1.6$ Pa, which shows no appreciable increase in T_{eff} after $t = 55$ μs. This increase in T_{eff} during the active phase of the discharge was also observed in the Langmuir probe studies performed by Čada *et*

al. [81] in reactive HiPIMS and was conjectured to be a consequence of gas rarefaction. The intense 'sputter wind' [62] from the target during the on-phase drives a compression and corresponding rarefaction phase [59]. A local reduction in neutral particle density would explain the electron heating observed towards the end of the on-time.

An increase in pressure produces an observable drop in T_{eff}. This is most evident at the time of the pulse termination (i.e. $t = 100\,\mu$s), when $T_{\text{eff}} = 1.7$, 1.1, 0.8 and 0.6 eV for increasing pressure. These results are, again, similar to those reported by Čada *et al.* [81]. In the off-time, a rapid decay in T_{eff} is observed for all pressures with the exception of $p = 1.6$ Pa, where a steady decay occurs. For all cases, T_{eff} remains stable during the off-time at values between 0.3 and 0.6 eV, somewhat higher than those found in [81]. The slight rise in T_{eff} towards the end of the off-time is likely due to the application of the pre-ionizer potential at $t \sim 300\mu$s. As with ion and electron densities, there is evidence of an increase in T_{eff} at $t \sim 40\mu$s (exhibited in plots of T_{eff} for $p = 0.8$ and 1.2 Pa) which may be the result of the passing ionisation wave.

5.3.1.4 Plasma and floating potentials

The plasma potential, Φ, was obtained from the second derivative of the I-V characteristic, where $\mathrm{d}^2 I_\mathrm{p}/\mathrm{d}V_\mathrm{b}^2 = 0$. However, since the signal-to-noise ratio adjacent to the plasma potential was insufficient to directly use the raw I-V data, a Savitzky-Golay filter [153] with second-order polynomial and a window width of 100 points was first applied. An example of a raw I-V characteristic (taken at $p = 3$ mTorr and $t = 50$ μs) and its second derivative are shown in figure 5.9a and again with the filter applied in figure 5.9b. The floating potential, V_f, is readily obtained from the raw I-V data and is defined as the point where $I_\mathrm{p} = 0$.

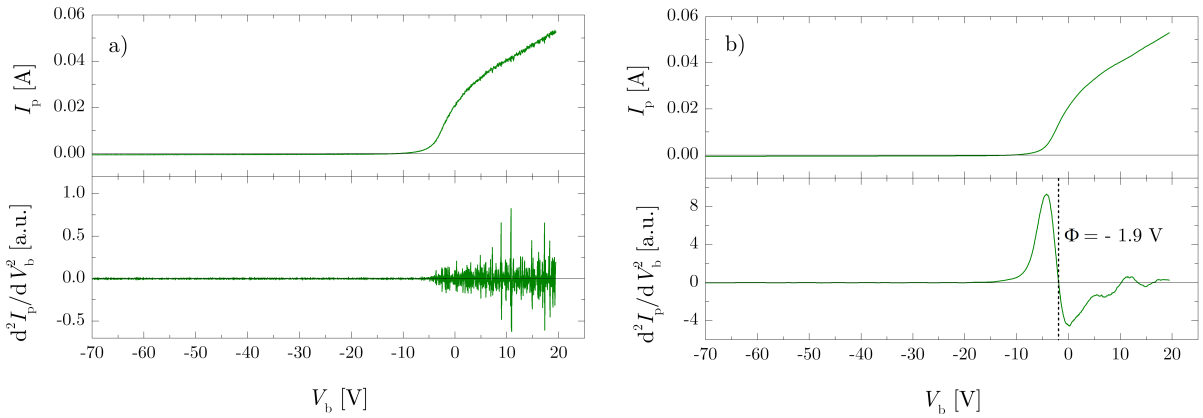

Figure 5.9. Raw (a) and filtered (b) I-V characteristics with their corresponding second derivatives. The plasma potential is found where $\mathrm{d}^2 I_\mathrm{p}/\mathrm{d}V_\mathrm{b}^2 = 0$ and can only be distinguished on the filtered data.

The time-evolution of Φ and V_f for different pressures are shown in figures 5.10. In the

initial stages of the pulse both Φ and V_f are highly negative, with values of V_f exceeding the maximum negative bias applied to the probe (-70 V) for times $t < 10\mu$s. It has been suggested that this highly negative floating potential immediately following the pulse onset may be caused by short-lived highly energetic electrons [127, 154]. After the initial stage of the active phase, Φ gradually increases from approximately -10 V and becomes positive before the termination of the pulse for $p = 0.4$ and 0.8 Pa reaching values of $+7$ and $+5$ V, respectively. This is somewhat similar to the evolution of the plasma potential as measured by Mishra *et al.* [84], Rauch *et al.* [155] and Liebig and Bradley [83] using an electron-emitting probe. For higher pressures, Φ approaches zero, but remains negative throughout the pulse on-time. In the immediate off-time, Φ peaks at values between 6 and 7 V before settling at an approximately constant value about 40 μs into the off-time, with $\Phi = 2 - 3$ V, independent of working gas pressure.

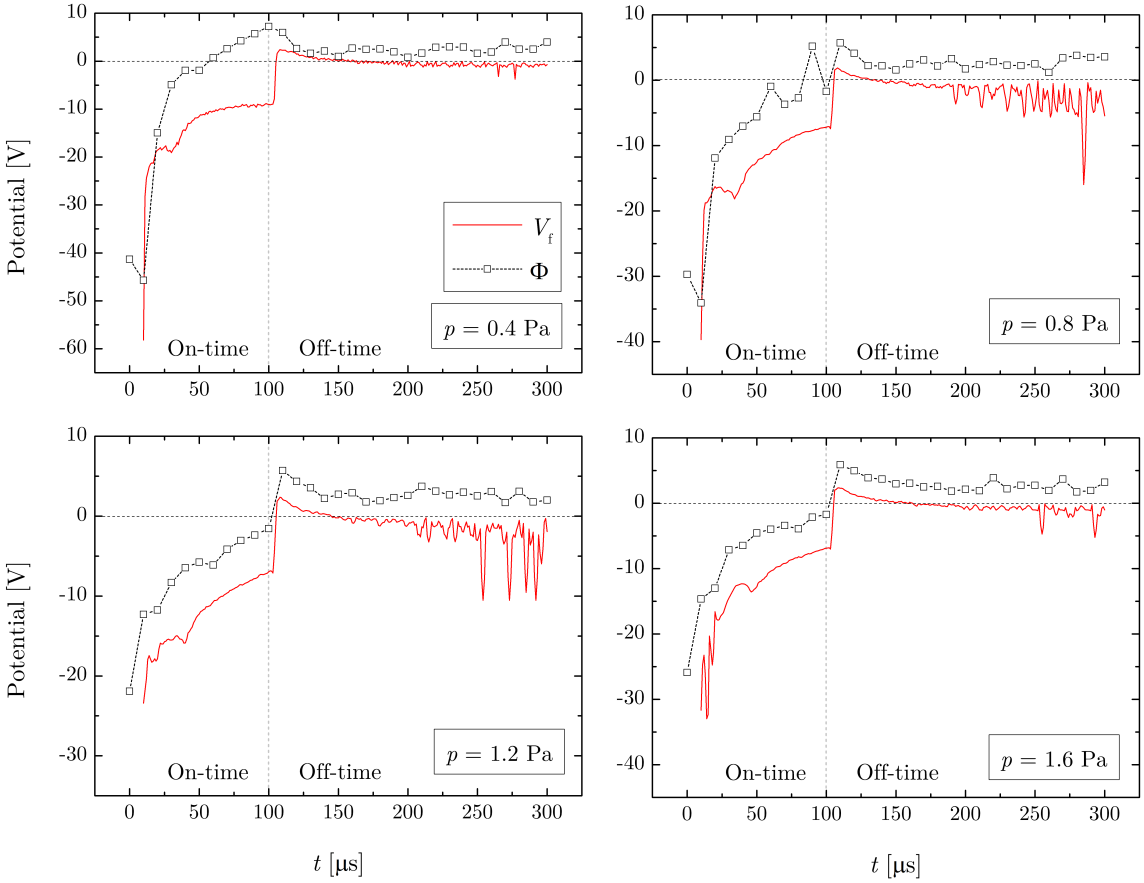

Figure 5.10. Time-evolution of the plasma potential, Φ, and floating potential, V_f, at position $z = 100$ mm, $r = 0$ mm in an Ar/O_2 discharge operating at pressures 0.4, 0.8, 1.2 and 1.6 Pa.

Beyond the initial stages of the active phase, V_f remains negative throughout the pulse on-time and follows Φ. There is a marked dip in V_f at $t = 25-50\mu$s across the investigated pressure range, coinciding with the initial peak in ion and electron densities (see figures

5.6 and 5.7). Directly after the voltage pulse termination, V_f goes positive before slowly decreasing to a value just below 0 V. The spikes in the plots for V_f beginning at $t \sim 200$ μs in figure 5.10 are due to the lower signal-to-noise ratios of the I-V characteristics collected at lower plasma densities, making it increasingly difficult to determine an accurate value for V_f.

5.3.2 Plasma dynamics at different axial distances

For the case of $p = 0.4$ Pa, time-resolved plasma parameters were also measured as a function of axial distance from the target surface, $z = 50 - 100$ mm, at a constant radial position in the center of the discharge ($r = 0$ mm). An overview of the dynamics of ion density (n_i), effective electron temperature (T_{eff}) and plasma potential (Φ) is given for different axial positions.

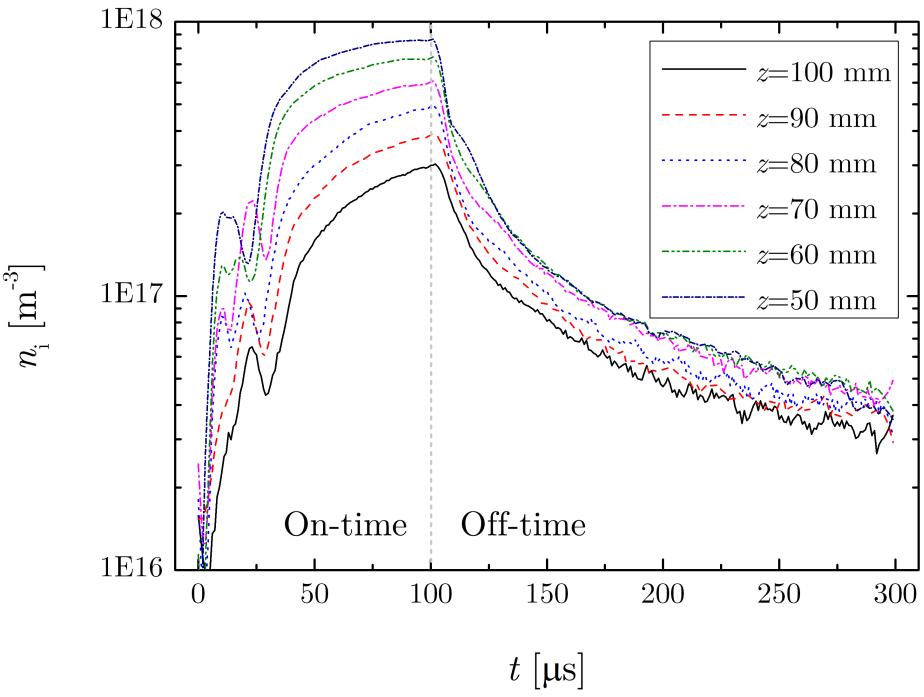

Figure 5.11. The temporal evolution of the ion density, n_i, at different axial distances from the target ($z = 50-100$ mm) in an Ar/O_2 discharge held a pressure of 0.4 Pa.

5.3.2.1 Ion density

The temporal evolutions of the ion density, for different axial distances from the target are shown in figure 5.11. As the probe was moved closer to the target surface, the peak value of n_i increased from 3.1 to 8.6×10^{17} m^{-3}. Again, the peak value of n_i occurs a short time after the termination of the voltage pulse for all cases, however, it peaks at slightly

earlier times for positions closer to the target; peaking at time $t = 101$ μs at position $z = 50$ mm and at $t = 103$ μs for $z = 100$ mm.

An interesting feature of the temporal evolutions of n_i shown in figure 5.11 is the multi-peak structure found at $t < 30$ μs. At positions $z = 90$ and 100 mm, only a single peak is evident at $t \sim 25\mu$s. However, at $z = 60 - 80$ mm, two peaks in n_i are clearly observable with them seemingly merging into a single peak centred on $t = 12\,\mu$s at $z = 50$ mm. It is possible that this observation is a consequence of multiple ion acoustic waves emanating from the target, however, more in-depth studies are required to uncover the driving mechanism.

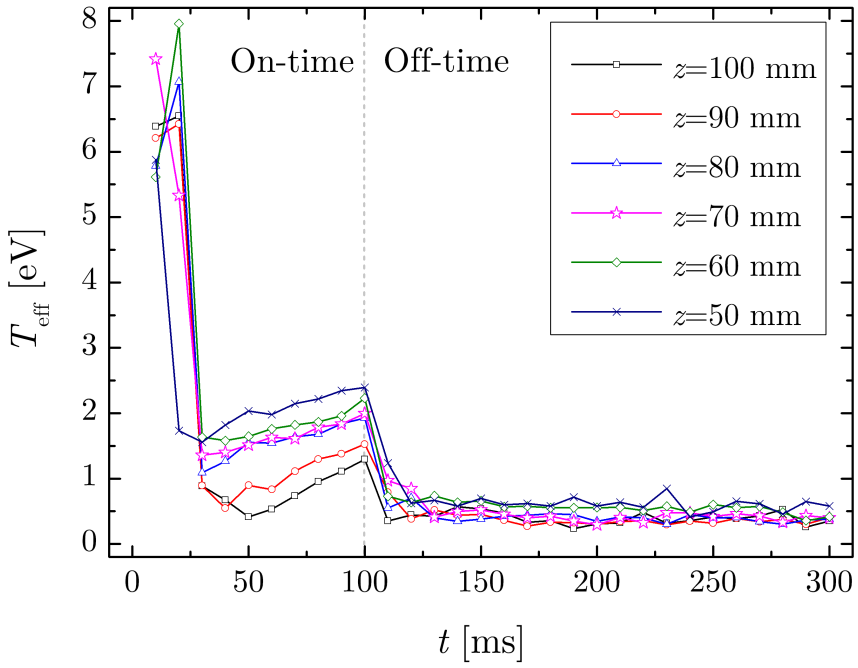

Figure 5.12. The temporal evolution of the effective electron temperature, T_{eff}, at different axial distances from the target ($z = 50 - 100$ mm) in an Ar/O_2 discharge held a pressure of 0.4 Pa.

5.3.2.2 Effective electron temperature

Time-resolved values of the effective electron temperature recorded at different axial distances are shown in figure 5.12. The shape of the temporal evolution is consistent across the range of axial positions; T_{eff} begins at a high value in the early on-time, decreases rapidly and then increases gradually until the end of the pulse. However, there are clear differences in the values of T_{eff} at different axial distances. The minimum value of T_{eff} during the on-time ranges from 0.4 to 1.5 eV at times $t = 30 - 50$ μs, occurring earlier for decreasing z. Similarly, $T_{\text{eff}} = 1.3 - 2.4$ eV at the termination of the pulse for $z = 100 - 50$

mm, respectively. An increase in T_{eff} for axial positions closer to the target was also reported by Sigurjónsson [156]. After the termination of the pulse, T_{eff} decreases rapidly to values < 1 eV, with typical values of $0.2 - 0.5$ eV with the higher values at positions closer to the target.

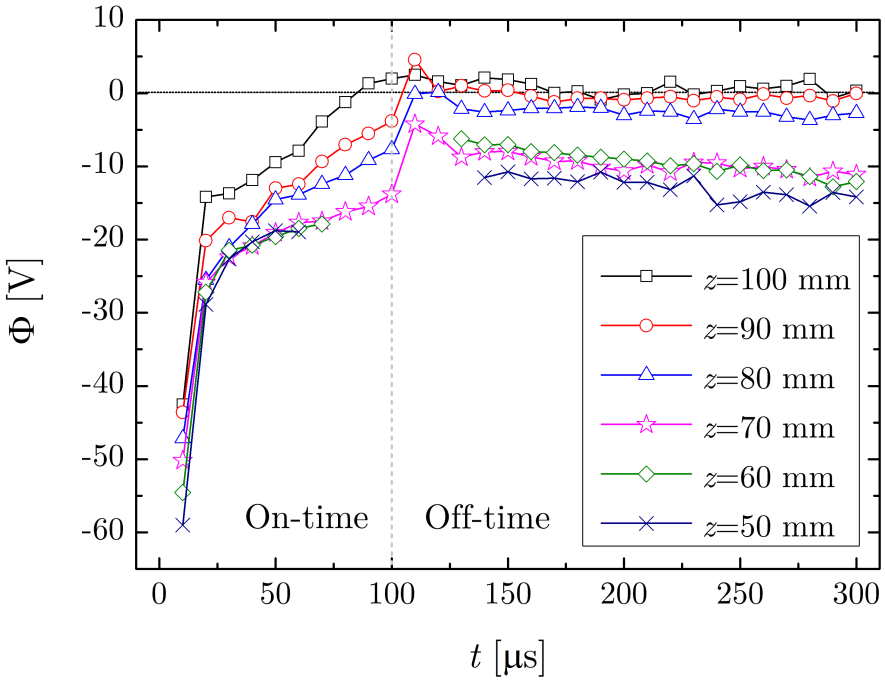

Figure 5.13. The temporal evolution of the plasma potential, Φ, at different axial distances from the target ($z = 50 - 100$ mm) in an Ar/O_2 discharge held a pressure of 0.4 Pa.

5.3.2.3 Plasma potential

The plots of the temporal evolution of Φ for different axial positions along the discharge centreline are presented in figure 5.13. The pattern of the evolving plasma potential is similar to those shown in figure 5.10; beginning at highly negative values and increasing steadily during the pulse on-time before jumping to a higher value when the discharge voltage pulse is terminated. With the exception of $z = 100$ mm, Φ at all positions remains negative during the active phase. At positions closer to the target, Φ also remains negative in the off-time ranging between values of -8 and -14 V for $z = 70 - 50$ mm. Farther away from the target, Φ is only slightly negative with values of -0.2 to -3 V, and even positive for $z = 100$ mm where $\Phi = 1 - 2$ V in the off-time. Both during the active phase and the discharge afterglow, Φ is found to be generally more negative for axial positions closer to the target. Values of Φ for positions $z = 50$ and 60 mm at times $t = 70 - 120$ are undetermined and not included in figure 5.13 as the electron saturation current is not achieved in the corresponding probe I-V characteristics. This was due to the drawn

electron current being greater than the maximum current range of the acquisition system (150 mA).

During the on-phase, the negative plasma potential measured in a typical substrate position, such as $z = 100$ mm, is a potential barrier that positive ions must overcome to exit the plasma. This can have consequences for coatings deposited on floating or grounded substrates where deposition rates may be lowered as a consequence of ionized sputtered particles being reflected away from the substrate. This has the potential to be of importance in HiPIMS due to the high degree of ionized sputtered flux incident upon the substrate [157]. Liebig and Bradley [83] determined that it is possible that only $\sim 30\%$ of the ionized sputtered particles would pass the barrier. Furthermore, in reactive discharges this may have consequences for increasing the flux of negative ion species to the developing film. Negative ions in HiPIMS discharges are discussed in more detail in the later chapters of this thesis.

5.3.3 Plasma dynamics at different radial positions

Time-resolved plasma parameters were measured as a function of radial distance from the discharge centreline, $r = 0 - 40$ mm, at a constant axial distance from the target surface: $z = 100$ mm. The Ar/O_2 discharge was operated at a constant total pressure of 0.4 Pa. An overview of the dynamics of n_i, T_{eff} and Φ is given for different radial positions.

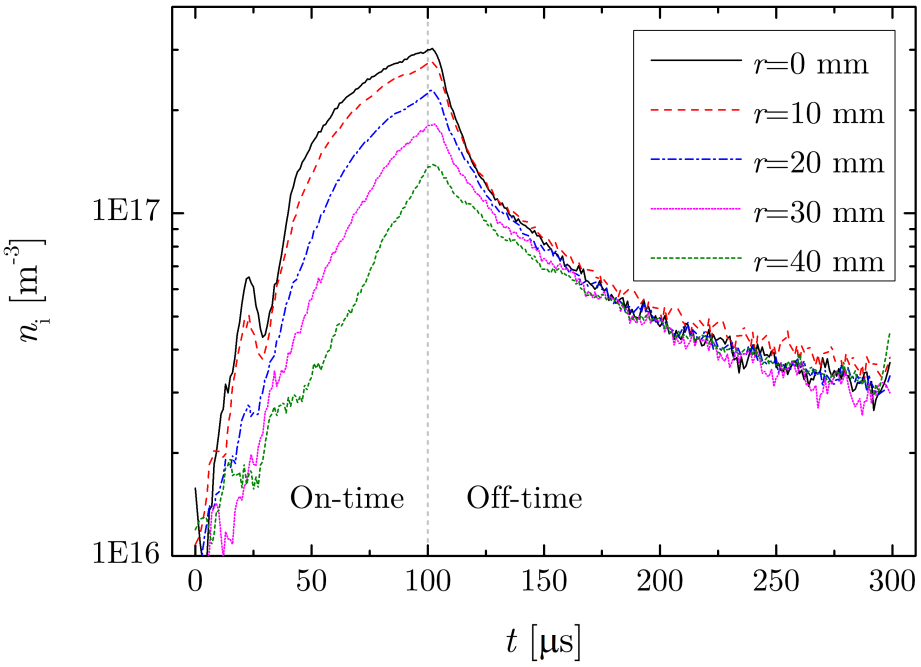

Figure 5.14. The temporal evolution of the ion density, n_i, at different radial positions ($r = 0 - 40$ mm) at a fixed distance of 100 mm away from the target, in an Ar/O_2 discharge held a pressure of 0.4 Pa.

5.3.3.1 Ion density

The temporal evolution of the ion density measured at different radial positions is shown in figure 5.14. The ion density is observed to decrease moving away from the centreline with peak values ranging from 1.4 to 3.1 $\times$ 10^{17} m^{-3} for increasing r. The peak value consistently occurs at t = 103 μs, somewhat after the pulse termination. The initial spike in n_i at $t \sim 30$ μs, possibly caused by an ion acoustic wave travelling from the target [59, 149], is observed to decrease from a value of 6.5 $\times$ 10^{16} m^{-3} at r = 0 mm to 1.7 $\times$ 10^{16} m^{-3} for at r = 40 mm.

5.3.3.2 Effective electron temperature

Time-resolved values of T_{eff} measured at different radial positions at a constant axial distance from the target are displayed in figure 5.15. After obtaining high values in the immediate on-time, T_{eff} is rapidly quenched in the early stages of the pulse to approximately 0.5 eV for $r = 0 - 20$ mm and 1.0 eV for $r = 30 - 40$ mm, before increasing steadily. For r = 0 and 10 mm, this increase in T_{eff} persists until the termination of the pulse reaching values of 1.3 and 1.0 eV, respectively. However, for radial positions farther away from the centreline the increase in T_{eff} ceases at t = 60 μs for r = 30 mm and t = 70 μs for r = 30 mm. There is no significant increase in T_{eff} observed for r = 20 mm.

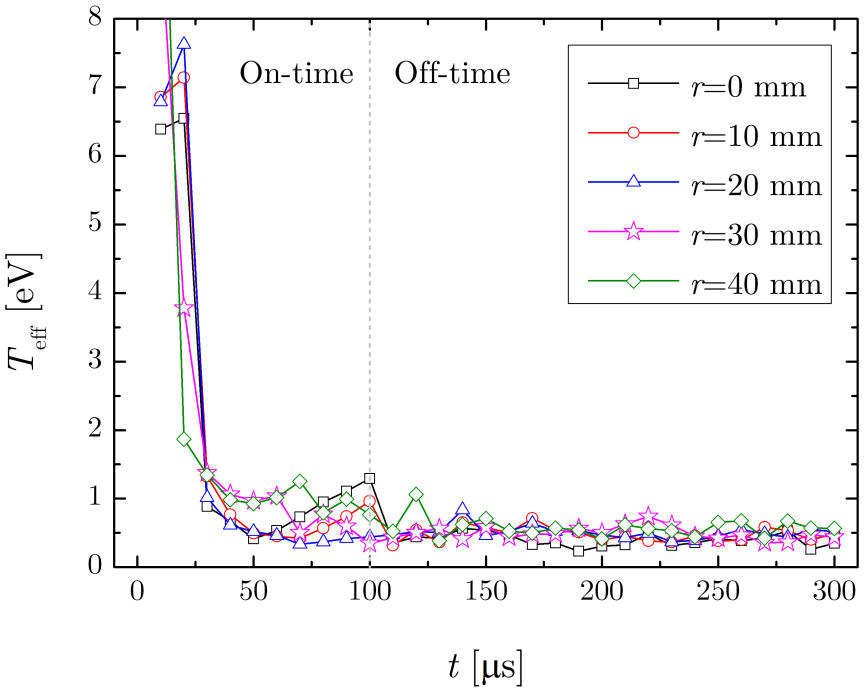

Figure 5.15. The temporal evolution of the effective electron temperature, T_{eff}, at different radial positions ($r = 0 - 40$ mm) at a fixed distance of 100 mm away from the target, in an Ar/O_2 discharge held a pressure of 0.4 Pa.

These results are consistent with the idea of the increase in T_{eff} being a result of a propagating compression and rarefaction wave [59]. The compression phase would lead to a decrease in T_{eff} due to the higher electron-neutral collision frequency as a result of a local neutral density increase. Conversely, the accompanying rarefaction phase would reduce the local neutral density, thereby decreasing the electron-neutral collision frequency and resulting in an increase in the effective electron temperature. By using an array of electrostatic probes measuring the ion saturation current, Horwat and Anders [59] were able to determine that the direction of the sputter wind was mainly away from the target surface. This would explain the decreasing n_{i} spike (see figure 5.14) for increasing r. Moreover, it can also help to understand the higher T_{eff} observed during the on-time for radial positions far away from the centreline; the compression caused by the sputter wind would be less pronounced at large r and so T_{eff} would remain higher by virtue of the reduced compression compared to radial positions directly opposite the target surface.

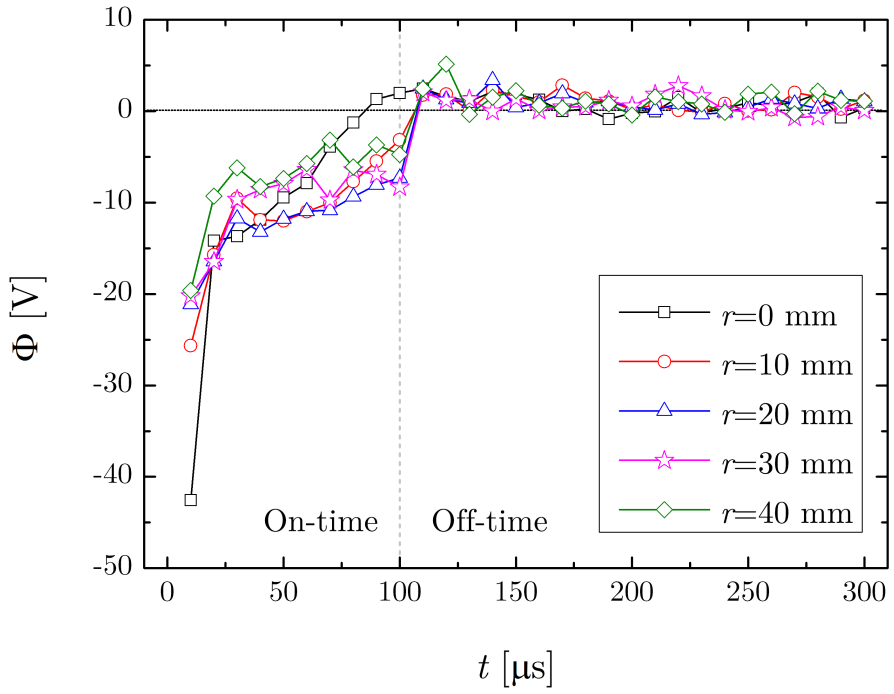

Figure 5.16. The temporal evolution of the plasma potential, Φ, at different radial positions ($r = 0 - 40$ mm) at a fixed distance of 100 mm away from the target, in an Ar/O_2 discharge held a pressure of 0.4 Pa.

5.3.3.3 Plasma potential

The temporal evolutions of the plasma potential, Φ, for varying radial positions at a fixed axial distance are shown in figure 5.16. With the exception of the late on-time ($t = 90 - 100$ μs) for $r = 0$ mm, Φ at all radial positions is negative throughout the active phase of the pulse. Upon the termination of the voltage pulse, Φ rapidly jumps

to a positive value ($\sim 2-4$ V) before settling at values either side of 0 V and ranging from -1.5 to 2 V. Although there are no large variations across the range of r, directly opposite the racetrack ($r = 20$ mm), Φ is somewhat more negative during the on-time than at other radial positions.

5.4 Conclusions

The spatiotemporal evolution of the plasma parameters during HiPIMS of Ti in an Ar/O_2 discharge have been determined by means of a single Langmuir probe. In addition, variations with working pressure were also investigated for a fixed position in the discharge.

The peak ion density was found to occur just after the termination of the voltage pulse and was of the order of 10^{17} m^{-3}, almost reaching 10^{18} m^{-3} at an axial distance of 50 mm from the target surface. These values of n_i are consistent with those found in [81] where a similar study was performed. However, the plasma densities found in pure Ar discharges are generally higher by about an order of magnitude [71, 72] than those observed here for Ar/O_2 mixtures, although it is worth noting that higher average powers were employed in those investigations. n_i was observed to increase for positions closer to the target surface and decrease for positions away from the discharge centreline at a fixed axial distance from the target of 100 mm.

The temporal evolution of the ion density displayed a dual-peak structure, with an initial peak in density appearing at $t \sim 25$ μs, before the absolute peak value was attained at the termination of the pulse as mentioned above. The first peak in n_i appeared earlier in time for positions closer to the target and diminished in magnitude for increasing radial distances away from the center of the chamber. It is thought that this initial peak is due to a compression and subsequent rarefaction wave [59] propagating through the discharge following the onset of an intense sputter wind. Moreover, the peak also occurred earlier in time and with a smaller amplitude for lower working pressures, further supporting this supposition. In the off-time, n_i exhibited a two-fold exponential decay with the first characteristic decay time range from 11.5 to 15.5 μs, increasing with pressure.

Immediately following the initiation of the voltage pulse, a high effective electron temperature was measured (as in [74, 76, 81]) before being quenched to values of $0.5-1.0$ eV in the middle of the active phase. Following this quenching, T_{eff} increased to $1.0-2.4$ eV until the termination of the pulse. The electron quenching was found to be more pronounced at positions directly above the target and most evident at $r = 20$ mm (over the racetrack). This phenomena is thought to be another consequence of a strong compression/rarefaction wave propagating from the target. T_{eff} was observed to decrease for increasing working pressure and increase for axial positions closer to the target.

The pattern of the temporal evolution of the plasma potential is similar for all conditions. At the on-set of the pulse, Φ was found to be highly negative before increasing

steadily during the on-time. Aside from the position $z = 100$ mm, $r = 0$ mm at a working pressure of 0.4 Pa, Φ remained negative throughout the pulse-on time with typical values ranging between -20 and -5 V. It was found that Φ was more negative for radial positions directly over the target and axial positions closer to the target surface. At distances far away from the target, Φ settled at values close to 0 V during the off-time. However, for $z = 70 - 50$ mm Φ remained negative during the off-time and was found to range from -8 to -14 V, being more negative for smaller z. A negative Φ in the substrate region essentially sets up a barrier for any post-ionized sputtered particles and may result in a reduction of the deposition rate on a grounded or floating substrate as suggested in [83, 84]. Discussions on deposition rates in reactive HiPIMS are given in chapter 8.

Although the dynamics of n_i, T_eff and Φ have been discussed here, negative ions also play a crucial role in reactive sputter deposition and will be the focus for much of the rest of this thesis, beginning with negative ion density measurements in HiPIMS discharges presented in chapter 6.

Chapter 6

Negative ion densities in reactive HiPIMS

6.1 Introduction

In reactive HiPIMS of a metallic target in the presence of electronegative gases, such as oxygen, significant amounts of negative ions are created where the dominant negative ion species is found to be O^- [158]. Energy-resolved mass spectroscopic studies have revealed three main energy populations of O^- ions within magnetron discharges [18] with the highest energy population possessing energies close to the absolute potential applied to the cathode. Bombardment by these high-energy negative ions can have detrimental effects on the structure [111], crystallinity [159] and electrical properties [125, 160] of the growing thin film. Furthermore, the presence of negative ions in the discharge can significantly influence the positive ion flux impinging upon plasma-facing surfaces [102] and therefore has implications for many plasma processing methods in addition to electrostatic probe diagnostics, where knowledge of ion fluxes through the sheath is needed in order to interpret measured I-V characteristics.

Although energy-resolved mass spectrometry is an extremely useful technique, without applying rigorous calibration procedures, it can only provide qualitative information regarding ion fluxes arriving at a surface rather than absolute values. Although energy-resolved mass spectrometry can be used to detect high energy negative ions originating from the target surface during the active phase, negative ions with energies lower than the electron temperature (< 1 eV) go undetected as they are unable to overcome the potential barrier within the sheath at the mass spectrometer sampling orifice and so alternative methods must be employed. An example of a method which is able to sample all energy populations of negative ions, and measure absolute negative ion densities is laser photodetachment [119, 145]. Laser photodetachment involves firing a laser pulse with a photon energy greater than that of the affinity of the target negative ion, into the plasma

discharge adjacent to an electron-collecting electrostatic probe that is positively biased with respect to the plasma potential, Φ. The subsequent increase in electron current collected by the probe is then used to determine a value of the local negative ion density, n_-. Laser photodetachment has been used successfully to determine the negative ion densities in reactive magnetron sputter deposition for different configurations including DC [120, 161] and bipolar-pulsed DC [141].

Alternatively, it is possible to determine the negative ion-to-electron ratio, $\alpha = n_-/n_e$, from the ratio of electron and ion saturation currents as obtained using a Langmuir probe. This technique has been discussed by Braithwaite and Allen [95] relevant to spherical Langmuir probes and by Bacal and Doucet [162] for long cylindrical probes (i.e. when $r_p/\lambda_D < 1$, where r_p is the probe radius and λ_D is the Debye length). Experimentally, this method has been compared with laser photodetachment measurements in a hybrid multi-cusp plasma generator by Nikitin *et al.* [136] who reported good agreement between the two methods in discharges where $n_- > n_e$ (i.e. $\alpha > 1$). Also, You *et al.* [137] reported that the Langmuir probe method of determining the temporal evolution of the O^- ion density in pulsed DC magnetron sputter deposition agreed within a factor of 2 to 5 with photodetachment measurements for highly electronegative discharges. Due to the inherent uncertainties and relatively large errors associated with Langmuir probe measurements, it is very difficult to obtain values for the negative ion fraction for electropositive discharges. During the driven-phase of pulsed DC reactive magnetron sputter deposition of titanium in the presence of oxygen, the electronegativity of the discharge was measured, by means of laser photodetachment, to be relatively low ($\alpha = 0.1-0.6$) [141]. As such, the Langmuir probe method of determining electronegativity is often restricted to the off-phase of pulsed discharges, as demonstrated in [137]. The apparent advantage that the Langmuir probe method provides over laser photodetachment is the simplicity of its implementation; no optical instruments or high-powered pulsed lasers are required. However, its applicability is typically restricted to highly electronegative plasmas such as the afterglow of an oxygen-containing discharge.

In this chapter, the temporal evolution of negative ion density during the off-time of reactive HiPIMS of titanium in an argon and oxygen gas mixture is investigated by the Langmuir probe method and briefly compared with measurements made using laser-aided photodetachment for different oxygen partial pressures. The presence of negative ions in a plasma directly influences the plasma potential, charge balance and emission from the plasma which in-turn drives the physical and chemical processes occurring at surfaces in contact with the discharge. The results presented here will serve to add to the knowledge base regarding oxygen negative ion dynamics that is relevant to many plasma-assisted processing methods.

6.2 Experimental set-up

The Langmuir probe and photodetachment data were collected on separate experimental set-ups. Langmuir probe measurements were collected using the same experimental equipment described in §4.1 and §5.2. Some details particular to this investigation are outlined in §6.2.1. However, due to the optical apparatus required, the laser photodetachment diagnostic was fitted to its own dedicated vacuum chamber mounted onto an optical bench. This vacuum chamber was equipped with a different magnetron source and HiPIMS power supply which will be briefly described in §6.2.2. As the experimental parameters were widely disparate for the two investigations, only a qualitative comparison is made.

6.2.1 Set-up for Langmuir probe measurements

The vacuum system in which the Langmuir probe measurements were made is described in §4.1 and a simplified schematic is presented in figure 6.1. The HiPIMS power supply was triggered by an external pulse generator (Thandar TG105) by which the applied voltage pulse width τ and frequency f were controlled. In this investigation, the voltage pulse on-time and frequency were maintained constant at $\tau = 100$ μs and $f = 100$ Hz respectively, giving an off-time $t_{\text{off}} = 9900$ μs. However, the pre-ionizer power supply was not utilized in this case in order to study the discharge afterglow more completely.

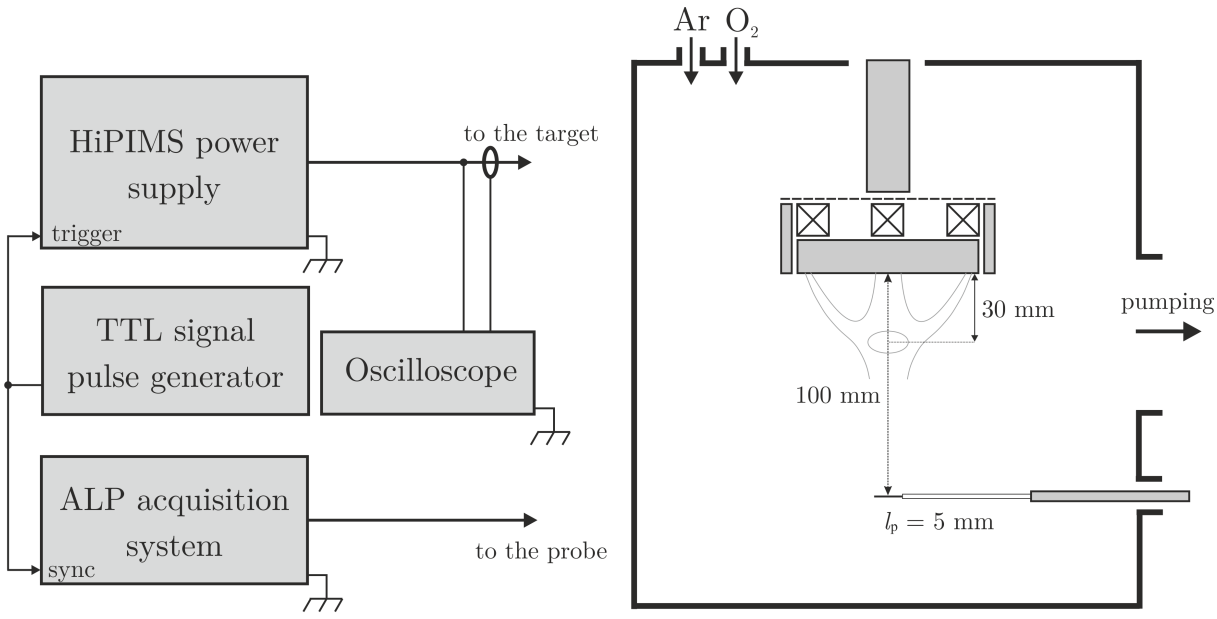

Figure 6.1. Schematic representation of the experimental set-up. The Langmuir probe was placed on the discharge axis at an axial distance 100 mm away from the target and controlled by the Impedans ALP acquisition system. The position of the magnetic null is also displayed at an axial distance of 30 mm from the target surface.

Argon (purity 99.995%) and oxygen (purity 99.9995%) gases were fed into the chamber through two independent mass flow controllers (MKS 1179A) while the total process gas pressure, $p_{\text{total}} = p_{\text{Ar}} + p_{\text{O}_2}$ (where p_{Ar} and p_{O_2} are the partial pressures of argon and oxygen respectively), was monitored using a capacitance manometer (MKS 628A) and kept constant at 0.93 Pa. A higher pressure was used here than in chapter 5 as no pre-ionizer was used to allow for stable, reproducible operation at lower working pressures. For discharges containing oxygen, the oxygen gas was introduced into the chamber at a sufficiently high flow rate such that the discharge transitioned into 'poisoned' mode, at which point the oxygen flow rate was then reduced in order to achieve the desired partial pressure. Here, four oxygen partial pressures were investigated; $p_{\text{O}_2}/p_{\text{total}} = 0.0$, 0.1, 0.3 and 0.5.

For this investigation, a constant $\overline{P_{\text{d}}} = 100$ W was maintained throughout. The discharge current-voltage-time waveforms for the tested conditions are presented in figure 6.2. The metallic mode (i.e. $p_{\text{O}_2}/p_{\text{total}} = 0.0$) current-voltage-time waveform differs significantly from that of the oxygen containing discharges, displaying a discharge current peak much earlier in the pulse and a higher absolute applied target potential throughout the pulse, resulting in a lower average current for a constant average discharge power. However, all discharges containing oxygen were operated in the 'poisoned' mode and held at the same pressure, hence those waveforms do not differ from one another significantly.

A cylindrical Langmuir probe was positioned 100 mm above the target surface at the centre of the discharge in a region of low magnetic flux density ($B < 10$ G). The probe was constructed using a 100 μm diameter tungsten wire fed through an alumina stem, leaving an exposed probe length of $l_{\text{p}} = 5$ mm. Time-resolved I-V characteristics were obtained using a commercial acquisition system (ALP, Impedans Ltd.) equipped with an internal delay generator, which was synchronized using the same pulse generator used to trigger the HiPIMS power supply, such that $t = 0$ was defined as the on-set of the HiPIMS voltage pulse. Two different time steps were used, $\Delta t = 10$ μs and 100 μs, for two different time ranges $t = 0$ μs to 500 μs and $t = 500$ μs to 3000 μs, respectively. The probe bias, V_{b}, was varied from -150 V to $+30$ V in steps of 0.05 V and the current resolution of the acquisition system was 4.5 nA. Each data point of the I-V characteristic was measured 50 times and the averages were recorded. In between data acquisition runs, a potential of -150 V was applied to the probe tip in order to sputter clean depositions from its surface.

6.2.2 Set-up for laser-aided photodetachment measurements

The principles of laser photodetachment are discussed in §4.2.3. The experimental set-up used here is shown schematically in figure 6.3 and is similar to that used in [120,137,141]. A 10 litre Al vacuum chamber was mounted with a 150 mm diameter circular planar

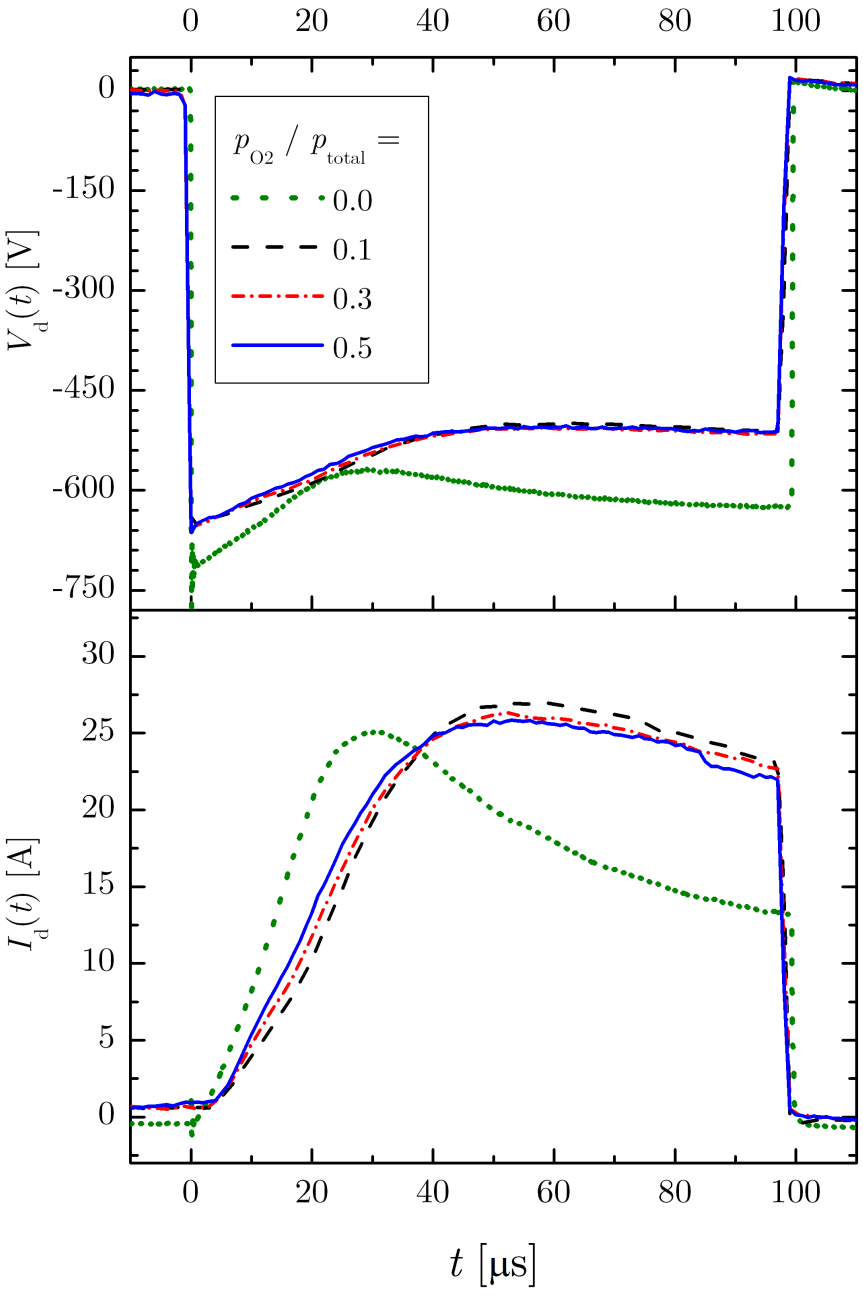

Figure 6.2. The voltage-current-time waveforms for the investigated HiPIMS discharge conditions: p_{O_2}/p_{total} = 0.0 (dot), 0.1 (dash), 0.3 (dash-dot) and 0.5 (solid). The pulse parameters were kept constant at τ = 100 μs, f = 100 Hz and $\overline{P_d}$ = 100 W.

magnetron source (GENCOA Ltd.) possessing an unbalanced magnetic field configuration and equipped with a Ti target (purity 99.995%). A base pressure of 10^{-4} Pa was achieved via the use of a turbomolecular pump (Pfeiffer, TMU 071P) back by a two-stage rotary pump (Edwards, E2M40). The target was powered by using an in-house built HiPIMS power supply capable of applying a voltage of 1.2 kV and sustaining a peak cur-

rent of up to 1.5 kA. A detailed description of this power supply is given by Liebig [163]. The HiPIMS power unit was externally triggered using a TTL digital pulse generator (Stanford Research Systems, DG645), maintaining a constant pulse width of 100 μs and a repetition rate of 100 Hz. The temporal evolution of the discharge voltage, $V_{\mathrm{d}}(t)$, and discharge current, $I_{\mathrm{d}}(t)$, were monitored using a high-voltage probe (Tektronix P5100) and a Pearson® current monitor (Model 3972) connected to a digital phosphor oscilloscope (Tektronix DPO3034). A constant $\overline{P_{\mathrm{d}}} = 200$ W was maintained throughout the photodetachment investigation.

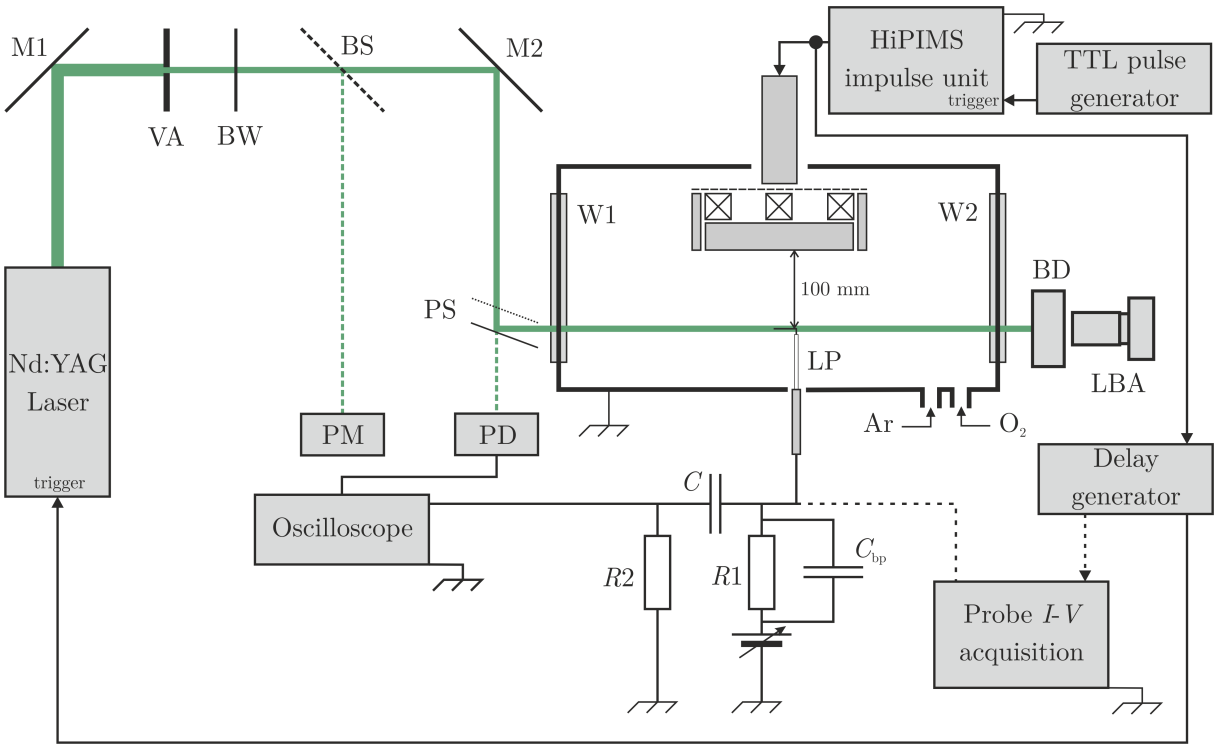

Figure 6.3. Schematic representation of the laser-aided photodetachment experimental set-up. Labelled components are explained in the text.

Research grade ($> 99.99\%$ purity) process gases (Ar and O_2) were fed in through two independent MFCs (MKS, 1179A) with the overall chamber pressure monitored using a capacitance manometer (MKS Baratron® 627). The two MFCs and manometer were operated via a MKS type 146 vacuum gauge measurement and control system. The overall pressure, p_{total}, was maintained at a constant 0.93 Pa with three oxygen partial pressures being investigated, where $p_{\mathrm{O_2}}/p_{\mathrm{total}} = 0.1$, 0.3 and 0.5.

The laser used to photodetach electrons from negative ions was a pulsed Q-switched Nd:YAG (Quantel Brilliant B) fitted with a frequency doubling module to produce light at a wavelength of 532 nm and an attenuation module to vary the power output of the laser. The laser pulse frequency was 10 Hz with a pulse width of $5 - 6$ ns, a beam divergence of 0.5 mrad and a maximum pulse energy of 450 mJ. From equation 4.16, to ensure $\Delta n_{-}/n_{-} \rightarrow 1$, a laser energy density of 300 $\pm$ 20 mJ cm^{-2} was used.

The laser beam was directed by a dichoric mirror (M1, figure 6.3) through a variable aperture (VA), which could be used to control the laser beam diameter. A 200 μm blocking wire (BW) was used to prevent direct interaction of the laser beam with the electrostatic probe, as discussed in §4.2.3.1. A beam splitter (BS) directed a known fraction of the laser beam to a power meter (PM, Gentec-EO Solo 2) calibrated with a correction factor to display the beam power at the position of the probe. After being directed to a periscope arrangement (PS) by a second dichoric mirror (M2) a small fraction of the beam was directed to a high-speed photodetector (PD) with a 1 ns rise time which was connected to the oscilloscope in order to monitor the timing of the laser pulse. The laser beam entered the chamber through window 1 (W1) and exited through window 2 (W2) before hitting the beam dump (BD) or laser beam analyser (LBA, USBeamPro Photon Inc. CMOS profiler). The laser beam, blocking wire and probe alignment were all performed with the laser operating at reduced power such that the laser beam analyser could be used without damaging the detector. During high-power operation, the beam dump was placed in-front of the laser beam analyser.

The electrostatic probe was located at a distance of 100 mm from the target surface along the discharge centreline and positioned such that the long-extension of the 'L'-shaped probe tip (long extension, 5 mm; short extension, 1 mm) was parallel with the beam. The probe tip was constructed from 100μm diameter tungsten wire fitted with a co-axial arrangement of two ceramic tubes, the outermost serving as a support and the inner tube acting to prevent contact between the probe tip and outer ceramic tube. The ceramic tube arrangement is identical to the one presented in figure 4.9 without the extension tube, T2. To minimize contamination of the probe surface, the probe tip was biased with a potential of -150 V for 60 s in order to sputter clean the surface before each experimental run. To collect photodetached electrons, the probe was operated in the electron saturation region and a probe bias $V_\mathrm{b} = \Phi + 25$ V was used. Φ was determined from the I-V characteristics obtained using the Langmuir probe I-V acquisition system (Impedans, ALP).

Photodetachment signals detected by the probe were obtained via a detection circuit consisting of a variable DC power supply attached to the probe and connected in series through a resistor ($R1 = 4.7\ \mathrm{k\Omega}$). A band-pass capacitor ($C_\mathrm{bp} = 1000\ \mu\mathrm{F}$) was used to allow the photoelectron current to bypass the power supply. A time-varying voltage across a second resistor ($R2 = 49\ \Omega$) was induced by the transient photoelectron current, which was measured by a voltage probe (Tektronix P6139A) and monitored using the oscilloscope. A second capacitor ($C = 33$ pF) was used to decouple the transient voltage induced by the photodetachment signal from the constant voltage provided by the power supply. The photodetachment current, I_pd, was obtained by dividing the measured voltage by $R2$. Optimization of the detection circuit is described by Bryant and Bradley [164]. To improve the signal-to-noise ratio, the transient voltage signals were averaged over 128

pulses. To monitor negative ion density at different times during the HiPIMS pulse, three different time steps were used, $\Delta t = 20$ μs, 100 μs and 1000 μs, for three different time ranges $t = 20$ μs to 200 μs, $t = 200$ μs to 500 μs and $t = 1000$ μs to 5000 μs, respectively.

6.3 Results and discussion

6.3.1 Langmuir probe

6.3.1.1 Electron density

The temporal evolutions of the electron density for the three different Ar/O_2 discharges and an Ar-only discharge are shown in figure 6.4. Density values were obtained from measured values of the electron saturation current and calculated using $I_{e,sat} = n_e A_p e \left(k_B T_e / 2\pi m_e\right)^{1/2}$ where A_p is the surface area of the probe and the electron temperature, T_e, was found assuming a Maxwellian distribution and taking the inverse gradient of a linear fit to the transition region of the $\ln(I_e)$-V_b characteristic, as in [137]. $I_{e,sat}$ was taken to be equal to the probe current at the plasma potential, Φ, which itself was found at the point of intersection between two linear fits applied to the transition and electron saturation region (as illustrated in figure 4.8).

During the on-time, the electron density is observed to follow the discharge current, $I_d(t)$. The O_2 partial pressure appeared to have little influence on the peak electron density: $n_{e-peak} = 1.9$, 1.6, 1.5 and 1.4×10^{17} m^{-3} for $p_{O_2}/p_{total} = 0.0$, 0.1, 0.3 and 0.5, respectively. However, the decay times do appear to be heavily dependent upon the O_2 partial pressure. There are three distinct decays in electron density observed; the initial decay occurs within the first $100 - 200$ μs following the termination of the pulse, the second decay occurs between $t = 300$ μs and 900 μs and a final decay phase is observed beyond $t = 1000$ μs. The characteristic decay times for the three phases are listed in table 6.1. In general, the characteristic decay times of electron density are observed to decrease for increasing oxygen partial pressure. This is especially evident during the second decay phase, where $\tau_{n2} = 550$ μs, 326 μs, 293 μs and 92 μs for increasing p_{O_2}/p_{total}, possibly suggesting that more electrons are lost via dissociative attachment processes for greater oxygen availability. These results are consistent with the relationship between the characteristic decay times for n_e and increasing oxygen partial pressure as presented in [137]. The final decay phase extending beyond 1 ms is characteristic of high-current, low duty cycle discharges and has been observed by several authors in HiPIMS discharges [76,81,165]. It has been speculated that the long plasma density decay times in HiPIMS are due to long-lived argon metastables undergoing de-excitation collisions with electrons in the plasma afterglow [78, 166].

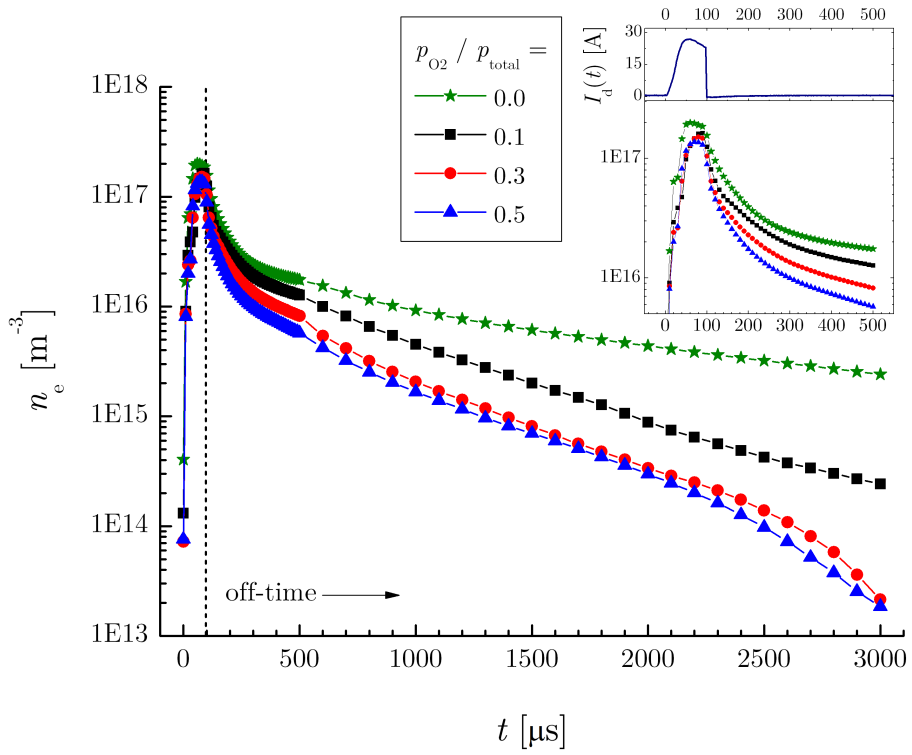

Figure 6.4. The temporal evolution of the electron density, n_e, for the four different oxygen partial pressures investigated. The inset displays a magnified plot of the temporal variation of n_e for $t = 0 - 500\,\mu$s along with the discharge current, $I_d(t)$, as measured whilst operating in the 'poisoned' mode for reference.

p_{O_2}/p_{total}	Initial decay time, τ_{n1} (μs)	Second decay time, τ_{n2} (μs)	Third decay time τ_{n3} (μs)
0.0	32	550	1050
0.1	22	326	603
0.3	18	293	551
0.5	17	92	611

Table 6.1. The characteristic decay times for the three decay phases of the electron density for different oxygen partial pressures.

6.3.1.2 Electron temperature

Plots of the temporal evolution of the electron temperature for the four different oxygen partial pressures are shown in figure 6.5. Examination of the ln (I_e)-V_b characteristic used to obtain a temperature measurement reveals distributions that are indistinguishable from a Maxwellian distribution. The peak electron temperature occurs at the start of the active phase ($t = 1 - 10$ μs) and is found to be higher for lower oxygen content; $T_{e-peak} = 35.2$ eV, 33.2 eV, 20.5 eV and 19 eV for increasing O_2 content. High effective electron temperatures measured at the on-set of the pulse have also been reported by Poolcharuansin and Bradley in the same experimental set-up [76], where the authors

observed a 'super-thermal' electron population in the first 4 μs of the voltage pulse. It was conjectured by the authors that the remnant electrons from a previous pulse are accelerated by the rapidly expanding cathode sheath during the initial phase of the pulse on-time. T_e is observed to decrease during the intermediate stages of the on-time. This quenching of the electron temperature during the on-phase has been reported previously in HiPIMS [81,150] as well as being observed in chapter 5. Towards the end of the active phase (see figure 4 inset), T_e increases to approximately 2 eV for the Ar-only case, 0.9 eV for $p_{O_2}/p_{total} = 0.1$ and 0.3 and to 1.7 eV for $p_{O_2}/p_{total} = 0.5$. This increase can be explained by the on-set of neutral gas rarefaction due to intense sputtering during the initial active phase ($t < 50$ μs). The local gas density reduction requires a higher electron-impact ionization rate constant to balance electron generation and therefore results in a higher electron temperature. It has also been suggested that the drop in T_e could be due to the more efficient coupling of electron energy to metal vapour as it displaces the process gas during intense sputtering, as shown in [65].

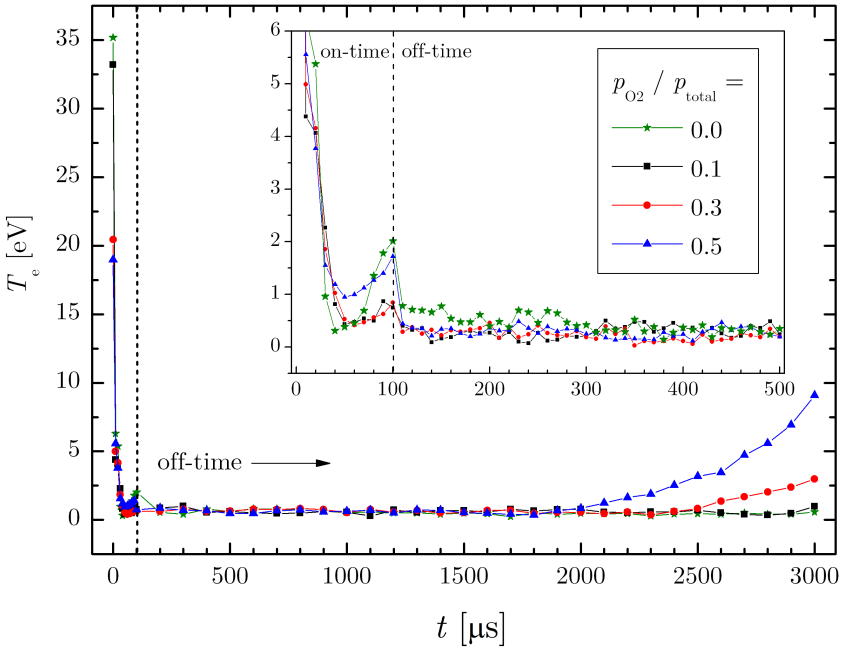

Figure 6.5. The temporal evolution of the electron temperature, T_e, for the four different oxygen partial pressures. The inset displays a magnified plot of the temporal evolution of T_e for the time period $t = 0$ to 500 μs. The rise in T_e at $t > 2000$ μs may be non-physical and caused by distortion of the Langmuir probe I-V characteristics measured in the late afterglow.

In the afterglow, T_e is observed to have a two-fold decay with an initially rapid decay to approximately 0.5 eV and a second, longer decay with T_e dropping to ~ 0.3 eV at $t = 1$ ms. However, as observed by other authors [99,137], the electron temperature begins to

rise in the extended afterglow when oxygen is present, and in this case, above 1 eV after 2 ms, even up to 9 eV for the case of $p_{O_2}/p_{total} = 0.5$ at $t = 3$ ms. This unexpected behaviour could be due to the uncertainty associated with measuring small values of T_e when using Langmuir probe I-V analyses. It was suggested in [137], that super-elastic collisions between electrons and excited argon and metastable oxygen molecules could induce electron heating in the afterglow. Another possible explanation is that a shift to higher effective electron temperatures is caused by electrons favourably undergoing attachment to oxygen atoms and molecules as they thermalize [167, 168] leaving proportionally more higher energy electrons in the population. This may lead to a higher effective electron temperature as detected by the probe. However, in the late afterglow, as the plasma degrades into an ion-ion state (i.e. when $n_- \sim n_i$) with an almost complete absence of electrons and the wall sheaths collapse it is very unlikely that a significant amount of high energy electrons would still be confined within the plasma. Although relatively high energy electrons can be generated via detachment reactions such as $O^- + O \rightarrow O_2 + e^-$ which liberates a 3.6 eV electron [169], this still does not account for the measured high values of T_e. Therefore it is assumed that the rise in T_e during the late afterglow is an artefact of the measurement technique and analysis when applied to plasma discharges possessing very low electron temperatures, rather than a physical mechanism. For higher T_e, the transition region is much more apparent in the I-V curve and electron temperature values can be readily extracted, such that similar inaccuracies are not present in the values of T_e obtained during the on-phase and early afterglow. To better understand the electron temperature variation in reactive HiPIMS, particularly in the extended afterglow, further investigation is certainly warranted.

6.3.1.3 Electronegativity and negative ion density

During the on-phase, the discharge is expected to be weakly electronegative (i.e. $\alpha < 1$) as shown in [137] and so a Langmuir probe is not suitable for measuring α under such conditions due to large relative errors in current readings. However, as will be shown below, the electronegativity increases in the extended off-phase (i.e. $\alpha > 1$) and associated errors in the probe technique have a smaller relative effect such that it is possible to determine a value for α from the measured electron-to-ion saturation current ratio, $I_{e,sat}/I_i$, as discussed in §4.2.1.1. For particular values of of α and γ, where $\gamma = T_e/T_-$, as discussed by Sheridan *et al.* [102], it is possible to determine an expected value for the positive ion current, I_i, exiting the plasma through the sheath surrounding the probe in an electronegative discharge using equation 4.12, reproduced here:

$$I_i = n_{e0} c_s A_p e \gamma^{-1/2} \left[\left(\frac{1}{2} \right)^{1/\gamma} + \frac{\alpha}{2} \right] \quad \text{for } \alpha > 1 \tag{6.1}$$

where n_e is the electron density far away from the sheath edge, $c_s = (k_B T_e/M_i)^{1/2}$ is the electropositive ion acoustic speed, $\gamma = T_e/T_-$ and $\alpha = n_-/n_e$ is the electronegativity of the discharge. For the value of M_i, as in §5.2, the proportions of the constituent positive ions were estimated by means of energy-resolved mass spectrometry. In this case, the calculated ion fractions were 0.57, 0.28, 0.12 and 0.03 for Ar^+, O_2^+, O^+ and Ti^+, respectively, giving an average positive ion mass, $\overline{M_i} \approx 35$ amu. Equation 6.1 is valid for planar surfaces as well as long cylindrical probes (i.e. for $r_p/s_p < 1$ where s_p is the probe sheath width) [102, 137]. Using equation 4.9, the probe sheath width when operating in the saturation regions is $\sim 10 - 20\lambda_D$. For the case of $T_e = 1$ eV and $n_e = 1 \times 10^{17}$ m^{-3}, $\lambda_D \sim 24\ \mu$m, giving $s_p \sim 240 - 480\ \mu$m $> r_p = 50\ \mu$m, thereby fulfilling the long cylinder approximation. Ignoring the small contribution to the current from negative ions and the thermal positive ion flux, the electron saturation current measured at the plasma potential Φ can be given by $I_{e,sat} = n_e A_p e\,(k_B T_e/2\pi m_e)^{1/2}$. The contribution to the current from negative ions, assuming they follow the Boltzmann relation, is given as $I_- = n_- A_p e\,(k_B T_-/2\pi M_-)^{1/2}$ where M_- is the negative oxygen ion mass (i.e. $M_- = M_{O^-} = 16$ amu, as O^- is the dominant negative ion [141]). However, this is only significant for very high negative ion densities and only approaches the value of $I_{e,sat}$ when $n_- \sim 2000 n_e$. Neglecting the negative ion contribution to the positive probe current and using equation 6.1, the ratio of the electron-to-ion saturation currents can be written as;

$$\frac{I_{e,sat}}{I_{i,sat}} = \left(\frac{2\pi m_e}{M_i}\right)^{-1/2} \left\{\frac{1}{\sqrt{\gamma}}\left[\left(\frac{1}{2}\right)^{1/\gamma} + \frac{\alpha}{2}\right]\right\}^{-1} \tag{6.2}$$

Therefore, in principle a measure of $I_{e,sat}/I_{i,sat}$ could be used to determine α provided that a value for γ is known, or estimated, in a similar manner as presented in [136] and [137]. In this investigation, a value of $\gamma = 10$ was assumed for the extended off-phase, since that $T_e \approx 0.3 - 0.5$ eV ($\approx 3500 - 6000$ K) as seen in figure 6.5 and the negative ion temperature is taken to be close to the background gas temperature: $T_- \approx T_{gas} \sim 300 - 800$ K [170]. Figure 6.6 shows the electron-to-ion saturation current ratio plotted as a function of time and normalized with respect to the electron-to-ion saturation current ratio as measured in the Ar-only discharge, which, using equation 6.2, can be written as:

$$\left[(I_{e,sat}/I_{i,sat})_{Ar/O_2} \,/\, (I_{e,sat}/I_{i,sat})_{Ar}\right] = \left(\frac{\overline{M_i}}{M_{Ar}}\right)^{1/2} \left\{\frac{1}{\sqrt{\gamma}}\left[\left(\frac{1}{2}\right)^{1/\gamma} + \frac{\alpha}{2}\right]\right\}^{-1} \sim \left\{\frac{1}{\sqrt{\gamma}}\left[\left(\frac{1}{2}\right)^{1/\gamma} + \frac{\alpha}{2}\right]\right\}^{-1} \tag{6.3}$$

where $I_{i,sat} = 0.5 n_{e0} c_s A_p e$ for $\alpha \to 0$ [102] and the ion mass dependence is approximated to unity (i.e. $\overline{M_i} \approx M_{Ar}$). This is justified as $\overline{M_i}$ for the Ar/O_2 gas mixture was found, by mass spectrometry, to be 35.2 amu, hence $\left(\overline{M_i}/M_{Ar}\right) \sim 0.94$.

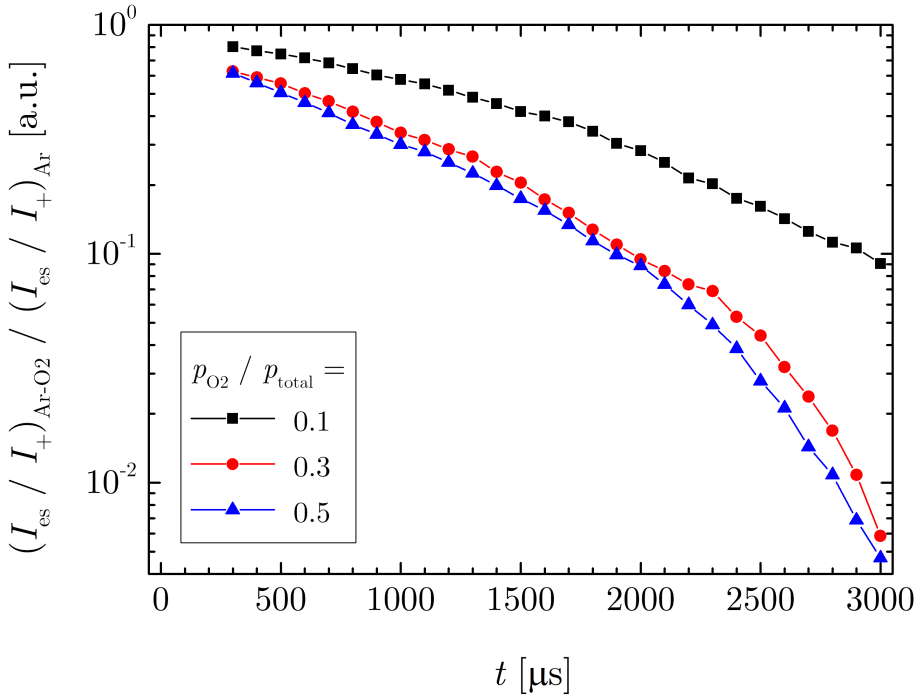

Figure 6.6. A semi-log plot of the temporal evolution of the electron-to-ion saturation current ratio normalized to a nominally identical, electropositive (Ar-only) discharge.

In magnetized discharges, electron saturation currents are generally reduced due to the slow cross-field transport of magnetized electrons, however, ions are not similarly affected due to their much larger gyroradii ($r_{gi} \sim 0.45$ m for $B \sim 10$ G, value determined from magnetic mapping - see figure 4.2). This often results in observed lower electron densities compared with ion densities as calculated using the electron and ion saturation currents measured by the probe, even though the plasma is considered quasi-neutral. For example, the absolute ion saturation current for $p_{O_2}/p_{total} = 0.0$ at $t = 80$ μs was 0.494 mA and the electron saturation current for the same condition was measured as 46.7 mA giving the measured electron-to-ion saturation current ratio as ~ 95, compared with the expected ratio, $I_{e,sat}/I_{i,sat} \sim 108$. By normalizing the current ratios to an electropositive condition ($\alpha \to 0$), any differences between electron and ion saturation currents caused by the magnetic field, or other effects, can be eliminated. By comparing the values in figure 6.6 with the values of the normalized electron-to-ion saturation current ratio as predicted by the fluid model (see equation 6.3), it is possible to obtain corresponding values of α (see figure 6.7).

Using this method, the time evolution of electronegativity in the extended off-time was determined and the results are presented in figure 6.8. From figure 6.8, the electronegativity of the discharge is observed to increase with time in the off-phase for all oxygen partial pressures. Furthermore, for increasing oxygen content, α is greater for all times

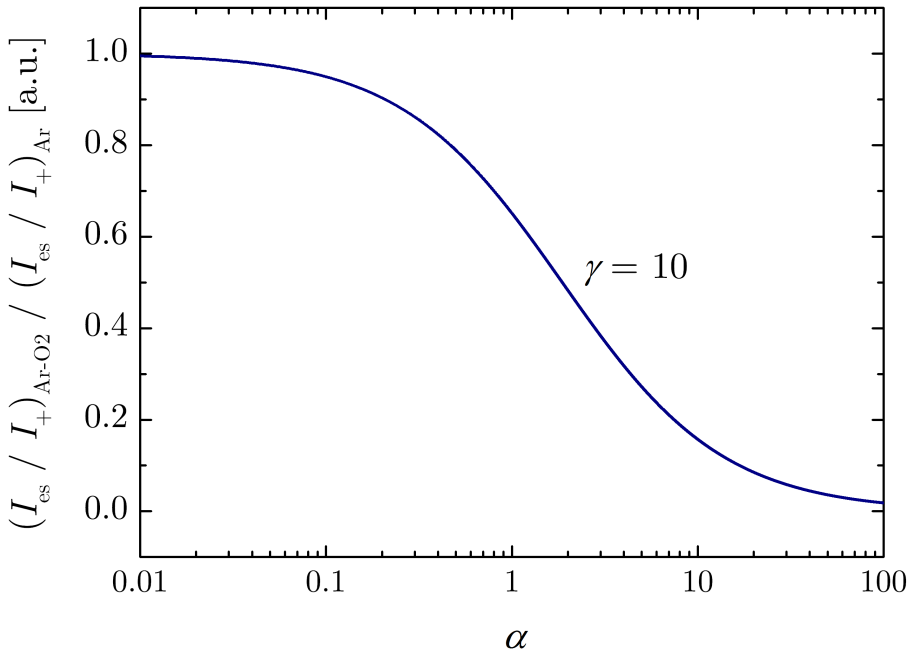

Figure 6.7. A plot of the normalized electron-to-ion saturation current ratio as a function of electronegativity, α, with $\gamma = T_e/T_- = 10$, according to the fluid model presented in [102] and equation 6.1.

beyond $t = 300$ μs and increases at a faster rate beyond $t = 2$ ms. The initial rise in α is approximately exponential (linear on semi-log plot) and increases for greater oxygen content. In the latter part of the off-phase (i.e. $t > 2$ ms), α is found to be very high, reaching peak values of $\alpha = 19$ (± 3), 316 (± 47) and 396 (± 59) for $p_{O_2}/p_{total} = 0.1$, 0.3 and 0.5, respectively. Particularly for 30% and 50% oxygen content discharges, the late afterglow appears to have degraded into an ion-ion state with a very low electron density.

This increase of electronegativity in the afterglow is well known for various plasma discharges containing electronegative gases including pulsed DC magnetron sputter deposition discharges in oxygen [137], multi-cusp hydrogen discharges [171], electron cyclotron resonance discharges [172] and pulsed-power chlorine inductively coupled plasma discharges [173].

From the values of α (figure 6.8) and the corresponding values of n_e (figure 3), it is straightforward to ascertain negative ion density values from $n_- = \alpha n_e$. The calculated values of n_- for all three oxygen partial pressures are shown as a function of time in figure 6.9. Results for $t < 120$ μs are discounted due to the large relative errors associated with the probe technique for small α, which would propagate through the calculations of n_-, leading to large uncertainties in both negative ion densities and values for electronegativity. Errors in α and n_- are estimated to be $\pm 15\%$ and $\pm 20\%$ respectively, by assuming an error of $\pm 15\%$ in γ and a $\pm 10\%$ error in n_e and calculating the subsequent propagation

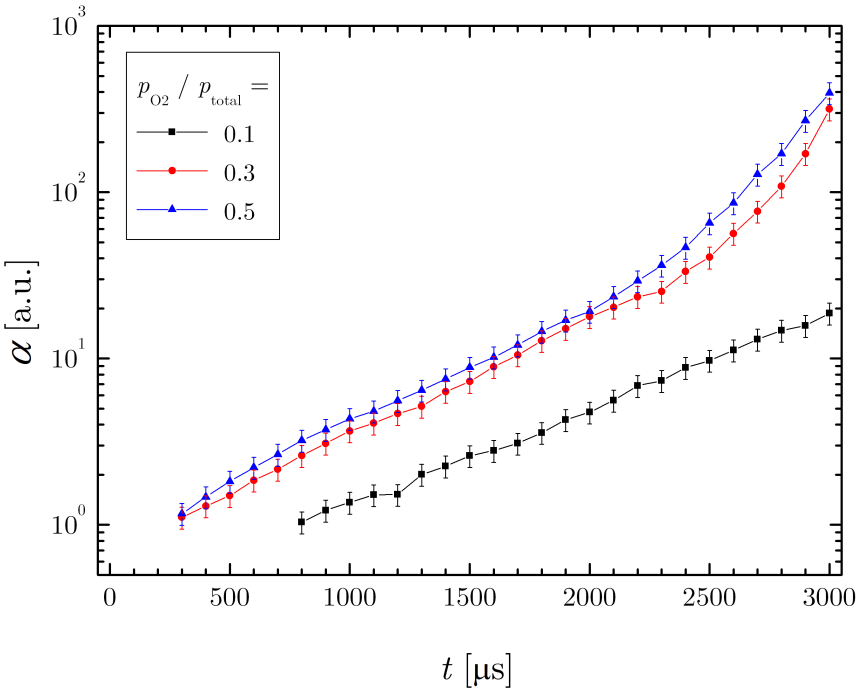

Figure 6.8. The temporal evolution of the electronegativity, $\alpha = n_-/n_e$, as measured for the three different oxygen partial pressures. Values of $\alpha < 1$ during the active phase and immediate afterglow are discounted as the analysis presented here is only valid for $\alpha > 1$. Error bars represent an uncertainty of approximately ±15%.

of uncertainty. The absolute negative ion density, n_-, is observed to decrease with time in the afterglow until $t \sim 1$ ms, where n_- appears to plateau at a value of approximately 5×10^{15} m^{-3} and even rise slightly for the cases of $p_{O_2}/p_{total} = 0.3$ and 0.5.

6.3.2 Simple plasma-chemical model

Here, a simple zero-dimensional plasma-chemical model (see §3.2.1.1) is used to analyse the results in the context of important volumetric chemical reactions and losses to the chamber walls.

6.3.2.1 Losses to walls

In the on-time, the discharge is sustained by the emission of secondary electrons from the cathode which subsequently facilitate electron impact ionization of background gas atoms, particularly in the region close to the target in a magnetron discharge. For this reason, the electron density generally follows the discharge power during the on-phase, which has been shown in an ionization region model developed for HiPIMS by Raadu *et al.* [174]. However, in the discharge afterglow, n_e decreases as electrons are lost primarily through

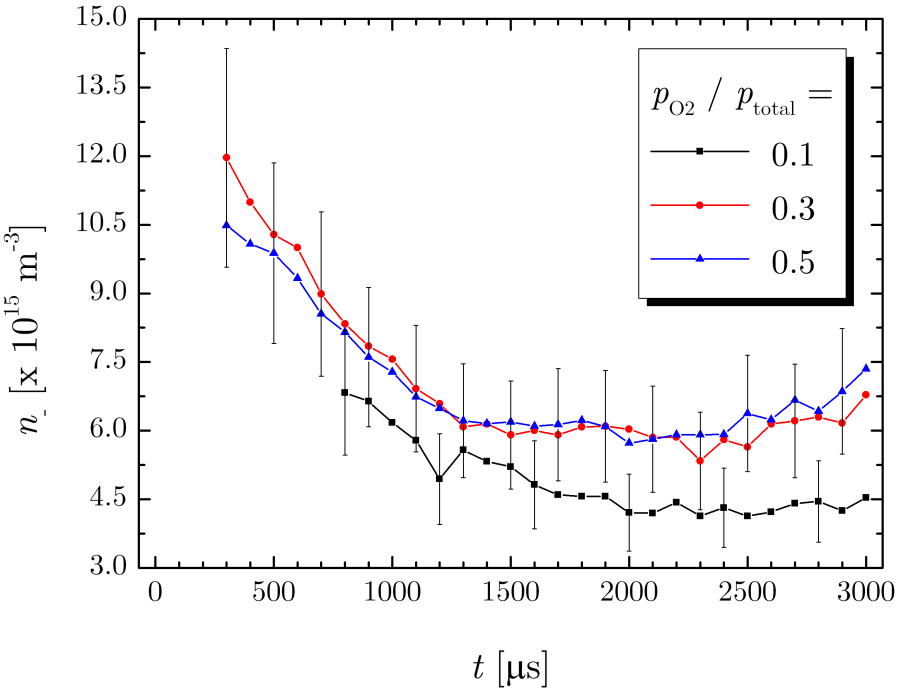

Figure 6.9. The temporal evolution of the oxygen negative ion density, n_-, as calculated from estimated values of α and measured values of n_e. Values corresponding to $\alpha < 1$ are discounted as the analysis presented here is only valid for $\alpha > 1$. Error bars represent an uncertainty of ±20% and are displayed for only one in every four data points to avoid clutter.

diffusive transport to the walls (for low pressure discharges) and via volume electron-ion recombination reactions.

In the presence of oxygen, negative ion formation is an additional channel contributing to electron loss. During the on-phase, it is thought that the primary mechanism for negative ion formation is dissociative electron attachment to oxygen molecules ($O_2 + e^- \rightarrow O^- + O$), which has a threshold energy of ~ 4.5 eV and an optimum cross section at $T_e \approx 6.8$ eV [175]. In the afterglow, T_e drops sharply and dissociative electron attachment to the ground state $O_2\,(X\,^3\Sigma_g)$ becomes negligible, however, electron attachment reactions with metastable oxygen molecules $O_2\,(A\,^3\Sigma_u^+,\ C\,^3\Delta_u,\ c\,^1\Sigma_u^-)$ may become important. Although not observed in this study due to the uncertainties associated with the probe technique, an increased negative ion density in the afterglow has been observed by other authors [171–173, 175] and has been attributed to a decrease in detachment reactions induced by electron-impact and a concurrent increase in negative ion formation via dissociative attachment to highly excited metastable oxygen molecules [137] and high Rydberg states [99]. In particular, dissociative attachment to metastable oxygen $O_2\,(A\,^3\Sigma_u^+,\ C\,^3\Delta_u,\ c\,^1\Sigma_u^-)$ may be an important reaction in the afterglow due to its increased rate coefficient, k_{at}^M, for decreasing T_e [98, 176].

In order to quantitatively evaluate the observed differences in electronegativity for different oxygen content in the HiPIMS discharge afterglow, the principal reaction routes involving the formation and destruction of metastable oxygen molecules and oxygen negative ions are considered. The reaction set involving metastable oxygen $O_2\,(A\,^3\Sigma_u^+,\ C\,^3\Delta_u,\ c\,^1\Sigma_u^-)$ are listed in table 6.2 and reactions involving atomic oxygen negative ions (O^-) are listed in table 6.3. For simplicity, metastable oxygen $O_2\,(A\,^3\Sigma_u^+,\ C\,^3\Delta_u,\ c\,^1\Sigma_u^-)$ will from here on in be denoted as O_2^M. O^- ions are considered to be the dominant negative ion species (i.e. $n_- \approx n_{O^-}$) while O_2^- and O_3^- densities are significantly smaller in comparison [158, 176] and are therefore not considered in this simple treatment. Another aspect to consider is the loss of O_2^M via diffusion and O^- via ambipolar diffusion to the chamber walls with rate coefficients $1/\tau_L$ and $1/\tau_{AD}$, respectively. Following [176], the effective rate coefficient of neutral metastable oxygen molecules interacting with the chamber walls, for a chamber with length L and radius R, is

$$\tau_- = \frac{\Lambda_0^2}{D_{O_2^M}} + \frac{2V\left(2-\gamma_{O_2^M}\right)}{Av_{O_2^M}}\gamma_{O_2^M}\ \text{sec} \tag{6.4}$$

where Λ_0 is the characteristic diffusion length;

$$\Lambda_0 = \left[\left(\frac{\pi}{L}\right)^2 + \left(\frac{2.405}{R}\right)^2,\right]^{-1/2} \tag{6.5}$$

$D_{O_2^M}$ is the neutral diffusion coefficient given by

$$D_{O_2^M} = \frac{eT_{gas}\lambda_i}{v_{O_2^M}M_{O_2^M}} \tag{6.6}$$

where $v_{O_2^M} = \left(8k_BT_{gas}/\pi M_{O_2^M}\right)^{1/2}$ is the neutral particle thermal speed, λ_i is the mean free path and $\gamma_{O_2^M} = 0.007$ [176] is the sticking coefficient for the neutral particle on the surface of the wall. The time constant for diffusive wall losses, τ_L, can be calculated by estimating values for the parameters on the RHS of equation 6.4. Λ_0 is calculated by assuming a diffuse plasma fills the chamber, hence $L = 0.3$ m and $R = 0.13$ m. $D_{O_2^M}$ is estimated for the three different partial pressures of oxygen using $\lambda_i^{-1} = (n_{Ar}\sigma_{Ar} + n_{O_2}\sigma_{O_2})$, where the collisional cross sections are $\sigma_{Ar} = 1.0\times10^{-18}$ m^2 [176] and $\sigma_{O_2} = 7.5\times10^{-19}$ m^2 [177] and the density of neutral gases are calculated from measured partial pressures, assuming ideal gas behaviour and a negligible ionization fraction. Using equations 6.4, 6.5 and 6.6, characteristic diffusive loss times of O_2^M are estimated to be $\tau_L \approx 49$ ms, 46 ms and 44 ms for increasing p_{O_2}/p_{total}. Since $\tau_L > t_{off}$, losses of O_2^M to the chamber walls during the plasma afterglow are neglected.

Reaction	Rate coefficient ($m^3\ s^{-1}$)	Reference
$e^- + O_2 \rightarrow O_2^M + e^-$	$k_{ex} = 1.13 \times 10^{-15} \exp(-3.94/T_e)$	[176]
$e^- + O_2^M \rightarrow O + O^-$	$k_{at}^M = 7.32 \times 10^{-16} T_e^{-1.072} \exp(-0.468/T_e)$	[176]
$e^- + O_2^M \rightarrow O + O + e^-$	$k_{diss} = 6.86 \times 10^{-15} \exp(-1.79/T_e)$	[176]
$e^- + O_2^M \rightarrow O + O(^1D) + e^-$	$k_{diss}^{1D} = 3.49 \times 10^{-14} \exp(-1.42/T_e)$	[176]
$O_2 + O_2^M \rightarrow 2O_2(b\,^1\Sigma_g^+)$	$k_{cr1} = 2.90 \times 10^{-19}$	[176]
$O_2 + O_2^M \rightarrow 2O_2$	$k_{cr2} = 2.80 \times 10^{-17}$	[175]
$Ar + O_2^M \rightarrow O_2(b\,^1\Sigma_g^+) + Ar$	$k_{Ar} = 8.60 \times 10^{-22}$	[178]

Table 6.2. List of plasma-chemical reactions involving metastable oxygen $O_2(A\,^3\Sigma_u^+, C\,^3\Delta_u, c\,^1\Sigma_u^-)$, denoted by O_2^M.

Reaction	Rate coefficient ($m^3\ s^{-1}$)	Reference
$e^- + O_2^M \rightarrow O + O^-$	$k_{at}^M = 7.32 \times 10^{-16} T_e^{-1.072} \exp(-0.468/T_e)$	[176]
$e^- + O^- \rightarrow O + 2e^-$	$k_{ed} = 5.47 \times 10^{-14} T_e^{0.22} \exp(-12.62/T_e)$	[176]
$O_2^+ + O^- \rightarrow O_2 + O$	$k_{mn1}^{O_2^+} = 2.0 \times 10^{-13} (300/T_{gas})^{-0.5}$	[179]
$O_2^+ + O^- \rightarrow 3O$	$k_{mn2}^{O_2^+} = 2.6 \times 10^{-14} (300/T_{gas})^{0.44}$	[176]
$O^+ + O^- \rightarrow 2O$	$k_{mn}^{O^+} = 2.0 \times 10^{-13} (300/T_{gas})^{-1}$	[179]
$O + O^- \rightarrow O_2 + e^-$	$k_{ad} = 1.40 \times 10^{-16}$	[176]
$Ar^+ + O^- \rightarrow O + Ar$	$k_{mn}^{Ar^+} = 1.40 \times 10^{-13}$	[98]

Table 6.3. List of plasma-chemical reactions involving atomic oxygen negative ions, O^-.

6.3.2.2 Volumetric reactions

In a HiPIMS discharge, the electron density is still significant long into the afterglow, for example $n_e \approx 3 \times 10^{14}$ m^{-3} at $t = 3$ ms for $p_{O_2}/p_{total} = 0.1$. Hence, negative ions generated in the plasma volume are generally confined by the potentials contained in the sheaths at the chamber walls during this time and therefore ambipolar diffusion of O^- to the walls can also be neglected for this case. Only when the plasma degrades into an ion-ion state does the electric field change significantly, allowing negative ions to be transported to the walls [180]. Neglecting wall losses and using the reaction sets listed in table 6.2 and 6.3, balance equations governing the rate of change of O_2^M and O^- in the discharge can be written as

$$\frac{dn_{O_2}^M}{dt} = k_{ex} n_e n_{O_2} - n_{O_2^M} \left(k_{at}^M n_e + k_{diss} n_e + k_{diss}^{1D} n_e + k_{cr1} n_{O_2} + k_{cr2} n_{O_2} + k_{Ar} n_{Ar} \right) \quad (6.7)$$

$$\frac{\mathrm{d}n_{\mathrm{O}^-}}{\mathrm{d}t} = k_{\mathrm{at}}^{\mathrm{M}} n_{\mathrm{e}} n_{\mathrm{O}_2^{\mathrm{M}}} - n_{\mathrm{O}^-}\left(k_{\mathrm{ed}} n_{\mathrm{e}} + k_{\mathrm{mn1}}^{\mathrm{O}_2^+} n_{\mathrm{O}_2^+} + k_{\mathrm{mn2}}^{\mathrm{O}_2^+} n_{\mathrm{O}_2^+} + k_{\mathrm{mn}}^{\mathrm{O}^+} n_{\mathrm{O}^+} + k_{\mathrm{ad}} n_{\mathrm{O}} + k_{\mathrm{mn}}^{\mathrm{Ar}^+} n_{\mathrm{Ar}^+}\right) \quad (6.8)$$

Given that n_{e} as measured during the active phase was found to be almost identical for the three oxygen partial pressures, it is suggested that a greater number of $\mathrm{O}_2^{\mathrm{M}}$ are generated for increasing oxygen content in the discharge via electron-impact excitation ($k_{\mathrm{ex}} n_{\mathrm{e}} n_{\mathrm{O}_2}$). During the afterglow, further generation of $\mathrm{O}_2^{\mathrm{M}}$ is unlikely due to the sharp drop in T_{e} and the associated drop in k_{ex}. The rate coefficients of the dominant loss terms in the afterglow are k_{cr1}, k_{cr2} and $k_{\mathrm{diss}}^{\mathrm{1D}}$, so a characteristic decay time of metastable oxygen can be estimated by averaging over the afterglow and from $\tau_{\mathrm{O}_2^{\mathrm{M}}} \approx \left(k_{\mathrm{cr1}} n_{\mathrm{O}_2} + k_{\mathrm{cr2}} n_{\mathrm{O}_2} + k_{\mathrm{diss}}^{\mathrm{1D}} n_{\mathrm{e}}\right)^{-1} \sim 1600\ \mu$s, 525 μs and 315 μs for increasing oxygen partial pressure. The $\tau_{\mathrm{O}_2^{\mathrm{M}}}$ values are much shorter than the calculated diffusive loss times and exhibit shorter times for increasing oxygen content, consistent with the results presented by You *et al.* [137]. Using the calculated decay times and the rate balance equation above, the estimated densities of oxygen metastables are $n_{\mathrm{O}_2^{\mathrm{M}}} = 1.3 \times 10^{18}$ m^{-3}, 1.5×10^{19} m^{-3} and 1.8×10^{19} m^{-3} for $p_{\mathrm{O}_2}/p_{\mathrm{total}} = 0.1$, 0.3 and 0.5, respectively, which are approximately an order of magnitude higher than n_{e} during the on-time.

As argued above, the higher the O_2 content of the discharge, the greater the amount of $\mathrm{O}_2^{\mathrm{M}}$ available at the beginning of the afterglow and therefore one would expect a higher negative ion density n_- and a greater rate of increase in electronegativity as electrons undergo dissociative attachment to $\mathrm{O}_2^{\mathrm{M}}$. Indeed, from figures 6.8, this is what is observed as the electronegativity increases for greater oxygen partial pressure. Furthermore, an associated and more pronounced decay in n_{e} is also observed for increasing oxygen content. In particular, the second decay phase of n_{e}, τ_{n2}, is found to be significantly shorter; $\tau_{\mathrm{n2}} = 326\ \mu$s, 293 μs and 92 μs across the range of $p_{\mathrm{O}_2}/p_{\mathrm{total}}$ for increasing oxygen content and substantially shorter than for the Ar-only discharge where $\tau_{\mathrm{n2}} = 550\ \mu$s. This could be evidence of increased negative ion formation for higher oxygen availability as electrons are lost in dissociative attachment to metastable oxygen. From figure 6.9, it is observed that the average value of negative ion density during the afterglow is somewhat higher for $p_{\mathrm{O}_2}/p_{\mathrm{total}} = 0.3$ and 0.5 ($\langle n_- \rangle \approx 7 \times 10^{15}$ m^{-3}) when compared with $p_{\mathrm{O}_2}/p_{\mathrm{total}} = 0.1$ ($\langle n_- \rangle \approx 3 \times 10^{15}$ m^{-3}). This agrees with a global model developed by Gudmundsson and Thorsteinsson [176] which demonstrated that for increasing Ar content in an Ar/O_2 discharge one can expect a decrease in n_-.

The oxygen negative ion density is observed to decrease in the afterglow with characteristic times of $\tau_- = 1.4$ ms, 2.1 ms and 2.5 ms for $p_{\mathrm{O}_2}/p_{\mathrm{total}} = 0.1$, 0.3 and 0.5, respectively. Considering the dominant loss terms (mutual neutralisation) for O^- ions and averaged plasma density values during the afterglow, effective characteristic decay

times can be estimated by

$$\tau_- = -\left[k_{\mathrm{at}}^{\mathrm{M}} \frac{n_{\mathrm{e}}}{n_{\mathrm{O}^-}} n_{\mathrm{O_2^M}} - \left(k_{\mathrm{mn1}}^{\mathrm{O_2^+}} n_{\mathrm{O_2^+}} + k_{\mathrm{mn}}^{\mathrm{O^+}} n_{\mathrm{O^+}} + k_{\mathrm{mn}}^{\mathrm{Ar^+}} n_{\mathrm{Ar^+}}\right)\right]^{-1} \tag{6.9}$$

with the positive ion species fractions estimated from energy-resolved mass spectrometry measurements as discussed above. Using equation 6.9, the expected characteristic decay times of negative ions are found to be 750 μs, 3.7 ms and 3.1 ms for increasing $p_{\mathrm{O_2}}/p_{\mathrm{total}}$. This is in approximate agreement with the experimentally determined values, to within a factor of 2, and also agrees insofar as that for low oxygen content (i.e. $p_{\mathrm{O_2}}/p_{\mathrm{total}} = 0.1$) the decay times are shorter than for higher oxygen content (i.e. $p_{\mathrm{O_2}}/p_{\mathrm{total}} = 0.3$ and 0.5). For increasing oxygen partial pressure, it is expected that larger amount of $\mathrm{O_2^M}$ are generated in the active phase which results in an increased rate of negative ion formation ($k_{\mathrm{at}}^{\mathrm{M}} n_{\mathrm{e}} n_{\mathrm{O_2}}^{\mathrm{M}}$) in the afterglow. However, it is speculated that increasing oxygen beyond a critical point will lead to a decreased formation rate of negative ions despite the increase in $n_{\mathrm{O_2}}^{\mathrm{M}}$, as n_{e} is observed to decrease for reduced Ar partial pressure in an $\mathrm{Ar/O_2}$ discharge [181]. It is possible that this critical point exists for $p_{\mathrm{O_2}}/p_{\mathrm{Ar}} > 1$, as the characteristic decay time of negative ions is observed to be a monotonically increasing function of oxygen partial pressure in the results presented here. Furthermore, the results presented here show that, for reactive HiPIMS, the decay of negative ion species in the afterglow is approximately an order of magnitude longer than those measured in reactive pulsed DC magnetron sputtering [137]. This could be a consequence of a longer electron density decay time in HiPIMS when compared with pulsed DC magnetron sputtering, which would facilitate negative ion formation via dissociative electron attachment for longer periods in the afterglow.

Although negative ions are assumed to be confined to the bulk plasma by the ambipolar electric field during the on-time and for afterglow investigated here, the long off-times in HiPIMS will generally result in the eventual collapse of this potential and a subsequent flux of negative ions to the chamber walls as well as any grounded substrates or processing surfaces. This can be a very important consideration for many plasma processing methods which rely upon the flux of reactive species to surfaces, such as reactive ion etching. Assuming the negative ions follow the Boltzmann relation, akin to electrons, the negative ion flux density to a surface is given by

$$\Gamma_- = n_- \left(\frac{k_{\mathrm{B}} T_-}{2\pi M_-}\right)^{1/2} \exp\left(-\frac{e\phi}{k_{\mathrm{B}} T_-}\right). \tag{6.10}$$

For even small sheath potential values, ϕ, the negative ion flux to the walls is strongly reduced, however, when the plasma enters an ion-ion state and the potential at the chamber walls collapses (i.e. $\phi \to 0$), negative ions are free to diffuse to the walls. Therefore, by assuming that the oxygen negative ions possess a temperature close to that of the

background gas (i.e. $T_- \approx T_{\text{gas}}$) and taking $n_- \approx 10^{15}$ m^{-3}, the flux of O^- negative ions to the chamber walls, in the absence of a potential, can be approximated using equation 6.10 and is found to be of the order of $10^{17} - 10^{18}$ m^{-2} s^{-1}. This is a non-negligible flux (for comparison, this is about 1% of the positive ion flux during the on-time is $\Gamma_{\text{i}} = n_{\text{i}} c_{\text{s}} \sim 10^{19} - 10^{20}$ m^{-2} s^{-1}) and may influence the properties of deposited or etched materials in plasma processing. Indeed, negative chlorine ions (Cl^-) generated in the off-time of an inductively couple plasma source have been associated with the suppression of 'notch' formation during the etching of poly-Si [173]. Further investigation into the temporal evolution of metastable oxygen molecules during reactive HiPIMS would greatly facilitate in the validation (or otherwise) of the simple chemical model employed here and help to better understand the oxygen negative ion dynamics during the discharge afterglow.

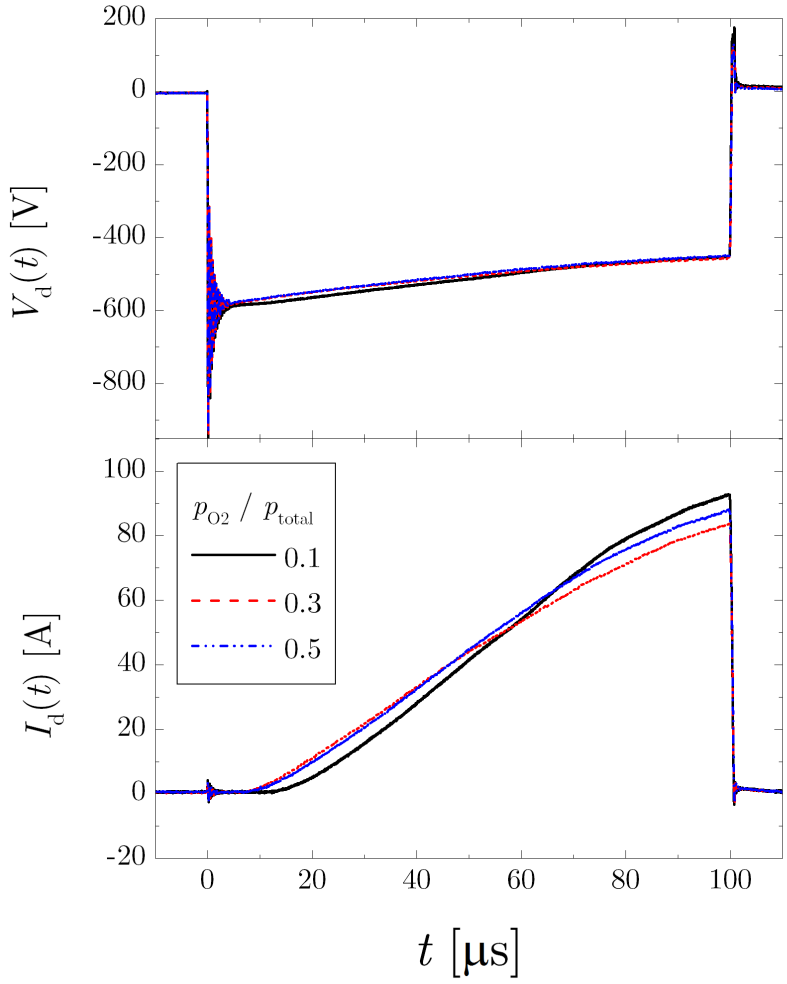

Figure 6.10. The HiPIMS discharge current, $I_{\text{d}}(t)$, and target potential, $V_{\text{d}}(t)$, waveforms for different oxygen partial pressures; $p_{\text{O}_2}/p_{\text{total}} = 0.1$, 0.3 and 0.5. The pulse width was 100 μs with a repetition rate of 100 Hz and and average discharge power of 200 W.

6.3.3 Laser-aided photodetachment

As outlined above, laser photodetachment measurements were made using a different experimental set-up than the one used for the Langmuir probe investigation. The HiPIMS discharge current and applied target potential waveforms are presented in figure 6.10 for the different oxygen partial pressures: $p_{O_2}/p_{total} = 0.1$, 0.3 and 0.5. The time-averaged discharge power was maintained at 200 W. The value of the peak power density varied between 0.21 and 0.24 kW cm^{-2}, corresponding to peak current density values of 0.46 − 0.56 A cm^{-2} across the range of oxygen partial pressures.

The delay time of the discharge current rise is slightly longer for $p_{O_2}/p_{total} = 0.1$ than for $p_{O_2}/p_{total} = 0.3$ and 0.5 with values of $\sim$ 13 μs and $\sim$ 8 μs, respectively. As the delay in the current on-set is longer for lower oxygen partial pressures, the peak current is necessarily higher for a constant average discharge power. As the applied potential does not vary significantly between the conditions, the disparity in the current delay times may be due to reduced poisoning of the target for lower oxygen partial pressures, which would alter the secondary electron emission coefficient.

6.3.3.1 Electron density and temperature

The waveforms presented in figure 6.10 are distinctly different from those shown in figure 6.2 for the Langmuir probe investigation. This results in a different temporal evolution in electron density, which is shown in figure 6.11a.

As with the Langmuir probe investigation, n_e was obtained from the measured electron saturation current via $I_{e,sat} = n_e A_p e \left(k_B T_e / 2\pi m_e\right)^{1/2}$, where T_e was found from the inverse gradient of a linear fit to the transition region of the $\ln(I_e)$-V_b plot. The temporal evolution of the electron temperature for different oxygen partial pressures is given in figure 6.11b. The measured peak density ranges from 1.7 to 2.2 $\times$ 10^{18} m^{-3} for increasing oxygen partial pressure, which is somewhat higher than those measured in the Langmuir probe investigation. The discrepancy in density values can be attributed to an increased average discharge power employed for the photodetachment investigation. Some n_e values are undetermined due to the electron saturation current exceeding the current range of the acquisition system, namely those at $40 < t < 140$ for both $p_{O_2}/p_{total} = 0.3$ and 0.5.

Possibly due to the lower time resolution employed here and some undetermined values in the early afterglow, n_e is observed to have a two-fold exponential decay in the off-time compared with the three-fold decay observed in §6.3.1.1. The first decay occurs between $t = 300$ and 900 μs, with the second decay evident at $t > 1000$ μs. The decay times are shown in table 6.4. The initial characteristic decay time, τ_{n1}, is observed to decrease with increasing p_{O_2}/p_{total}, possibly as a result of increased electron loss via dissociative attachment. τ_{n1} values in table 6.4 are consistent with those of τ_{n2} in table 6.1, suggesting the initial decay observed here is the same as the second decay phase observed in §6.3.1.1.

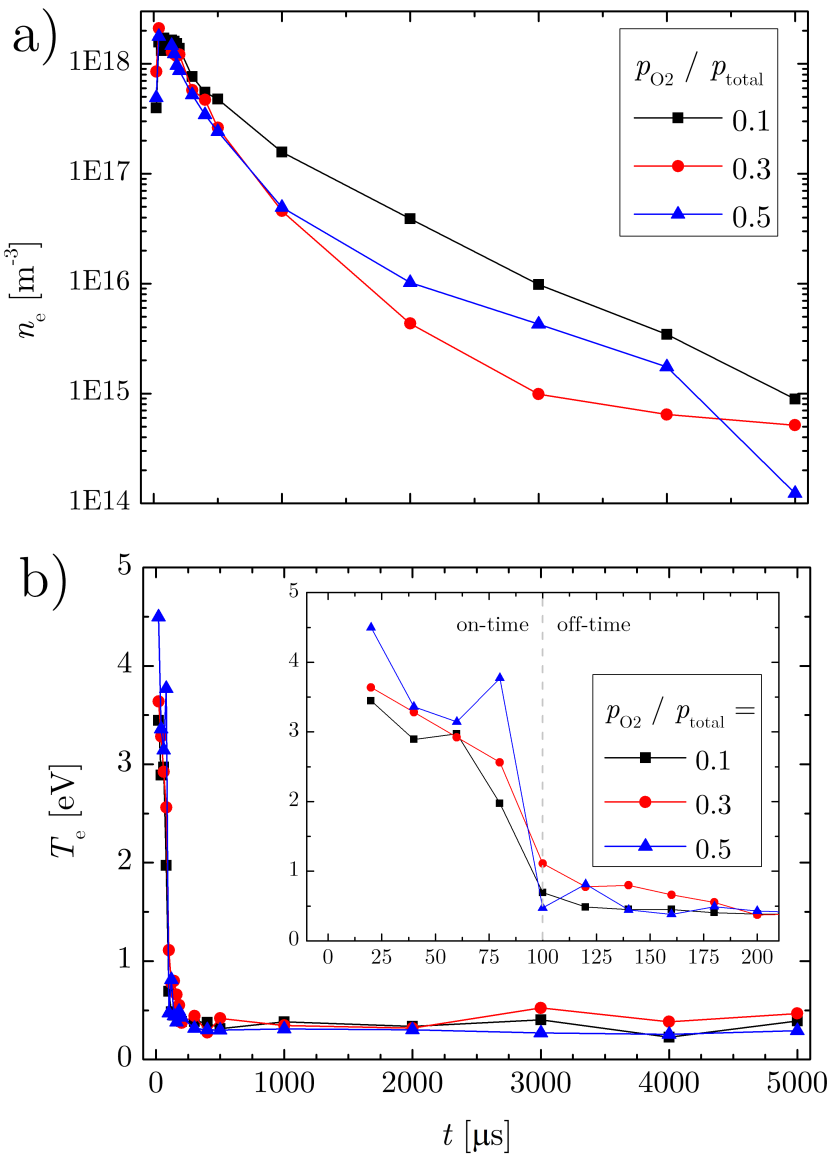

Figure 6.11. The temporal evolution of the (a) electron density, n_e, and (b) electron temperature, T_e, for different oxygen partial pressures in an Ar/O_2 discharge. For clarity, the plot inset in (b) shows the expanded time $t = 0 - 200$ of the temporal evolution of T_e.

The temporal evolution of the electron temperature is shown in figure 6.11b for different oxygen content. Here, T_e is consistently higher during the active phase of the pulse compared with those presented in §6.3.1.2 with $T_{e-peak} = 2 - 4.5$ eV, increasing with p_{O_2}/p_{total}. This is in contrast to the trend in T_{e-peak} found during the Langmuir probe investigation, however, differences in discharge power, current and geometry result in significant changes to the composition of the plasma and to the time-evolution of plasma parameters. It is suggested that due to the higher discharge current used here, a greater degree of process gas rarefaction will take place thereby resulting in higher electron temperatures during the on-time. In the off-time, T_e rapidly decays to $\sim 0.3 - 0.5$ eV and remains in that range for the extended afterglow.

p_{O_2}/p_{total}	Initial decay time, τ_{n1} (μs)	Second decay time, τ_{n2} (μs)
0.1	346	703
0.3	164	470
0.5	91	577

Table 6.4. The characteristic decay times for the two decay phases of the electron density for different oxygen partial pressures.

6.3.3.2 Electronegativity and negative ion density

The ratio of negative ion density to electron density, $\alpha = n_-/n_e$, can be readily determined by the ratio of the increase in the probe current due to the collection of photodetached electrons (photoelectrons) to the probe current in the absence of a laser pulse, $\Delta I_p/I_p$, as shown in equation 4.15. I_p is determined directly from the Langmuir probe I-V characteristic and ΔI_p from the voltage drop across $R2$ in figure 6.3. Figure 6.12 shows the current pulse from the photoelectrons at different temporal positions in the discharge pulse for $p_{O_2}/p_{total} = 0.1$, where electron current is measured as a negative current. As the active phase of discharge pulse evolves, ΔI_p increases in magnitude from -9.4 mA to -18 mA between $t = 40$ μs and $t = 80$ μs. During the off-time, a decrease in the absolute value of ΔI_p is observed, from -12.2 mA at $t = 180$ μs to -0.8 mA at $t = 1000$ μs. It is worth noting that due to a stray DC signal, the zero-position is not constant at different times during the pulse. This DC off-set was taken into account when extracting ΔI_p from the probe current pulses.

In order to determine α from probe current pulses like those shown in figure 6.12, the probe current operating in the electron saturation region in the absence of the laser pulse is required. However, as explained in §6.3.3.1, electron saturation current measurements for some time steps were undetermined due to current over-range issues and as a consequence, values for α and n_- are also undetermined for those same points.

The temporal evolution of the negative ion-to-electron density ratio, α, as obtained using equation 4.15, is given in figure 6.13. For all cases, α is observed to be less than unity during the on-time with values increasing with p_{O_2}/p_{total}. For $p_{O_2}/p_{total} = 0.3$, α increases to a peak value of 2.7 at $t = 3000$ μs before decreasing in the extended off-time. For other oxygen partial pressures, α increases slowly in the early off-time before rising at a greater rate beyond $t = 3000$ μs to $\alpha = 2.4$ and 3.9 at $t = 5000$ μs for $p_{O_2}/p_{total} = 0.1$ and 0.5, respectively. It is not yet understood why the trend in α deviates significantly for $p_{O_2}/p_{total} = 0.3$ from those exhibited for the cases of $p_{O_2}/p_{total} = 0.1$ and 0.5.

The origin of the different trend in α observed for the case of $p_{O_2}/p_{total} = 0.3$ is not fully understood. Firstly, the photodetachment data presented here was recorded once only rather than as a repeated experiment and, due to the blatant deviation from the other cases, it remains a possibility that an error occurred in the data acquisition for

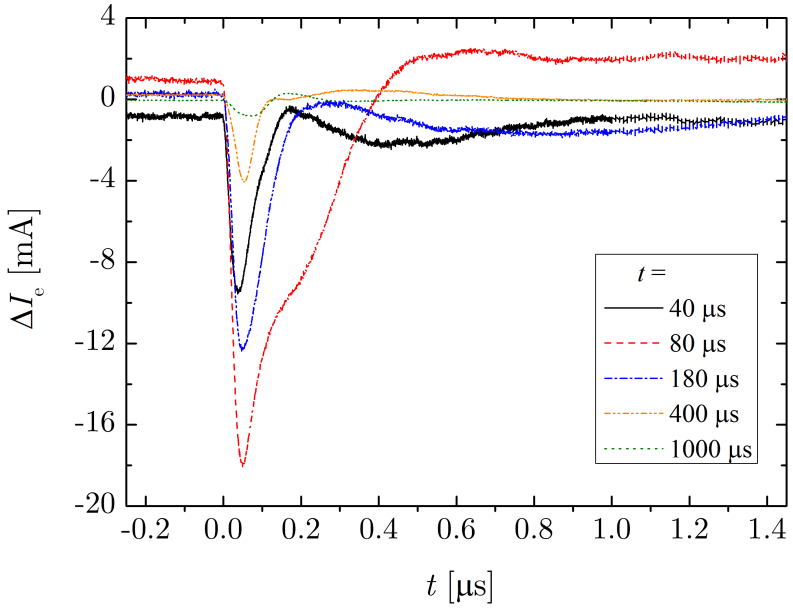

Figure 6.12. Photodetachment signals collected by a positively biased, cylindrical Langmuir probe operating in the electron saturation region positioned coaxially within the laser beam. Signals represent the additional electron current, ΔI_p, as measured at different temporal positions in an Ar/O_2 discharge pulse where $p_{O_2}/p_{total} = 0.1$.

the $p_{O_2}/p_{total} = 0.3$ case. However, it is also possible to illustrate some differences in the plasma chemistry by qualitatively considering the different background gas compositions. It is expected that with greater oxygen content, larger numbers of O_2^M metastable molecules will be formed during the active phase of the pulse and therefore more will be available to form negative ions via dissociative attachment reactions in the afterglow. However, the mutual neutralization reactions of O^- ions with O^+ and O_2^+ possess somewhat larger rate coefficients than the mutual neutralization reaction between O^- and Ar^+ (see table 6.3). Hence, for greater oxygen content, O^- ion formation may be expected to increase, however losses via mutual neutralization may increase concurrently. It is suggested that there is a balance between these two competing processes and some form of optimum value of p_{O_2}/p_{total} may exist, for which higher α values are obtained. However, without a comprehensive chemical model (more rigorous than the one employed in §6.3.2.2) and multiple repeat experimental investigations, it is not possible to say whether this is a valid explanation. More work in this direction is certainly warranted.

The temporal evolutions of the oxygen (O^-) negative ion density, $n_- = \alpha n_e$, are shown in figure 6.14 for different p_{O_2}/p_{total}. During the on-time, n_- initially increases for all cases with slightly higher values for increasing oxygen partial pressure. Due to the long off-times in HiPIMS, densities of charged species are very low at the beginning of each pulse and it is understandable that all species, including negative ions, experience

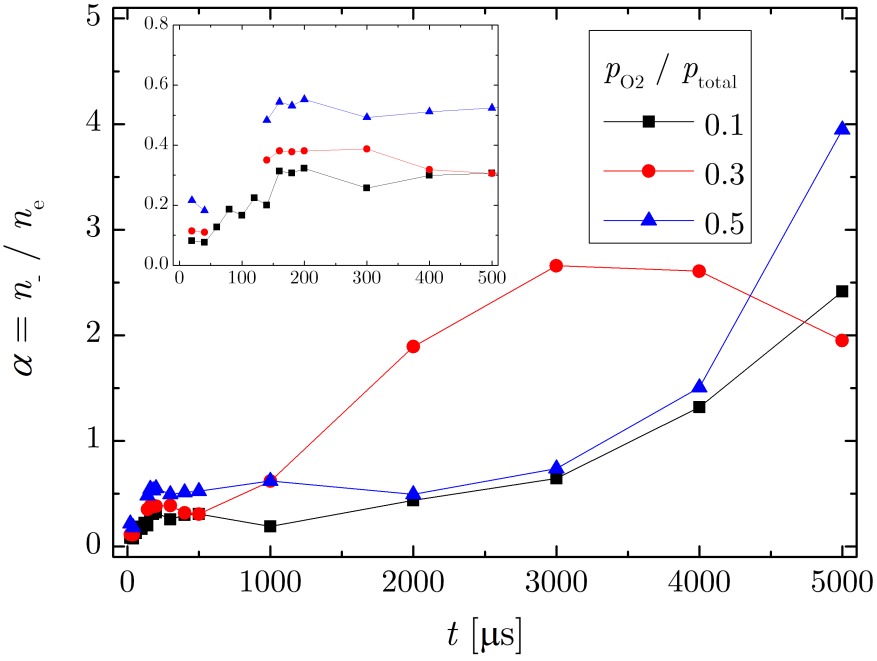

Figure 6.13. The temporal evolution of the electronegativity, α, for different oxygen partial pressures in an Ar/O_2 discharge as obtained via laser-aided photodetachment. For clarity, the plot inset shows the expanded time $t = 0 - 500$ of the temporal evolution of α.

an increase following the on-set of the discharge pulse. This is in contrast to higher duty cycles as used in pulsed DC magnetron sputter deposition, where significant negative ion populations remaining from the previous pulse cycle can be destroyed via electron-impact detachment at a greater rate of formation resulting in an overall decrease in n_- at the beginning of the on-time [137]. For $p_{O_2}/p_{total} = 0.1$, it was found that n_- increased in the immediate off-time ($t = 100 - 200$ μs), consistent with the investigation performed by You *et al.* [137] using the same experimental set-up as well as by other authors [171–173]. For $p_{O_2}/p_{total} = 0.3$ and 0.5, this increase in n_- in the off-time is not observed due to missing values around the time of the pulse termination. The peak n_- values, which are found in the early on-time ($t = 140 - 160$ μs), are 4.6, 4.7 and 7.1×10^{17} m^{-3} for increasing oxygen content. This higher n_- compared to those measured using the Langmuir probe could be due to the higher electron density in the photodetachment study. Furthermore, the increased discharge current may also result in a larger amount of metastable oxygen available to undergo negative ion formation via dissociative electron attachment. Beyond $t = 200$ μs, n_- decreases with characteristic decay times of ~ 1580 μs, 746 μs and 468 μs for increasing p_{O_2}/p_{total}. A shorter decay for increasing oxygen content is consistent with experimental observations by You *et al.* [137].

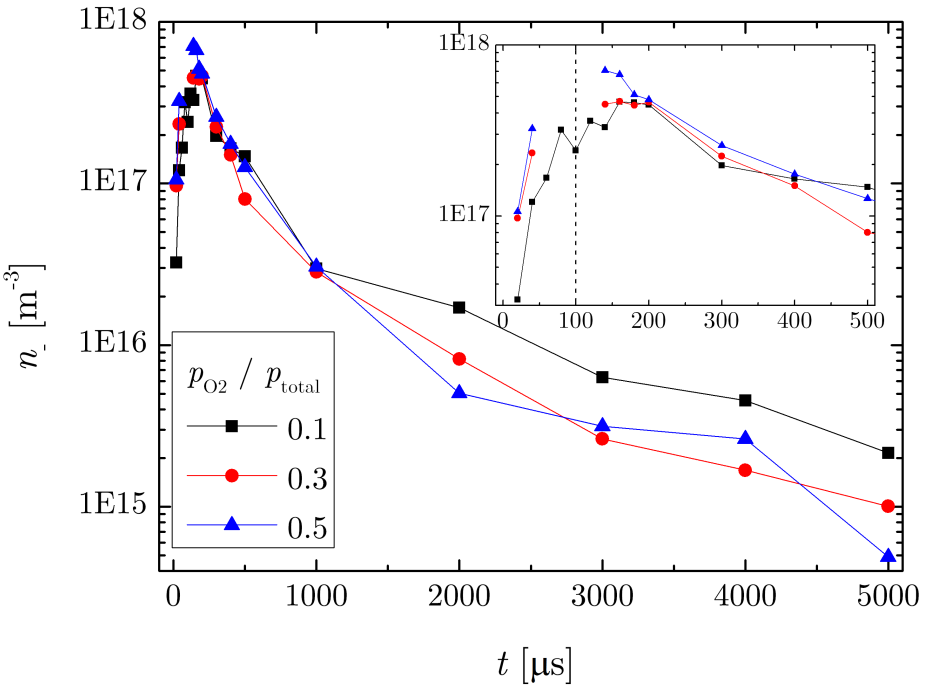

Figure 6.14. The temporal evolution of the oxygen negative ion density, n_-, for different oxygen partial pressures in an Ar/O_2 discharge as obtained via laser-aided photodetachment. For clarity, the plot inset shows the expanded time $t = 0 - 500$ of the temporal evolution of n_-.

6.3.3.3 Comparison with Langmuir probe

Due to the differences in discharge power, discharge current and geometry, direct quantitative comparisons of α and n_- as obtained using the Langmuir probe and laser photodetachment investigations are difficult. However, the values of α determined using both methods and for all oxygen partial pressures are plotted alongside each other in figure 6.15. Although $\gamma = T_e/T_- = 10$ was used in the Langmuir probe study, values of α determined using the ion fluid model have also been plotted for the case of $\gamma = 1$. In general, α values determined by the Langmuir probe technique are higher than those measured via photodetachment. This may be caused by an over-estimation of T_e as obtained from Langmuir probe I-V characteristics, which would result in too high value of γ being used to determine α from equation 6.3. The agreement between the two methods is somewhat better for $\gamma = 1$, however, it is not a significant improvement over $\gamma = 10$. The ideal correlation is plotted in figure 6.15 as a dashed line, and it is clear that the actual correlation deviates from this ideal somewhat. Although, a relatively strong correlation still exists between the two methods (solid line). Like in [136, 137, 161], this demonstrates the applicability of a Langmuir probe to approximate values of α and n_- in electronegative discharges, but also highlights the importance of considering its limitations.

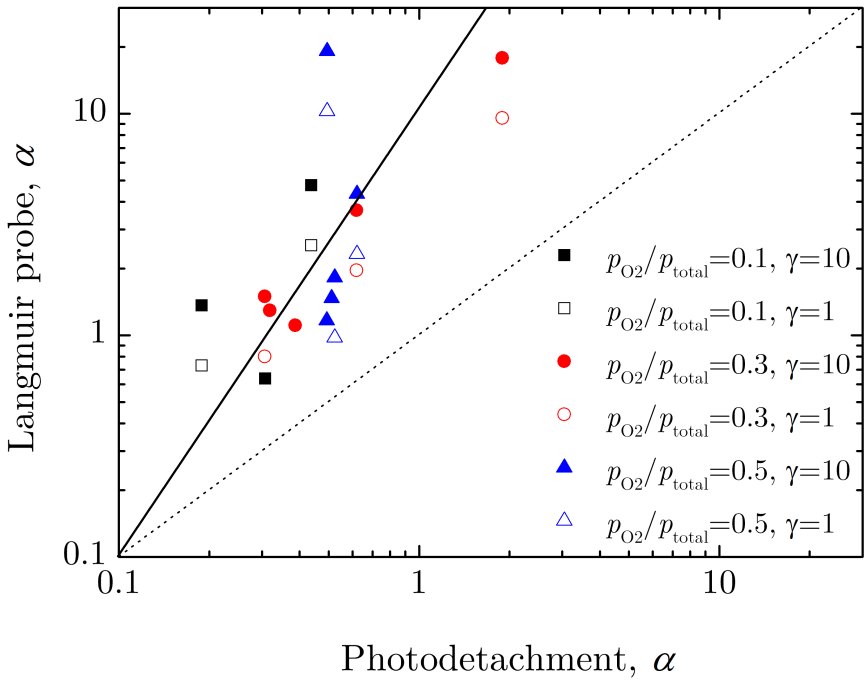

Figure 6.15. Values of electronegativity, α, estimated by the Langmuir probe method for $\gamma = T_e/T_- = 1$ (open) and 10 (solid) plotted against those determined directly by photodetachment. The dashed line indicates the ideal correlation where both α values are equal.

6.4 Conclusions

The temporal evolution of oxygen negative ion density and electronegativity in the discharge afterglow during HiPIMS of titanium in an Ar/O_2 atmosphere has been estimated by means of a single Langmuir probe and compared with values obtained using laser-aided photodetachment. In the Langmuir probe investigation, average oxygen negative ion densities in the afterglow were estimated to be of the order of 10^{15} m^{-3}, with values slightly higher for increased oxygen content. For all oxygen partial pressures, n_- was observed to decrease in the off-time with long decay times; $\tau_- = 1.4$ ms, 2.1 ms and 2.5 ms for $p_{O_2}/p_{total} = 0.1$, 0.3 and 0.5, respectively. The increase in the n_- characteristic decay times for increasing oxygen content was attributed to higher densities of metastable oxygen molecules available at the beginning of the afterglow which can subsequently undergo dissociative electron attachment to form negative ions. This, coupled with confinement of negative ions to be plasma bulk by the ambipolar electric field, resulted in a relatively constant oxygen negative ion density for most of the off-time, in contrast to the more rapidly decaying electron density. Hence, electronegativity was observed to increase monotonically in the afterglow, reaching peak values of $\alpha = n_-/n_e = 19$ ($\pm$3), 316 ($\pm$47) and 396 ($\pm$59) at $t = 3$ ms over the range of p_{O_2}/p_{total} investigated.

In the photodetachment study, oxygen negative ion densities were found to peak in

the early afterglow at values of the order of 10^{17} m^{-3}. The higher n_- compared to those found in the Langmuir probe study was attributed to the higher n_e attained during the active phase, whereby the greater availability of electrons permits the formation of more negative ions via dissociative electron attachment to oxygen molecules or metastables. Despite exhibiting a strong correlation, a comparison between the α values determined by photodetachment and those estimated using a fluid model of the ion current to a Langmuir probe in electronegative discharges revealed that α estimated by the Langmuir probe method are generally a factor of 8-15 larger than those measured using photodetachment. The applicability of using a Langmuir probe to approximate values of α and n_- in electronegative discharges has been demonstrated, but the importance of realising its limitations is also highlighted.

It was also concluded that a negative ion flux of the order of $10^{17} - 10^{18}$ m-2 s^{-1} could be expected at the chamber walls and substrate surface once the plasma afterglow transitions into an ion-ion state, which could have implications for many plasma processing methods. Although both of the aforementioned techniques can be used to determine or estimate negative ion densities, no knowledge of the negative ion energy distribution is obtained, which is also very important for understanding plasma-surface interactions and determining thin film properties. In the next chapter, the energy distributions of negative oxygen ions in reactive HiPIMS are considered.

Chapter 7

Negative ion energy distributions in reactive HiPIMS

7.1 Introduction

As discussed in chapter 3, the introduction of an electronegative gas such as oxygen into the discharge results in the production of negative ion species, many of which occupy a population with energies of the order of the applied target potential. Although Langmuir probes and laser-aided photodetachment can be employed to give information regarding negative ion densities (as in chapter 6), negative ion energy distributions are more readily obtained from energy-resolved mass spectrometry.

A brief overview of negative ion energy distributions in magnetron sputtering is given in §3.3.1 and a discussed of their effects on deposited thin film is provided in §3.3.4. In this chapter, energy distributions of negative ions in pre-ionized HiPIMS discharges containing oxygen are measured by means of energy-resolved mass spectrometry for a number of different discharge conditions. Although different inert gases mixed with oxygen and different target materials are investigated, much of the work was carried out during the reactive HiPIMS of Ti in an Ar/O_2 discharge.

Due to their abundance and associated effects on growing films (see §3.3.4), particular emphasis is placed on O^- ions in the high energy population. The shape of the high energy peaks of the O^- ion energy distributions for different average discharge powers $\overline{P_d}$ measured during reactive HiPIMS of Ti in an Ar/O_2 discharge are compared to two models: i) a theoretical Thompson energy distribution incorporating an energy offset to account for acceleration due to the time-dependent target potential and ii) the target potential distribution weighted by the discharge current (similar to the model employed by Mišina *et al.* [118]). The latter approach implies that the intensity of high energy O^- ions is proportional to the discharge current. Additionally, the attenuation of high energy O^- ions in the vicinity of the substrate is investigated as a function of the pressure-

distance product pd, where p is the total gas pressure and d is the target-to-substrate distance. Furthermore, the effects of pulse width, oxygen partial pressure and choice of target material and inert gas on the production of high-energy O^- ions are also discussed.

7.2 Experimental set-up

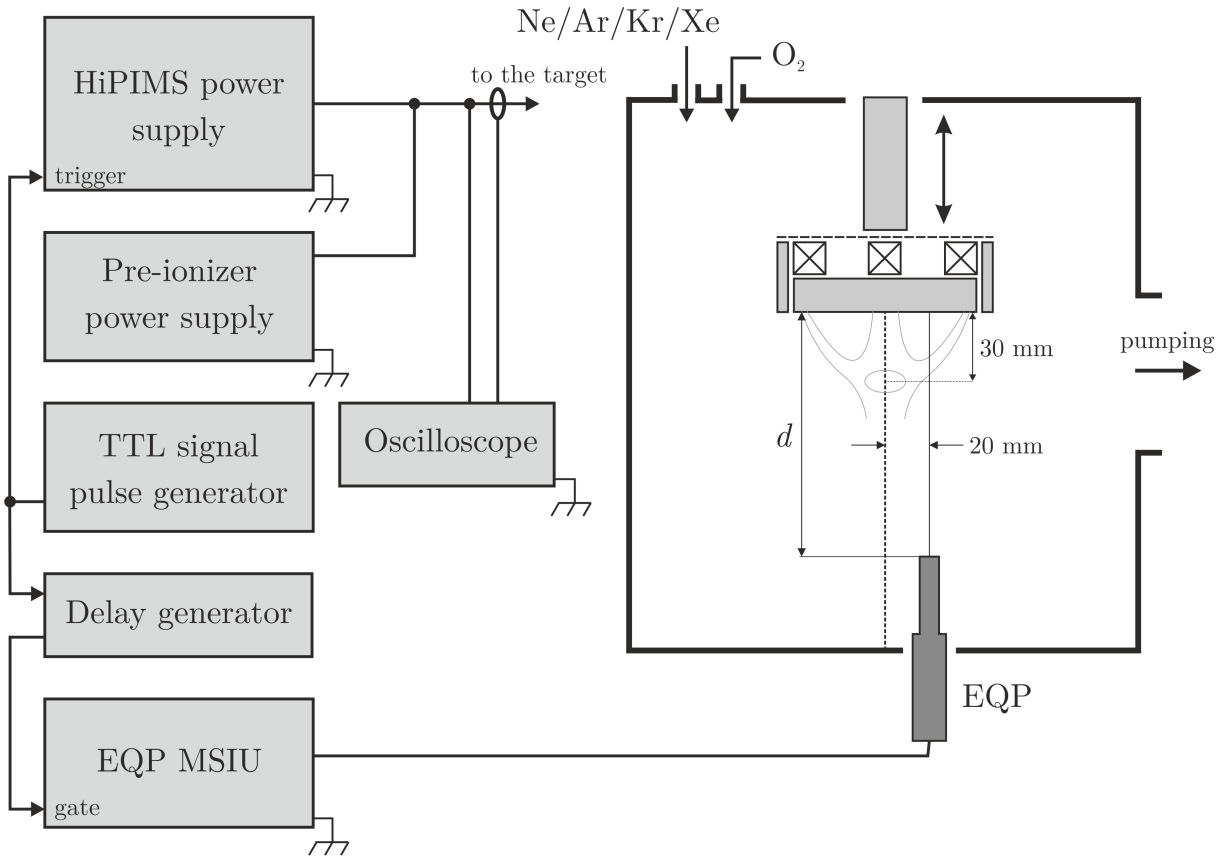

Figure 7.1. Schematic representation of the experimental set-up. The EQP was positioned directly over the racetrack (20 mm off-axis) moved axially with respect to the target from $d = 50$ to 100 mm. The magnetic null is indicated at 30 mm above the target surface.

The experimental set-up is described in §4.1. A number of different target materials were equipped to the magnetron source; metallic Ti, Nb, Cu, W and Al target materials (at least 99.95% purity) were investigated. The pre-ionizer power supply was used in tandem with the HiPIMS impulse unit in order to facilitate operation at lower pressures than afforded by the HiPIMS power supply alone. The voltage pulse width τ and frequency f were controlled by using an external pulse generator (Thandar TG105) to trigger the HiPIMS power supply unit. The most heavily investigated pulse parameters were $\tau = 100$ μs and $f = 100$ Hz, although τ was varied between 40 and 200 μs, and f between 50 and 200 Hz. Inert gases (Ne, Ar, Kr, Xe) and oxygen gases (> 99.995% purity) were introduced into the chamber with flow rates controlled by two independent and identical mass flow

controllers (MKS 1179A). The total working gas pressure, $p_{\text{total}} = p_{\text{Ar}} + p_{\text{O}_2}$, was monitored using a capacitance pressure gauge (MKS 628A) and was varied between 0.33 and 2 Pa. To obtain the desired oxygen partial pressure, the oxygen flow rate was increased beyond the hysteresis transition from metallic to poisoned mode and then reduced as necessary. The target voltage $V_{\text{d}}(t)$ was measured using a high voltage probe (Tektronix P5100) and the discharge current $I_{\text{d}}(t)$ was measured using a DC coupled current probe (Tektronix TCP202) which were both connected to a digital oscilloscope (Tektronix TDS3014, 100 MHz bandwidth). The average discharge power,$\overline{P_{\text{d}}}$, was monitored in real-time using the same oscilloscope, calculated as the mean of the product of $V_{\text{d}}(t)$ and $I_{\text{d}}(t)$ and controlled by manually varying the initial target potential V_0 provided by the HiPIMS power supply.

Energy distributions of negative ions were measured using an energy-resolved mass spectrometer (EQP 300, Hiden Analytical Ltd.) placed at a distance d axially away from the target surface and pointing perpendicular to the target racetrack (20 mm from the centreline) to obtain enhanced count rates [112]. In order to measure the effect of target-to-substrate distance on measured negative ion intensity at the substrate, d was varied from 50 to 100 mm. A schematic illustration of the experimental set-up is shown in figure 7.1. The EQP probe was equipped with a 100 μm diameter orifice which acted as the substrate surface and the probe end cap was held at ground potential. Time-averaged negative ion energy distribution functions were measured against ground potential by scanning the internal reference potential with an energy resolution of 0.5 eV and the EQP was configured to monitor a constant mass-to-charge ratio (m/z), depending upon the species being investigated. Tuning of the mass spectrometer was performed according to the recommended protocol provided by the manufacturer and described in appendix A.

7.3 Results and discussion

7.3.1 Time-averaged negative ion energy distributions

The time-averaged energy distributions of different negative species were measured for a number of different conditions by varying the discharge parameters. Figure 7.2 shows an example of the temporal variation of $V_{\text{d}}(t)$ and $I_{\text{d}}(t)$ for the following discharge parameters; $p = 0.33$ Pa, $p_{\text{O}_2}/p_{\text{total}} = 0.2$, $\overline{P_{\text{d}}} = 100$ W, $\tau = 100$ μs and $f = 100$ Hz.

The mass spectra of both positive and negative ions obtained under the discharge conditions given above are presented in figures 7.3a and 7.3b, respectively. When recording the positive and negative mass spectra, the static energy analyser was tuned to monitor constant pass energy of 2 eV and 3 eV, as this was found to be the most probable energy for Ar^+ and O^-, respectively. From figure 7.3b, O^- appears to be the most abundant of the negative species in the discharge while little to no oxygen compound species were detected in the negative ion mass spectra. The reason for this is due to the energy-

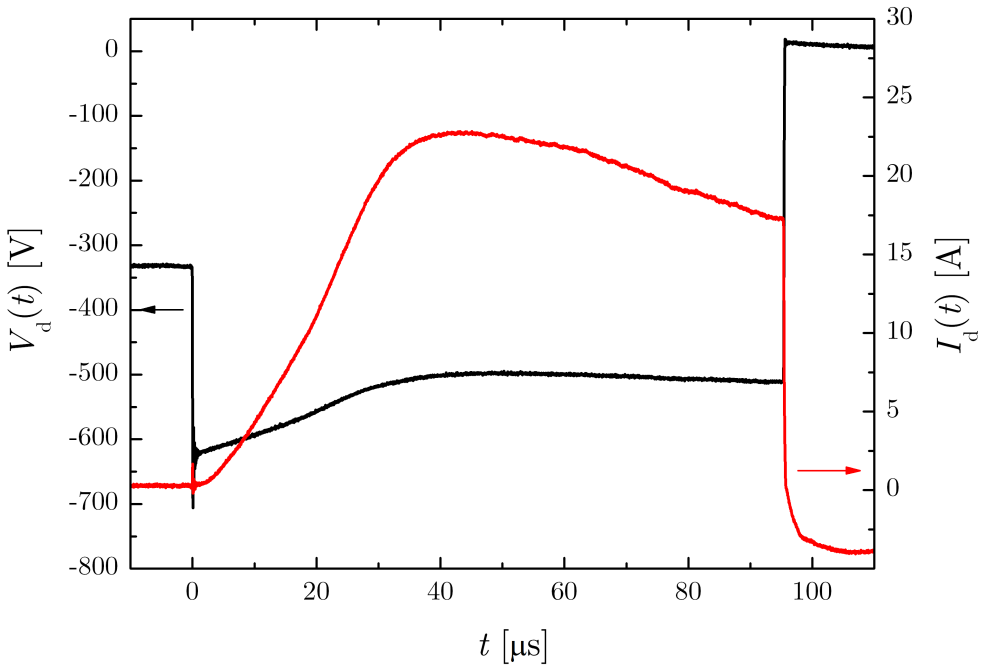

Figure 7.2. The voltage-current-time characteristic for the HiPIMS of Ti in an Ar/O_2 discharge as described in the text. The peak charge density is approximately 0.52 A cm^{-2}.

selective nature of the instrument and can be made clear by examining the time-averaged energy distributions of the oxygen compound negative ions which are given in figure 7.4. From the energy distributions of TiO^-, TiO_2^- and TiO_3^- as illustrated in figure 7.4, it is observed that these species are detected predominantly at high energies and are hence not present in the negative ion mass spectrum where the pass energy is fixed at 2 eV. Table 7.1 shows a list of the negative ion species for which energy distributions are shown in figure 7.4, with their corresponding m/z values.

From figure 7.4, O^- is observed to be the most abundant negative species across the entire energy range ($0 < E < 800$ eV) at the position of the orifice, which corroborates with previous studies performed by other authors regarding negative ions in reactive magnetron sputtering where oxygen is employed as the reactive gas [20, 117].

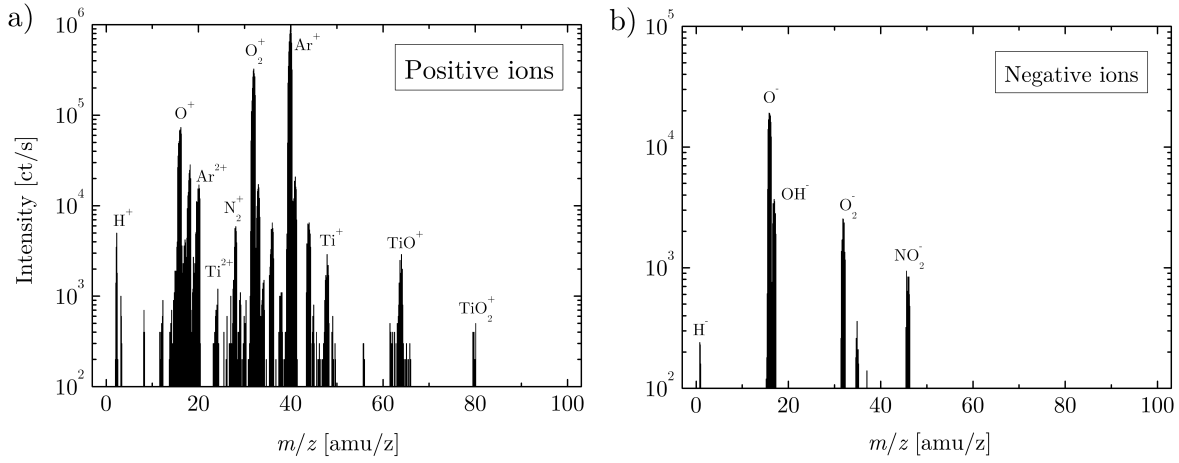

Figure 7.3. Mass spectra of positive (a) and negative (b) ions generated in reactive HiPIMS of Ti in an Ar/O_2 mixture where $p_{O_2}/p_{total} = 0.2$. The EQP was set to sample at a constant pass energy of 3 and 2 eV for the positive and negative mass spectrum, respectively.

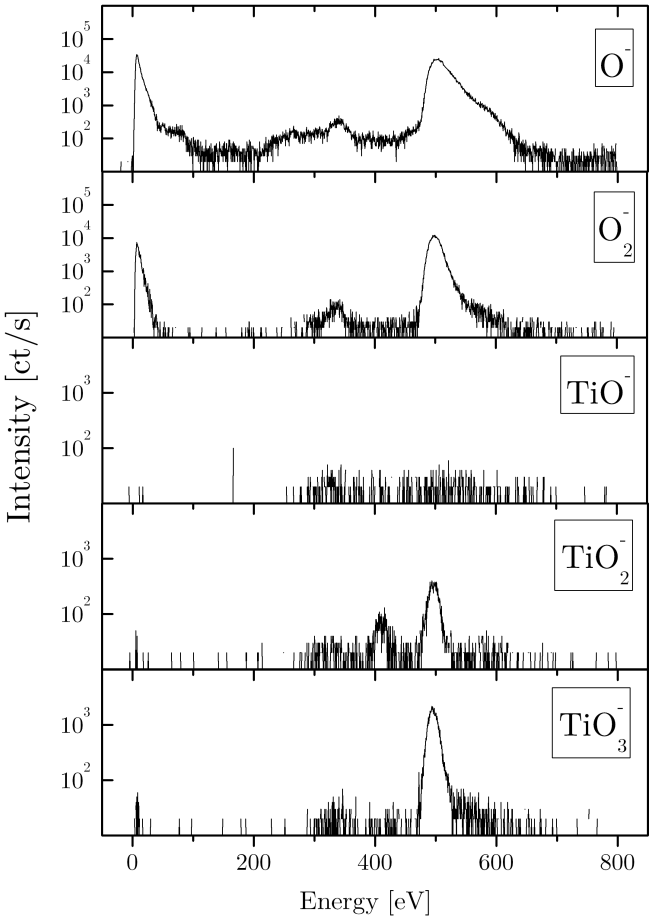

Figure 7.4. Measured energy distributions of O^-, O_2^-, TiO^-, TiO_2^- and TiO_3^- in reactive HiPIMS of Ti in an Ar/O_2 mixture where $p_{O_2}/p_{total} = 0.2$. The maximum absolute target potential applied to the cathode during the HiPIMS on-phase was 700 V. The average on-phase absolute target potential was ~ 500 V.

Species	Mass-to-charge ratio (amu/z)
O^-	16
O_2^-	32
TiO^-	64
TiO_2^-	80
TiO_3^-	96

Table 7.1. List of detected negative species alongside their corresponding mass-to-charge ratios (amu/z).

Also similar to results presented by other authors [20, 110, 116], the shape of the O energy distribution reveals three main ion populations; low, medium and high energy. The ions contributing to the low energy peak ($E < 70$ eV) are either generated at the target surface and experience energy loss due to collisions or are formed in the plasma bulk via the post-ionisation of sputtered particles. It is also possible that low energy negative ions are formed inside the target sheath or pre-sheath via electron attachment or dissociative electron attachment processes rather than at the target surface and are hence accelerated by only a fraction of the cathode potential. However, the low electron density within the sheath makes the formation of negative ion species inside the sheath unlikely. It should be noted that very low energy O^- ions formed in the plasma bulk go undetected by the EQP. The formation mechanism of these O^- ions is typically dissociative electron attachment involving background oxygen molecules (i.e. $O_2 + e^- \rightarrow O^- + O$). As a consequence, O^- ions formed via this mechanism have temperatures close to that of the background gas and therefore possess insufficient energy to overcome the potential barrier at the grounded orifice. The potential barrier is on the order of the local electron temperature (typically $1 - 4$ eV, as shown in chapters 5 and 6). In order to investigate O^- ions formed in this way, different methods such as laser-aided photodetachment are employed, as in chapter 6.

The medium-energy peaks (70 eV $< E <$ 420 eV) originate from accelerated clusters (O_2^-, TiO^-, TiO_2^- etc...) dissociating as a result of collisions in the plasma bulk en route to the EQP orifice. Upon dissociation, the energy of the cluster is shared between its fragments according to the ratio of the fragment masses. This effect is most evident in the energy distribution of TiO_2^-, where a smaller peak at $E \sim 410$ eV is observed alongside the higher energy peak at $E \sim 495$ eV (see figure 7.4). The energy ratio of these two peaks is 0.83, which is almost identically equal to the mass ratio of TiO_2 to TiO_3 ($M_{TiO_2}/M_{TiO_3} \approx 80/96$), suggesting that the lower energy peak in the TiO_2^- distribution is a result of TiO_3^- molecules dissociating into TiO_2^- and O during transportation to the orifice. There is also a small peak centred about $E \sim 334$ eV, which is equal to the target potential applied by the pre-ionizer during the pulse off-phase (evident in figure 7.2).

The high-energy ions ($E >$ 420 eV) are formed at the target surface via attachment

processes and subsequently accelerated through the cathode sheath. As can be seen in figure 7.4, TiO_2^- and TiO_3^- ions are only observed at high energies corresponding approximately to the average target potential during the on-time, suggesting that such ions are produced exclusively at the target surface and not in the plasma bulk. Moreover, their narrow energy distribution compared with the high-energy O^- ion population also suggests that TiO_2^- and TiO_3^- ions are released from the target by ion-assisted desorption rather than by physical sputtering.

7.3.2 High-energy population of O^- ions

The current-voltage-time waveforms for different average discharge powers ($\overline{P_d}$ = 25, 50 and 100 W) are presented in figure 7.5. In each instance, other discharge parameters were maintained constant at f = 100 Hz, τ = 100 μs and p = 0.33 Pa while the target-to-orifice distance was also constant at d = 100 mm. The time-averaged energy distributions of high energy O^- ions as obtained using these different average discharge powers were compared with two models outlined below.

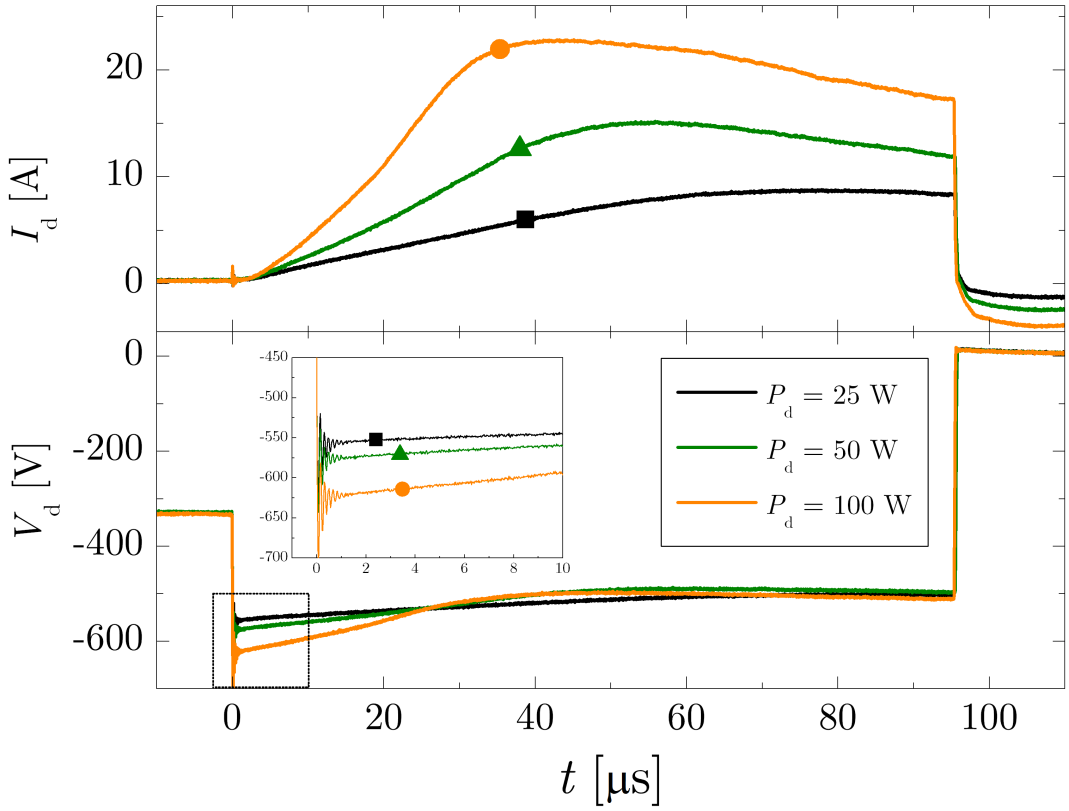

Figure 7.5. The time variation of the HiPIMS discharge current $I_d(t)$ and target potential $V_d(t)$ for different average discharge powers $\overline{P_d}$ = 25, 50 and 100 W during HiPIMS of Ti in an Ar/O_2 discharge where p_{O_2}/p_{total} = 0.2. Inset is a magnified plot of the target potential for t = 0 to 10 μs.

As discussed by Mráz and Schneider [18, 116], by assuming the high energy O^- ions

are sputtered from the target surface with a Thompson energy distribution [32] before being accelerated in the cathode fall, it is possible to describe the theoretical negative ion energy distribution in a pulsed plasma by

$$f\left(E\right) \sim \int_{\text{pulse}} g\left(t\right) \frac{E - E_0\left(t\right)}{\left[\left(E - E_0\left(t\right)\right) + U_\text{s}\right]^3} \text{d}t \tag{7.1}$$

$$g(t) = \begin{cases} 1 & \text{for } E_0(t) \leq E \\ 0 & \text{for } E_0(t) > E, \end{cases}$$

where E is the energy of the sputtered particle, U_s is the surface binding energy and E_0 is the energy offset, defined as $E_0(t) = qeV_\text{d}(t)$ where q is the charge state and e is the elementary charge. The energy of the sputtered particle is offset due to subsequent acceleration in the cathode sheath, which is in-turn determined by the time-dependent target potential $V_\text{d}(t)$. The full energy distribution in equation 7.1 is obtained by integrating over the entire on-phase of the pulse; $V_\text{d}(t)$ was obtained directly from the oscilloscope and the surface binding energy U_s of oxygen on a titanium oxide surface was taken to be 7 eV as proposed by Kubart *et al.* [182].

Additionally, the high energy population of the measured O^- ion energy distribution was also compared to the target potential distribution function (as discussed in [116]) weighted by the discharge current waveform $I_\text{d}(t)$, hence assuming the intensity of high energy O^- ions is proportional to the discharge current, but that their energy is unaffected by sputtering. This distribution function was calculated as follows;

$$f\left(qeV_\text{i}\right) \sim F \sum_{t=0}^{t<\tau} \xi(t) I_\text{d}(t), \qquad V_\text{i} \in \langle V_\text{min},\, V_\text{max} \rangle \tag{7.2}$$

$$\xi(t) = \begin{cases} 1 & \text{for } V_\text{d}(t) \in \left\langle V_\text{i} - \frac{\Delta V_\text{d}}{2},\, V_\text{i} + \frac{\Delta V_\text{d}}{2} \right\rangle \\ 0 & \text{for } V_\text{d}(t) \notin \left\langle V_\text{i} - \frac{\Delta V_\text{d}}{2},\, V_\text{i} + \frac{\Delta V_\text{d}}{2} \right\rangle \end{cases}$$

where V_i, V_min, V_max and ΔV_d are the accelerating potential difference, absolute minimum and maximum values of the target potential and the potential difference interval used to separate the measured target potential range into discrete values (in this case $\Delta V_\text{d} = 5$ V), respectively. The distribution was also multiplied by a scaling factor F for normalized comparison with the measured intensity of high-energy O^- ions. The theoretical Thompson distributions with energy off-set (from equation 7.1), current-weighted target potential distributions (from equation 7.2) and the measured O^- ion energy distributions for $\overline{P_\text{d}} = 25$, 50 and 100 W are plotted in figure 7.6, with the corresponding HiPIMS waveforms displayed in figure 7.5.

As illustrated in figure 7.6, the high energy population of O^- ions is not well represented by the modified Thompson energy distribution, consistent with the results reported

by Mráz and Schneider [116]. It is thought that the disagreement between the theoretical distribution and experimental data arises primarily due to neglecting any collisional effects occurring between the target and substrate. By using the expected energy distribution of sputtered particles as calculated by SRIM [183] and subsequently accounting for gas phase transport, Mahieu *et al.* [110] have shown much better agreement with experimental data for the energy distributions of O^- ions in reactive DCMS.

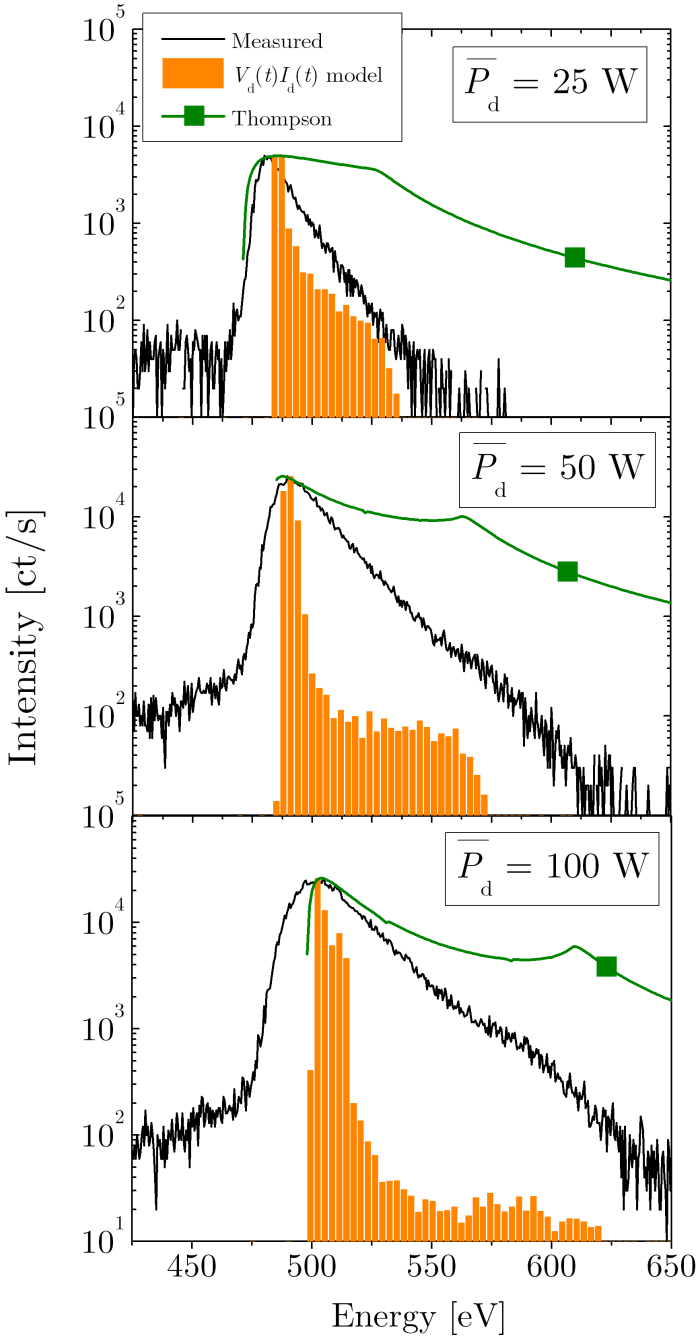

Figure 7.6. The measured energy distribution of high energy O^- ions (black line) alongside the modified Thompson distribution (green line) and current-weighted target potential distribution (histogram).

Although the target potential distribution function seems to match the high energy region of the measured energy distribution of O^- ions well for $\overline{P_d} = 25$, this is not the case for $\overline{P_d} = 50$ or 100 W. The implication of these results is that the energy distribution of high energy O^- ions created in reactive HiPIMS cannot be readily determined by the target potential distribution function, particularly at higher average discharge powers. This is in contrast to the results reported by Mraz and Schneider [116], whereby the authors concluded that the high energy range of the O^- ion energy distribution can be determined exclusively by the target potential distribution function during the reactive pulsed DCMS of Al in an Ar/O_2 atmosphere. It was further speculated that negative ion generation by desorption from the target surface must then be the dominant formation mechanism. However, the results presented here suggest that in reactive HiPIMS of Ti in an Ar/O_2 gas mixture, the high energy O^- ions are formed as a consequence of electron tunnelling or attachment to O atoms at the target surface. The surface O^- ions formed at the target surface are subsequently sputtered and accelerated in the cathode fall region and hence possess additional energy provided by the sputtering event. This additional energy, however, is not explained by the theoretical Thompson distribution alone and the gas transport phase may need to be considered, in-line with the more rigorous treatment presented by Mahieu *et al.* [110].

7.3.3 Changing pressure and target-to-substrate distance

Figure 7.7a shows the energy distributions of the high energy population of O^- ions for different total operating pressures (p = 0.33, 0.67, 1.34 and 2.00 Pa), measured at a constant axial position d = 100 mm. The average discharge power was maintained constant at $\overline{P_d}$ = 100 W and the pulse parameters were also constant; τ = 100 μs and f = 100 Hz. The intensity of the high energy O^- ion signal is observed to decrease rapidly with increasing p. The peak position of the high energy O^- ions in figure 7.7a is observed to shift to lower energies for increasing pressure. This is attributed to a lower absolute target potential during the HiPIMS pulse on-phase being required to maintain a constant discharge power for operation at higher pressures. A significant decrease in the intensity of high energy O^- ions was also observed for operating at a constant pressure (p = 1.34 Pa) but varying the target-to-substrate distance d, as shown in figure 7.7b.

The rapid decrease in the number of O^- ions detected for both an increasing pressure at a fixed distance d = 100 mm and for a constant pressure at increasing distance away from the target can be understood by considering the transport of O^- ions formed at the target surface through the background gas to the EQP probe. Using a simple binary collision analysis similar to that discussed in [184], it is possible to approximate the amount of high energy O^- ions impacting a substrate at a given distance away from the target and given a certain pressure and gas mixture. For the simple treatment presented here, there

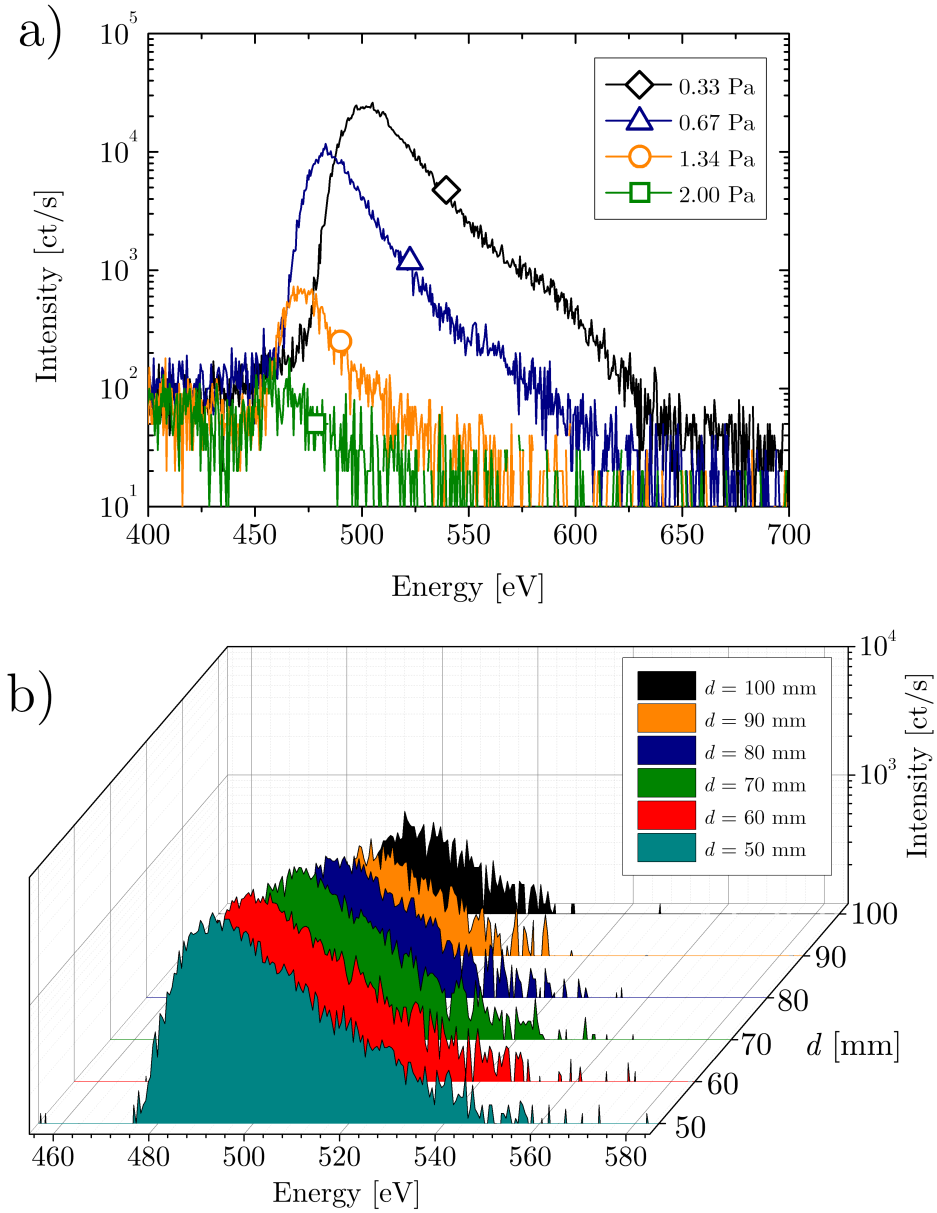

Figure 7.7. The high energy region of the energy distributions of O^- ions measured for (a) different pressures at a constant $d = 100$ mm, and for (b) different target-to-substrate distances, d, for a constant $p = 1.34$ Pa.

are several approximations made:

1. Negative ions are hard spheres with a radius equal to that of the Pauling radius.

2. Negative ions interact only with neutral Ar gas atoms and O_2 molecules via elastic collisions. This assumption is justified due to the low particle ionization fraction outside of the magnetic trap (typically 10^{-2} to 10^{-4} [28]).

3. The background gas behaves like an ideal gas in thermal equilibrium at temperature T_{gas}, whereby the neutral particle density can be calculated by $n_{\mathrm{g}} = p/k_{\mathrm{B}}T_{\mathrm{gas}}$. The

background gas particles are also hard spheres with a radius equal to the van der Waals radius.

4. Gas density is uniform between the target and substrate; hence gas rarefaction effects and the sputtered vapour are not accounted for. The latter is justified by the low sputtering yield of reactive magnetron sputtering operated in poisoned mode.

5. Thermal motion of gas is neglected as T_{gas} is taken to be uniform and equal room temperature ($T_{\text{gas}} = 300$ K), thus the background gas can be considered stationary relative to the fast moving high energy negative ions ($T_{\text{eff,O}^-} \gg T_{\text{gas}}$).

6. Any elastic collision deflects the negative ion sufficiently to make it undetectable. This approximation is employed due to the small acceptance angle of the EQP probe for detecting high energy ions [139].

Given the above approximations, it is possible to calculate the collisional cross section $\sigma = \pi b^2$ where b is the impact parameter equal to the sum of the radii of the two colliding particles. The effective cross sections for a singly-charged negative atomic oxygen ion colliding with neutral argon atoms and oxygen molecules are given by

$$\sigma_{\text{Ar}} = \pi \left(r_{\text{Ar}} + r_{\text{O}^-}\right)^2$$

$$\sigma_{\text{O}_2} = \pi \left(r_{\text{O}_2} + r_{\text{O}^-}\right)^2 \tag{7.3}$$

where $r_{\text{O}^-} = 176$ pm, $r_{\text{Ar}} = 188$ pm and $r_{\text{O}_2} = 152$ pm. With the cross sections from equation 7.3, the effective total cross section of an Ar/O_2 gas mixture where $p_{\text{O}_2}/p_{\text{total}} = 0.2$ is calculated to be 3.9×10^{-19} m^2. By neglecting the motion of the background gas relative to the high energy negative ions, the mean free path can be found straightforwardly by

$$\lambda = \frac{1}{n_{\text{Ar}}\sigma_{\text{Ar}} + n_{\text{O}_2}\sigma_{\text{O}_2}} \tag{7.4}$$

where n_{Ar} and n_{O_2} are the particle densities of Ar and O_2, respectively. For $p_{\text{O}_2}/p_{\text{total}} = 0.2$ and $p_{total} = 0.67$ Pa, from equation 7.4 the mean free path is calculated to be approximately 16 mm. Since the negative ions that make it to the detector are assumed to be the uncollided fraction of initial flux, the probability χ of detecting the negative ions with the orifice at a distance d above the target surface is

$$\chi = \exp\left(-\frac{d}{\lambda}\right) \tag{7.5}$$

As well as varying n_{g} for a constant $d = 100$ mm, the position of the orifice was also varied from $d = 50$ to 100 mm for two total gas pressures, $p = 0.67$ and 1.34 Pa. The HiPIMS discharge parameters were again maintained constant ($f = 100$ Hz, $\tau = 100$ μs

and $\overline{P_{\mathrm{d}}} = 100$ W). The energy distribution was integrated for $E > 425$ eV and plotted against the pressure-distance product (pd) in figure 7.8, and is used to gain insight to the effects of both pressure and distance on the intensity of high energy negative ions arriving at the orifice.

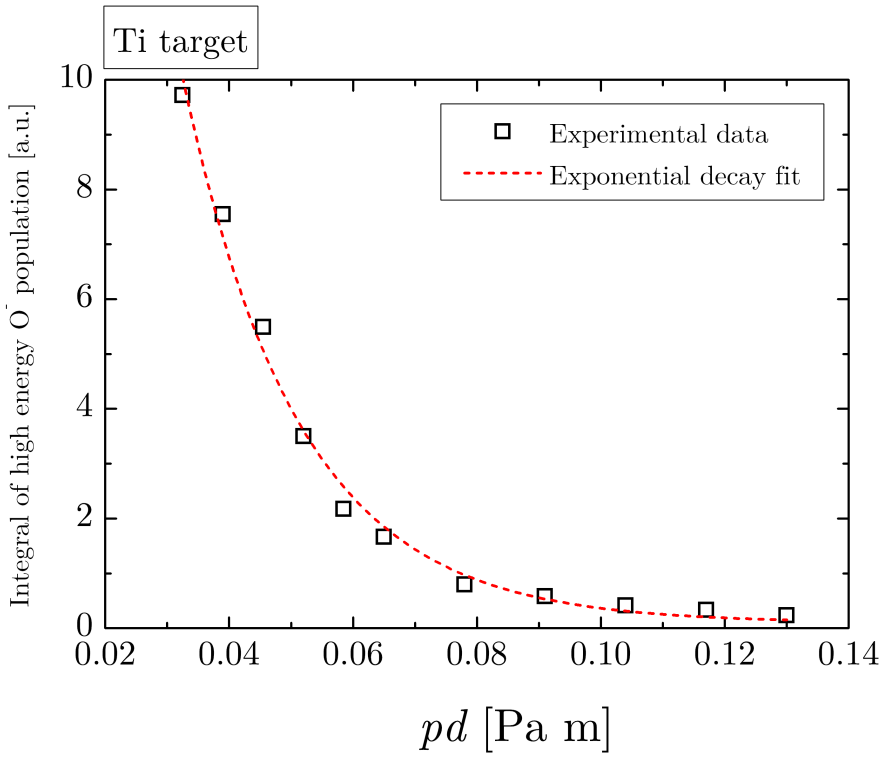

Figure 7.8. The integral of the high-energy population ($E > 425$ eV) of O^- ions plotted against the pressure-distance product (Ti target).

From equation 7.5 and assuming ideal gas behaviour, the probability χ for a high energy negative ion to be transported uncollided over a distance d in an 80:20 Ar/O_2 gas mixture can be shown to be

$$\chi = \exp\left[-\frac{\sigma_{\mathrm{t}}}{k_{\mathrm{B}}T_{\mathrm{gas}}}pd\right] \tag{7.6}$$

where σ_{t} is the effective total cross section. When equation 7.6 is compared with the fit to the experimental data in figure 7.8, the yielded effective collisional cross section is $\sigma_{\mathrm{t}} = 2.2 \times 10^{-19}$ m^2.

To investigate any effects caused by the metal vapour, a similar investigation to that detailed above was performed using a Nb target. Measured O^- energy distributions for $p = 0.33$, 0.67 and 1.34 Pa at a fixed $d = 100$ mm, and for $d = 50 - 100$ mm at a fixed $p = 0.67$ Pa are shown in figures 7.9a and 7.9b, respectively. The energy distributions were integrated for $E > 550$ eV and plotted against the corresponding values of pd and illustrated in figure 7.10. Comparing the exponential fit to equation 7.6, the effective collisional cross section for high-energy O^- ions traversing an 80:20 Ar/O_2 discharge

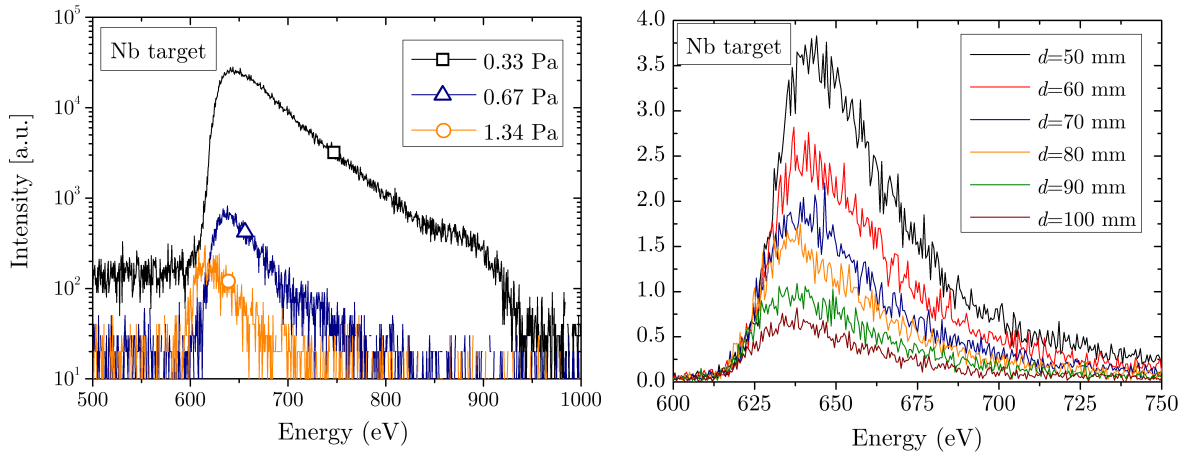

Figure 7.9. The high energy population of the energy distributions of O^- ions measured for (a) different pressures at a constant $d = 100$ mm, and for (b) different target-to-substrate distances, d, for a constant $p = 0.67$ Pa obtained during reactive HiPIMS of Nb.

during reactive HiPIMS of Nb was found to be $\sigma_{t,Nb} = 2.1 \times 10^{-19}$ m^2. As the effective cross sections are approximately equal for Ti and Nb targets, it is suggested that the gas-phase transport of O^- is independent of the target material. This may not be the case for higher power densities or longer pulse widths where the displacement of the process gases in-front of the target surface and its subsequent replacement by metal gas is more pronounced.

Both effective cross sections are almost a factor of 2 smaller than the collisional cross section as calculated by assuming the approximations as outlined above (3.9×10^{-19} m^2). The measured total effective cross section is found to be smaller for a number of possible reasons. In the treatment above, no angular dependence is taken into account. It is possible that some O^- ions are still detected by the EQP after experiencing very small angle deflections, resulting in a lower measured cross section. Furthermore, local gas heating in the vicinity of the target and gas rarefaction effects (see [185]) have been ignored.

Gas heating and rarefaction in DCMS has been widely reported [185–189] but investigations in HiPIMS are not as fully developed. Due to the higher sputtered flux and stronger 'sputter wind' during the pulse on-phase in HiPIMS, it is expected that the gas heating and rarefaction effects may be exaggerated in comparison to DCMS. Simulations by Kadlec [64] predicted the transfer of momentum from sputtered Ti atoms to Ar gas atoms can result in heating of the neutral gas up to approximately 1 eV ($\approx 11,000$ K) in the vicinity of the target erosion track. This supposition has been supported by spatio-temporally resolved optical imaging of plasma emissions as performed by Liebig *et al.* [65] and Hecimovic *et al.* [66], where both sets of authors observed a decrease in the Ar^0 neutral emissivity above the target surface during the pulse on-phase of HiPIMS operation.

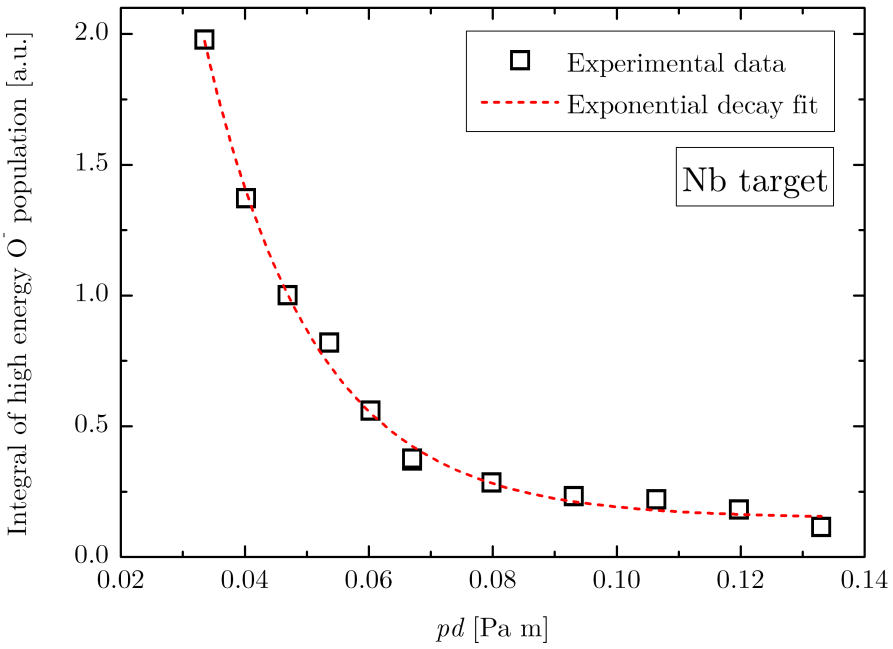

Figure 7.10. The integral of the high-energy population ($E > 550$ eV) of O^- ions plotted against the pressure-distance product (Nb target).

Furthermore, Horwat and Anders [59] used current-time waveforms as evidence for strong gas compression and rarefaction effects in the pre-target region for HiPIMS of copper in argon. It was also suggested by the same authors that another, more straightforward effect may contribute to gas heating. An elevated target surface temperature due to previous HiPIMS pulses may be responsible for local gas heating and density reduction. Indeed, this effect has been reported by Anders [40] for a hot Nb target. It is possible that the decrease in the number of high energy O^- ions detected when increasing the target-to-orifice distance is less pronounced than anticipated due to the assumption of a uniform gas density and temperature distribution.

Knowledge of the attenuation of high energy negative ions at the substrate with respect to controlled discharge conditions (i.e. pressure and target-to-substrate distance) may be utilized in order to suppress or even eliminate the detrimental effects caused to growing films by the bombardment of high energy negative ions. One possible method would be to increase the effective collisional cross section via the introduction of heavier rare gases such as Kr or Xe, which is discussed in §7.3.6. However, in addition to reducing the impingement of high energy negative ions at the substrate this may also have consequences, detrimental or otherwise, for the deposition rate. Deposition rate measurements in reactive HiPIMS in different inert gases mixed with O_2 are discussed further in chapter 8.

7.3.4 Changing pulse width

The applied target potential and discharge current waveforms for different pulse widths ($\tau = 40 - 200$ μs, in increments of 20 μs) are shown in figure 7.11 for a fixed initial target potential $V_0 = 670$ V and fixed repetition frequency, $f = 100$ Hz. The oxygen partial pressure was also maintained constant at 20% of the total pressure, 0.4 Pa. The orifice of the EQP was positioned directly above the target racetrack at a distance of 100 mm away from the target surface. The energy per pulse, E_p, ranged from 0.36 to 1.75 J corresponding to average discharge powers, $\overline{P_d} = 36$ to 175 W for increasing τ.

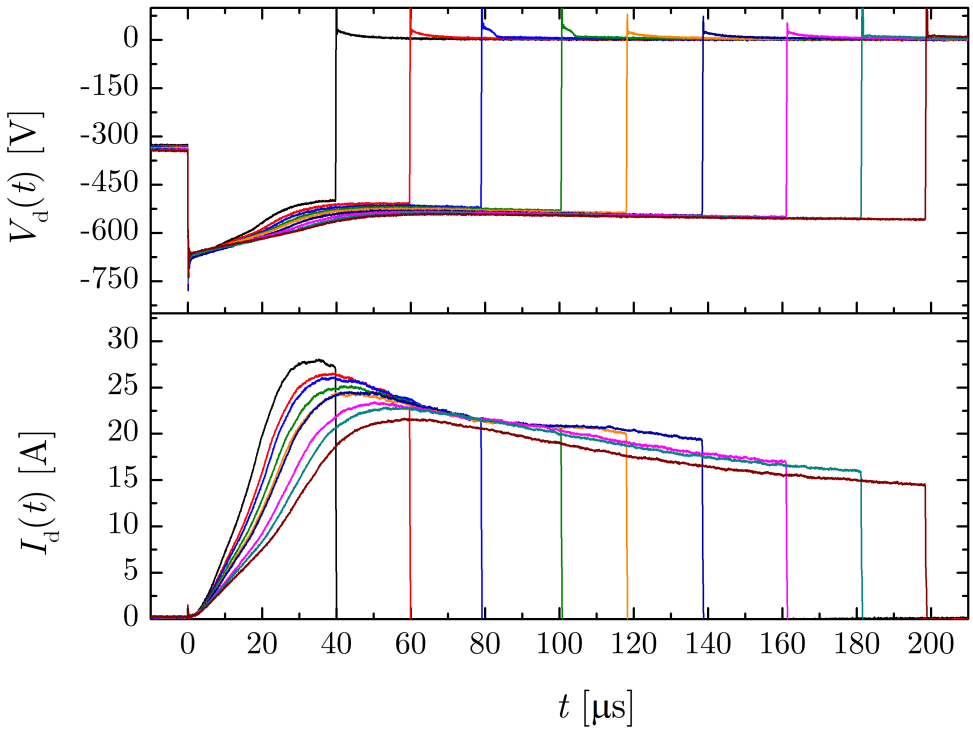

Figure 7.11. Temporal evolution of $V_d(t)$ and $I_d(t)$ for different pulse widths, τ.

The time-averaged energy distributions of the high energy population of O^- ions obtained for different τ are shown in figure 7.12a. To avoid clutter, only cases for $\tau = 40$, 80, 120, 160 and 200 μs are shown. The arrows indicate the average absolute applied target potential during the pulse on-time for $t > 20$ μs, which is observed to increase from 501 V to 553 V for increasing τ and is almost exactly coincident with the peaks of the high-energy population of the O^- IEDs. The differences in V_d for different τ are not significant early in the pulse, but are more pronounced in the latter stages of the pulse, where I_d is high and the discharge is in a quasi-steady state. During this period of high I_d, sputtering will be more intense than in the initial stages of the discharge pulse ($0 < t < 20$ μs) and it is from here that the changes in the position of the peak of the high energy population in the O^- IED originates. This suggests that the emission of high energy O^- ions from the target surface is influenced heavily by the number of ions arriving at the target, further

supporting the notion of high energy O^- ions being sputtered from the target surface prior to acceleration rather than simply desorbed and subsequently accelerated in the cathode sheath.

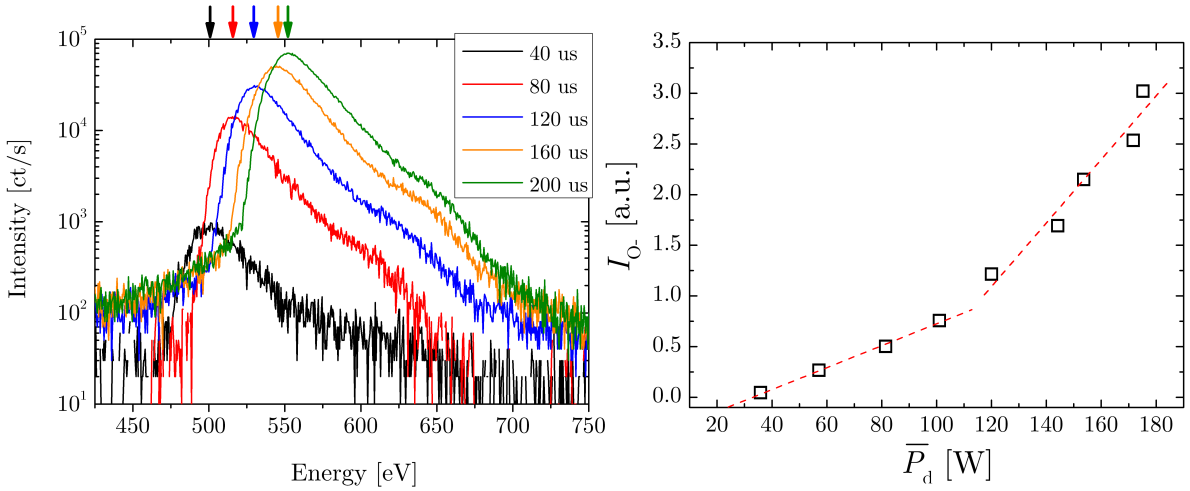

Figure 7.12. (a) The high energy population of the measured O^- ion energy distributions (IEDs) for different pulse widths, τ, and (b) the integral of the high energy population of the O^- IEDs shown in (a) plotted against the corresponding average discharge power, $\overline{P_d}$ measured for different τ.

To obtain a measure of the amount of O^- ions, the energy distribution was integrated for $E > 425$ eV and plotted against the average discharge power for changing τ as illustrated in figure 7.12b. The amount of O^- ions detected at a grounded substrate (in this case, the EQP orifice) is observed to have a two-fold linear relationship with $\overline{P_d}$. The slope of the linear fit to the data points for $\overline{P_d} > 100$ W, is larger than the slope of the linear fit to data points at lower average discharge powers. At higher power densities, the abundance of multiply-charged ions in HiPIMS discharges is expected to increase. The multiply-charged ions liberate more secondary electrons via Auger neutralization and subsequent electron emission as a result of an increased ionization potential compared with singly-charged ions [36]. As discussed below, the ion-induced secondary electron emission coefficient is correlated to the emission of O^- ions [19] and it is suggested that due to a greater population of multiply-charged ions a greater yield of O^- is observed. This suggestion is tentative at present and warrants further investigation.

Here it has been determined that the emission of high energy O^- ions increases with $\overline{P_d}$, however the average discharge power is not the only factor contributing to negative oxygen ion emission. Another important parameter to consider is the secondary electron emission yield, γ_{se}, which is considered constant for a fully poisoned Ti target (i.e. completely covered in a titanium oxide layer) and identical gas mixture of Ar/O_2 in an 80:20 ratio in the studies shown so far in this chapter. In the next sections, changes in γ_{se} must be considered as the target material and gas mixtures are varied, both of which influence γ_{se}. Changes in sputter yields for different target material and process gas combinations

must be considered and the gas-phase transport may also be important for different gas mixtures. These effects are discussed below.

7.3.5 Target effects

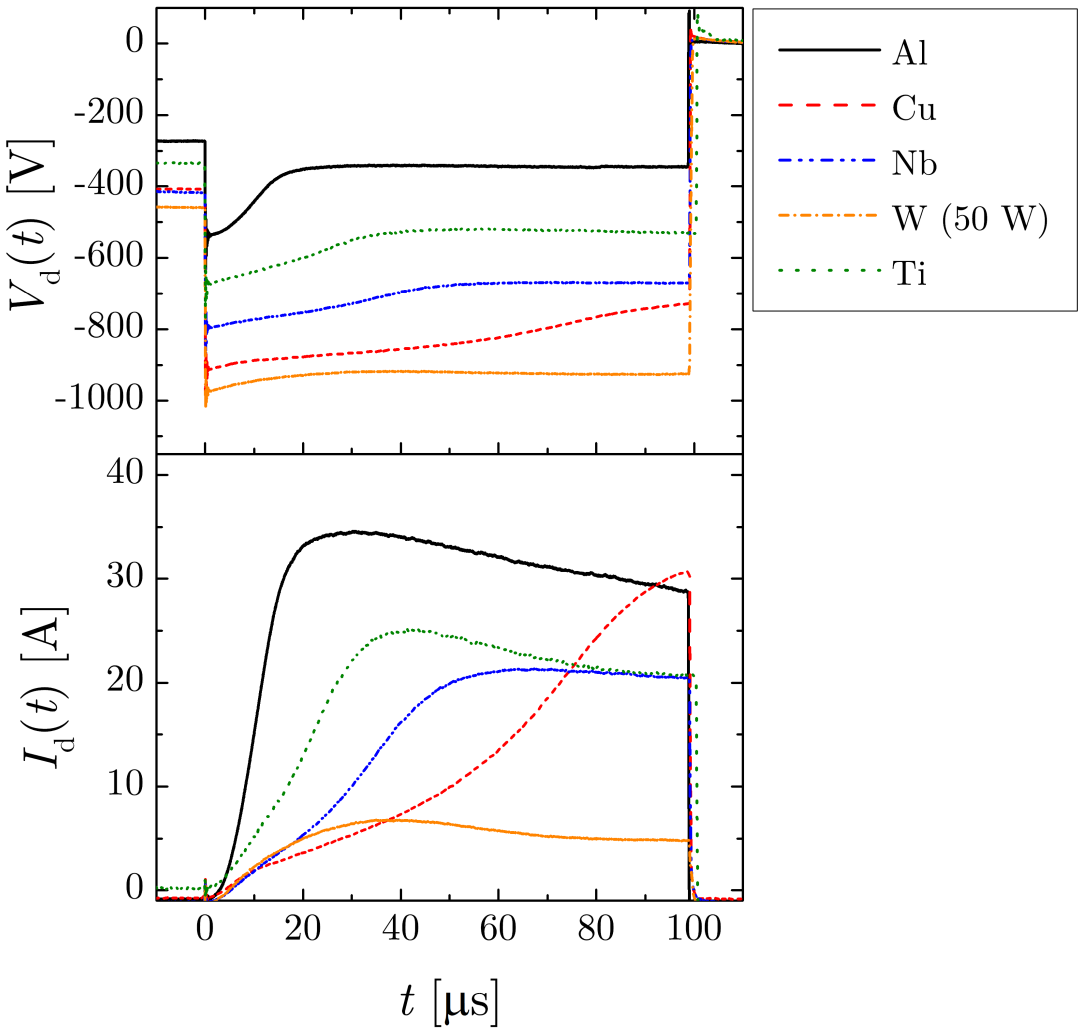

Figure 7.13. The temporal evolution of the applied target potential, $V_d(t)$, and discharge current, $I_d(t)$, during the reactive HiPIMS of Al, Cu, Nb, W and Ti in an Ar/O_2 discharge. The averaged discharge power, $\overline{P_d}$, was maintained at 100 W for Al, Cu, Nb and Ti targets, and 50 W for the W target.

The energy distributions of O^- ions were measured during reactive HiPIMS of five different target materials (Al, Cu, Nb, Ti, W) in an Ar/O_2 gas mixture. In all cases, the same discharge pulse parameters were used ($\tau = 100$ μs, $f = 100$ Hz) and the oxygen partial pressure was kept constant such that $p_{O_2}/p_{total} = 0.2$ where $p_{total} = 0.4$ Pa. The average discharge power, $\overline{P_d}$, was maintained at 100 W, however, $\overline{P_d} = 50$ W was used for the W target due to the low discharge current drawn. Waveforms of $I_d(t)$ and $V_d(t)$ measured

during reactive HiPIMS of the different target materials are shown in figure 7.13. Averaged over the full target area, (A_t = 44 cm^2), the peak current density, j_{peak} = 0.16 − 0.79 A cm^{-2} with the highest recorded value for the Al target and lowest for the W target.

The energy spectra of O^- ions recorded during reactive HiPIMS of Al, Cu, Nb, Ti and W are shown in figure 7.14. During acquisition, the orifice of the EQP was positioned directly above the target racetrack at a distance of 100 mm away from the target surface. The peak of the high energy population approximately corresponds to the average value of the the discharge potential during the pulse on-time (shown as a dashed line), although the peak occurs at a somewhat smaller energy due to the negative ions having to overcome the potential in the sheath at the grounded EQP orifice.

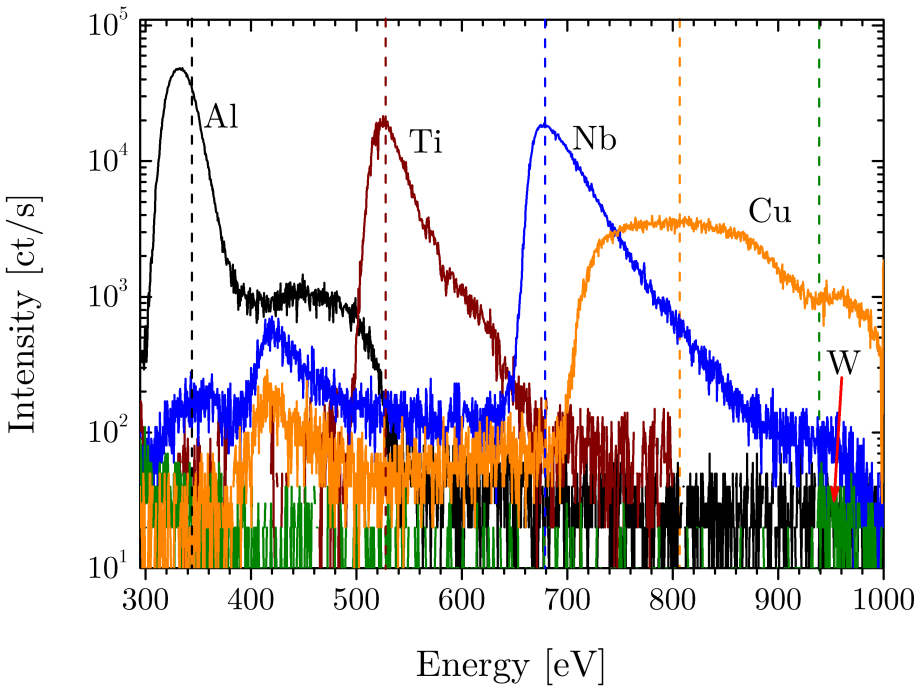

Figure 7.14. Energy distributions of the high energy O^- population for different targets used in reactive HiPIMS in an Ar/O_2 gas mixture. The dashed lines represent the corresponding average discharge potential during the pulse on-time.

After analysing the variations in the discharge voltage during the transition from poisoned to metallic mode in reactive magnetron sputtering, Depla *et al.* [88] calculated values of the ion-induced secondary electron emission (ISEE) coefficient for different oxidised target materials. Mahieu and Depla [19] extended this study to show that the emission of O^- ions is strongly correlated to the ISEE coefficient in reactive DC magnetron sputtering.

It is assumed that the amount of O^- ions formed at the target surface is proportional to the integral of the high energy population, I_{O^-}. The O^- ion energy distributions in

figure 7.14 were integrated for $E > 295$, 425, 625, 675 and 900 for the Al, Ti, Nb, Cu and W targets, respectively, to obtain values of I_{O^-}. Following [19], the difference in sputtering yields is compensated for by dividing I_{O^-} by the total number of sputtered O atoms, as given by

$$N_O = I_+ Y_{total} \frac{z}{1+z} \tag{7.7}$$

where Y_{total} is the total sputtering yield, z is the stoichiometry of the metal oxide (MO_z), and I_+ is the positive ion current at the target, calculated from $I_+ = \overline{I_d}(1+\gamma_{se})^{-1}$ with $\overline{I_d}$ being the average discharge current during the pulse on-time. Sputtering during the off-time due to the pre-ionizer is ignored as it does not contribute to the high energy population in the O^- energy distribution due to the lower applied target potential compared with the on-time. Values of Y_{total} and γ_{se} were taken from [88] for the Ti, Nb, Al and Cu targets. For the W target, $Y_{total} = 0.3$ is taken from [190] and $\gamma_{se} = 0.041$ from [191]. The values of I_{O^-}/N_O are plotted against corresponding γ_{se} in figure 7.15.

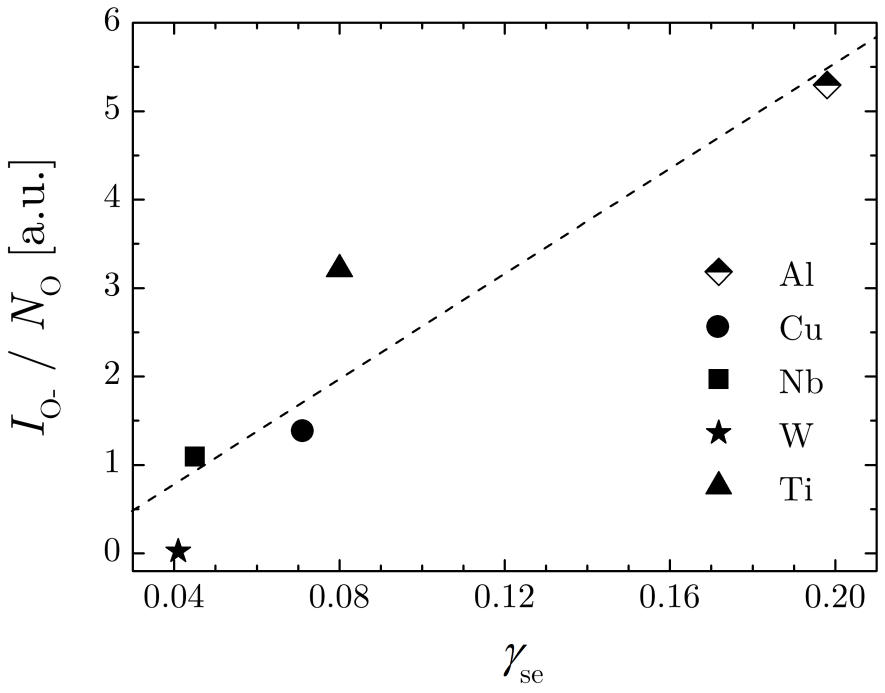

Figure 7.15. Plot of the measured O^- ion yield, I_{O^-}/N_O, for the different target materials against the corresponding secondary electron emission coefficient, γ_{se}.

From figure 7.15 and consistent with [19], there is an evident relationship between high energy O^- ion emission and the ISEE coefficient. Previous studies by Vogan *et al.* [192, 193] had previously reported a relationship between the emission of secondary electrons and the yield of O^- ions, however, ion-induced potential secondary electron

emission was precluded due to the use of Na^+ ions which possess insufficient ionization energy to liberate an electron via the Auger mechanism [194]. For magnetron sputter deposition, inert gases with high ionization energies are typically used, hence potential electron emission cannot be neglected; the results presented here and in [19] are therefore more applicable to many plasma processing systems.

7.3.6 Inert gas effects

The ion-induced secondary electron emission is dependent upon both the target material, its condition [37] and the ionization potential, $\mathcal{E}_{iz}$, of the bombarding ion. All of the studies discussed thus far in this chapter have incorporated the same gas mixture (i.e. Ar/O_2 with $p_{O_2}/p_{total} = 0.2$) and so any effects of ionization potential on the emission of secondary electrons (and O^- ions) have been neglected. However, by varying the inert gas mixed with oxygen, it is possible to investigate these effects.

During the reactive HiPIMS of Ti in a gas mixture of X/O_2 where X = Ne, Ar, Kr or Xe, all pulse parameters were maintained constant ($\tau = 100$ μs, $f = 100$ Hz and $\overline{P_d} = 100$ W), with the exception of the Xe/O_2 gas mixture where only a maximum $\overline{P_d} = 50$ W was achievable whilst maintaining constant f and τ. As before, the total operating pressure was maintained at 0.4 Pa with a 20% O_2 partial pressure and the orifice of the EQP was located at a distance of 100 mm away from the target surface and above the racetrack. Figure 7.16 shows the $I_d(t)$ and $V_d(t)$ waveforms for the different gas mixtures.

The O^- ion energy distributions measured during the reactive HiPIMS of Ti in discharges of the different gas mixtures described above are shown in figure 7.17. From figure 7.17, it is clear that where X = Ne and Ar, significant amounts of high energy O^- ions are detected. In contrast, for X = Kr and Xe, relatively small amounts of O^- are observed at high energies.

As in §7.3.5, a measure of the amount of high energy O^- ions, I_{O^-}, is obtained by integrating the high energy population of the energy distribution. The sputtering yield is compensated for (see equation 7.7) with values of Y_{total} for the different incident ions estimated using SRIM [183]. The yield of high-energy O^- ions divided by the number of sputtered oxygen atoms, I_{O^-}/N_O, is plotted against the ionization energy of the inert gas used, $\mathcal{E}_{iz}$, in figure 7.18. The number of O^- ions emitted from the target surface is observed to increase with $\mathcal{E}_{iz}$.

As reported by Baragiola *et al.* [36], the potential secondary electron emission from metal surfaces for different incident ions satisfies a least-squares fit described by equation 2.5 and reproduced here:

$$\gamma_{se,p} \approx 0.032\,(0.78\mathcal{E}_{iz} - 2\phi) \tag{7.8}$$

where ϕ is the work function of the metal. ϕ is assumed constant since the target condition

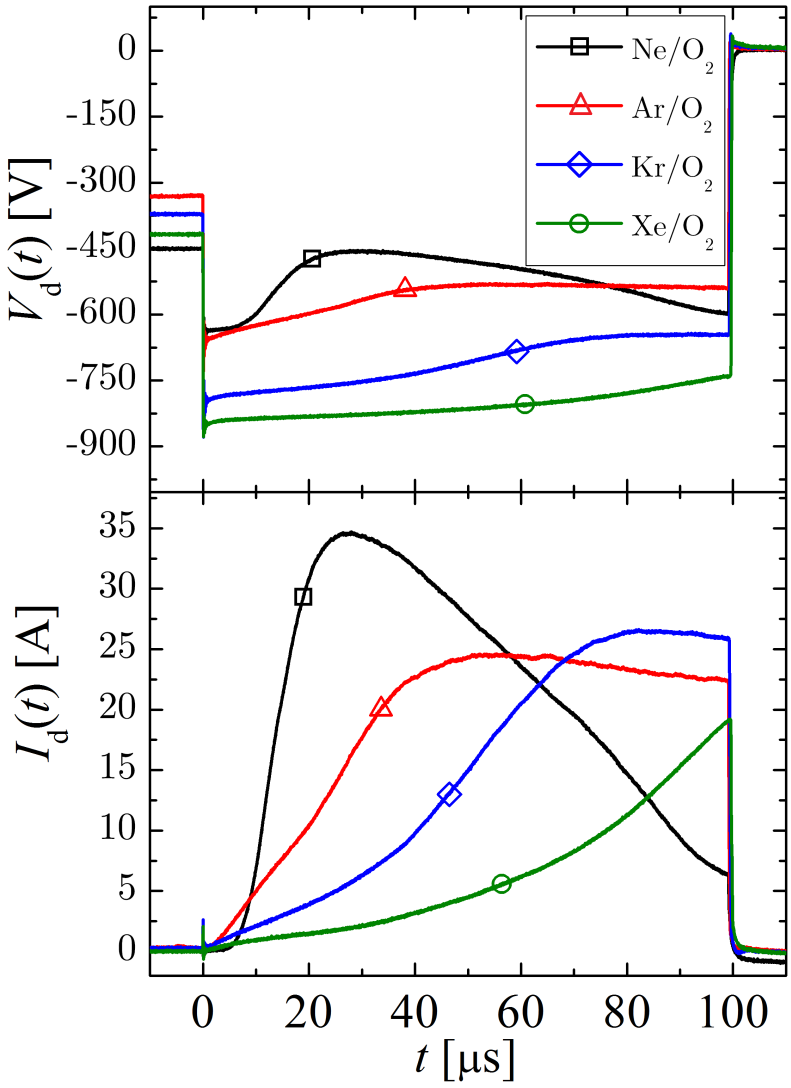

Figure 7.16. The temporal evolution of $V_\mathrm{d}(t)$ and $I_\mathrm{d}(t)$ measured during the reactive HiPIMS of Ti in gas mixtures of $X/\mathrm{O_2}$ where X = Ne, Ar, Kr or Xe.

is nominally identical for each of the gas mixtures used. That is to say that any significant changes in $\gamma_\mathrm{se,p}$ between the different inert gases mixed with oxygen is expected to arise from changes in $\mathcal{E}_\mathrm{iz}$. Even though kinetic electron emission may be important for oxide-covered surfaces for low-energy ion bombardment ($E < 1$ keV) [37], potential electron emission will be considerable due to its lower energy threshold and any changes in $\gamma_\mathrm{se,p}$ are likely to be correlated to $\mathrm{O^-}$ ion emission as in figure 7.15 and in [19]. Accordingly, for increasing $\mathcal{E}_\mathrm{iz}$ of the sputtering ions an associated increase in $\mathrm{O^-}$ emission can be expected.

For different gas compositions, the gas-phase transport of $\mathrm{O^-}$ ions from the target surface to the substrate changes. For a known composition, it is possible to approximate

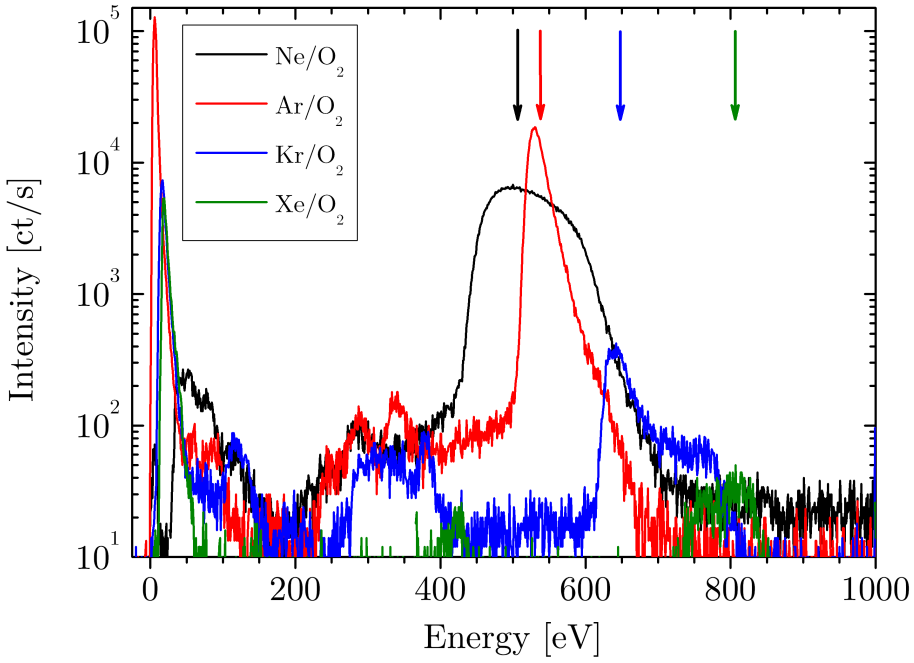

Figure 7.17. Energy distributions of the high energy O^- population obtained during reactive HiPIMS of Ti in gas mixtures of X/O_2 where X = Ne, Ar, Kr or Xe. The arrows indicate the corresponding average value of V_d during the pulse on-time.

the probability of a particle ejected from the target reaching the substrate. In a similar fashion to the simple hard sphere model presented in §7.3.3, the mean free path of O^- ions traversing the chamber can be expressed as

$$\lambda = \frac{1}{n_{O_2}\sigma_{O_2} + n_X\sigma_X} \tag{7.9}$$

where n_{O_2} and n_X are the neutral gas densities of oxygen and species X, respectively. The collisional cross sections of O_2 and X interacting with O^- ions are denoted by σ_{O_2} and σ_X, respectively. Cross sections are calculated using $\sigma_i = \pi\left(r_{O^-} + r_i\right)^2$ where the radii were approximated to the van der Waals radii as follows: $r_{O^-} = 176$ pm, $r_{Ar} = 188$ pm, $r_{O_2} = 152$ pm, $r_{Ne} = 154$ pm, $r_{Kr} = 202$ pm and $r_{Xe} = 216$ pm [195]. For a known target-to-substrate distance ($d = 100$ mm), the probability of an O^- ion impacting the substrate can be estimated by

$$\chi = \exp\left(-\frac{d}{\lambda}\right). \tag{7.10}$$

Using the assumptions above and considering no other loss mechanisms, the O^- yield directly from the target can be obtained by multiplying the measured I_{O^-} by a correction factor of χ^{-1}. The values of $I_{O^-}/\chi N_O$ are plotted against the ionization energies of the

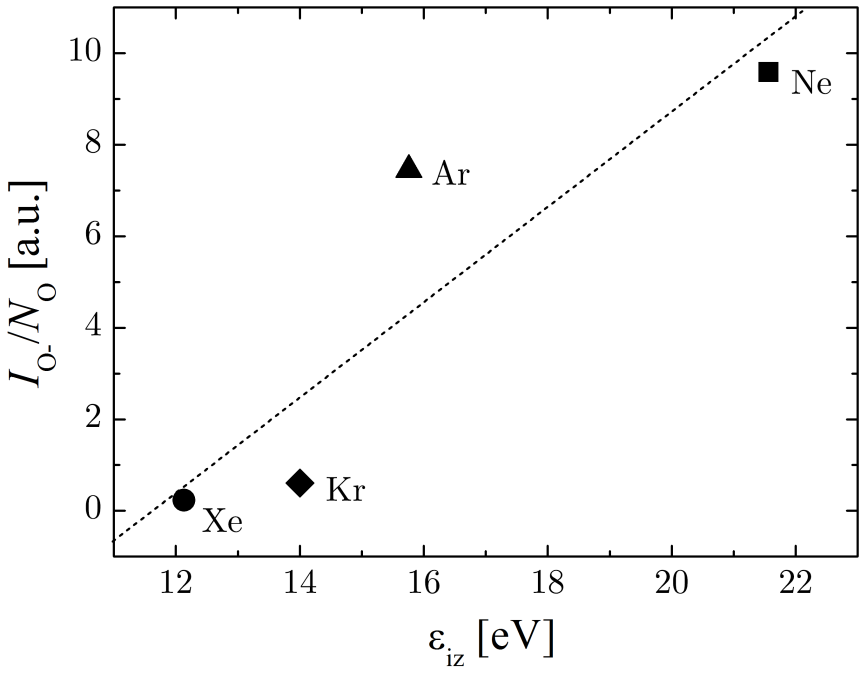

Figure 7.18. Experimentally determined O^- yield, I_{O^-}/N_O, as a function of the ionization energy, $\mathcal{E}_{iz}$, of X in the X/O_2 gas mixture.

corresponding inert gases mixed with O_2 in figure 7.19. When the gas-phase transport is corrected for, the case of Ne/O_2 deviates significantly from the linear trend connecting the points representing X = Ar, Kr and Xe. From figure 7.16, there is a current peak in the initial stages of the Ne/O_2 discharge pulse followed by a steady decline in $I_d(t)$. It is possible that the erosion of the oxide layer during this period of intense sputtering prevents the formation of significant amounts of O^- ions at the target surface.

So far, it has been assumed that the inert gas ion is the primary sputtering ion and any changes in the ion-induced secondary electron emission have been related directly to the ionization potential of the inert gas. However, by changing the inert gas it is probable that the ion composition will also vary. Due to differences in the electron impact ionization (EII) cross sections, the fraction of inert gas-to-oxygen ions in the discharge is likely to change for the different gas mixtures. For instance, Ne has a significantly lower EII cross section when compared with O_2, whereas Ar, Kr and Xe possess EII cross sections comparable to that of O_2 at typical sputter ion energies [196]. Therefore, it is reasonable to expect that the ratio of inert gas-to-oxygen ions for the Ne/O_2 mixture will be lower than for O_2 mixed with Ar, Kr or Xe. A reduction in this ratio would shift the average ionization potential of the sputtering species toward the value for oxygen (13.62 eV for atomic oxygen) thereby influencing the effective ion-induced secondary electron emission coefficient and consequently, the emission of O^- ions from the target surface. Considering the changing ion composition, a change in the effective ionization potential of the sputter

ion may account for the anomalous data point for the Ne/O_2 gas mixture illustrated in figure 7.19. With a lower effective ionization potential, the Ne data point would be more in line with the trend exhibited by the other three gas mixtures.

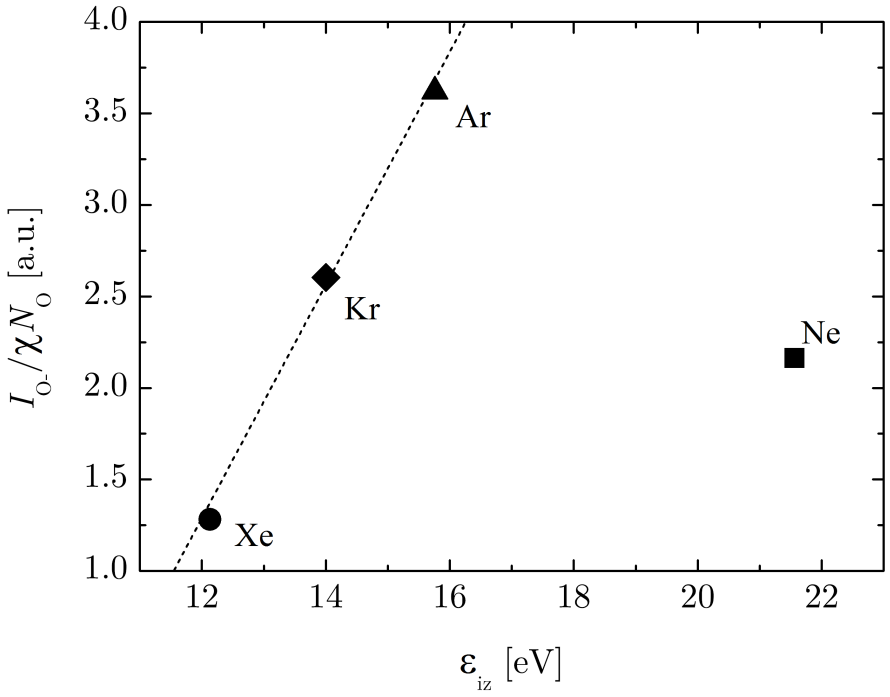

Figure 7.19. Experimentally determined O^- yield with correction factor compensating for the gas-phase transport, $I_{O^-}/\chi N_O$, as a function of the ionization energy, $\mathcal{E}_{iz}$, of X in the X/O_2 gas mixture.

Despite the simplified treatment, a clear correlation between O^- emission and both γ_{se} and $\mathcal{E}_{iz}$ was found for different target materials and different inert gases mixed with O_2, respectively. The results presented here highlight the importance of choosing a suitable target material for applications where the emission of high energy negative ions may influence the growing thin film or be detrimental to the application. For example and as briefly discussed in [19], when choosing materials with high γ_{se} for use in plasma display panels it would be prudent to avoid oxides in order to prevent bombardment and destruction of the phosphor layer by high energy O^- ions. Furthermore, it has been shown that it is possible to tailor the flux of high energy O^- ions incident upon a grounded substrate by selecting different inert gases to mix with oxygen during reactive HiPIMS of a specific target material. The latter may be important when depositing thin films sensitive to high energy negative oxygen ion bombardment, such as AZO films where an increase in resistivity was observed for films bombarded by high energy negative oxygen ions [23].

7.4 Conclusions

The energy distributions of negative ions have been measured for reactive high power impulse magnetron sputtering of a Ti target in an Ar/O_2 atmosphere where $p_{O_2}/p_{total} = 0.2$ operating in the fully poisoned mode for different discharge parameters. As expected, it was found that O^- is the most abundant negative species by approximately an order of magnitude. Furthermore, the energy distribution of O^- ions could be divided into three broad energy categories; low-, medium- and high-energy. Energy distributions of compound species were also obtained and it was concluded that TiO_2^- and TiO_3^- are generated almost exclusively at the target surface and are released from the target by ion-assisted desorption.

From comparing the high energy population of O^- ions at different average discharge powers, it was found that neither a theoretical Thompson distribution nor a current-weighted target potential distribution is sufficient when describing the shape of the high energy population. It is therefore suggested that, akin to the discussion presented by Mahieu *et al.* [110], O^- ions undergo electron attachment prior to or during the sputtering event. After sputtering, the O^- ions are subsequently accelerated by the cathode fall and experience collisions with background gas particles en route to the substrate hence shifting the high energy region of the O^- ion energy distribution away from a Thompson energy distribution.

By changing the target-to-substrate distance and chamber pressure, it was found that the integrated intensities of the high energy O^- ions are a function of the pressure-distance product. The effective collisional cross section of high energy O^- ions interacting with an 80:20 background gas mixture of Ar and O_2 respectively is $\sigma_t \approx 2 \times 10^{-19}$ m^2 for both Ti and Nb targets. It is suggested that the measured cross section appears smaller than the expected value of 3.9×10^{-19} m^2 due to strong local gas heating and density reduction effects in the pre-target region.

Increasing the voltage pulse width increased the average discharge power for a constant initial target potential, as I_d is given more time to evolve. This increase in $\overline{P_d}$ resulted in a higher yield of high energy O^- ions detected at a grounded substrate, with the peak energy shifting in accordance with the absolute average cathode potential applied during steady-state region of the discharge pulse.

Consistent with results reported by Mahieu and Delpa [19], a correlation between O^- emission and the ion-induced secondary electron emission coefficient of different target materials was found. In addition, large differences in O^- yield were also observed when employing different inert gases mixed with O_2. The decreased high energy O^- ion flux detected by the EQP for gas mixtures incorporating heavier inert gases was attributed to their lower ionization energies and consequently lower potential electron emission coefficients. Both of these observations may have important consequences for

reactive magnetron sputter deposition of thin oxide films sensitive to high energy O^- ion bombardment. Although it may be desirable to control the yield of high energy O^- ions by changing the working gas mixture, the choice of inert gas also influences the development of the growing film and, more importantly from an economical perspective, the deposition rate. These factors must also be considered and indeed, the deposition rate as measured during the reactive HiPIMS of Ti in discharges mixed with oxygen and different inert gases is discussed in the next chapter.

Chapter 8

Inert gas effects on the deposition rate during reactive HiPIMS

8.1 Introduction

Possibly the main drawback of HiPIMS, is the almost universally reported reduced *power normalized* deposition rate when compared with conventional direct current magnetron sputtering (DCMS). The normalized deposition rate for non-reactive HiPIMS has been observed to be typically $30 - 85\%$ [45, 197] of the value measured during equivalent DCMS operation. There are several mechanisms thought to be responsible for this apparent reduction in deposition rate and they have been the subject of some recent publications [44, 198]. Due to the increased ionization of sputtered species that occurs in a HiPIMS discharge there exists a so-called *return effect* whereby a non-negligible fraction of the ionized sputtered material is back-attracted to the target surface [44, 198, 199]. Another major issue is the less than proportional scaling of the sputter yield with incident ion energy, often referred to as the *yield effect* [44, 68]. HiPIMS typically employs higher absolute target potentials when compared with DCMS and hence lower average ion currents are necessary for the same time-averaged power. The deposition rate is typically proportional to the sputter yield; however the sub-proportional scaling of sputter yield with incident ion energy results in a decreased normalized deposition rate for increased absolute target potential values. Other effects include the ion species effect [44], transport effects [50, 51], coating effects [44, 45], power-switching effects [44] and magnetic field effects [198]. Anders [44] has presented a detailed treatment of the main mechanisms affecting the deposition rate during non-reactive HiPIMS. Also, Vlček and Burcalová developed expressions for deposition rates in a phenomenological model for HiPIMS [200].

In reactive HiPIMS, the composition of the discharge and the extent of the target coverage/poisoning are important aspects to consider. In the case of sputtering oxides, the oxygen reacts with the target surface to varying degrees mostly dependent upon the ion

contribution to the discharge current and the reactive gas flow rate resulting in a metallic target partially or completely covered with a compound layer. It is known that many oxide compounds suffer from a lower deposition rate than their pure metal counterparts [201] and so the reduced normalized deposition rate in HiPIMS when compared with DCMS can be of great concern in reactive sputtering.

As discussed in previous chapters, large amounts of high energy negative ions are generated during reactive DCMS [17, 20, 110, 116, 117] and reactive HiPIMS [158] in the presence of electronegative gases such as oxygen. It is possible that the bombardment of the substrate by the high-energy population of the negative ions will lead to resputtering of the growing film and result in a reduction of the effective deposition rate. Despite this, there are some promising aspects of reactive HiPIMS including hysteresis-free operation [69] and even deposition rates measured to be higher than those achieved in the equivalent DCMS process [12, 69, 202]. For example, Sarakinos *et al.* [69] found that the deposition rate of TiO_x thin films increased by up to 40% for HiPIMS of a $TiO_{1.8}$ target when compared with DCMS. Also, the measured deposition rates during the assisted HiPIMS of titanium have been correlated to the crystal formation phase of the deposited TiO_2 [203], meaning the deposition rate could be potentially used as a control parameter.

The work presented in this chapter focuses on the measured static normalized deposition rates of titanium oxide during reactive HiPIMS of titanium in a gas mixture of X/O_2, where X = Ne, Ar, Kr or Xe. The primary mechanisms affecting the deposition rate are briefly discussed and deposition rates measured in reactive HiPIMS are compared to measurements made in nominally equivalent reactive DCMS discharges for $d = 100$ mm, and also to those made in equivalent non-reactive (metallic) HiPIMS discharges.

8.2 Experimental set-up

8.2.1 Chamber and magnetron set-up

The vacuum chamber is described in detail in chapter 4. To avoid effects associated with the degree of target erosion, the magnetron was equipped with a new titanium target (99.95% purity) with a diameter of 75 mm and powered by the HiPIMS power supply built in-house, described in detail in §4.1.2. In addition to the HiPIMS power supply, a low power ($\leq$ 10 W) pre-ionization unit was used to facilitate operation at low pressure and to allow for greater reproducibility of pulse waveforms, which is also described in chapter 4 as well as in [75]. By means of an external pulse generator (Thandar TG105), the pulse width τ and frequency f were kept constant at 100 μs and 100 Hz, respectively.

Process gases were introduced into the chamber at flow rates controlled by two independent mass flow controllers (MKS 1179A). The total working gas pressure, $p_{\text{total}} = p_X + p_{O_2} = 0.4$ Pa (X = Ne, Ar, Kr, Xe), was monitored using a capacitance pressure

gauge (MKS 628A). Metallic deposition rates were also recorded for comparison, where $p_{O_2} = 0$, thus $p_{\text{total}} = p_X$. All working gases used in this investigation were of a purity of at least 99.995%. A schematic of the experimental apparatus is given in figure 8.1.

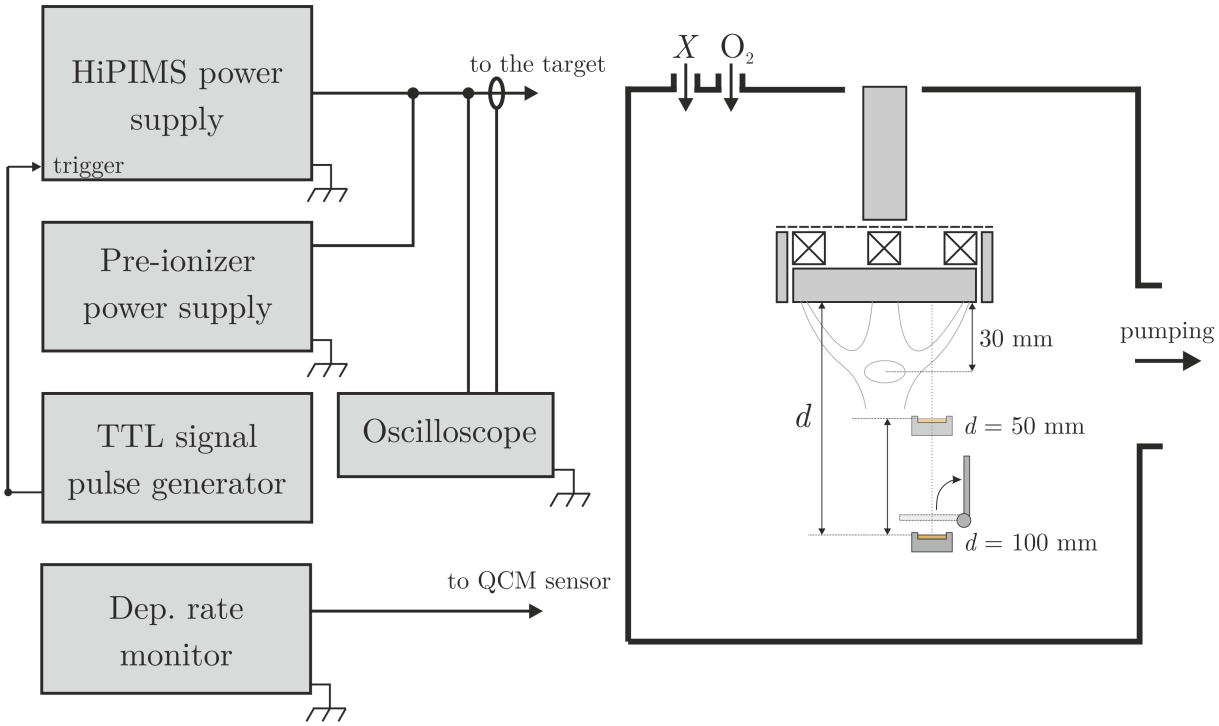

Figure 8.1. Schematic representation of the experimental set-up. The QCM was moved axially with respect to the target into two positions; $d = 50$ and 100 mm. The shield was placed in front of the QCM to prevent deposition on the sensor whilst the discharge was active but no measurements were being recorded.

To obtain the desired oxygen partial pressure during reactive mode, the oxygen flow rate was increased beyond the hysteresis transition from metallic to poisoned mode and then reduced as necessary to maintain a constant oxygen partial pressure; $p_{O_2} = 0.2p_{total}$. The target voltage $V_d(t)$ was measured using a high voltage probe (Tektronix P5100) and the discharge current $I_d(t)$ was measured using a DC coupled current probe (Tektronix TCP202) which were both connected to a digital oscilloscope (Tektronix TDS3014). The average discharge power, $\overline{P_d}$, was monitored in real-time using the same oscilloscope, calculated as the mean of the product of $V_d(t)$ and $I_d(t)$ and controlled by manually varying the initial target potential V_0 provided by the power supply.

8.2.2 Deposition rate measurements

Deposition rates were measured by means of a quartz crystal microbalance (QCM) with the exposed face of the gold-coated sensor crystal (6 MHz) grounded and the opposite side connected to a thin film deposition monitor (Maxtek TM-400, Inficon). The sensor

crystal was placed directly above the racetrack facing the target surface at two different axial distances, $d = 50$ and 100 mm (see figure 8.1). Reading directly from the DAC output of the deposition rate monitor, the film thickness was monitored as a function of time using a voltage probe (Tektronix P6139A) over a period of 500 s. The output range of monitor was 0 to 5 V, corresponding to a thickness range of 0 to 100 Å (i.e. a step of 0.05 V/Å). For calculation of the film thickness, the deposited film was assumed to be stoichiometric titania with a density of 4.26 g/cm^2 during reactive sputtering and pure metallic titanium with a density of 4.51 g/cm^2 for measurements in metallic mode. Prior to any deposition rate measurements, the discharge was operated in metallic mode with a pressure of 0.93 Pa in the presence of the relevant inert gas (zero oxygen flow) for 15 minutes in order to sputter-clean the target surface. For reactive sputter deposition, the oxygen flow was then increased until the desired partial pressure was obtained, before the discharge was operated for a further 15 minutes in order to obtain an equilibrium state. During this run-in procedure, the QCM was protected by a stainless steel shield, which could be removed without breaking vacuum. The same initial procedure was employed for each deposition rate measurement.

8.3 Results and discussion

8.3.1 HiPIMS pulse waveforms

Waveforms of the discharge current $I_\mathrm{d}(t)$ and potential $V_\mathrm{d}(t)$ for the different gas mixtures ($X/\mathrm{O_2}$ where X = Ne, Ar, Kr or Xe) are shown in figure 8.2 alongside the equivalent waveforms measured in metallic mode (zero oxygen flow). The discharge parameters were as follows: $\overline{P_\mathrm{d}} = 100$ W, $f = 100$ Hz, $\tau = 100$ μs, $p_\mathrm{total} = 0.4$ Pa and $p_{\mathrm{O_2}}/p_\mathrm{total} = 0.2$. For the case of $\mathrm{Xe/O_2}$, the average discharge power was maintained at 50 W due to the power supply being unable to maintain an average discharge power of 100 W without lengthening the pulse width τ or increasing the pulse frequency f.

There are some stark contrasts between the reactive and metallic waveforms. In reactive mode, the $\mathrm{Ne/O_2}$ discharge exhibits the highest discharge current peak (~ 35 A), whereas during the sputtering of Ti using only Ne, the discharge current peak is much lower (~ 20 A). The measured discharge current waveforms during metallic sputtering in Ar and Kr discharges both show evidence of an initial peak which may be associated with gas compression and rarefaction [59]. Such peaks in $I_\mathrm{d}(t)$ don't occur for the $\mathrm{Ar/O_2}$ and $\mathrm{Kr/O_2}$ mixtures, which may be a consequence of a reduced sputter yield and thus a lower degree of gas rarefaction. Also evident from figure 8.2 is a clear increase in V_d for heavier inert gases mixed with $\mathrm{O_2}$ to maintain a constant average discharge power. The increase in the absolute target potential can be attributed to the lower secondary electron emission yield γ_se for heavier inert gases. The differences in $V_\mathrm{d}(t)$ for inert gas only discharges are

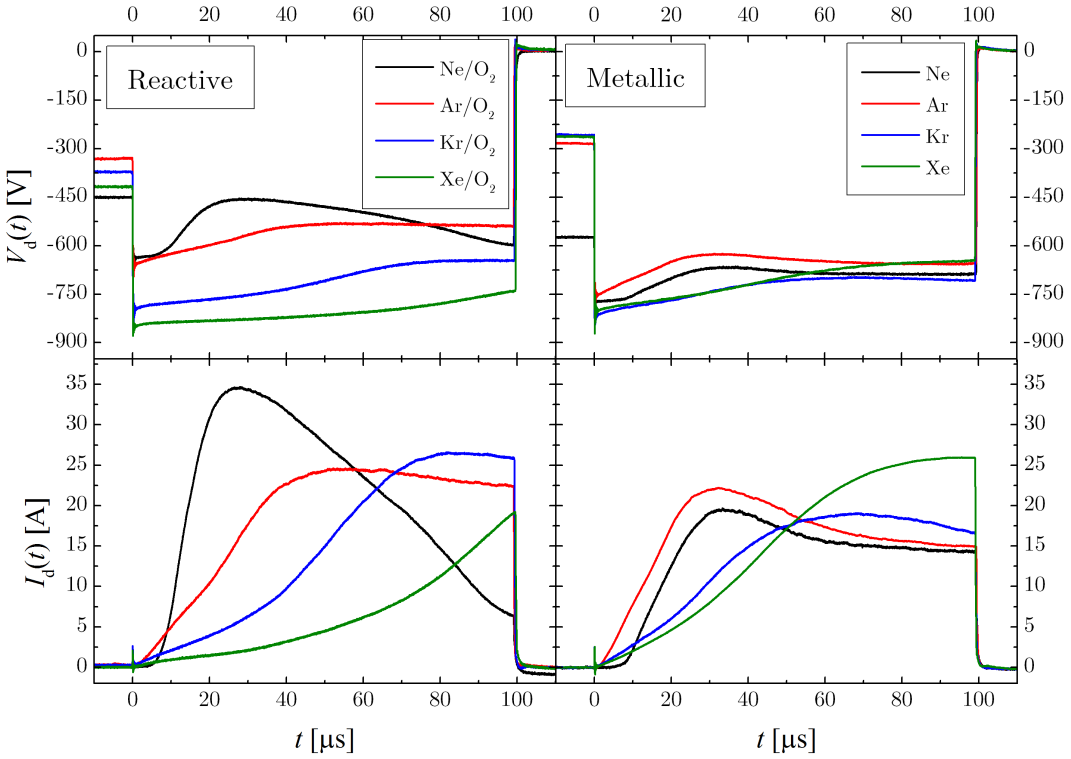

Figure 8.2. The discharge current and potential waveforms for the reactive and metallic HiPIMS discharges in the presence of the indicated gas mixtures. The average discharge power was maintained at a constant $\overline{P_\mathrm{d}} = 100$ W for the all cases, with the exception of Xe/O_2 where $\overline{P_\mathrm{d}} = 50$ W.

much less pronounced.

As discussed in §7.3.6, less energy is released during neutralization of heavier inert gases which results in a lower ion-induced potential secondary electron emission yield, $\gamma_{\mathrm{se,p}}$. Since all reactive discharges were operated in poisoned mode, changes in the secondary electron emission due to the target condition are ignored as the target is assumed, in all cases, to be completely covered by an oxide layer. Neglecting kinetic electron emission for values of $V_\mathrm{d} < 1$ kV [44], then $\gamma_{\mathrm{se}} \approx \gamma_{\mathrm{se,p}}$ and the absolute potential applied to the target necessary to achieve a constant power would be larger for discharges containing heavier inert gases. The reduced average discharge current for heavier inert gas species is a consequence of maintaining a constant time-averaged discharge power using a larger target potential. The averaged discharge potential during the pulse on-phase was calculated as

$$\overline{V_\mathrm{d}} = \frac{1}{\tau}\int_0^\tau V_\mathrm{d}(t)\,\mathrm{d}t \tag{8.1}$$

and the average discharge current density was evaluated by

$$\overline{j_\mathrm{d}} = \frac{1}{A_\mathrm{t}\tau}\int_0^\tau I_\mathrm{d}(t)\,\mathrm{d}t \tag{8.2}$$

where A_t is the area of the target (44 cm^2). Figure 8.3 shows the average target potential

and average discharge current density during the pulse on-time calculated from the waveforms shown in figure 8.2 plotted against the mass of the inert gas. In reactive mode, the average target voltage during the pulse on-time varies significantly between the gas mixtures, ranging from $\overline{V_\mathrm{d}} = 521$ V for Ne/O_2 to $\overline{V_\mathrm{d}} = 807$ V for Xe/O_2 with corresponding average current densities ranging from $\overline{j_\mathrm{d}} = 0.46$ to 0.14 A/cm^2. In metallic mode, the variation is less apparent with $\overline{V_\mathrm{d}} = 650 - 728$ V and $\overline{j_\mathrm{d}} = 0.30 - 0.36$ A/cm^2 across the different inert gas discharges.

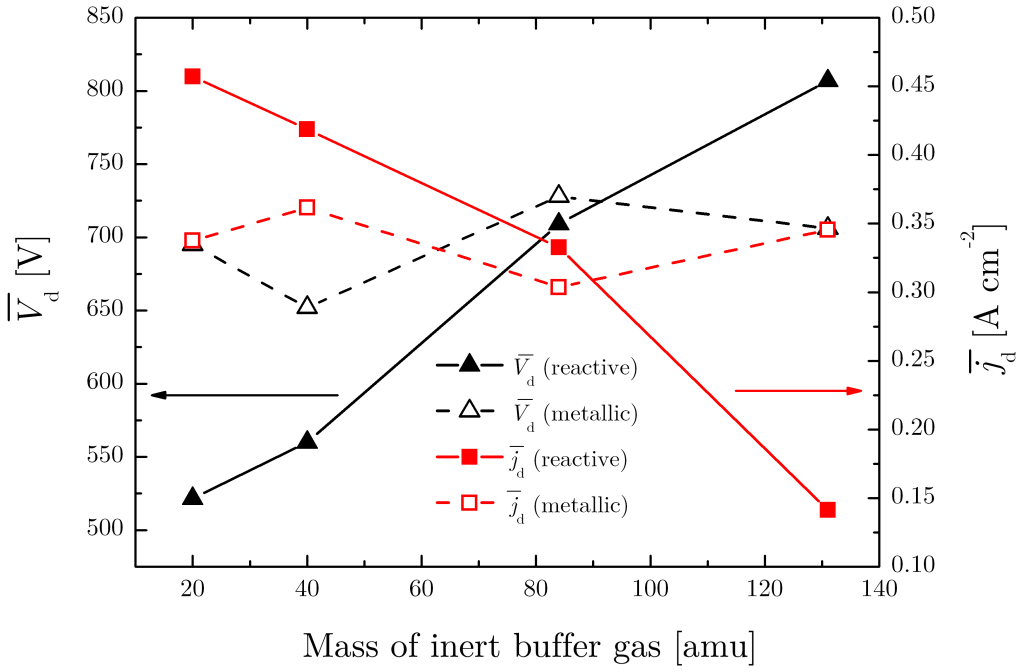

Figure 8.3. The average pulse values of the target potential $\overline{V_\mathrm{d}}$ (triangles) and the target current density $\overline{j_\mathrm{d}}$ (squares) versus the mass of the inert gas for both reactive (solid line) and metallic (dashed line) modes. These values correspond to the waveforms shown in figure 8.2.

8.3.2 Deposition rates

The normalized deposition rates, D_n, measured using a QCM during reactive HiPIMS of titanium at two different axial distances from the target surface ($d = 50$ and 100 mm) for the four different gas mixtures are shown in figure 8.4 alongside D_n as measured during metallic sputtering in the four inert gases with the QCM sensor placed at $d = 100$ mm. For an increased target-to-QCM distance, D_n in reactive mode was found to be lower by a factor of approximately 2 for all gas mixtures. Furthermore, the deposition rate in metallic mode is larger for all inert gases by a factor of approximately 10-15. However, the trends in D_n at $d = 100$ mm in both reactive and metallic modes are consistent (i.e. increasing with inert gas mass with the exception of Xe).

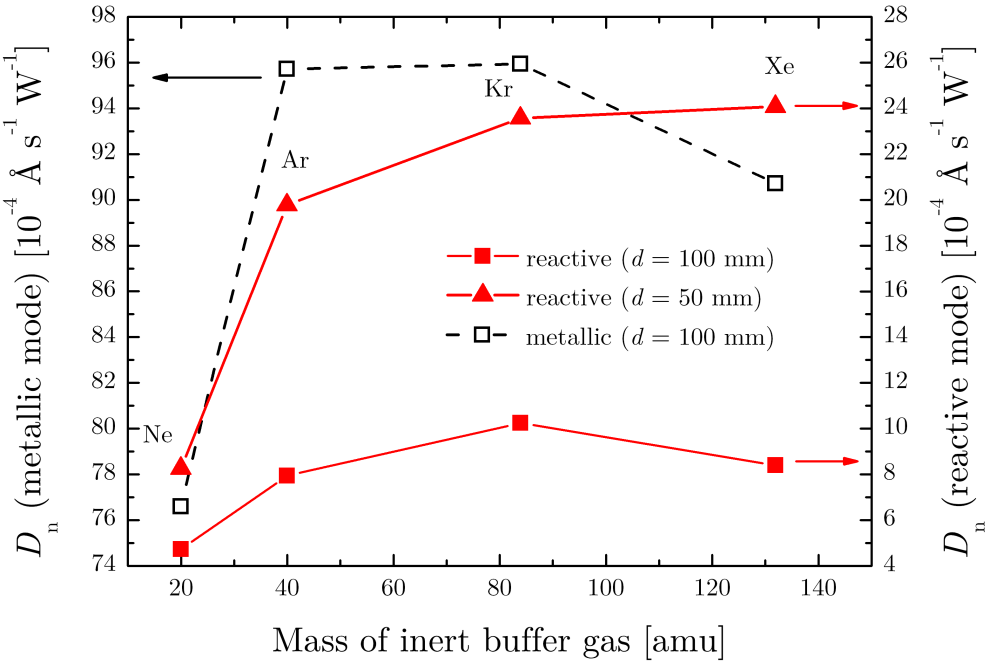

Figure 8.4. Power normalized deposition rates measured in reactive HiPIMS at two different axial distances d (50 and 100 mm) away from the target surface for the four gas mixtures alongside D_n as measured in metallic mode for $d = 100$ mm as a function of the inert gas mass. Note the different scaling for reactive and metallic modes.

Sputter yields, Y, calculated using SRIM [183] are predicted to have a negative correlation with inert ion mass for a TiO_2 target (see figure 8.5), consequently one would expect a similar trend in the deposition rate. Furthermore, due to the decreasing average discharge current with increasing ion mass, it isn't unreasonable to expect a reduced value for D_n for discharges containing heavier inert gases. However, D_n was observed to increase with the mass of the inert gas, with the exception of the Xe/O_2 gas mixture at $d = 100$ mm. It is noted that during SRIM calculations, the default surface binding energy of titanium dioxide provided by SRIM was employed.

Based on the phenomenological model of HiPIMS developed by Vlček and Burcalová [200], Čapek *et al.* [198] obtained an expression for normalized deposition rate during HiPIMS operation;

$$D_n \propto (1 - \eta\beta)\,\frac{\overline{V_d}^{-1/2}}{1 + \gamma_{se}} \tag{8.3}$$

where η is the ionization fraction of sputtered particles ($0 \leq \eta \leq 1$) and β is the probability of ionized sputtered vapour returning to the target surface ($0 \leq \beta \leq 1$). From equation 8.3, the yield effect dictates that any increase in the $\overline{V_d}$ results in a lower deposition rate normalized to the average discharge power by a factor that is approximated to be $\overline{V_d}^{-1/2}$,

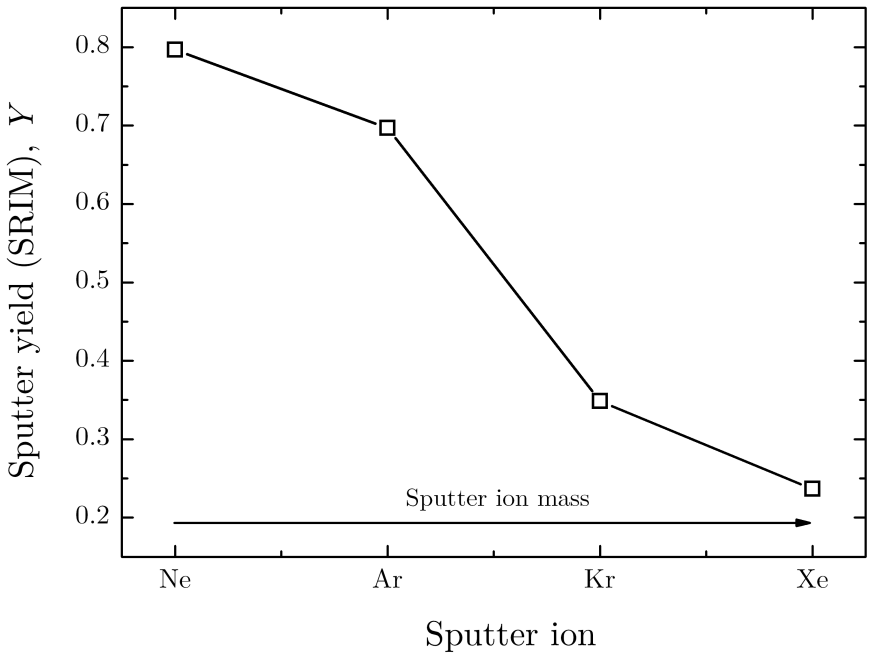

Figure 8.5. SRIM predictions for the sputter yields, Y, of different inert gas ions normally incident upon a TiO_2 surface. Ion energies were assumed to be the value of $e\overline{V_d}$ measured for the different gas mixtures.

suggesting D_n should decrease with increasing inert gas mass according to the values of $\overline{V_d}$ in figure 8.3. However, a decrease in γ_{se} with increasing inert ion mass would suggest an increase in D_n. Although in HiPIMS, it is often the case that a significant fraction of the sputtering ions are back-attracted target ions and such the γ_{se} is a combination of the secondary electron emission due to sputtering by gas ions, γ_{mg}, and electron emission due to self sputtering, γ_{mm}, viz. $\gamma_{se} \sim \gamma_{mg}(1 - m_t) + \gamma_{mm} m_t$ where m_t is the fraction of the ion flux incident upon the target containing target ions. However, the primary means of secondary electron emission is assumed to be ion-induced potential emission ($\gamma_{mg} \sim \gamma_{se,p}$), where the potential emission coefficient can be expressed as in equation 2.5 [36];

$$\gamma_{se,p} \approx 0.032\,(0.78\mathcal{E}_{iz} - 2\phi) \tag{8.4}$$

where $\mathcal{E}_{iz}$ is the ionization energy of the ion incident upon the target and ϕ is the work function for a metal target, or the energy gap for an insulating material. Due to the low ionization energy of titanium ($\mathcal{E}_{iz} = 6.83$ eV [204]) compared with twice its work function ($2\phi = 8.66$ eV [205]), the contribution to γ_{se} by self sputtering is low (i.e. $\gamma_{mg} \gg \gamma_{mm}$, hence $\gamma_{se} \sim \gamma_{se,p}$. For this simple treatment, multiply-charged ions are neglected, the inert gas ions are considered to be the primary sputtering ions and the work function of titanium is assumed to be approximately equal to the energy required to liberate an electron from a titanium oxide surface (estimated by the energy gap of titanium oxide,

3.82 eV [206]).

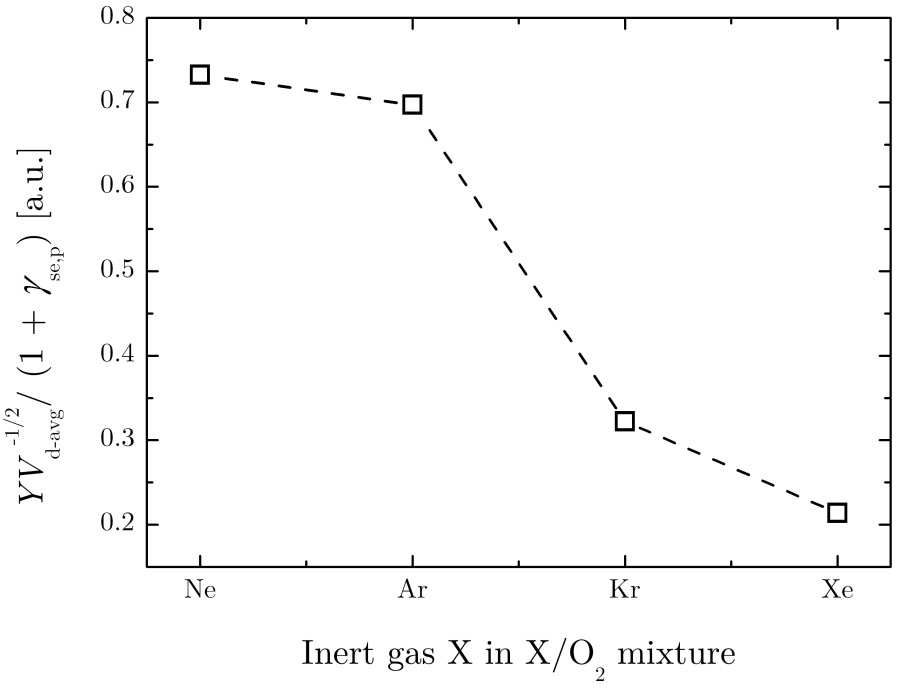

Figure 8.6. Normalized values of $Y\overline{V_{\text{d}}}^{-1/2}/(1+\gamma_{\text{se,p}})$ calculated from the values shown in figure 8.3 and $\gamma_{\text{se,p}}$ values obtained using equation 8.4, used to illustrate the expected trend of the deposition rate as a function of inert gas mass. This excludes any affects of η and β (see equation 8.3).

Normalized values for $\overline{V_{\text{d}}}^{-1/2}/(1+\gamma_{\text{se,p}})$ were calculated by using the measured $\overline{V_{\text{d}}}$ shown in figure 8.3 and the $\gamma_{\text{se,p}}$ values estimated from equation 8.4. The values of this factor were multiplied by the sputter yields, Y, predicted by SRIM and are displayed in figure 8.6. The relationship between the expected deposition rate and the sputter ion mass shown in figure 8.6 is very similar to sputter yields, Y, as predicted by SRIM calculations (see figure 8.5). For DCMS, $\eta\beta \rightarrow 0$ and from equation 8.3, the decrease in D_{n} with increasing sputter ion mass is expected. However, $\eta\beta > 0$ for HiPIMS and therefore the same trend may not hold. Furthermore, the value of $\eta\beta$ is expected to vary for different gas mixtures. Comparing the measured deposition rates in figure 8.4 and the trend of the factors affecting deposition rate shown in Figure 6, it follows that $\eta\beta$ must display a significant decrease for heavier inert gas mixtures. Following [198];

$$\beta \propto \frac{1}{\overline{V_{\text{d}}}} \tag{8.5}$$

hence there is a reduced probability of ionized sputtered vapour returning to the target surface for heavier inert gases due to the increase in $\overline{V_{\text{d}}}$ (see figure 8.3), which is the reverse trend predicted by the yield effect. The ionization probability η is dependent on many

parameters, the most obvious being the neutral flux from target surface, local electron temperature, the ionization potential of the sputtered vapour and the self-sputter yield. A systematic approach to analysing the effects of the inert gas choice for reactive HiPIMS on the parameters η and β warrants further investigation, but is beyond the scope of this thesis.

8.3.3 Comparison with reactive DCMS

The normalized deposition rates of TiO_2 for equivalent reactive DCMS discharges, using the same process conditions were also measured for a target-to-QCM distance $d = 100$ mm. Figure 8.7 shows the comparison between the power normalized deposition rates for both HiPIMS (D_{HPM}) and DCMS (D_{DC}) of Ti in the presence of O_2 mixed with Ne, Ar, Kr or Xe alongside the ratio of the two; $\sigma = D_{\mathrm{HPM}}/D_{\mathrm{DC}}$.

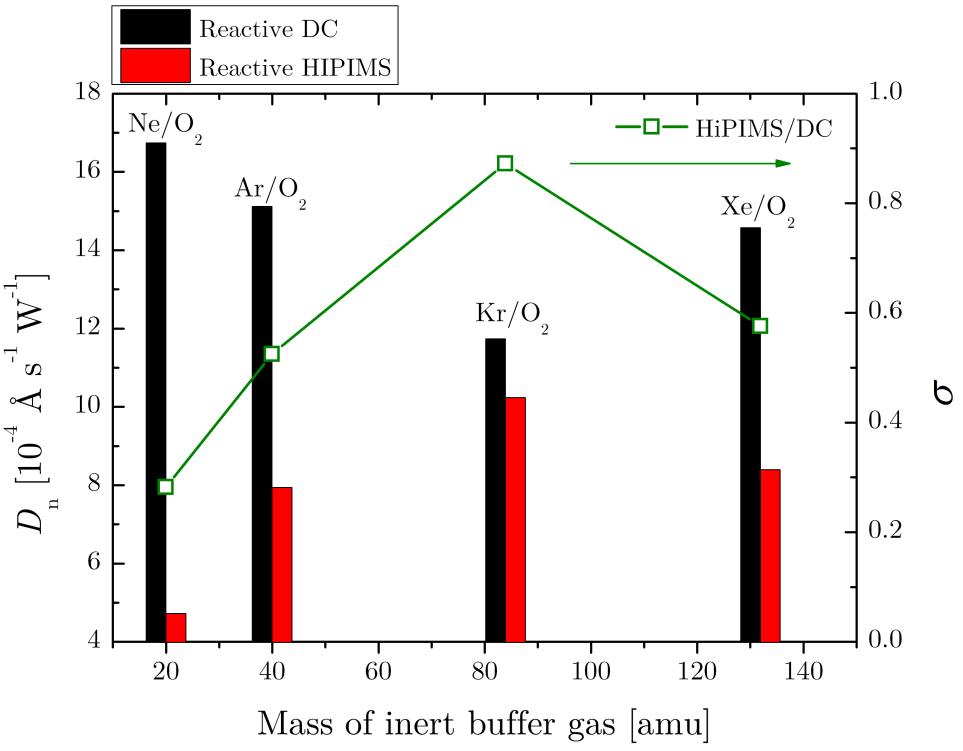

Figure 8.7. Normalized deposition rate comparison between DCMS (black bar, left column) and HiPIMS (red bar, right column) for different inert gases mixed with oxygen, with the ratio, $\sigma = D_{\mathrm{HPM}}/D_{\mathrm{DC}}$, of the two values over-plotted (open squares).

In agreement with the predicted sputter yields given in figure 8.5, D_{DC} shows a decrease with inert gas mass, whereas D_{HPM} is observed to follow the inverse trend for the cases of Ne, Ar and Kr. Consequently, σ increases markedly for increasing inert gas mass mixed with O_2, with the exception of the Xe/O_2 gas mixture. Due to the lower average discharge power used for the Xe/O_2 mixture (50 W compared with 100 W) and the significantly lower peak current density recorded during the pulse on-time, the racetrack width is

expected to be smaller [207], thereby reducing the active area of the target which could lead to a reduction in deposition rate relative to the other gas mixtures. Furthermore, in the formulation of equation 8.3, the potential drop within the discharge is assumed to occur only within the cathode sheath such that the ions impinging upon the target are taken to possess energies equal to the applied target potential. However, as the plasma possesses a finite impedance, a portion of the potential drop necessarily occurs across the plasma itself and not exclusively within the cathode sheath. As a result, the energy of the impinging ions is likely to be somewhat lower than assumed, consequently reducing the predicted sputter yield and by extension, the expected deposition rate [208]. It is conjectured that a higher proportion of the applied target potential is dropped over the Xe/O_2 plasma bulk when compared with the other gas mixtures, given the comparatively larger mass of Xe. If this is the case, a proportional reduction in the incident ion energy follows and hence a discrepancy between the measured and expected deposition rate will arise. Also, as the relationship between D_n and inert gas mass appears to follow the same trend for both metallic and reactive HiPIMS operation, it is suggested that re-sputtering by negative ions is not a significant factor. That is not to say that bombardment by negative O^- ions has no influence on the development and properties of the deposited thin films.

For the case of Kr/O_2, not only is the normalized deposition rate observed to be higher than for Ar/O_2 during HiPIMS operation, it is also comparable to the value measured in reactive DCMS; $\sigma = 0.87$. Additionally, the high-energy negative ion production at the target surface is reduced in a Kr/O_2 discharge when compared with the case of Ar/O_2. This is because, in general, the intensity of high-energy O^- ions impinging upon the substrate decreases with the secondary electron emission coefficient, as discussed in chapter 7. Taking into consideration that no optimization of the process conditions was attempted in this investigation and the results from chapter 7, it seems plausible that employing Kr as the buffer gas alongside oxygen during reactive HiPIMS of Ti in favour of Ar would be beneficial in terms of the power normalized deposition rate as well as reducing detrimental effects caused by energetic negative ion bombardment.

8.4 Conclusions

The deposition rates in reactive HiPIMS of titanium in the presence of O_2 and one of four different inert gases (Ne, Ar, Kr and Xe) have been measured by means of a quartz crystal microbalance located directly above the target erosion track. The power normalized deposition rates, D_n, were found to increase with the mass of inert gas in both metallic and reactive modes, with the exception of the Xe/O_2 gas mixture. This is contrary to the trend expected by both the yield effect and predictions based on sputter yield calculations by SRIM. In reactive mode, the Kr/O_2 gas mixture produced the highest

measured value for $D_n = 1.02 \times 10^{-3}$ Å s^{-1} W^{-1}. For all inert gases, values of D_n measured in metallic mode were approximately a factor of $10 - 15$ higher than those observed in reactive mode. The observed increase of D_n with the mass of inert gas was partially attributed to a decreased return effect in the heavier gases. However, it was concluded that additional work must be done in order to ascertain the determining mechanism governing this correlation. Additionally, it was found that DCMS and HiPIMS displayed opposing trends of normalized deposition rate with the mass of inert gas used, again with the exception of the Xe/O_2 case. The deviation from the trends in deposition rates for both DCMS and HiPIMS in the case of Xe/O_2 are thought to arise from unaccounted for differences in the plasma impedance and the erosion racetrack width, which affect the energy of sputter ions and the active target area, respectively. Interestingly and despite no optimization, the ratio of the two deposition rates was close to unity for the case of Kr/O_2; the normalized deposition rate of HiPIMS was found to be 87% of the value recorded in DCMS. However, it remains to be determined whether Kr offers additional advantages compared with other inert gases beyond an apparent increase in normalized deposition rate and a decrease in the amount of high energy negative ions ejected from the target surface.

Chapter 9

Conclusions

The aim of this thesis is to contribute to the body of knowledge regarding reactive HiPIMS and to help better understand reactive HiPIMS discharges. In an attempt to achieve this, a selection of plasma diagnostic techniques have been used to investigate various aspects of the reactive HiPIMS process. The dynamics of fundamental plasma parameters such as ion and electron density ($n_{\mathrm{i,e}}$), effective electron temperature (T_{eff}), negative ion density (n_{-}) and the plasma (Φ) and floating (V_{f}) potentials were investigated by means of a Langmuir probe. Laser-aided photodetachment was also employed to measure n_{-} with results being compared to those acquired via the Langmuir probe technique. Energy-resolved mass spectrometry was used to investigate oxygen negative ion energy distributions and deposition rate measurements during the reactive HiPIMS of Ti in the presence of oxygen were determined by means of a quartz crystal microbalance (QCM).

In chapter 5, the spatiotemporal evolution of the plasma parameters during HiPIMS of Ti in an Ar/O_2 discharge have been determined by means of a single Langmuir probe. Peak values of n_{i} were found to be of the order of $10^{17}-10^{18}$ m^{-3}, with values increasing for positions closer to the target. Much of the behaviour of the the plasma parameters in both time and spatial dimensions can be understood by considering a transient compression of the process gas followed by a rarefaction phase propagating away from the target surface. For instance, the time-resolved behaviour of n_{i} and n_{e} exhibited a dual peak structure with an initial peak occurring at $t \sim 25$ μs, before the absolute peak value was attained at the termination of the pulse. The initial peak was delayed for increasing pressure and appeared earlier in time at positions closer to the target. Furthermore, the observed quenching of T_{eff} and its subsequent increase toward the end of the pulse on-time is also consistent with a propagating region of increased gas density followed by rarefaction of the background gas. Both Φ and V_{f} were observed to be highly negative in the immediate on-time before increasing steadily during the active phase of the pulse.

Negative ion formation occurs in discharges containing electronegative gases such as oxygen and the presence of negative ions can significantly influence plasma parameters as well as the ion flux exiting the plasma. Hence, knowledge of negative ion dynamics is an

important consideration for reactive magnetron sputter deposition.

The temporal evolution of oxygen negative ion density and electronegativity ($\alpha = n_-/n_e$) in the discharge afterglow during HiPIMS of titanium in an Ar/O_2 atmosphere was estimated by means of a single Langmuir probe for different oxygen partial pressures and compared with values obtained using laser-aided photodetachment in chapter 6. In the Langmuir probe investigation, average oxygen negative ion densities in the afterglow were estimated to be of the order of 10^{15} m^{-3}, with values slightly higher for increased oxygen content. It was also determined that the decay in n_e during the off-time occurs more rapidly than the decay in n_-, resulting in a highly electronegative afterglow with peak values of $\alpha = 19(\pm3)$, $316(\pm47)$ and $396(\pm59)$ over the range of p_{O_2}/p_{total} investigated. By using a simple plasma-chemical model, the increasing α with p_{O_2}/p_{total} was attributed to higher densities of metastable oxygen molecules available at the beginning of the afterglow which can subsequently undergo dissociative electron attachment to form negative ions. Furthermore, once the discharge degrades into an ion-ion state, the negative ion flux to the substrate was estimated to be of the order of $10^{17} - 10^{18}$ m^{-2} s^{-1}, which could influence the development of a growing thin film.

In the photodetachment study, oxygen negative ion densities were found to peak in the early afterglow at values of the order of 10^{17} m^{-3}. The higher n_- compared to those found in the Langmuir probe study was attributed to the higher n_e attained during the active phase, whereby the greater availability of electrons permits the formation of more negative ions via dissociative electron attachment to oxygen molecules or metastables. Values of α estimated by the Langmuir probe were found to be typically a factor of $8 - 15$ larger than those measured using photodetachment. Although the applicability of using a Langmuir probe to approximate values of α and n_- in electronegative discharges was demonstrated, the importance of realising its limitations was also highlighted.

Although the temporal evolution of negative ion density in the discharge is insightful, it is also very important to consider the negative ion energy distributions for understanding plasma-surface interactions and tailoring thin film properties. In chapter 7, the energy distributions of negative oxygen ions were measured by means of energy-resolved mass spectrometry.

Consistent with previous studies performed in reactive magnetron sputter deposition [116, 118], the time-averaged energy distributions of O^- ions were found to contain three broad energy populations. The high energy population was observed to posses an energy tail extending beyond the maximum applied target potential. By comparing the shape of the energy spectrum of the high energy population to a Thompson energy distribution of sputtered particles it was concluded that high energy O^- ions gain kinetic energy from sputtering events at the target surface before undergoing acceleration in the cathodic sheath. The deviation of the energy spectrum from the Thompson energy distribution was attributed to gas-phase transport effects.

The effective collisional cross section of O^- interacting with the background gas, measurements of O^- ion energy distributions were made during reactive HiPIMS of both Ti and Nb for varying pressure-distance, *pd*, values. A cross section, $\sigma_t \approx 2 \times 10^{-19}$ m^2, was found to be independent of target choice. This deviated somewhat from the cross section expected by employing a simple hard-sphere approximation ($\sim 4 \times 10^{-19}$ m^2), with the disagreement attributed to effects of gas rarefaction that were neglected in the simple hard-sphere treatment.

By changing target materials, a correlation between O^- emission and the ion-induced secondary electron emission coefficient of different target materials was found. Moreover, large differences in the O^- yield were also observed when employing different inert gases mixed with O_2. A decreased high energy O^- ion flux for gas mixtures incorporating heavier inert gases was attributed to their lower ionization energies and consequently lower potential electron emission coefficients. It was suggested that these observations may have important consequences for reactive magnetron sputter deposition of thin oxide films sensitive to high energy O^- ion bombardment. Although it may be desirable to control the yield of high energy O^- ions by changing the working gas mixture, the choice of inert gas also influences the development of the growing film and, more importantly from an economical perspective, the deposition rate.

In chapter 8, the deposition rates in reactive HiPIMS of titanium in the presence of O_2 and one of four different inert gases (Ne, Ar, Kr and Xe) were measured by means of a quartz crystal microbalance in a typical substrate position and compared with those measured in DCMS and inert (metallic) HiPIMS. Contrary to predications made by SRIM, the power normalized deposition rates, D_n, were found to increase with the mass of inert gas in both metallic and reactive modes, with the exception of the Xe/O_2 gas mixture. The observed increase of D_n with the mass of inert gas was partially attributed to a decreased return effect in the heavier gases, however, further investigation is necessary to determine the underlying mechanisms driving the observed trend. In reactive mode, the highest measured value of D_n was 1.02×10^{-3} Å s^{-1} W^{-1} in the Kr/O_2 gas mixture which, despite no optimization, was found to be 87% of the value of D_n recorded in the nominally equivalent reactive DCMS discharge. For all inert gases, values of D_n measured in metallic mode were approximately a factor of $10 - 15$ higher than those observed in reactive mode.

Finally, combining the results from chapters 7 and 8, it was suggested that during reactive HiPIMS of oxides it may be beneficial to employ Kr rather than Ar as the inert gas mixed with O_2, as it offers both an increased power-normalized deposition rate and a lower yield of high energy O^- ions impinging upon the substrate. Xe may also offer similar advantages, but its use comes with a much higher monetary cost. Further studies, as briefly outlined below, are required in order to ascertain whether or not this is a viable strategy to adopt during reactive HiPIMS in the presence of oxygen.

9.1 Suggestions for future work

Although it was concluded that high-energy O^- ions are sputtered from the target surface before undergoing acceleration in the cathode sheath, a deviation from the Thompson energy distribution of sputtered particles was still apparent. A more rigorous treatment of the gas-phase transport, somewhat akin to that presented by van Aeken *et al.* [184] or the semi-empirical model of the transport of sputtered particles by Liebig [163], which incorporates effects such as the ionisation probability, back-attraction of ionised sputtered vapour to the target, the two-stream instability [50] and scattering of sputtered particles by the background gas may be able to provide a robust explanation for the deviation of the measured energy distribution of the high-energy O^- ions from a simple Thomson energy distribution of sputtered particles. Furthermore, time-resolved measurements of negative oxygen ion energy distributions may also be compared to the model to study transient effects and used to determine the temporal position in the discharge pulse from which the large flux of high-energy O^- originates. Some measurements of the time-resolved O^- ion energy distribution are presented in appendix B.

A very interesting observation made during the studies presented in this thesis was the large difference in high energy O^- emission for different inert gases mixed with oxygen. The prospect of tailoring the yield of O^- ions by using different inert gas mixtures warrants more intense investigation across an array of different discharge conditions. Although a correlation between lower O^- ion emission and higher normalized deposition rate was found, the same trend in deposition rate for different inert gases existed in metallic mode, thereby suggesting re-sputtering of deposited films was negligible. However, that is not to say that bombardment by high energy O^- ions has no effect on the development of thin films at the substrate. Further studies may focus on thin film analysis in order to attribute the differences in the plasma properties as presented here with consequences for thin film properties. For example, ellipsometry studies would be able to determine any differences in the refractive index of TiO_2 deposited under different conditions and reveal whether using a Kr/O_2 mixture rather than Ar/O_2 is indeed beneficial from an application perspective.

Only limited variations in discharge pulse parameters were discussed in this thesis, however, it was still found that power normalized deposition rates in reactive HiPIMS were close to those obtained in conventional DCMS, particularly for reactive sputtering in Kr/O_2. By investigating a wider parameter space, it may be possible to optimize the reactive HiPIMS process such that the deposition rate matches, or even surpasses, that of the equivalent DCMS process. Furthermore, virtually all of the studies presented here were performed in poisoned mode, however, it is often desirable to operate a reactive discharge in the transition region of the hysteresis curve. By employing some form of process feedback control of the oxygen flow rate such as optical emission [209], it is

worth exploring the possibility of operating in this regime during reactive HiPIMS and investigating the consequential effects by means of both plasma diagnostics and thin film analysis.

9.2 Outlook

Although many studies have been performed concerning both conventional reactive DC magnetron sputter deposition and non-reactive HiPIMS, there is somewhat of a shortage of information available in the literature regarding plasma parameters in reactive HiPIMS discharges.

The work presented in this thesis has covered some of the important aspects related to the reactive HiPIMS process, such as the spatiotemporal evolution of plasma parameters in typical substrate positions, measurements of the densities and energy distributions of negative oxygen species in a number of different discharge conditions and the static power-normalized deposition rate of TiO_2 as compared with that measured in the equivalent reactive DCMS process. However, as alluded to above, there is a vast parameter space in which to investigate and the conditions presented here represent only a small portion of that space. Furthermore, there are several issues raised by the work presented here that are still outstanding. The deviation of the high-energy O^- ion energy distribution from a Thompson distribution of sputtered particles was not completely resolved, which also brings into question the exact formation mechanism(s) of negative ions at, or close to, the target surface. Though the shape of the energy distribution deviates from the expected distribution, O^- ions are detected with energies exceeding that of the peak absolute applied target potential and so the extra kinetic energy is thought to originate from sputtering events. This suggests that negative oxygen ions can 'sit' on the metallic target surface as negative ions, but require agitation (i.e. sputtering) before being released and accelerated in the cathode sheath. The high-energy O^- emission was also found to depend heavily on the choice on inert buffer gas mixed with O_2, however, the resulting ion composition and subsequent effects on negative ion emission from the target are considered only in a speculative manner rather than being determined experimentally. Moreover, discussions here have been limited almost exclusively to the properties of the discharge and any relations to thin film properties have not been addressed. Understanding correlations between plasma parameters and thin film properties is of extreme importance from an applications perspective and, although film properties of coatings deposited using reactive HiPIMS have been reported by several authors [11, 13–15, 43, 93], there is much potential for further exploration in this regard.

It is evident that, although this thesis achieves its aim insofar as adding to the body of knowledge concerning the plasma properties of reactive HiPIMS discharges, there is still much work remaining. It is hoped that the work presented here will inspire future

research to resolve any outstanding issues raised and further develop the understanding of reactive HiPIMS and discover exciting new applications for this relatively new addition to magnetron sputter deposition technology.

Acknowledgements

I would like to take this opportunity to express my gratitude and appreciation to my supervisor, Professor James Bradley, firstly for presenting me with the opportunity to study within his research group and secondly for all of the guidance and support he has provided over the duration of my time in Liverpool. I would also like to extend my thanks to the other academic members of the research group, including James Walsh, Xin Tu, Mark Bowden, Paul Bryant and Dmitry Samsonov, who sadly is no longer with us.

The contributions of the technical staff are also acknowledged. I would like to thank the maestro of the mechanical workshop that is Alan Roby, for his help building vacuum chamber fittings, the shield for the deposition rate sensor and for all of the various modifications to plasma diagnostic equipment. Alan Edwards and John Lynch are also thanked for their help with the HiPIMS power supply and general troubleshooting regarding anything electronic. Jill Anson is gratefully acknowledged for her efficient administration of the departmental stores, as is Lindsey Clarke for her equally efficient management of my travel and research-related orders and so is Larry Barnes for his pro-active approach to building management.

I am particularly grateful to the other members of the research group. I would like to thank Bernd and Nu who guided me through the initial stages of my project, Steve for his help with the photodetachment measurements and TJ, Fred, MJ, Mohammad, Ed, Ni, Francis, Kirsty, Jun-Seok, Andy, Tom and Zaenab for their valuable daily discussions and assistance.

Outside of the group, I owe my thanks to Sam Bort from Hiden Analytical for his advice regarding the operation of the EQP, to Diederik Depla and Wouter Leroy for their advise on measuring negative ion energy distributions, as well as to Peter Kelly and Glen West for their useful contributions and discussions regarding an on-going investigation in reactive HiPIMS.

I wish to thank all of my friends and family who provided me with the encouragement and motivation to complete this thesis with a special thank you to my partner, Alessandra, for her unconditional love and support.

Finally, I would to thank the University of Liverpool and the Engineering and Physical Sciences Research Council for funding my studentship as part of the Fusion Doctoral Training Network.

References

[1] I. Langmuir, "Oscillations in ionized gases," *Proceedings of the National Academy of Sciences*, vol. 14, pp. 627–637, 1928.

[2] H. M. Mott-Smith, "History of 'Plasmas'," *Nature*, vol. 233, no. 5316, p. 219, 1971.

[3] R. Waits, "Planar magnetron sputtering," *Journal of Vacuum Science & Technology*, vol. 15, no. 2, pp. 179–187, 1978.

[4] U. Helmersson, M. Lattemann, J. Bohlmark, A. P. Ehiasarian, and J. T. Gudmundsson, "Ionized physical vapor deposition (IPVD): A review of technology and applications," *Thin Solid Films*, vol. 513, no. 12, pp. 1 – 24, 2006.

[5] V. Kouznetsov, K. Mack, J. M. Schneider, U. Helmersson, and I. Petrov, "A novel pulsed magnetron sputter technique utilizing very high target power densities," *Surface and Coatings Technology*, vol. 122, no. 23, pp. 290 – 293, 1999.

[6] J. Bohlmark, J. Alami, C. Christou, A. P. Ehiasarian, and U. Helmersson, "Ionization of sputtered metals in high power pulsed magnetron sputtering," *Journal of Vacuum Science & Technology A*, vol. 23, no. 1, pp. 18–22, 2005.

[7] J. T. Gudmundsson, N. Brenning, D. Lundin, and U. Helmersson, "High power impulse magnetron sputtering discharge," *Journal of Vacuum Science & Technology A*, vol. 30, no. 3, p. 030801, 2012.

[8] S. Konstantinidis and R. Snyders, "Reactive ionized physical vapor deposition of thin films," *The European Physical Journal Applied Physics*, vol. 56, p. 24002, 2011.

[9] E. Wallin and U. Helmersson, "Hysteresis-free reactive high power impulse magnetron sputtering," *Thin Solid Films*, vol. 516, no. 18, pp. 6398 – 6401, 2008.

[10] T. Kubart, M. Aiempanakit, J. Andersson, T. Nyberg, S. Berg, and U. Helmersson, "Studies of hysteresis effect in reactive hipims deposition of oxides," *Surface and Coatings Technology*, vol. 205, Supplement 2, pp. S303 – S306, 2011. 2010 Special Issue Proceedings of the 12th International Conference on Plasma Surface Engineering.

[11] T. Kubart, M. Čada, D. Lundin, and Z. Hubička, "Investigation of ionized metal flux fraction in hipims discharges with Ti and Ni targets," *Surface and Coatings Technology*, vol. 238, pp. 152 – 157, 2014.

[12] K. Sarakinos, J. Alami, C. Klever, and M. Wuttig, "Process stabilization and enhancement of deposition rate during reactive high power pulsed magnetron sputtering of zirconium oxide," *Surface and Coatings Technology*, vol. 202, pp. 5033–5035, July 2008.

[13] A. Ehiasarian, P. Hovsepian, L. Hultman, and U. Helmersson, "Comparison of microstructure and mechanical properties of chromium nitride-based coatings deposited by high power impulse magnetron sputtering and by the combined steered cathodic arc/unbalanced magnetron technique," *Thin Solid Films*, vol. 457, no. 2, pp. 270 – 277, 2004.

[14] M. Aiempanakit, U. Helmersson, A. Aijaz, P. Larsson, R. Magnusson, J. Jensen, and T. Kubart, "Effect of peak power in reactive high power impulse magnetron sputtering of titanium dioxide," *Surface and Coatings Technology*, vol. 205, no. 20, pp. 4828 – 4831, 2011.

[15] A. P. Ehiasarian, A. Vetushka, Y. A. Gonzalvo, G. Sáfrán, L. Székely, and P. B. Barna, "Influence of high power impulse magnetron sputtering plasma ionization on the microstructure of TiN thin films," *Journal of Applied Physics*, vol. 109, no. 10, p. 104314, 2011.

[16] Q. Luo, S. Yang, and K. Cooke, "Hybrid HIPIMS and DC magnetron sputtering deposition of tin coatings: Deposition rate, structure and tribological properties," *Surface and Coatings Technology*, vol. 236, no. 0, pp. 13 – 21, 2013.

[17] M. Zeuner, H. Neumann, J. Zalman, and H. Biederman, "Sputter process diagnostics by negative ions," *Journal of Applied Physics*, vol. 83, no. 10, p. 5083, 1998.

[18] S. Mráz and J. M. Schneider, "Influence of the negative oxygen ions on the structure evolution of transition metal oxide thin films," *Journal of Applied Physics*, vol. 100, no. 2, p. 023503, 2006.

[19] S. Mahieu and D. Depla, "Correlation between electron and negative O^- ion emission during reactive sputtering of oxides," *Applied Physics Letters*, vol. 90, no. 12, p. 121117, 2007.

[20] T. Welzel, S. Naumov, and K. Ellmer, "Ion distribution measurements to probe target and plasma processes in electronegative magnetron discharges. I. Negative ions," *Journal of Applied Physics*, vol. 109, no. 7, p. 073302, 2011.

[21] J. Cuomo, R. Gambino, J. M. E. Harper, and J. D. Kuptsis, "Origin and effects of negative ions in the sputtering of intermetallic compounds," *IBM Journal of Research and Development*, vol. 21, pp. 580–583, Nov 1977.

[22] T. Minami, J. ichi Oda, J. ichi Nomoto, and T. Miyata, "Effect of target properties on transparent conducting impurity-doped ZnO thin films deposited by DC magnetron sputtering," *Thin Solid Films*, vol. 519, no. 1, pp. 385 – 390, 2010.

[23] H. C. Nguyen, T. T. Trinh, T. Le, C. V. Tran, T. Tran, H. Park, V. A. Dao, and J. Yi, "The mechanisms of negative oxygen ion formation from Al-doped ZnO target and the improvements in electrical and optical properties of thin films using off-axis dc magnetron sputtering at low temperature," *Semiconductor Science and Technology*, vol. 26, no. 10, p. 105022, 2011.

[24] V. Sittinger, O. Lenck, M. Vergöhl, B. Szyszka, and G. Bräuer, "Applications of HIPIMS metal oxides," *Thin Solid Films*, vol. 548, pp. 18 – 26, 2013.

[25] D. M. Mattox, *Handbook of Physical Vapor Deposition (PVD) Processing*. Burlington, USA: Elsevier Inc., 2010.

[26] T. Boyd and J. Sanderson, *The Physics of Plasmas*. New York, USA: Cambridge University Press, 2003.

[27] F. F. Chen, *Introduction to Plasma Physics and Controlled Fusion*. New York, USA: Springer, 2006.

[28] M. A. Lieberman and A. J. Lichtenberg, *Principles of Plasma Discharges and Materials Processing*. Hoboken, USA: Wiley, second ed., 2005.

[29] D. Frank-Kamenezki, *Plasma - der vierte Aggregatzustand*. Moscow, Russia: Verlag Progress, 1963.

[30] K. T. A. L. Burm, "Plasma: The fourth state of matter," *Plasma Chemistry and Plasma Processing*, vol. 32, pp. 401–407, Feb. 2012.

[31] A. Bogaerts, E. Neyts, R. Gijbels, and J. van der Mullen, "Gas discharge plasmas and their applications," *Spectrochimica Acta Part B: Atomic Spectroscopy*, vol. 57, pp. 609–658, Apr. 2002.

[32] M. W. Thompson, "The energy spectrum of ejected atoms during the high energy sputtering of gold," *Philosophy Magazine*, vol. 18, pp. 377–414, 1968.

[33] P. Sigmund, "Theory of Sputtering. I. Sputtering Yield of Amorphous and Polycrystalline Targets," *Phys. Rev.*, vol. 184, pp. 383–416, Aug 1969.

[34] M. Thompson, "Physical mechanisms of sputtering," *Physics Reports*, vol. 69, no. 4, pp. 335 – 371, 1981.

[35] H. D. Hagstrum, "Theory of Auger Ejection of Electrons from Metals by Ions," *Phys. Rev.*, vol. 96, pp. 336–365, Oct 1954.

[36] R. Baragiola, E. Alonso, J. Ferron, and A. Oliva-Florio, "Ion-induced electron emission from clean metals," *Surface Science*, vol. 90, no. 1928, pp. 240–255, 1979.

[37] A. Phelps and Z. Petrovic, "Cold-cathode discharges and breakdown in argon: surface and gas phase production of secondary electrons," *Plasma Sources Science and Technology*, vol. 8, pp. R21 – R44, 1999.

[38] D. Mattox, "Particle bombardment effects on thin film deposition: A review," *Journal of Vacuum Science Technology A: Vacuum, Surfaces, and Films*, vol. 7, pp. 1105–1114, May 1989.

[39] R. D. Gryse, J. Haemers, W. Leroy, and D. Depla, "Thirty years of rotatable magnetrons," *Thin Solid Films*, vol. 520, no. 18, pp. 5833 – 5845, 2012.

[40] A. Anders, "Discharge physics of high power impulse magnetron sputtering," *Surface and Coatings Technology*, vol. 205, Supplement 2, pp. S1 – S9, 2011. 2010 Special Issue Proceedings of the 12th International Conference on Plasma Surface Engineering.

[41] P. Vašina, M. Meško, M. Ganciu, J. Bretagne, C. Boisse-Laporte, L. de Poucques, and M. Touzeau, "Reduction of transient regime in fast preionized high-power pulsed-magnetron discharge," *Europhysics Letters*, vol. 72, no. 3, p. 390, 2005.

[42] M. Lattemann, A. Ehiasarian, J. Bohlmark, P. Persson, and U. Helmersson, "Investigation of high power impulse magnetron sputtering pretreated interfaces for adhesion enhancement of hard coatings on steel," *Surface and Coatings Technology*, vol. 200, no. 2223, pp. 6495 – 6499, 2006. EMRS 2005 Symposium K Protective Coatings and Thin Films.

[43] S. Konstantinidis, A. Hemberg, J. P. Dauchot, and M. Hecq, "Deposition of zinc oxide layers by high-power impulse magnetron sputtering," *Journal of Vacuum Science Technology B: Microelectronics and Nanometer Structures*, vol. 25, pp. L19–L21, May 2007.

[44] A. Anders, "Deposition rates of high power impulse magnetron sputtering: Physics and economics," *Journal of Vacuum Science & Technology A: Vacuum, Surfaces, and Films*, vol. 28, no. 4, p. 783, 2010.

[45] M. Samuelsson, D. Lundin, J. Jensen, M. A. Raadu, J. T. Gudmundsson, and U. Helmersson, "On the film density using high power impulse magnetron sputtering," *Surface and Coatings Technology*, vol. 205, no. 2, pp. 591–596, 2010.

[46] A. P. Ehiasarian, "High-power impulse magnetron sputtering and its applications," *Pure and Applied Chemistry*, vol. 82, pp. 1247–1258, Apr. 2010.

[47] K. Sarakinos, J. Alami, and S. Konstantinidis, "High power pulsed magnetron sputtering: A review on scientific and engineering state of the art," *Surface and Coatings Technology*, vol. 204, no. 11, pp. 1661 – 1684, 2010.

[48] J. Bohlmark, U. Helmersson, M. VanZeeland, I. Axnäs, J. Alami, and N. Brenning, "Measurement of the magnetic field change in a pulsed high current magnetron discharge," *Plasma Sources Science and Technology*, vol. 13, no. 4, p. 654, 2004.

[49] D. Lundin, U. Helmersson, S. Kirkpatrick, S. Rohde, and N. Brenning, "Anomalous electron transport in high power impulse magnetron sputtering," *Plasma Sources Science and Technology*, vol. 17, no. 2, p. 025007, 2008.

[50] D. Lundin, P. Larsson, E. Wallin, M. Lattemann, N. Brenning, and U. Helmersson, "Cross-field ion transport during high power impulse magnetron sputtering," *Plasma Sources Science and Technology*, vol. 17, p. 035021, Aug. 2008.

[51] P. Poolcharuansin, B. Liebig, and J. W. Bradley, "More evidence for azimuthal ion spin in HiPIMS discharges," *Plasma Sources Science and Technology*, vol. 21, p. 015001, Feb. 2012.

[52] A. Kozyrev, N. Sochugov, K. Oskomov, A. Zakharov, and A. Odivanova, "Optical studies of plasma inhomogeneities in a high-current pulsed magnetron discharge," *Plasma Physics Reports*, vol. 37, no. 7, pp. 621–627, 2011.

[53] A. P. Ehiasarian, A. Hecimovic, T. de los Arcos, R. New, V. Schulz-von der Gathen, M. Böke, and J. Winter, "High power impulse magnetron sputtering discharges: Instabilities and plasma self-organization," *Applied Physics Letters*, vol. 100, no. 11, p. 114101, 2012.

[54] A. Anders, P. Ni, and A. Rauch, "Drifting localization of ionization runaway: Unraveling the nature of anomalous transport in high power impulse magnetron sputtering," *Journal of Applied Physics*, vol. 111, no. 5, p. 053304, 2012.

[55] N. Brenning and D. Lundin, "Alfvén's critical ionization velocity observed in high power impulse magnetron sputtering discharges," *Physics of Plasmas*, vol. 19, no. 9, p. 093505, 2012.

[56] N. Brenning, D. Lundin, T. Minea, C. Costin, and C. Vitelaru, "Spokes and charged particle transport in hipims magnetrons," *Journal of Physics D: Applied Physics*, vol. 46, no. 8, p. 084005, 2013.

[57] G. Y. Yushkov and A. Anders, "Origin of the delayed current onset in high-power impulse magnetron sputtering," *IEEE Transactions on Plasma Science*, vol. 38, pp. 3028–3034, Nov. 2010.

[58] A. Anders, J. Andersson, and A. Ehiasarian, "High power impulse magnetron sputtering: Current-voltage-time characteristics indicate the onset of sustained self-sputtering," *Journal of Applied Physics*, vol. 102, no. 11, p. 113303, 2007.

[59] D. Horwat and A. Anders, "Compression and strong rarefaction in high power impulse magnetron sputtering discharges," *Journal of Applied Physics*, vol. 108, no. 12, p. 123306, 2010.

[60] T. de los Arcos, V. Layes, Y. A. Gonzalvo, V. S. von der Gathen, A. Hecimovic, and J. Winter, "Currentvoltage characteristics and fast imaging of hppms plasmas: transition from self-organized to homogeneous plasma regimes," *Journal of Physics D: Applied Physics*, vol. 46, no. 33, p. 335201, 2013.

[61] J. Lin, J. J. Moore, W. D. Sproul, S. Lee, and J. Wang, "Effect of negative substrate bias on the structure and properties of ta coatings deposited using modulated pulse power magnetron sputtering," *Plasma Science, IEEE Transactions on*, vol. 38, pp. 3071–3078, Nov 2010.

[62] D. W. Hoffman, "A sputtering wind," *Journal of Vacuum Science & Technology A*, vol. 3, no. 3, pp. 561–566, 1985.

[63] S. M. Rossnagel and H. R. Kaufman, "Charge transport in magnetrons," *Journal of Vacuum Science & Technology A*, vol. 5, no. 4, pp. 2276–2279, 1987.

[64] S. Kadlec, "Simulation of neutral particle flow during high power magnetron impulse," *Plasma Processes and Polymers*, vol. 4, no. S1, pp. S419–S423, 2007.

[65] B. Liebig, N. S. J. Braithwaite, P. Kelly, and J. Bradley, "Spatial and temporal investigation of high power pulsed magnetron discharges by optical 2D-imaging," *Thin Solid Films*, vol. 519, pp. 1699–1704, Dec. 2010.

[66] A. Hecimovic, T. de los Arcos, V. S. von der Gathen, M. Boeke, and J. Winter, "Temporal evolution of the radial plasma emissivity profile in HIPIMS plasma discharges," *Plasma Sources Science and Technology*, vol. 21, no. 3, p. 035017, 2012.

[67] J. Andersson and A. Anders, "Gasless sputtering: Opportunities for ultraclean metallization, coatings in space, and propulsion," *Applied Physics Letters*, vol. 92, no. 22, p. 221503, 2008.

[68] J. Emmerlich, S. Mráz, R. Snyders, K. Jiang, and J. M. Schneider, "The physical reason for the apparently low deposition rate during high-power pulsed magnetron sputtering," *Vacuum*, vol. 82, pp. 867–870, Apr. 2008.

[69] K. Sarakinos, J. Alami, and M. Wuttig, "Process characteristics and film properties upon growth of TiO_x films by high power pulsed magnetron sputtering," *Journal of Physics D: Applied Physics*, vol. 40, pp. 2108–2114, Apr. 2007.

[70] J. T. Gudmundsson, J. Alami, and U. Helmersson, "Evolution of the electron energy distribution and plasma parameters in a pulsed magnetron discharge," *Applied Physics Letters*, vol. 78, no. 22, pp. 3427–3429, 2001.

[71] J. Gudmundsson, J. Alami, and U. Helmersson, "Spatial and temporal behavior of the plasma parameters in a pulsed magnetron discharge," *Surface and Coatings Technology*, vol. 161, no. 23, pp. 249 – 256, 2002.

[72] J. Bohlmark, J. Gudmundsson, J. Alami, M. Latteman, and U. Helmersson, "Spatial electron density distribution in a high-power pulsed magnetron discharge," *IEEE Transactions on Plasma Science*, vol. 33, pp. 346–347, April 2005.

[73] A. Vetushka and A. P. Ehiasarian, "Plasma dynamic in chromium and titanium HIPIMS discharges," *Journal of Physics D: Applied Physics*, vol. 41, p. 015204, Jan. 2008.

[74] J. T. Gudmundsson, P. Sigurjonsson, P. Larsson, D. Lundin, and U. Helmersson, "On the electron energy in the high power impulse magnetron sputtering discharge," *Journal of Applied Physics*, vol. 105, no. 12, p. 123302, 2009.

[75] P. Poolcharuansin, B. Liebig, and J. Bradley, "Plasma parameters in a pre-ionized HiPIMS discharge operating at low pressure," *IEEE Transactions on Plasma Science*, vol. 38, pp. 3007–3015, Nov. 2010.

[76] P. Poolcharuansin and J. W. Bradley, "Short- and long-term plasma phenomena in a HiPIMS discharge," *Plasma Sources Science and Technology*, vol. 19, p. 025010, Apr. 2010.

[77] A. Hecimovic and A. P. Ehiasarian, "Time evolution of ion energies in hipims of chromium plasma discharge," *Journal of Physics D: Applied Physics*, vol. 42, no. 13, p. 135209, 2009.

[78] A. Anders and G. Y. Yushkov, "Plasma "anti-assistance" and "self-assistance" to high power impulse magnetron sputtering," *Journal of Applied Physics*, vol. 105, no. 7, p. 073301, 2009.

[79] J. Alami, J. T. Gudmundsson, J. Bohlmark, J. Birch, and U. Helmersson, "Plasma dynamics in a highly ionized pulsed magnetron discharge," *Plasma Sources Science and Technology*, vol. 14, no. 3, p. 525, 2005.

[80] A. P. Ehiasarian, A. Vetushka, A. Hecimovic, and S. Konstantinidis, "Ion composition produced by high power impulse magnetron sputtering discharges near the substrate," *Journal of Applied Physics*, vol. 104, no. 8, p. 083305, 2008.

[81] M. Čada, Z. Hubička, P. Adámek, J. Klusoň, and L. Jastrabík, "Time-resolved plasma parameters in the hipims discharge with Ti target in Ar/O_2 atmosphere," *Surface and Coatings Technology*, vol. 205, Supplement 2, pp. S317 – S321, 2011. 2010 Special Issue Proceedings of the 12th International Conference on Plasma Surface Engineering.

[82] A. E. Ross, R. Sangins, B. Treverrow, M. M. M. Bilek, and D. R. McKenzie, "Optimizing efficiency of ti ionized deposition in hipims," *Plasma Sources Science and Technology*, vol. 20, no. 3, p. 035021, 2011.

[83] B. Liebig and J. W. Bradley, "Space charge, plasma potential and electric field distributions in HiPIMS discharges of varying configuration," *Plasma Sources Science and Technology*, vol. 22, no. 4, p. 045020, 2013.

[84] A. Mishra, P. J. Kelly, and J. W. Bradley, "The evolution of the plasma potential in a HiPIMS discharge and its relationship to deposition rate," *Plasma Sources Science and Technology*, vol. 19, no. 4, p. 045014, 2010.

[85] J. Bohlmark, M. Lattemann, J. Gudmundsson, A. Ehiasarian, Y. A. Gonzalvo, N. Brenning, and U. Helmersson, "The ion energy distributions and ion flux composition from a high power impulse magnetron sputtering discharge," *Thin Solid Films*, vol. 515, no. 4, pp. 1522 – 1526, 2006.

[86] J. Andersson, A. P. Ehiasarian, and A. Anders, "Observation of Ti^{4+} ions in a high power impulse magnetron sputtering plasma," *Applied Physics Letters*, vol. 93, no. 7, p. 071504, 2008.

[87] S. Rossnagel and J. Cuomo, "Ion beam bombardment effects during films deposition," *Vacuum*, vol. 38, no. 2, pp. 73 – 81, 1988.

[88] D. Depla, S. Heirwegh, S. Mahieu, J. Haemers, and R. De Gryse, "Understanding the discharge voltage behavior during reactive sputtering of oxides," *Journal of Applied Physics*, vol. 101, no. 1, p. 013301, 2007.

[89] M. Aiempanakit, A. Aijaz, D. Lundin, U. Helmersson, and T. Kubart, "Understanding the discharge current behavior in reactive high power impulse magnetron sputtering of oxides," *Journal of Applied Physics*, vol. 113, no. 13, pp. –, 2013.

[90] W. Sproul, D. Christie, and D. Carter, "The Reactive Sputter Deposition of Aluminum Oxide Coatings Using High Power Pulsed Magnetron Sputtering (HPPMS)," *47th Annual Technical Conference Proceedings*, pp. 96–100, April 2004. Dallas, TX, Society of Vacuum Coaters.

[91] J. Davis, W. Sproul, D. Christie, and M. Geisler, "High Power Pulse Reactive Sputtering of TiO_2," *47th Annual Technical Conference Proceedings*, pp. 215–218, April 2004. Dallas, TX, Society of Vacuum Coaters.

[92] G. Greczynski, J. Jensen, and L. Hultman, "CrN_x Films Prepared by DC Magnetron Sputtering and High-Power Pulsed Magnetron Sputtering: A Comparative Study," *IEEE Transactions on Plasma Science*, vol. 38, pp. 3046–3056, Nov 2010.

[93] S. Konstantinidis, J. Dauchot, and M. Hecq, "Titanium oxide thin films deposited by high-power impulse magnetron sputtering," *Thin Solid Films*, vol. 515, no. 3, pp. 1182 – 1186, 2006. Proceedings of the 33rd International Conference on Metallurgical Coatings and Thin Films 2006.

[94] E. Stoffels, W. W. Stoffels, D. Vender, M. Haverlag, G. M. W. Kroesen, and F. J. de Hoog, "Negative ions in low pressure discharges," *Contributions to Plasma Physics*, vol. 35, no. 4-5, pp. 331–357, 1995.

[95] N. Braithwaite and J. Allen, "Boundaries and probes in electronegative plasmas," *Journal of Physics D: Applied Physics*, vol. 1733, 1988.

[96] E. Stoffels, W. W. Stoffels, and G. M. W. Kroesen, "Plasma chemistry and surface processes of negative ions," *Plasma Sources Science and Technology*, vol. 10, pp. 311–317, May 2001.

[97] I. A. Kossyi, A. Y. Kostinsky, A. A. Matveyev, and V. P. Silakov, "Kinetic scheme of the non-equilibrium discharge in nitrogen-oxygen mixtures," *Plasma Sources Science and Technology*, vol. 1, no. 3, p. 207, 1992.

[98] S. Panda, D. J. Economou, and M. Meyyappan, "Effect of metastable oxygen molecules in high density power-modulated oxygen discharges," *Journal of Applied Physics*, vol. 87, no. 12, pp. 8323–8333, 2000.

[99] W. Ding, L. Pinnaduwage, C. Tav, and D. McCorkle, "The role of high Rydberg states in enhanced O^- formation in a pulsed O_2 discharge," *Plasma Sources Science and Technology*, vol. 8, pp. 384–391, 1999.

[100] P. Devynck, J. Auvray, M. Bacal, P. Berlemont, J. Bruneteau, R. Leroy, and R. A. Stern, "Photodetachment technique for measuring H^- velocities in a hydrogen plasma," *Review of Scientific Instruments*, vol. 60, no. 9, pp. 2873–2878, 1989.

[101] R. Hemsworth, H. Decamps, J. Graceffa, B. Schunke, M. Tanaka, M. Dremel, A. Tanga, H. D. Esch, F. Geli, J. Milnes, T. Inoue, D. Marcuzzi, P. Sonato, and P. Zaccaria, "Status of the iter heating neutral beam system," *Nuclear Fusion*, vol. 49, no. 4, p. 045006, 2009.

[102] T. E. Sheridan, P. Chabert, and R. W. Boswell, "Positive ion flux from a low-pressure electronegative discharge," *Plasma Sources Science and Technology*, vol. 8, no. 3, p. 457, 1999.

[103] J. Los and J. Geerlings, "Charge exchange in atom-surface collisions," *Physics Reports*, vol. 190, no. 3, pp. 133 – 190, 1990.

[104] W. R. Koppers, B. Berenbak, D. Vlachos, U. van Slooten, and A. W. Kleyn, "Low-energy hydrogen-ion scattering from metal surfaces:Trajectory analysis and negative-ion formation," *Phys. Rev. B*, vol. 57, pp. 13246–13257, May 1998.

[105] B. Bahrim, B. Makarenko, and J. Rabalais, "Mechanism of negative ion formation in low velocity collisions at surfaces," *Surface Science*, vol. 542, pp. 161–166, Sept. 2003.

[106] N. Lorente, A. Borisov, D. Teillet-Billy, and J. Gauyacq, "Parallel velocity assisted charge transfer: F ion formation at Al(111) and Ag(110) surfaces," *Surface Science*, vol. 429, pp. 46–53, June 1999.

[107] B. Bahrim, D. Teillet-Billy, and J. Gauyacq, "O^- ions in front of a metal surface: Application to an O (^{1}D, ^{1}S) quenching process," *Physical Review B*, vol. 50, no. 11, 1994.

[108] D. Teillet-Billy, B. Bahrim, and J. Gauyacq, "Multi-electron and multi-state effects in the charge transfer processes between oxygen and metal surfaces," *Nuclear Instruments and Methods in Physics Research B*, vol. 100, pp. 296–301, 1995.

[109] A. G. Borisov and V. A. Esaulov, "Negative ion formation in the scattering of atoms and ions from dielectric surfaces," *Journal of Physics: Condensed Matter*, vol. 12, no. 13, p. R177, 2000.

[110] S. Mahieu, W. P. Leroy, K. Van Aeken, and D. Depla, "Modeling the flux of high energy negative ions during reactive magnetron sputtering," *Journal of Applied Physics*, vol. 106, no. 9, p. 093302, 2009.

[111] S. Seeger, K. Harbauer, and K. Ellmer, "Ion-energy distributions at a substrate in reactive magnetron sputtering discharges in Ar/H_2S from copper, indium, and tungsten targets," *Journal of Applied Physics*, vol. 105, no. 5, p. 053305, 2009.

[112] T. Welzel and K. Ellmer, "The influence of the target age on laterally resolved ion distributions in reactive planar magnetron sputtering," *Surface and Coatings Technology*, vol. 205, Supplement 2, pp. S294 – S298, 2011. 2010 Special Issue Proceedings of the 12th International Conference on Plasma Surface Engineering.

[113] M. Macias-Montero, F. J. Garcia-Garcia, R. lvarez, J. Gil-Rostra, J. C. Gonzlez, J. Cotrino, A. R. Gonzalez-Elipe, and A. Palmero, "Influence of plasma-generated negative oxygen ion impingement on magnetron sputtered amorphous sio2 thin films during growth at low temperatures," *Journal of Applied Physics*, vol. 111, no. 5, p. 054312, 2012.

[114] E. D. van Hattum, A. Palmero, W. M. Arnoldbik, H. Rudolph, and F. H. P. M. Habraken, "On the ion and neutral atom bombardment of the growth surface in magnetron plasma sputter deposition," *Applied Physics Letters*, vol. 91, no. 17, p. 171501, 2007.

[115] K. Tominaga and T. Kikuma, "Energetic oxygen ions in the reactive sputtering of the Zr target in Ar + O_2 atmosphere," *Journal of Vacuum Science & Technology A*, vol. 19, no. 4, pp. 1582–1585, 2001.

[116] S. Mráz and J. M. Schneider, "Energy distribution of O ions during reactive magnetron sputtering," *Applied Physics Letters*, vol. 89, no. 5, p. 051502, 2006.

[117] P. Pokorný, M. Mišina, J. Bulíř, J. Lančok, P. Fitl, J. Musil, and M. Novotný, "Investigation of the negative ions in Ar/O_2 plasma of magnetron sputtering discharge with Al:Zn target by ion mass spectrometry," *Plasma Processes and Polymers*, vol. 8, no. 5, pp. 459–464, 2011.

[118] M. Misina, J. W. Bradley, H. Backer, Y. Aranda-Gonzalvo, S. K. Karkari, and D. Forder, "Investigation of the pulsed magnetron discharge by time- and energy-resolved mass spectrometry," *Vacuum*, vol. 68, no. 2, pp. 171 – 181, 2002.

[119] M. Bacal, "Photodetachment diagnostic techniques for measuring negative ion densities and temperatures in plasmas," *Review of Scientific Instruments*, vol. 71, no. 11, pp. 3981–4006, 2000.

[120] S. Scribbins, M. Bowes, and J. W. Bradley, "The spatial distribution of negative oxygen ion densities in a dc reactive magnetron discharge," *Journal of Physics D: Applied Physics*, vol. 46, p. 045203, Jan. 2013.

[121] E. Bultinck and A. Bogaerts, "Particle-in-cell/monte carlo collisions treatment of an ar/o 2 magnetron discharge used for the reactive sputter deposition of tio x films," *New Journal of Physics*, vol. 11, no. 10, p. 103010, 2009.

[122] J. W. Bradley, S. K. Karkari, and A. Vetushka, "A study of the transient plasma potential in a pulsed bi-polar dc magnetron discharge," *Plasma Sources Science and Technology*, vol. 13, no. 2, p. 189, 2004.

[123] N. Paik, "Raman and XPS studies of DLC films prepared by a magnetron sputter-type negative ion source," *Surface and Coatings Technology*, vol. 200, no. 7, pp. 2170 – 2174, 2005.

[124] D. J. Kester and R. Messier, "Predicting negative ion resputtering in thin films," *Journal of Vacuum Science & Technology A*, vol. 4, no. 3, pp. 496–499, 1986.

[125] K. Ellmer and T. Welzel, "Reactive magnetron sputtering of transparent conductive oxide thin films: Role of energetic particle (ion) bombardment," *Journal of Materials Research*, vol. 27, pp. 765–779, Feb. 2012.

[126] J. J. Hanak and J. P. Pellicane, "Effect of secondary electrons and negative ions on sputtering of films," *Journal of Vacuum Science & Technology*, vol. 13, pp. 406–409, Jan 1976.

[127] P. Poolcharuansin, *The development of electrical plasma diagnostics for HiPIMS discharges*. PhD thesis, University of Liverpool, 2012.

[128] P. Vašina, M. Meško, J. C. Imbert, M. Ganciu, C. Boisse-Laporte, L. de Poucques, M. Touzeau, D. Pagnon, and J. Bretagne, "Experimental study of a pre-ionized high power pulsed magnetron discharge," *Plasma Sources Science and Technology*, vol. 16, no. 3, p. 501, 2007.

[129] H. M. Mott-Smith and I. Langmuir, "The theory of collectors in gaseous discharges," *Physical Review*, vol. 28, pp. 727–763, Oct 1926.

[130] F. F. Chen, *Chapter 4: Electric probes, Plasma Diagnostic Techniques*. New York, USA: Academic, 1965. Eds. R. H. Huddlestone and S. L. Leonard.

[131] V. A. Godyak and V. I. Demidov, "Probe measurements of electron-energy distributions in plasmas: what can we measure and how can we achieve reliable results?," *Journal of Physics D: Applied Physics*, vol. 44, p. 269501, July 2011.

[132] J. E. Allen, R. L. F. Boyd, and P. Reynolds, "The collection of positive ions by a probe immersed in a plasma," *Proceedings of the Physical Society. Section B*, vol. 70, no. 3, p. 297, 1957.

[133] I. B. Bernstein and I. N. Rabinowitz, "Theory of electrostatic probes in a low density plasma," *Physics of Fluids*, vol. 2, no. 2, pp. 112–121, 1959.

[134] F. F. Chen, "Langmuir probe analysis for high density plasmas," *Physics of Plasmas (1994-present)*, vol. 8, no. 6, pp. 3029–3041, 2001.

[135] R. F. Fernsler, "Modeling langmuir probes in multi-component plasmas," *Plasma Sources Science and Technology*, vol. 18, no. 1, p. 014012, 2009.

[136] A. Nikitin, F. E. Balghiti, and M. Bacal, "Comparison of negative ion density measurements by probes and by photodetachment," *Plasma Sources Science and Technology*, vol. 5, pp. 37–42, 1996.

[137] S. D. You, R. Dodd, a. Edwards, and J. W. Bradley, "A study of the plasma electronegativity in an argonoxygen pulsed-dc sputter magnetron," *Journal of Physics D: Applied Physics*, vol. 43, p. 505205, Dec. 2010.

[138] J. Benedikt, A. Hecimovic, D. Ellerweg, and A. von Keudell, "Quadrupole mass spectrometry of reactive plasmas," *Journal of Physics D: Applied Physics*, vol. 45, p. 403001, Oct. 2012.

[139] E. Hamers, W. van Sark, J. Bezemer, W. Goedheer, and W. van der Weg, "On the transmission function of an ion-energy and mass spectrometer," *International Journal of Mass Spectrometry and Ion Processes*, vol. 173, pp. 91–98, 1998.

[140] R. Trainham, C. Jacquot, D. Riz, A. Simonin, K. Miyamoto, Y. Fujiwara, and Y. Okumura, "Negative ion sources for neutral beam injection into fusion machines," *Review of Scientific Instruments*, vol. 69, no. 2, pp. 926–928, 1998.

[141] R. Dodd, S.-D. You, P. M. Bryant, and J. W. Bradley, "Negative ion density measurements in a reactive dc magnetron using the eclipse photodetachment method," *Plasma Sources Science and Technology*, vol. 19, no. 1, p. 015021, 2010.

[142] S. Kajita, S. Kado, and S. Tanaka, "Eclipse laser photodetachment method for avoiding probe surface ablation in negative ion measurement," *Plasma Sources Science and Technology*, vol. 14, no. 3, p. 566, 2005.

[143] L. C. Lee and G. P. Smith, "Photodissociation and photodetachment of molecular negative ions. VI. Ions in $O_2/CH_4/H_2O$ mixtures from 3500 to 8600 å," *The Journal of Chemical Physics*, vol. 70, no. 4, p. 1727, 1979.

[144] H. Amemiya and T. Suzuki, "Measurement of negative ions by photodetachment with YAG laser in discharge plasmas," *Japanese Journal of Applied Physics*, vol. 29, no. 9, pp. L1712–L1715, 1990.

[145] M. Bacal, "Plasma diagnostics in negative ion sources," *Plasma Sources Science and Technology*, vol. 2, no. 3, pp. 190–197, 1993.

[146] G. Sauerbrey, "Verwendung von schwingquarzen zur wägung dünner schichten und zur mikrowägung," *Zeitschrift für Physik*, vol. 155, pp. 206–222, 1959.

[147] J. Gudmundsson, "The high power impulse magnetron sputtering discharge as an ionized physical vapor deposition tool," *Vacuum*, vol. 84, no. 12, pp. 1360 – 1364, 2010. Selected Papers from the Proceedings of The Tenth International Symposium on Sputtering and Plasma Processes, 8th10th July 2009, Kanazawa, Japan.

[148] J. E. Allen, "Probe theory - the orbital motion approach," *Physica Scripta*, vol. 45, no. 5, p. 497, 1992.

[149] K. B. Gylfason, J. Alami, U. Helmersson, and J. T. Gudmundsson, "Ion-acoustic solitary waves in a high power pulsed magnetron sputtering discharge," *Journal of Physics D: Applied Physics*, vol. 38, pp. 3417–3421, Sept. 2005.

[150] A. D. Pajdarová, J. Vlček, P. Kudláček, and J. Lukáš, "Electron energy distributions and plasma parameters in high-power pulsed magnetron sputtering discharges," *Plasma Sources Science and Technology*, vol. 18, p. 025008, May 2009.

[151] G. Wenig, M. Schulze, P. Awakowicz, and A. V. Keudell, "Modelling of pulsed low-pressure plasmas and electron re-heating in the late afterglow," *Plasma Sources Science and Technology*, vol. 15, pp. S35–S43, May 2006.

[152] H. Bäcker, J. W. Bradley, P. J. Kelly, and R. D. Arnell, "Using langmuir probes to measure the plasma decay rates in pulsed RF magnetron discharges," *Journal of Physics D: Applied Physics*, vol. 34, no. 18, p. 2709, 2001.

[153] A. Savitzky and M. J. E. Golay, "Smoothing and differentiation of data by simplified least squares procedures," *Analytical Chemistry*, vol. 36, no. 8, pp. 1627–1639, 1964.

[154] J. W. Bradley and T. Welzel, "Physics and phenomena in pulsed magnetrons: an overview," *Journal of Physics D: Applied Physics*, vol. 42, p. 093001, May 2009.

[155] A. Rauch, R. J. Mendelsberg, J. M. Sanders, and A. Anders, "Plasma potential mapping of high power impulse magnetron sputtering discharges," *Journal of Applied Physics*, vol. 111, no. 8, p. 083302, 2012.

[156] P. Sigurjónsson, "Spatial and temporal variation of the plasma parameters in a high power impulse magnetron sputtering (HiPIMS) discharge," Master's thesis, University of Iceland, 2008.

[157] P. Poolcharuansin, M. Bowes, T. J. Petty, and J. W. Bradley, "Ionized metal flux fraction measurements in HiPIMS discharges," *Journal of Physics D: Applied Physics*, vol. 45, no. 32, p. 322001, 2012.

[158] M. Bowes, P. Poolcharuansin, and J. W. Bradley, "Negative ion energy distributions in reactive HiPIMS," *Journal of Physics D: Applied Physics*, vol. 46, p. 045204, Jan. 2013.

[159] S.-M. Kim, Y.-S. Rim, M.-J. Keum, and K.-H. Kim, "Study on the electrical and optical properties of ITO and AZO thin film by oxygen gas flow rate," *Journal of Electroceramics*, vol. 23, no. 2-4, pp. 341–345, 2009.

[160] O. Michikami and M. Asahi, "YBaCuO epitaxial film formation by magnetron sputtering with facing targets I. effects of target and substrate positions," *Japanese Journal of Applied Physics*, vol. 30, no. 5R, p. 939, 1991.

[161] V. Straňák, J. Blažek, S. Wrehde, P. Adámek, Z. Hubička, M. Tichý, P. Špatenka, and R. Hippler, "Study of electronegative Ar/O_2 discharge by means of langmuir probe," *Contributions to Plasma Physics*, vol. 48, pp. 503–508, July 2008.

[162] M. Bacal and H. Doucet, "Production of negative ion-rich plasma by electron attachment in low pressure gases," *IEEE Transactions on Plasma Science*, pp. 91–99, 1973.

[163] B. Liebig, *Invasive and non-invasive diagnostics of high power impulse magnetron sputtering (HiPIMS) discharges*. PhD thesis, University of Liverpool, 2012.

[164] P. M. Bryant and J. W. Bradley, "Optimum circuit design for the detection of laser photodetachment signals," *Plasma Sources Science and Technology*, vol. 22, p. 015014, Feb. 2013.

[165] H. Bäcker and J. W. Bradley, "Observations of the long-term plasma evolution in a pulsed dc magnetron discharge," *Plasma Sources Science and Technology*, vol. 14, no. 3, p. 419, 2005.

[166] V. Sushkov, H. T. Do, M. Cada, Z. Hubicka, and R. Hippler, "Time-resolved tunable diode laser absorption spectroscopy of excited argon and ground-state titanium atoms in pulsed magnetron discharges," *Plasma Sources Science and Technology*, vol. 22, no. 1, p. 015002, 2013.

[167] Y. Itikawa, A. Ichimura, K. Onda, K. Sakimoto, K. Takayanagi, Y. Hatano, M. Hayashi, H. Nishimura, and S. Tsurubuchi, "Cross sections for collisions of electrons and photons with oxygen molecules," *Journal of Physical and Chemical Reference Data*, vol. 18, no. 1, pp. 23–42, 1989.

[168] Y. Itikawa and A. Ichimura, "Cross sections for collisions of electrons and photons with atomic oxygen," *Journal of Physical and Chemical Reference Data*, vol. 19, no. 3, pp. 637–651, 1990.

[169] E. A. Bogdanov, A. A. Kudryavtsev, and L. D. Tsendin, "The effect of electron detachment on the diffusive decay of a low-pressure electronegative plasma," *Technical Physics Letters*, vol. 27, pp. 652–655, Aug. 2001.

[170] C. Vitelaru, D. Lundin, G. D. Stancu, N. Brenning, J. Bretagne, and T. Minea, "Argon metastables in HiPIMS: time-resolved tunable diode-laser diagnostics," *Plasma Sources Science and Technology*, vol. 21, p. 025010, Apr. 2012.

[171] M. B. Hopkins, M. Bacal, and W. G. Graham, "Enhanced volume production of negative ions in the post discharge of a multicusp hydrogen discharge," *Journal of Applied Physics*, vol. 70, no. 4, p. 2009, 1991.

[172] S. Samukawa, H. Ohtake, and T. Mieno, "Pulsetime-modulated electron cyclotron resonance plasma discharge for highly selective, highly anisotropic, and charge-free etching," *Journal of Vacuum Science & Technology A*, vol. 14, no. 6, pp. 3049–3058, 1996.

[173] T. Ahn, K. Nakamura, and H. Sugai, "Negative ion measurements and etching in a pulsed-power inductively coupled plasma in chlorine," *Plasma Sources Science and Technology*, vol. 5, pp. 139–144, 1996.

[174] M. A. Raadu, I. Axnäs, J. T. Gudmundsson, C. Huo, and N. Brenning, "An ionization region model for high-power impulse magnetron sputtering discharges," *Plasma Sources Science and Technology*, vol. 20, no. 6, p. 065007, 2011.

[175] J. A. Wagner and H.-M. Katsch, "Negative oxygen ions in a pulsed RF-discharge with inductive coupling in mixtures of noble gases and oxygen," *Plasma Sources Science and Technology*, vol. 15, no. 1, p. 156, 2006.

[176] J. T. Gudmundsson and E. G. Thorsteinsson, "Oxygen discharges diluted with argon: dissociation processes," *Plasma Sources Science and Technology*, vol. 16, pp. 399–412, May 2007.

[177] A. P. Hickman, M. Medikeri-Naphade, C. D. Chapin, and D. L. Huestis, "Fine structure effects in the O^+-O collision frequency," *Geophysical Research Letters*, vol. 24, no. 2, pp. 119–122, 1997.

[178] R. D. Kenner and E. A. Ogryzlo, "Deactivation of O_2 ($A\,^3\Sigma_u^+$) by O_2, O, and Ar," *International Journal of Chemical Kinetics*, vol. 12, no. 7, pp. 501–508, 1980.

[179] D. X. Liu, P. Bruggeman, F. Iza, M. Z. Rong, and M. G. Kong, "Global model of low-temperature atmospheric-pressure He + H_2O plasmas," *Plasma Sources Science and Technology*, vol. 19, p. 025018, Apr. 2010.

[180] A. Kudryavtsev and L. Tsendin, "On the possibility of negative ion concentration growth between pulses of discharge current in oxygen," *Technical Physics Letters*, vol. 26, no. 7, pp. 582–587, 2000.

[181] J. T. Gudmundsson, T. Kimura, and M. A. Lieberman, "Experimental studies of O_2/Ar plasma in a planar inductive discharge," *Plasma Sources Science and Technology*, vol. 8, pp. 22–30, Feb. 1999.

[182] T. Kubart, T. Nyberg, and S. Berg, "Modelling of low energy ion sputtering from oxide surfaces," *Journal of Physics D: Applied Physics*, vol. 43, no. 20, p. 205204, 2010.

[183] "SRIM: Stopping Range of Ions in Matter." Available at: http://www.srim.org, Accessed: 20-10-2012.

[184] K. V. Aeken, S. Mahieu, and D. Depla, "The metal flux from a rotating cylindrical magnetron: a Monte Carlo simulation," *Journal of Physics D: Applied Physics*, vol. 41, no. 20, p. 205307, 2008.

[185] S. M. Rossnagel, "Gas density reduction effects in magnetrons," *Journal of Vacuum Science & Technology A*, vol. 6, no. 1, pp. 19–24, 1988.

[186] G. M. Turner, "Monte Carlo calculations of gas rarefaction in a magnetron sputtering discharge," *Journal of Vacuum Science & Technology A*, vol. 13, no. 4, pp. 2161–2169, 1995.

[187] A. Palmero, H. Rudolph, and F. Habraken, "Study of the gas rarefaction phenomenon in a magnetron sputtering system," *Thin Solid Films*, vol. 515, no. 2, pp. 631 – 635, 2006. Proceedings of the Eighth International Conference on Atomically Controlled Surfaces, Interfaces and Nanostructures and the Thirteenth International Congress on Thin Films.

[188] F. Jimenez, S. D. Ekpe, and S. K. Dew, "Inhomogeneous rarefaction of the process gas in a direct current magnetron sputtering system," *Journal of Vacuum Science & Technology A*, vol. 24, no. 4, pp. 1530–1534, 2006.

[189] A. Kersch, W. Morokoff, and C. Werner, "Selfconsistent simulation of sputter deposition with the Monte Carlo method," *Journal of Applied Physics*, vol. 75, no. 4, pp. 2278–2285, 1994.

[190] T. Kubart, T. Polcar, O. Kappertz, N. Parreira, T. Nyberg, S. Berg, and A. Cavaleiro, "Modelling of magnetron sputtering of Tungsten Oxide with Reactive Gas Pulsing," *Plasma Processes and Polymers*, vol. 4, no. S1, pp. S522–S526, 2007.

[191] P. C. Smith, B. Hu, and D. N. Ruzic, "Low-energy ion-induced electron emission from gas-covered surfaces," *Journal of Vacuum Science & Technology A*, vol. 12, no. 5, pp. 2692–2700, 1994.

[192] W. Vogan, S. Walton, and R. Champion, "The role of O and Cl adsorbates on the secondary emission properties of tungsten," *Surface Science*, vol. 459, no. 1-2, pp. 14–22, 2000.

[193] W. Vogan and R. Champion, "Oxygen adsorption on a Si (100) substrate: effects on secondary emission properties," *Surface Science*, vol. 492, pp. 83–90, 2001.

[194] A. Bonanno, A. Amoddeo, and A. Oliva, "Kinetic threshold in ion-induced electron emission from polycrystalline W," *Nuclear Instruments and Methods in Physics Research Section B: Beam Interactions with Materials and Atoms*, vol. 46, no. 14, pp. 456 – 459, 1990.

[195] A. Bondi, "van der Waals volumes and radii," *The Journal of Physical Chemistry*, vol. 68, no. 3, pp. 441–451, 1964.

[196] D. Rapp and P. Englander-Golden, "Total Cross Sections for Ionization and Attachment in Gases by Electron Impact. I. Positive Ionization," *The Journal of Chemical Physics*, vol. 43, no. 5, pp. 1464–1479, 1965.

[197] U. Helmersson, M. Lattemann, J. Alami, J. Bohlmark, A. Ehiasarian, and J. Gudmundsson, "High power impulse magnetron sputtering discharges and thin film growth: A brief review," *48th Annual Technical Conference Proceedings*, pp. 458–464, April 2005. Albuquerque, NM, Society of Vacuum Coaters.

[198] J. Čapek, M. Hála, O. Zabeida, J. E. Klemberg-Sapieha, and L. Martinu, "Deposition rate enhancement in HiPIMS without compromising the ionized fraction of the deposition flux," *Journal of Physics D: Applied Physics*, vol. 46, no. 20, p. 205205, 2013.

[199] D. J. Christie, "Target material pathways model for high power pulsed magnetron sputtering," *Journal of Vacuum Science & Technology A: Vacuum, Surfaces, and Films*, vol. 23, no. 2, p. 330, 2005.

[200] J. Vlček and K. Burcalová, "A phenomenological equilibrium model applicable to high-power pulsed magnetron sputtering," *Plasma Sources Science and Technology*, vol. 19, p. 065010, Dec. 2010.

[201] M. Scherer and P. Wirz, "Reactive high rate dc sputtering of oxides," *Thin Solid Films*, vol. 119, pp. 203–209, 1984.

[202] R. Chistyakov, "High deposition rate sputtering," May 24 2005. US Patent 6,896,773.

[203] V. Straňák, A.-P. Herrendorf, S. Drache, M. Čada, Z. Hubička, M. Tichy, and R. Hippler, "Highly ionized physical vapor deposition plasma source working at very low pressure," *Applied Physics Letters*, vol. 100, no. 14, p. 141604, 2012.

[204] A. James and M. Lord, *Macmillan's Chemical and Physical Data*. London, UK: Macmillan Press, 1992.

[205] D. R. Lide, *CRC Handbook of Chemistry and Physics*. Boca Raton, FL, USA: CRC Press, 2003.

[206] N. Sakai, Y. Ebina, K. Takada, and T. Sasaki, "Electronic band structure of titania semiconductor nanosheets revealed by electrochemical and photoelectrochemical studies," *Journal of the American Chemical Society*, vol. 126, no. 18, pp. 5851–5858, 2004.

[207] G. Clarke, A. Mishra, P. J. Kelly, and J. W. Bradley, "Cathode current density distributions in high power impulse and direct current magnetron sputtering modes," *Plasma Processes and Polymers*, vol. 6, no. S1, pp. S548–S553, 2009.

[208] A. Anders, "Deposition Rates of High Power Impulse Magnetron Sputtering," *51st Annual Technical Conference Proceedings*, p. 271, April 2008. Chicago, IL, Society of Vacuum Coaters.

[209] M. Audronis, V. Bellido-Gonzalez, and B. Daniel, "Control of reactive high power impulse magnetron sputtering processes," *Surface and Coatings Technology*, vol. 204, no. 14, pp. 2159 – 2164, 2010.

[210] M. Palmucci, N. Britun, T. Silva, R. Snyders, and S. Konstantinidis, "Mass spectrometry diagnostics of short-pulsed HiPIMS discharges," *Journal of Physics D: Applied Physics*, vol. 46, no. 21, p. 215201, 2013.

Appendices

Appendix A

Tuning the EQP and data acquisition

A.1 Tuning the EQP

As shown in figure 4.1, the EQP connects to a PC through a mass spectrometer interface unit (MSIU) and is controlled via the *MASsoft* program provided by the manufacturer. Through this software it is possible to adjust the potentials applied to the electrostatic lenses of the EQP. A summary of the various components of the EQP and their corresponding electrodes is given above, however, the most routinely tuned variables are V_{ext}, V_{lens1}, V_{lens2}, V_{focus2} and V_{en} (see figure 4.11), the most appropriate values of which are dependent upon chamber geometry, discharge power, working gas pressure and ion energy.

In order to find the optimum values of each variable, the EQP is operated in *AutoTune* mode, whereby the potential applied to each electrode is scanned through a pre-set range with a maximum signal intensity found and recorded for use in subsequent experiments. Electrodes not to be tuned are set to remain constant, including the mass-selection variable which is chosen to equal the m/z value for the species of interest (e.g. $m/z = 40$ for Ar^+ or 16 for O^+). Typically, the first variable tuned is the energy analyser transmission energy, V_{en}, before tuning variables in the order of the ion flight path: V_{ext}, V_{lens1}, V_{lens2} and then V_{focus2}. The scanning ranges used in the tuning of these electrodes are listed in table A.1 (reverse polarity for negative ion sampling).

Electrode	Variable	Scanning range (V)
Energy	V_{en}	−20 to +50
Extractor	V_{ext}	−100 to 0
Lens 1	V_{lens1}	−200 to 0
Lens 2	V_{lens2}	−250 to −50
Focus 2	V_{focus2}	−370 to −50

Table A.1. Scanning ranges used for tuning the EQP. Note: reverse polarity was used for sampling negative ions.

In some instances multiple peaks occur when scanning a variable. For V_{ext}, the peak

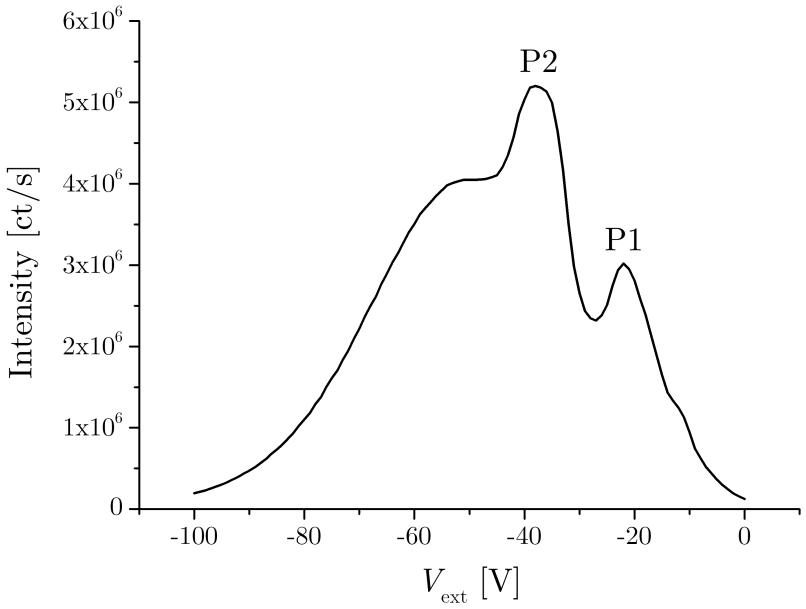

Figure A.1. Scan of extractor potential, V_{ext}, whilst sampling Ar^+ ions. A two-peak structure is evident with P1 at $V_{\text{ext}} \sim -20$ V and P2 at $V_{\text{ext}} \sim -40$ V.

closest to 0 V was chosen, as high potentials at the extractor can result in the generation of a secondary discharge between the cover plate and extractor electrode. Since ions from this secondary discharge did not originate in the main processing plasma, false signals would be recorded. Figure A.1 shows an example of a V_{ext} scan obtained by sampling Ar^+ from a magnetron sputtering discharge. Two peaks are clearly visible with P1 occurring at $V_{\text{ext}} \sim -20$ V and P2 at $V_{\text{ext}} \sim -40$ V. In this instance, $V_{\text{ext}} = -40$ was automatically selected, however, it is desirable to use the lowest value of V_{ext} for which a maximum occurs. For the next iteration of the *AutoTune* process, the scan range of V_{ext} was narrowed to -25 V to 0 V to ensure that P1 is identified as the optimum value. This procedure was used for any scan exhibiting a multiple-peak structure, with the lowest peak values chosen for V_{ext} and V_{lens1}. For V_{lens2} and V_{focus2}, peaks at higher absolute potentials are chosen and not those closest to 0 V, therefore the scanning range (table A.1) for these two variables begins at -50 V. Tuning scans of each variable were performed a minimum of three times in succession before optimum values for the electrodes were set. More scans were used if the characteristic curves did not stabilise after three cycles.

In addition to the electrostatic lens potentials, the potential applied across the dynode detector (multiplier), V_{mult}, also requires optimisation. A typical operating curve of the multiplier potential is shown in figure A.2. The multiplier potential was chosen such that the intensity of the signal did not vary significantly over a range of V_{mult} (i.e. a plateau region). A value of $V_{\text{mult}} = 2200$ V was initially adopted, with the value increasing over time as the detector degraded. A maximum value of 3000 V can be applied to the multiplier.

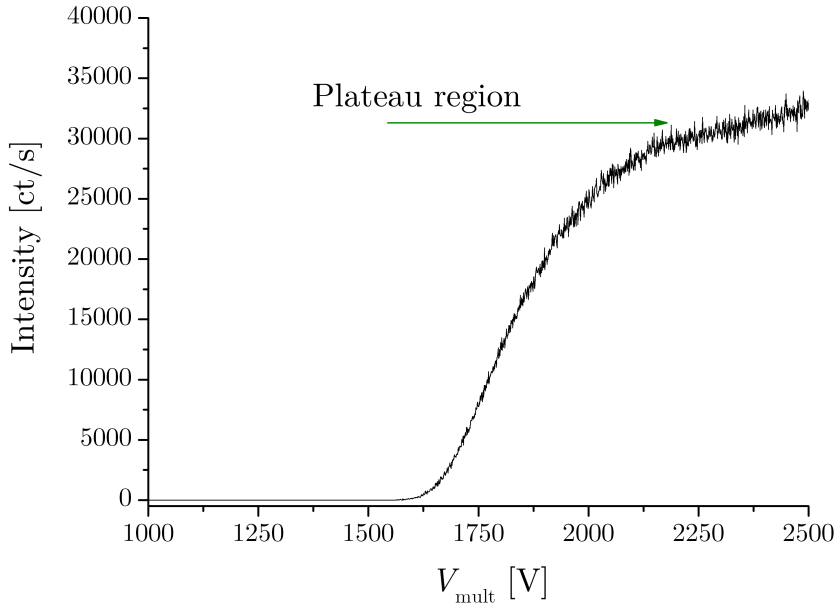

Figure A.2. Scan of multiplier potential, V_{mult}, whilst sampling Ar^+ ions. The plateau region occurs at $V_{\text{mult}} > 2200$.

A.2 Data acquisition

The system software (*MASsoft*), was used to both tune the electrode values and to acquire data. Once electrode values had been tuned, their values were imported to an experiment file to be used for data acquisition.

Ion mass spectra (m/z): The bias applied to the quadrupole was scanned to obtain count rates across a pre-set m/z range. The maximal m/z range of the EQP300 is $0.4 - 300$ amu/z, however, for applications involving exclusively light elements, this range was limited to $m/z = 0 - 100$ amu/z. The energy analyser was set to select for the most probable energy of Ar^+ and O^- ions for positive and negative ion sampling, respectively. For mass distributions presented here, three spectra were obtained and an average spectrum was calculated. Examples of the positive and negative ion mass spectra obtained from an Ar/O_2 discharge are shown in figure A.3.

Positive ion energy distributions: To obtain positive ion energy distributions (IEDs), all tuned electrodes are held constant aside from the V_{en} value, which scans the ion drift path through the energy analyser, permitting the transmission of ion energies equal to qV_{en}. The quadrupole selects for a single m/z value, allowing the investigation of separate species.

Negative ion energy distributions: Negative IEDs can be obtained in an identical

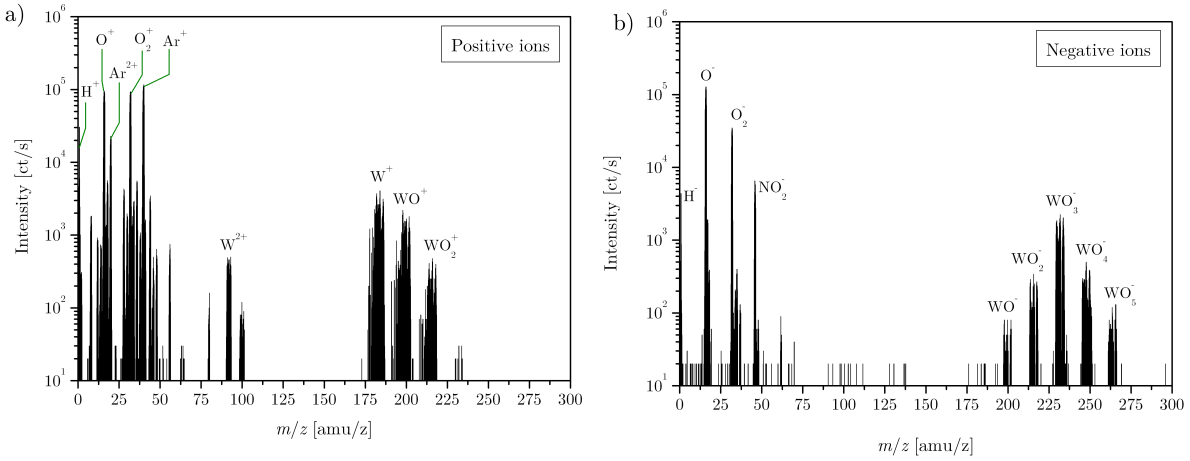

Figure A.3. Positive (a) and negative (b) ion mass spectra obtained during reactive magnetron sputtering of W in an Ar/O_2 discharge.

manner to that of positive IEDs, albeit with the polarity of the electrodes reversed. However, as the range of V_{en} is only 0 to $\pm$ 100 V, and negative ion energies can extend beyond the value of the absolute target potential (up to almost 1 kV), it isn't possible to obtain the full energy distribution by scanning V_{en}. For this reason, a different strategy was employed, namely the use of a high-voltage reference potential, $V_{ref} = 0$ to ± 1000 V. Figure A.4 shows the electrode set-up at the front of the EQP, with a reference potential applied to the energy sector. The ion pass energy is now equal to $q\,(V_{en} + V_{ref})$. Hence, by setting $V_{en} = 0$ V and scanning through values of V_{ref} it is possible to access the high-energy populations of the negative IEDs.

Time-resolved measurements: To investigate the temporal evolution of ion mass and energy distributions, the EQP can be operated in gating mode. In gating mode, the detector is controlled by a TTL-level input with a pulse width of 10 μs and is provided by a delay generator synchronized with the discharge potential pulse (see figure 4.1). The delay time was altered to sample at different points within the pulse and discharge afterglow. As the gating is applied to the back of the EQP system (i.e. the detector), one must compensate for the ion transit time through the probe when performing time-resolved measurements. According to the manufacturer, the probe transit time is given by

$$t_{trans} = s_{ext}\frac{\sqrt{2M_i}}{\sqrt{e\,(V_{en} - V_{ext})} + \sqrt{|eV_{axis}|}} + s_{en}\sqrt{\frac{M_i}{|2eV_{axis}|}} + s_{mass}\sqrt{\frac{M_i}{|2eV_{te}|}} + s_{det}\sqrt{\frac{M_i}{|eV_{dyn}|}} \quad \text{(A.1)}$$

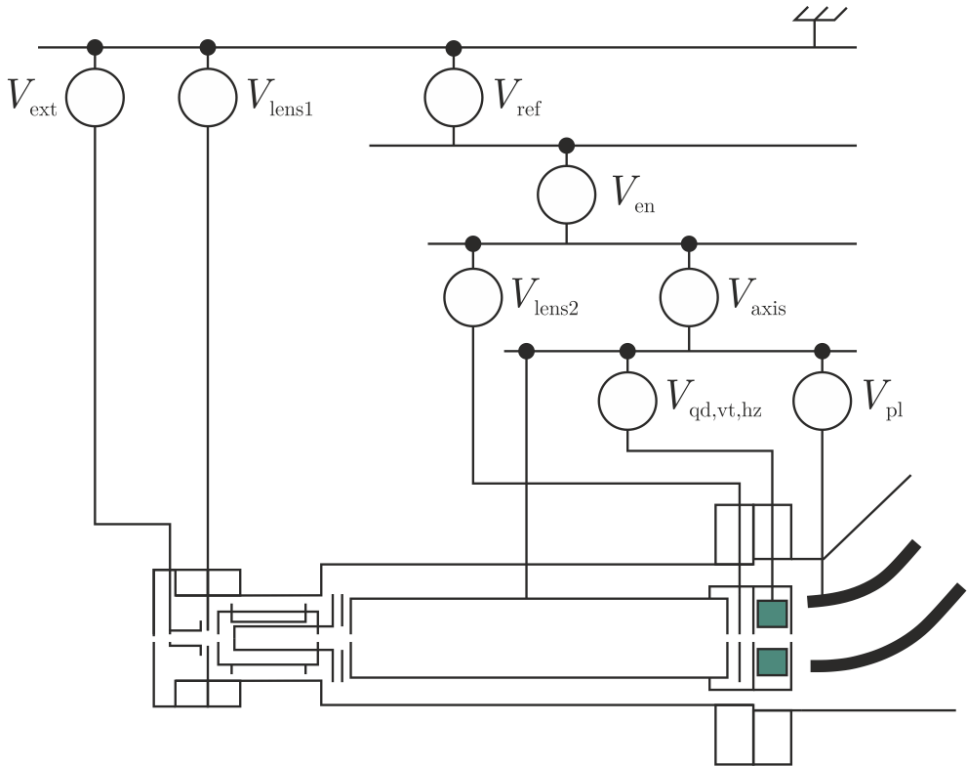

Figure A.4. Diagram of electrode voltage supplies to the front-end of the EQP, with an internal reference potential, V_{ref}.

where M_{i} is the ion mass, V_{te} and V_{dyn} are the transit energy and 1st dynode potentials, respectively. s_{ext}, s_{en}, s_{mass} and s_{det} are the flight distances through the extractor region, energy analyser, mass filter and detector region, and are equal to 4.0, 27.4, 20.0 and 1.6 cm, respectively. The default values of $V_{\text{te}} = 3$ V and $V_{\text{dyn}} = -1200$ V set by *MASsoft* were maintained with reverse polarities used for negative ion sampling. Transit times are typically of the order of $50 - 200$ μs.

Detector: The SEM detector has two main variables that can be set: settle time and dwell time. The settle time determines how long the detector pauses before counting begins and allows for electron components to settle. This was set to a value of 100 ms. The dwell time is the acquisition time of the detector and was also set to 100 ms for routine operation. However, for low count rates (i.e. $< 10^3$ counts/s) a dwell time of 300 ms was used to improve the signal-to-noise ratio.

All collected data files were exported in the comma separated variable (.csv) format and analysed using external software such as *OriginPro* and *MATLAB*.

Appendix B

Time-resolved O^- ion energy distributions

The experimental set-up used here was the same as that described in chapters 4 and 7. Time-resolved O^- ion energy distributions were measured for a reactive HiPIMS discharge in an Ar/O_2 discharge with a 20% oxygen content. The time-evolution of the discharge current and applied target potential is shown in figure B.1. The voltage pulse width and frequency were 100 μs and 100 Hz, respectively and the average discharge power was held at 100 W. The orifice of the EQP was placed 100 mm above the target surface and facing the racetrack. Triggering of the SEM detector was executed by a TTL-level input with a pulse width of 10 μs and moved through the discharge pulse using an external delay generator with a time step of 20 μs for $t = 10 - 250$ μs. Both the settle and dwell times of the detector were set to 100 ms.

As outlined in appendix A, the triggering occurs at the detector and the transit time of ions through the flightpath of the EQP must be compensated for. As provided by the manufacturer, the ion transit time through the mass spectrometer is given by

$$t_{\text{trans}} = s_{\text{ext}} \frac{\sqrt{2M_{\text{i}}}}{\sqrt{e\left(V_{\text{en}} - V_{\text{ext}}\right)} + \sqrt{|eV_{\text{axis}}|}} + s_{\text{en}} \sqrt{\frac{M_{\text{i}}}{|2eV_{\text{axis}}|}} + s_{\text{mass}} \sqrt{\frac{M_{\text{i}}}{|2eV_{\text{te}}|}} + s_{\text{det}} \sqrt{\frac{M_{\text{i}}}{|eV_{\text{dyn}}|}} \quad \text{(B.1)}$$

where the tuned electrode values are given in table B.1 alongside the flightpath distances through the EQP. The ion mass, M_{i}, for O^- ions is estimated to be 16 amu ($\sim 2.66 \times 10^{-26}$ kg), giving a transit time of 46.7 μs according to equation B.1. To access the high-energy population of the O^- energy distribution, V_{en} was set to zero and the reference potential, V_{ref}, was scanned such that $V_{\text{en}} = V_{\text{ref}}$. To calculate t_{trans} for high-energy O^- ions, V_{en} was estimated to be the value of V_{ref} at which the peak of the high-energy population occurs

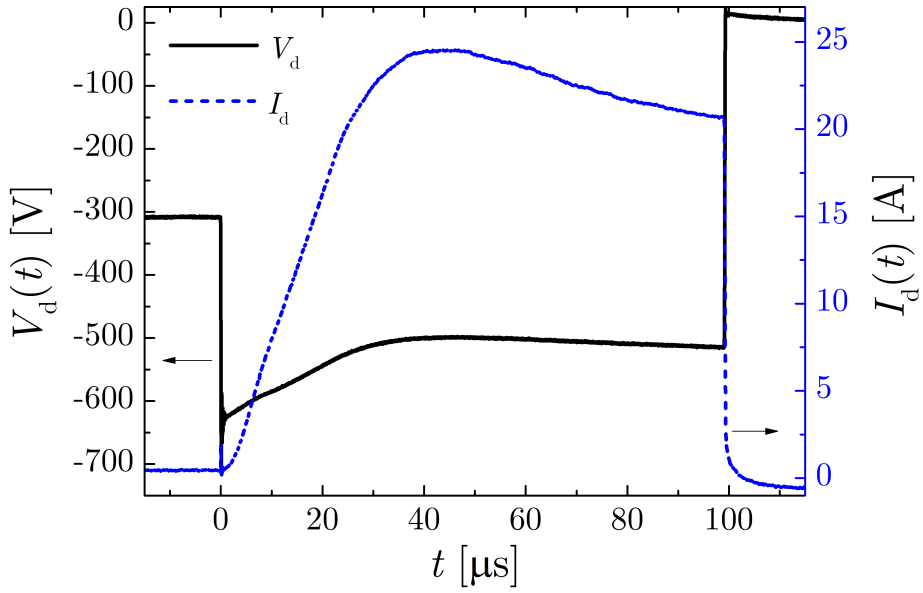

Figure B.1. The HiPIMS discharge current, $I_d(t)$, and target potential, $V_d(t)$, waveform. The pulse width was 100 μs with a repetition rate of 100 Hz and and average discharge power of 100 W.

(−520 V).

Flight distances		Electrode potentials	
Parameter	Value (cm)	Parameter	Value (V)
s_{ext}	4.0	V_{en}	0
s_{en}	27.4	V_{ext}	−59
s_{mass}	20.0	V_{axis}	40
s_{dat}	1.6	V_{te}	3
		V_{dyn}	1200

Table B.1. Flight distances and electrode potentials.

Corrected for t_{trans}, the O^- ion energy distributions measured at different times, t, within the pulse period are presented in figure B.2. From $t = 10 - 60$ μs, there is only a very small signal corresponding to the high-energy population. At $t = 70 - 110$ μs there is a significant high-energy O^- ion signal, with the maximum observed at $t = 70$ μ. As well as changes in intensity with time, the high-energy peak also experiences an energy shift due to the time-variation of the applied target potential, $V_d(t)$.

To obtain a measure of the number of O^- ions arriving at the virtual substrate (in arb. units), I_{O^-}, the ion energy distributions were integrated for $E > 425$ eV. The temporal evolution of I_{O^-} is plotted alongside $I_d(t)$ in figure B.3. There is a ~ 70 μs time delay before the appearance of high-energy O^- ions, which is not accounted for by the finite time taken to traverse the chamber from the target surface to the EQP orifice. Assuming the high-energy O^- ions posses an average kinetic energy of 520 eV,

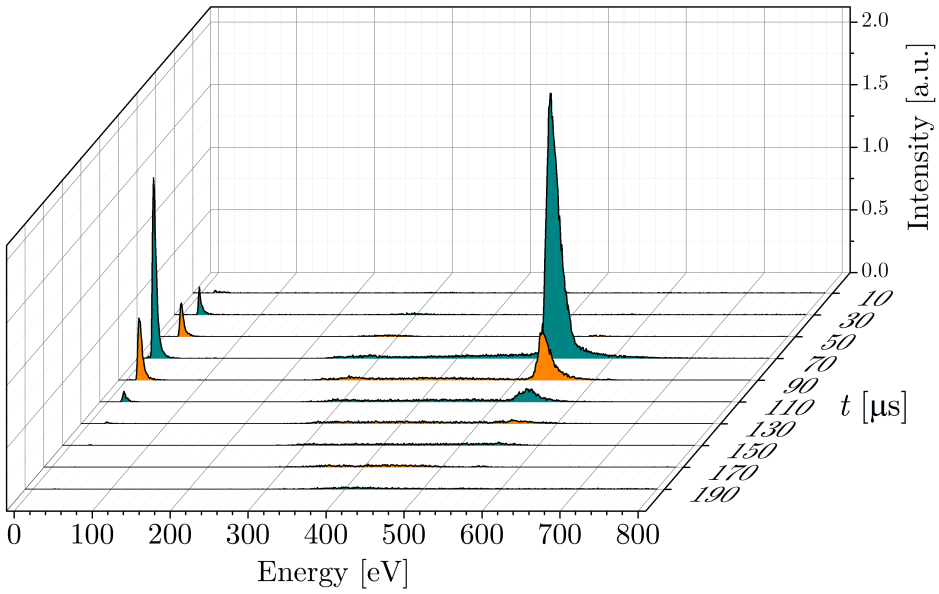

Figure B.2. O^- ion energy distributions measuring during reactive HiPIMS of Ti in an Ar/O_2 discharge at different times, t, during the pulse.

and a corresponding velocity of 79 km s^{-1}, the travel time from the target to the EQP (100 mm) is approximately 1.3 μs, which evidently doesn't account for the length of the observed delay.

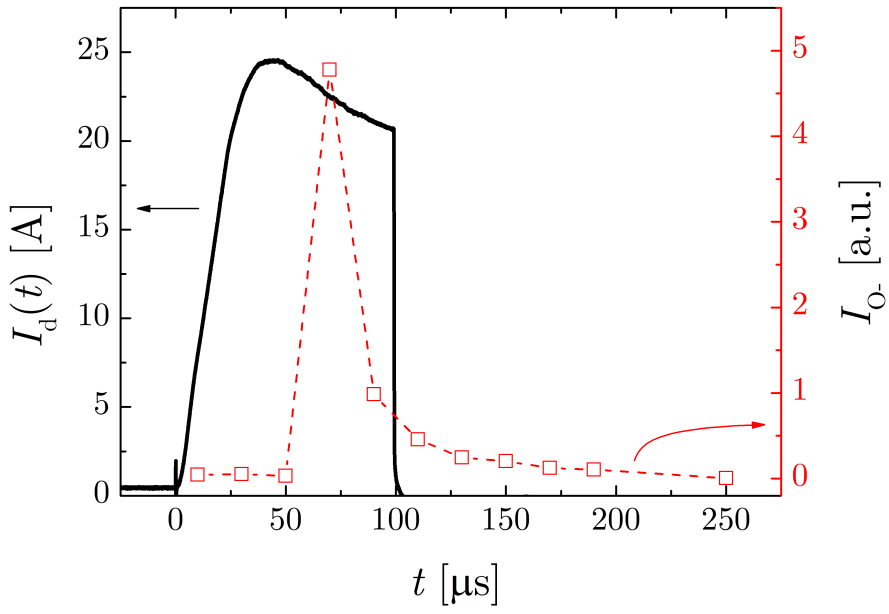

Figure B.3. The time-resolved integrated intensity of the high-energy O^- population, I_{O^-}, plotted alongside the time-varying discharge current, $I_d(t)$.

An anomalous time delay has also been reported for high-energy metallic ions in

HiPIMS by Palmucci *et al.* [210] where a 12 μs delay in the arrival of high-energy Ti^+ ions was observed after accounting for both transit times through the instrument and from the target to the orifice.

After peaking at $t = 70$ μs, I_{O^-} decays for the rest of the on-time and into the afterglow. The results presented here show that the majority of the high-energy O^- ions originate from a narrow time period during the active phase. It is suggested that since the sputtering of O^- ions occurs much more readily from a poisoned target (see figure 4.6) then the sharp decrease in I_{O^-} beyond $t = 70$ μs could be a consequence of reduced poisoning of the target surface following a period of intense sputtering during the first half of the pulse on-time. It could also be due to a change in the ISSE as the plasma transitions from a gas dominated discharge to one dominated by metallic ions. Ti has a lower ionization energy than both Ar and O, resulting in a lower ISSE (see equation 2.4) and an associated lower O^- yield as observed in chapter 7.